EMIC Wave Association With Geomagnetic Storms, the Plasmasphere, and the Radiation Belts

By

Alexa J. Halford
MS (Colorado, Boulder)

A thesis submitted to the University of Newcastle
for the degree of
Doctor of Philosophy
Faculty of Science and IT, Mathematical and Physical Sciences,
Centre for Space Physics
September 2012

MS (Colorado, Boulder) , 2012.

Typeset in LaTeX 2_ε.

0.1 Statement of Originality

This thesis contains no material which has been accepted for the award of any other degree or diploma in any university or other tertiary institution and, to the best of my knowledge and belief, contains no material previously published or written by another person, except where due reference has been made in the text. I give consent to this copy of my thesis, when deposited in the University Library**, being made available for loan and photocopying subject to the provisions of the Copyright Act 1968.
**Unless an Embargo has been approved for a determined period.

0.2 Acknowledgement of Collaboration

I hereby certify that the work embodied in this thesis has been done in collaboration with other researchers, or carried out in other institutions. I have included as part of the thesis a statement clearly outlining the extent of collaboration, with whom and under what auspices.

0.3 Acknowledgment of Authorship

I hereby certify that the work embodied in this thesis contains a published paper/s/scholarly work of which I am a joint author. I have included as part of the thesis a written statement, endorsed by my supervisor, attesting to my contribution to the joint publication/s/scholarly work.

Alexa J. Halford
MS (Colorado, Boulder)

Acknowledgements

I would like to thank my parents and siblings for all their support not just during this PhD, but throughout my life. I would like to thank my academic family including Paul Nevins, Dr. Mark Engebretson, Dr. Dan Baker, Dr. Colin Waters, Dr. Murray Sciffer and the rest of the space physics groups at Augsburg, LASP, and Newcastle. I am very grateful to Dr. Reiner Friedel and Dr. Josef Koller for their invitation out to LANL and for their help while I was visiting. I would like to thank my advisors Dr. Brian Fraser and Dr. Steve Morley for all their advice and guidance throughout the last few years. And last but not least I would like to thank my partner Dr. Seth Rittenhouse for his continued support and shoulder to lean on.

Contents

List of Figures

List of Tables

Abstract

Electromagnetic Ion Cyclotron (EMIC) waves have recently been considered an important process in the magnetosphere and in particular contribute to electron loss in the radiation belts. Here we describe the characteristics of EMIC waves under different magnetospheric conditions, their relationship to the plasmasphere and plasmaspheric plumes, and start examining the ability of EMIC waves to resonate with radiation belt electrons using data from the Combined Release and Radiation Effect Satellite (CRRES). The CRRES mission was operational from 25 July, 1990 until 21 October, 1991. It had an orbital period of 9 hrs and 52 minutes and was able to observe the magnetospheric region of $3 < L < 8$, magnetic local times (MLT) between 14:00 - 08:00 hr, and magnetic latitudes (Mlat) between $\pm 30^{\circ}$. CRRES observed 913 EMIC waves and 124 geomagnetic storms. Due to the lack of coverage around noon, the majority of EMIC waves were found to occur in the dusk sector at MLT = 15 hr and at L = 6. The highest occurrence rates for EMIC waves occurred during the main phase of geomagnetic storms, when it is expected that there may be overlap between the cold plasmaspheric plasma and the hot ring current plasma.

The role of the cold plasmaspheric plasma has been examined. It was found that EMIC waves were observed in regions with enhanced cold plasma densities under all magnetospheric conditions except for the pre-onset phase of a geomagnetic storm, which may be due to the small number of events. As CRRES was not always able to observe the boundaries of either the plasmasphere or a plasmaspheric plume during each orbit, a superposed epoch was created of the observed densities at L-values between 3 and 8 for the region between 14 hr$<$ MLT $<$18 hr, the region where plasmaspheric plumes are expected to

be observed, for each phase of the 124 geomagnetic storms observed by CRRES. During the main phase of the geomagnetic storms, an increase in the plasmaspheric number density was observed between $5 < L < 7$. This is consistent with the idea of plasmaspheric plumes forming during this phase. However, the mean location of the EMIC wave events during the main phase of a geomagnetic storm falls in the middle of the plume, not on the boundary as suggested by some theories. It has been predicted that EMIC waves need negative density gradients in order to grow to observable levels and to propagate effectively through the magnetosphere. No significant correlation between local density gradients and the occurrence of EMIC waves was found.

EMIC waves have been suggested as a mechanism for electron particle loss in the radiation belts. It was found that for electrons with energies of 1.25 - 10 MeV, there were EMIC wave events where the pitch angle diffusion extended into the loss cone. It is expected that after bounce averaging the diffusion coefficients will exceed the strong diffusion regime under most magnetospheric conditions for electron energies between 1.25 and 2 MeV. On average the highest diffusion coefficients were observed during the main phase of geomagnetic storms.

CRRES has greatly increased the communities understanding of EMIC waves and their role within the Earth-Space environment. It has been shown where and when to expect to see these waves, how plumes, but more importantly enhanced cold plasma densities, play a large role in EMIC wave occurrence, and how EMIC waves are able to resonate with radiation belt electrons contributing to the main phase loss in the radiation belts. This thesis concludes with a look towards continuations of this work and future research projects which will help address some of the raised and unanswered questions throughout the thesis.

1

The Solar - Terrestrial Environment

1.1 Introduction

Space physics studies the geophysical environment and the effects of violent space weather events which have been found to have an increased impact on our modern technology [e.g. Baker, 1998, Gonzalez et al., 1994, Kane, 2005, Lundstedt, 2006, Pulkkinen, 2007]. One of the first observed effects of space weather on technology occurred during WWI when radio controllers heard dispersed whistler waves characterised by a descending tone in the radio wave spectrum and were misidentified as falling bombs [Barkhausen, 1913, Barr et al., 2000, Kivelson and Russell, 1995, Stix, 1990]. With the advancement of ground and satellite observations we have gained a greater insight into the Sun- Earth space environment leading to more robust design of satellites, a new understanding of radio communications, information about ground induced currents associated with the

corrosion of pipe lines and overloading of electrical power grid systems, along with more accurate measurements using the Global Positioning System, GPS [Allen et al., 1959, Baker, 1998, Lundstedt, 2006]. With this advancement of technology and its dependence on the geospace environment, there has been an increased interest in understanding the near Earth - space system and its associated phenomena along with serious efforts to predict space weather effects.

The geospace environment is defined as the region of space dominated by the Earth's magnetic field [Kivelson and Russell, 1995, Lathuillere et al., 2002, Pulkkinen, 2007, Singh et al., 2010]. This ranges from the outer boundary (the magnetopause) which separates the Earth's magnetic field from the solar wind to the inner boundary, the base of the ionosphere, separating the conducting atmosphere from the neutral atmosphere [Parks, 1991]. Violent events on the Sun eject radiation and particles which can reach the Earth and cause disruptions of the geomagnetic field and its currents. These events can be observed in situ with satellites and remotely by magnetometers and radars on the ground [Baker, 1998]. It is through these and other observations combined with theoretical models and computer simulations, that we can learn more about the near - Earth space environment, the phenomena which occur in this region, and will in the future help provide predictions of space weather effects.

In this thesis we will investigate a specific topic which plays an important role in space weather monitoring, electromagnetic ion cyclotron (EMIC) waves, and their relationship to geomagnetic storms, the plasmasphere, and the radiation belts. This thesis will use data from the Combined Release and Radiation Effect Satellite (CRRES).

1.1.1 Thesis outline

This chapter will introduce the Sun-Earth system including a brief description of the magnetosphere and associated regions and currents, the ionosphere and its associated currents, particle motion and finally geomagnetic storms.

Chapter 2 reviews the theoretical background to EMIC waves, how they are generated, how they propagate, and where and when we expect to find them in the magnetosphere.

The previous work described in this chapter provides the basis for the following research in the thesis. The theory discussed helps refine the study of the in situ properties of EMIC waves and their relationship to geomagnetic storms, the dynamics of the plasmasphere and relativistic electrons in the radiation belts.

Chapter 3 contains background on the CRRES satellite, data and the methods of processing and analysing magnetic field data. A discussion is provided about the ground based indices used to define geomagnetic storms as well as the indices used to explain the plasmaspheric developments throughout geomagnetic storms.

Chapter 4 considers the general properties of EMIC waves observed during the CRRES mission, and their relationship to geomagnetic storm and non-storm times.

Chapter 5 investigates the relationship between EMIC waves and geomagnetic storms using precise storm definitions. We also compare storm definitions used by ground studies to explain differences found between ground and satellite studies.

Chapter 6 looks at the relationship between EMIC waves and the cold plasma in the plasmasphere and plasmaspheric drainage plumes. We consider the densities observed when EMIC waves are present and also show the average shape of the plasmasphere in the dusk sector during geomagnetic storms. Three case studies are presented on the association of EMIC waves with density gradients produced in the plasmapause or plasma plumes.

Chapter 7 studies the relationship between EMIC waves and high energy electrons in the radiation belts. We determine the average diffusion coefficients found under different magnetospheric conditions to help determine if EMIC waves are able to act as a loss mechanism for the radiation belts during geomagnetic storms and more specifically the main phase.

Finally in Chapter 8 we summarise the results from the thesis and suggest future avenues of research.

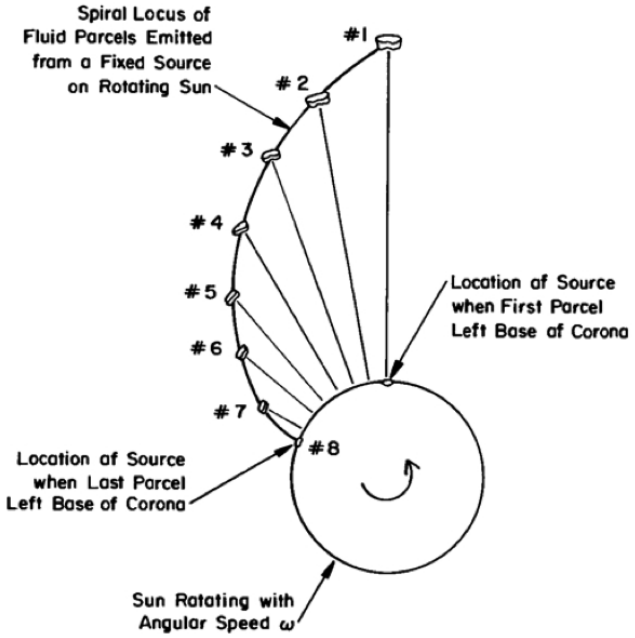

FIGURE 1.1: Schematic illustrating the path that particles from the Sun take to reach the Earth. It is the activity on the Eastern limb of the Sun that has a direct path to the Earth [Kivelson and Russell, 1995].

1.2 The Sun and Interplanetary medium

Space weather effects seen at Earth originate at the Sun, which is a giant ball of gas held together by its own gravitational force. The Sun is a differentially rotating fluid body of a diameter of 1.39×10^6 km with an average rotation time of 25.4 days, and is composed primarily of hydrogen (73%) and helium (25%) but has trace amounts of heavier particles including ionised oxygen and iron [Kivelson and Russell, 1995, Moussas et al., 2005]. The Sun's atmosphere is usually divided into separate layers according to density and temperature. There is a continuous outflow of the Sun's outer layer called the corona which is an ionised plasma. This is the solar wind (SW) and has an imbedded magnetic field, the interplanetary magnetic field (IMF) [Parker, 1965]. Sun spots and coronal holes, where many of the space weather effects originate in the Sun, can continue producing solar storms for multiple rotations allowing events to appear on a 27 day period equivalent

to one solar rotation plus the movement of the Earth around its orbit.

There are two types of storms on the Sun that are found to have large impacts on the Earth's magnetic environment; the Coronal Mass Ejection (CME) and Co-rotating Interaction Regions (CIR). A CME is a sudden explosion where large amounts of solar plasma are ejected from the corona into the solar wind [Balogh et al., 1999, Cliver and Hudson, 2002, Gosling, 1996, Wagner, 1984]. During this expulsion upwards of 10^{25} Joules of energy may be released. A CME will typically travel faster than 500 km s^{-1} in the solar wind accompanied by an increased magnetic field intensity and can sometimes be seen to appear with a period of 27 days if the region is active for more than one solar rotation [Tsurutani et al., 1997]. CIRs occur when regions of high-speed solar wind streams interact with slower upstream regions in the solar wind creating a compression region. Due to the compression a region of increased magnetic field strength is created and co-rotates with the Sun [Laughlin et al., 2008, Tsurutani et al., 2006]. CMEs are found to be more common during the solar maximum years while CIRs are commonly found during solar minima. The differences in the geo-effectiveness between these two structures as well as how they may interact with the magnetosphere will be considered in Section 1.6.

Since the solar wind conductivity is large, in this system it may be considered as infinite, and Ohm's law can be written as

$$\mathbf{E} + \frac{1}{c}\mathbf{u} \times \mathbf{B} = 0, \tag{1.1}$$

where the plasma is said to be frozen into the IMF [Kivelson and Russell, 1995, Parks, 1991]. Due to the frozen field condition, a parcel of solar plasma travels radially away from the Sun dragging the Sun's magnetic field with it while the other end of the magnetic field line is still connected to the Sun and continues to rotate. This leads to the Archimedes spiral pattern observed in the IMF and SW and presented in Figure 1.1 [Moussas et al., 2005, Wilcox, 1966]. For a frozen in plasma, the magnetic flux through a closed surface moving with the plasma will be constant, and conversely the fluid element on a magnetic field line will remain on that same field line [Parks, 1991]

$$\Phi = \int \mathbf{B} \cdot d\mathbf{S} = constant. \tag{1.2}$$

In this scenario the magnetic field lines are moving through a system carrying the particles, or equivalently, the particles are frozen into the magnetic field lines [Baumjohan and Treumann, 1997, Chen, 1984, Kivelson and Russell, 1995].

The solar wind consists predominantly of hydrogen with some helium upwards of 25%. The helium observed tends to be doubly ionised due to the high temperatures [Gosling et al., 1980, Gruntman, 1994]. Some studies have found that the ratio of singly ionised to doubly ionised helium can reach 10 - 30%. The average SW characteristics at the distance of the Earth, 1 AU (Astronomical Unit) or 1.5×10^8 km, are particle velocities of $\approx$ 450 km s^{-1}, densities of $\approx 7cm^{-3}$ and magnetic field intensities of $\approx$ 7 nT [Gosling et al., 1980, Hundhausen et al., 1970, Kivelson and Russell, 1995, Lockwood, 2005, Neugebauer and Snyder, 1966, 1967, Tascione, 1994]. These average values can change drastically on time scales of minutes, to decades with extremes of 200 km s^{-1} to exceeding 1800 km s^{-1}, and densities between 3 to 40 cm^{-3} [Kivelson and Russell, 1995, Lockwood, 2005, Tascione, 1994]. The SW at this distance is super Alfvenic and sees the magnetic field of the Earth as a rigid obstacle in its path.

1.3 The Earth's Magnetic field

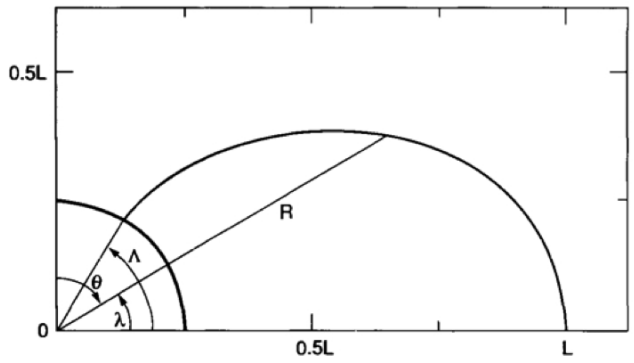

FIGURE 1.2: A visual representation of an L -Shell [Kivelson and Russell, 1995].

The Earth's dipole magnetic field is tilted away from the axis of rotation by 11° and

the axis of rotation is tilted 23.5° from the vertical with the Sun's ecliptic plane [Kivelson and Russell, 1995]. The geomagnetic field encompasses the Earth shielding it, the atmosphere, and the ionosphere from direct solar radiation and impact with the solar wind.

When discussing magnetospheric phenomena, it is easy to consider the magnetic field lines, which are defined as tangent everywhere to the magnetic field direction. The equation for a dipole field line in spherical coordinates is

$$R = Lsin^2\theta,$$

where L is the distance from the centre of the Earth to the field line crossing at the magnetic equator in planetary radii called the McIlwain L shell parameter or L-value and θ is the angle from the magnetic equatorial plane of the Earth [McIlwain, 1966, Parks, 1991] and seen in Figure 1.2. This can be expressed in terms of the magnetic latitude, λ, giving

$$R = Lcos^2(\lambda). \tag{1.3}$$

This estimate for a dipole field helps map events seen on the ground to their equatorial location in space and vice versa (a look up table for these values found within the CRRES orbit can be found in Appendix B.4). A further extension of this is to consider L-Shells, shells around the Earth of constant magnetic flux. In a perfect dipole field these L-shells would be similar to layers of an onion skin, but as the magnetosphere becomes distorted so does this analogy. The motion of particles and the adiabatic invariants used to describe the shape of the magnetosphere are given in more detail in section 1.5.

The plasma found inside the magnetosphere consists primarily of electrons and protons with small amounts of heavier ions (e.g. helium and oxygen). The source of most magnetospheric plasma is the ionosphere and atmosphere, although some hydrogen (and trace amounts of heavier ions such as helium and oxygen) can come from the solar wind. The interaction of the Earth's magnetosphere with the solar wind may be associated with either open or closed field lines. For open field lines, one end is connected to the Earth and the other is connected to the IMF while a closed field line has both ends connected to the Earth. This distinction becomes important when considering the particle movement in relation to the SW, IMF, and the geomagnetic field. Particles on closed field lines will

stay in the magnetosphere until they are either lost through collisions with the ionosphere or neutral atmosphere, or move onto open field lines. Particles on open field lines are able to enter the magnetosphere and magnetospheric particles are able to be lost to the SW.

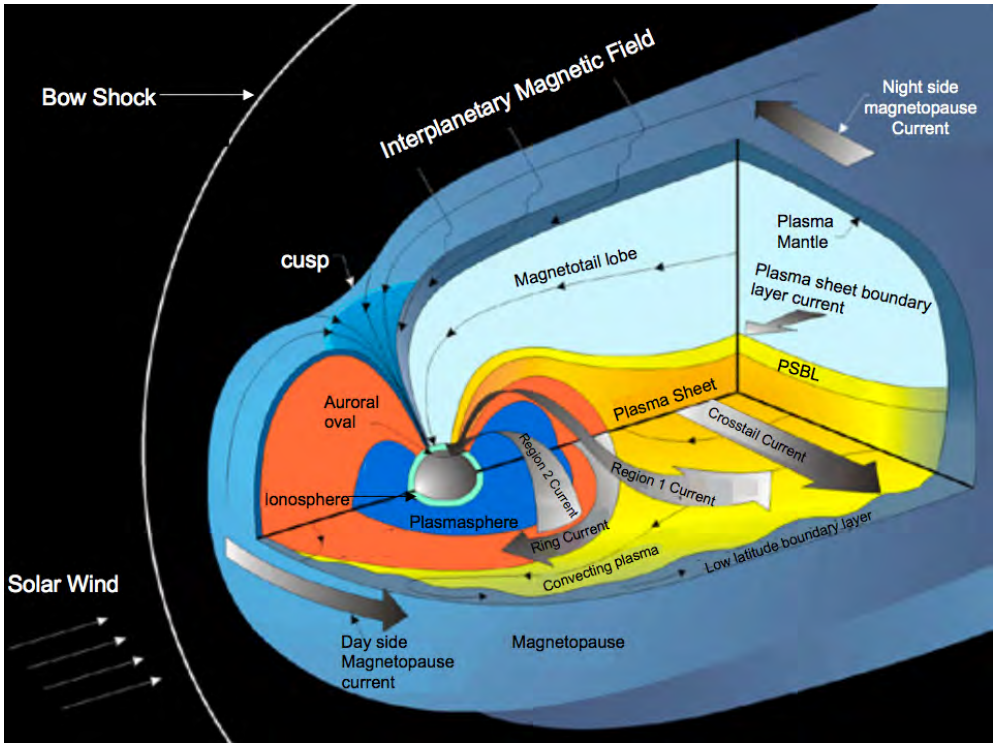

FIGURE 1.3: The magnetosphere and its different regions which have different plasma characteristics. In this cartoon the currents are highlighted [Lewis, 2011].

The Earth's magnetic field shields the ionosphere, atmosphere, and below from direct contact with the solar wind and solar radiation. As the SW and the IMF impinge on the magnetosphere, the SW compresses the dayside and stretches out the night side or tail, lengthening the magnetosphere as seen in Figure 1.3 [Dungey, 1965, Johnson, 1960]. The super Alfvenic solar wind is drastically slowed on encountering the magnetosphere creating a shocked region called the bow shock. Behind this region is a transition or boundary layer separating the SW plasma from the more stable magnetospheric plasma on closed field lines; the magnetopause. At the magnetopause the SW particles can enter

the magnetosphere through a process called reconnection [Parker, 1957, Petschek, 1964, Vasyliunas, 1975]. At the nose of the magnetosphere, there is a pressure balance between the SW dynamic pressure and the magnetospheric magnetic pressure. This stand off distance is usually between 8 and 12 R_E depending on SW conditions [Chapman and Ferraro, 1940, Kivelson and Russell, 1995, and references therein] .

When the IMF is in the southward or in the opposing direction to the geomagnetic field lines, reconnection may occur due to a breakdown of the convective limit in the inductive equation [Parker, 1957, Parks, 1991, Vasyliunas, 1975]. This process of opening the geomagnetic field lines to the solar wind allows SW particles into the magnetosphere. When the IMF reconnects with the field lines at the magnetopause, one end is connected to the Earth while the other end remains connected to the SW as shown in Figure 1.4. The end connected to the SW moves at the SW velocity and sweeps the field line anti-sunward towards the tail of the magnetosphere [Dungey, 1965], creating an increase in the magnetic flux in the tail region, which can also be depicted as an increase of energy in the tail lobes (Figure 1.3). As this pressure increases reconnection occurs in the tail leading to a release of energy out of the magnetosphere via plasmoids down the tail or into the inner magnetosphere and eventually out through the ionosphere or magnetopause. Even during northward IMF there is a section of the magnetosphere which will have a magnetic field of opposing direction, allowing reconnection to occur and thus SW energy to enter the magnetosphere (bottom Panel of Figure 1.4) though this does not add magnetic flux to the magnetotail. Reconnection is thought to be the primary process which controls the amount of energy transferred into the magnetosphere from the SW, and the convection of these field lines through the magnetosphere plays an important role in magnetospheric processes.

The amount of SW energy transmitted into the magnetosphere by reconnection is approximately controlled by the clock angle, θ_c, defined as the polar angle between the IMF projected into the y-z plane in GSM coordinates and the z-axis in GSM coordinates (described in Appendix A along with other commonly used coordinate systems) [Akasofu, 1980, 1983, Gonzalez, 1990]. The larger the southward component of the IMF, the larger the surface area over which reconnection can occur, and the more SW plasma can enter

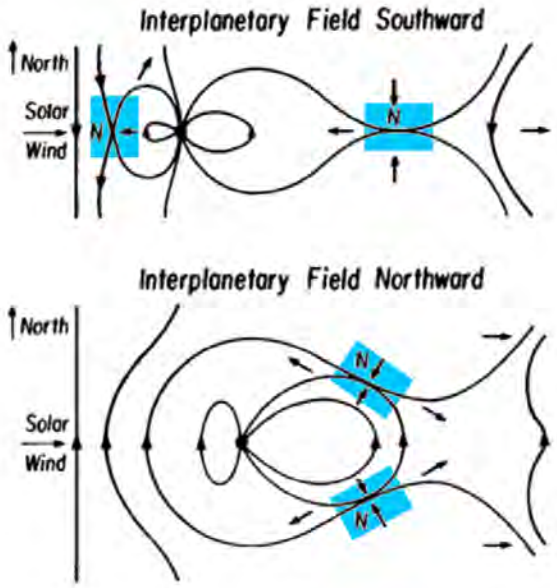

FIGURE 1.4: A cartoon of the Dungey convection model [Russell, 1999]. In the top panel southward IMF is shown to reconnect on the day side with Earth's magnetic field lines which are then dragged towards the night side by the SW and finally reconnect in the tail region. The lower panel show how northward IMF will drape around the magnetosphere and reconnect on the night side where there are regions of opposing field lines.

the magnetosphere [Akasofu, 1983, Cowley, 2003, Gonzalez, 1990]. Allowing the clock angle (which is dependent on both B_z and B_y) to determine the rate of reconnection in models states that during northward IMF there is no energy transferred between the SW and the magnetosphere. However this is not realistic since there are still areas of reconnection during northward IMF as shown in Figure 1.4 [Gonzalez, 1990]. However, the clock angle is still a useful proxy in correlating IMF conditions to large scale geomagnetic activity and space weather phenomena.

1.3.1 Regions of the Magnetosphere

Magnetotail

The magnetotail is defined as the region of the magnetosphere which is stretched downstream away from the Sun as seen in Figure 1.3. This region acts as an energy storage sink for the rest of the magnetosphere where energy can be released during storms and substorms. Within the tail is the plasma sheet which consists of hot, kilovolt particles with number densities of the order 0.1 - 1 cm^{-3}. For the most part, the plasma sheet lies on closed field lines and the particles are trapped. Plasmoids which are plasma populations on closed loops of magnetic flux not connected to either the Earth or the SW, form in the plasma sheet due to reconnection processes in the inner magnetosphere at around 20 R_E [e.g. Baker et al., 1999, Cowley, 2003, Halford et al., 2008, Ieda et al., 1998]. These plasmoids are estimated to carry about 2×10^{14} Joules of energy anti-sunward down the tail of the magnetosphere during a substorm [Ieda et al., 1998]. The length of the magnetotail depends on the current geomagnetic conditions. Dungey [1965] considered the convection pattern of magnetic footprints in the polar cap and estimated the tail to be on the order of 600 R_E in length. The width of the magnetotail can be determined by balancing the tail's magnetic pressure with the SW thermal and magnetic pressure. Typically the radius of the tail is found to be $R_T = 20R_E$.

Plasmasphere

The plasmasphere is a cold dense torus of trapped plasma containing mainly hydrogen but also helium, and oxygen ions. It is conventionally considered to start at about 1000 km above the Earth, where the hydrogen ions becomes more common than oxygen ions in the ionosphere, and extends outward towards L-shells of 4 - 8 depending on geomagnetic conditions [Borovsky and Denton, 2008, Darrouzet et al., 2008, Goldstein, 2006, Kotova, 2007, Lemaire and Gringauz, 1998, Spasojevic et al., 2003]. The first observations of the plasmasphere were made in the early 1960's and this region has been studied extensively since. Many of the earlier studies used whistler mode waves from the ground to observe

the well defined outer density gradient called the plasmapause [Carpenter, 1988, Carpenter and Smith, 1964, Fraser et al., 2005a, Horwitz et al., 1984, and references therein].

The plasmasphere consists of a cold ($\approx$ 1 eV), dense (10 - 10,000 cm^{-3}) plasma populated mainly by plasma from the dayside ionosphere, and co-rotates with the Earth [Darrouzet et al., 2008, Goldstein, 2006, Kotova, 2007, Lathuillere et al., 2002]. The plasma population is dominated by hydrogen ($\approx$ 80%) and has minor constituents of helium (10 - 20%) and ionised oxygen (depending on geomagnetic activity a few to several percent) [Goldstein, 2006]. A typical ratio of hydrogen to helium to oxygen is $\approx$ 82:15:3 [Darrouzet et al., 2009, and references therein]. Under prolonged quiet geomagnetic conditions plasmasphere dynamics are controlled by the ionospheric refilling process. When the magnetosphere is disturbed, plasmaspheric dynamics are dominated by sunward plasma convection including dayside reconnection. During this time the plasmasphere is eroded and plasmaspheric plumes, as seen in Figure 1.5, may be formed.

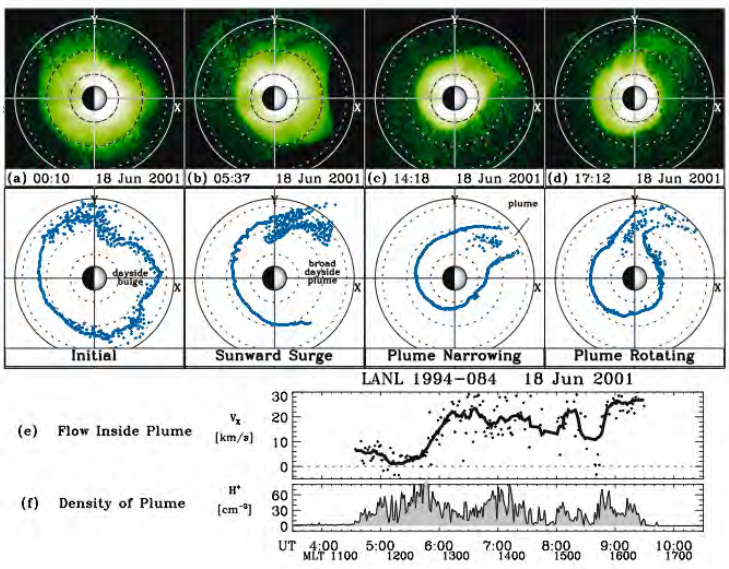

FIGURE 1.5: The top row shows the EUV plasmasphere on 18 June 2001 with the Sun at the right with the plume edges shown in the second row. The bottom row are in situ measurements from a LANL geosynchronous satellite [Goldstein, 2006]. The formation of a plume can be observed and will be discussed in more detail in Chapter 6.

The outer boundary of the plasmasphere, the plasmapause, is characterised by a steep decrease in density from 10 - 100 cm^{-3} to $\approx 1cm^{-3}$. This boundary can be found on average at 4 R_E but during quiet times may move out to $5 - 6R_E$, or beyond during extended quiet conditions [Lathuillere et al., 2002]. The plasmasphere can overlap both the radiation belts and the ring current which facilitates wave generation and particle loss processes under more active magnetospheric conditions. This process and region will be discussed in more detail in Chapters 2 and 6.

Radiation Belts

The Van Allen radiation belts consists of two belts with the inner belt located around $1.2 \leq L \leq 2R_E$ and the outer belt at $3 \leq L \leq 7R_E$ as shown in Figure 1.6 [Meredith et al., 2009, White, 1966]. They overlap the plasmasphere and are characterised by trapped particles with temperatures above 100 keV [Gintzburg, 1966, Lathuillere et al., 2002, White, 1966]. The outer belt is highly sensitive to geomagnetic storms while the inner belt is only affected by the most severe storms, for example the Halloween Storms of 2003 [Baker et al., 2004]. The slot region between these two belts is created by particle loss due to VLF Hiss dynamics in the plasmasphere, but can be filled during large geomagnetic storms. Waves in the magnetosphere are able to energise and remove particles from this region of space, which will be discussed in more detail in Chapters 2 and 7.

1.3.2 Magnetospheric Current Systems

The Chapman-Ferraro or magnetopause current, seen in Figure 1.7, is created at the boundary of the SW and the magnetosphere (Figure 1.3). When particles from the SW encounter the geomagnetic field, they experience the Lorentz force, $q(\mathbf{u} \times \mathbf{B})/c$, which is dependent on the charge of the particle. This diverts the ions and electrons in opposite directions creating a current which produces a positive increase in the magnetic field observed at the surface of the Earth at the equator. The magnetopause current closes through the crosstail current which is produced by the stretching and thinning of the magnetotail region (Figure 1.7). The tail current consists of the regions of opposed magnetic field lines

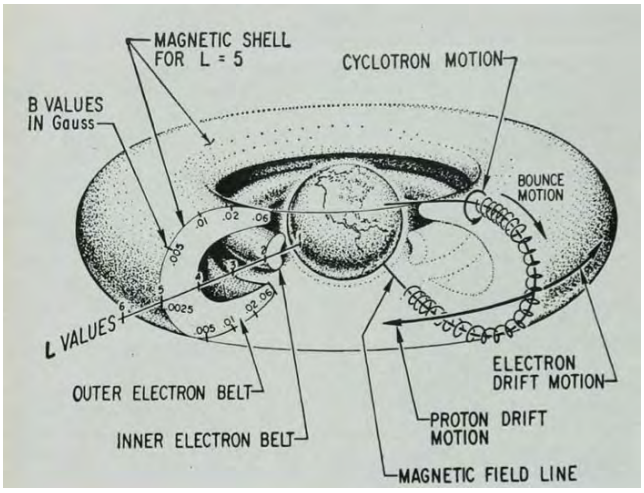

FIGURE 1.6: The radiation belts and particle motion in the inner magnetosphere [White, 1966].

near the equatorial plane which creates a current sheet with current flowing from dawn to dusk (Figure 1.3) [Akasofu and Lanzerotti, 1975, Fejer, 1965, Obayashi and Nishida, 1968, Parks, 1991]. Both the cross tail current and magnetopause current can also close through the region 1 currents into the ionosphere as shown in Figures 1.7 and 1.8. Thus an increase in magnetospheric convection can also increase the region 1 currents [Baumjohan and Treumann, 1997, Kivelson and Russell, 1995, Obayashi and Nishida, 1968, Parks, 1991].

The substorm current wedge forms due to the disruption of the cross tail current during substorm events [Baker et al., 1996, Lui, 2000]. The cross tail current then closes on the night side in the ionosphere forming a wedge shape, and accelerates particles into the inner magnetosphere. This allows for particles to be lost into the ionosphere, and creates a path for energy to be released from the tail lobes as shown in Figure 1.7.

The ring current forms a complete ring around the Earth at about 4-6 R_E, potentially overlapping with the plasmasphere and radiation belts [Daglis et al., 1999, Daglis, 2006, Friedel and Korth, 1997, Williams, 1983]. This full current is the sum of two current systems the symmetric and asymmetric, or partial, ring currents (Figure 1.7) [Daglis, 2006] and is the result of particle drifts in the magnetic field (discussed in Section 1.5).

Trapped particles, the particles that are able to complete at least one full orbit around the Earth before they are lost, create the symmetric ring current, while the asymmetric ring current contains particles which are lost before they are able to complete a full orbit. While the symmetric ring current closes with itself, the asymmetric ring current closes in the ionosphere through the region 2 currents as shown in Figures 1.7 and 1.8 [Kivelson and Russell, 1995, Parks, 1991]. Under quiet geomagnetic conditions the symmetric ring current is weak compared with the asymmetric ring current. During a geomagnetic storm, the ring current, along with the entire inner magnetosphere, is injected with an abundance of keV particles on closed field lines, and thus becomes stronger. An increase in the strength of the ring current causes a decrease in the magnetic field observed on the Equator at the Earth's surface.

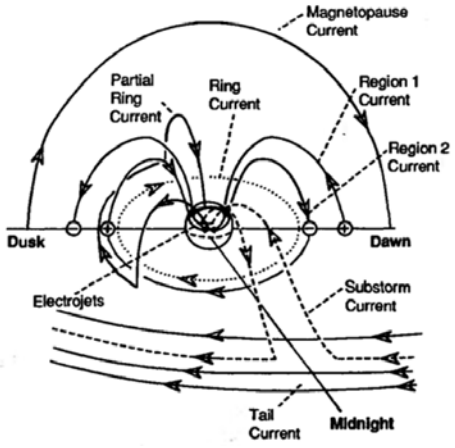

FIGURE 1.7: Cartoon of the symmetric and asymmetric ring currents. The particles in the symmetric current are trapped and their drift paths make complete orbits around the Earth. The particles in the asymmetric ring current are unable to complete a full drift orbit and are primarily lost to the magnetopause. The substorm current wedge is also shown in this figure [Kivelson and Russell, 1995].

1.4 The Ionosphere

The ionosphere is located between 50 km and 500 km above the surface of the Earth and is commonly thought of as a boundary between the neutral atmosphere and the magnetosphere, but can also be described as being embedded within the neutral atmosphere [e.g. Baumjohan and Treumann, 1997, Parks, 1991, Pierrard et al., 2009, Reynolds et al., 2001]. From an atmospheric perspective, the ionosphere is the section of the atmosphere where solar radiation ionises the atmospheric particles. Alternatively from a magnetospheric perspective the ionosphere is the part of the magnetosphere where particles can be lost due to collisions with the neutral atmospheric particles or where the conductivity is changed substantially allowing for parallel electric fields which can change a particle's pitch angle. As the ionosphere separates the magnetosphere from the neutral atmosphere and ground, waves occurring in the magnetosphere must transit through this region if they are to be observed by ground instrumentation. The wave may be affected by the ionospheric properties.

The most understood ionospheric current system is the Sq current, which is not dependent on magnetospheric activity [e.g. Kivelson and Russell, 1995, Tascione, 1994]. This current is set up by the solar heating of the ionosphere and atmosphere. On the day side of the Earth there are two cells of current centred at noon. Both cells flow from dawn to dusk with epicentres around 30° magnetic latitude. This is used to create the Dst and Sym-H indices described in Chapter 3.

There are two major currents in the ionosphere which are dependent on magnetospheric activity; the Pederson current and the Hall current, which close the region 1 and 2 currents (Figure 1.8) [e.g. Akasofu and Lanzerotti, 1975, Parks, 1991, Tascione, 1994, Willis, 1970]. The Pederson current is in the direction of the electric field and perpendicular to the local geomagnetic field. This current results from collisions between magnetospheric and atmospheric particles. The Hall current is created from the motions of both the ions and electrons due to the $\mathbf{E} \times \mathbf{B}$ drift. Since the ions are exposed to a larger area where they can come into contact with other particles, the ions are more susceptible to collisions with atmospheric particles than the electrons and more easily lost or

deflected leading to the electrons carrying the current [Tascione, 1994]. These currents are relatively localised when compared to magnetospheric currents.

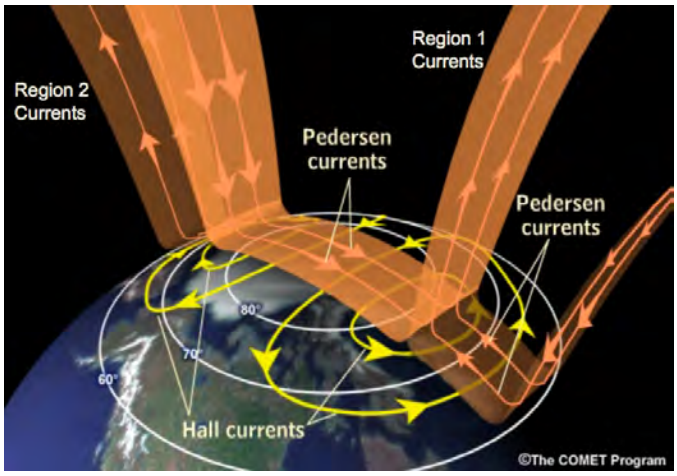

FIGURE 1.8: A cartoon of the Pedersen and Hall currents in the ionosphere [COMET Program].

1.5 Adiabatic Invariants and Particle Motion

The motion of particles in the magnetosphere dictates the development of current systems and thus induces changes to the magnetic field at the surface of the Earth. The motion of charged particles in the magnetosphere is governed by the Lorentz force:

$$F_L = q\mathbf{E} + \frac{q}{c}(\mathbf{u} \times \mathbf{B}), \tag{1.4}$$

where q is the charge of the particle, $\mathbf{E}$ is the electric field, $\mathbf{u}$ is the velocity of the particle, and $\mathbf{B}$ is the magnetic field [Baumjohan and Treumann, 1997, Chen, 1984]. In the absence of an electric field and the magnetic field is constant, the particle follows a circular path defined by the cyclotron frequency Ω_s,

$$\Omega_s = \frac{qB}{m_s c}, \tag{1.5}$$

where m is the mass of the particle species s. The particle moves in a circular path around a magnetic field line with ions and electrons rotating in opposite directions due to the

dependence on q. From the cyclotron frequency the Larmor, or gyro radius is

$$r_{L,s} \equiv \frac{u_\perp}{\Omega_s} = \frac{m_s c u_\perp}{qB}, \tag{1.6}$$

where $u_\perp$ is the perpendicular velocity of the particle. Here we can see that the Larmor radius is directly proportional to the mass of the particle, thus ions have a larger radius than electrons. Tables B.1 and B.2 show the gyro radii for electrons and protons respectively for a given L-value (assuming dipole field) and energy.

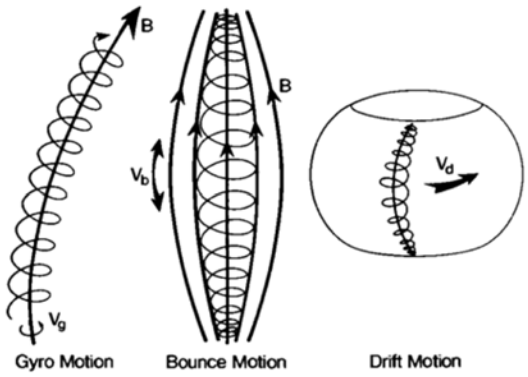

FIGURE 1.9: The motion of particles in the inner magnetosphere due to the three adiabatic invariants [Russell, 1999]. The gyro motion of the particle is the circular motion around a field line. The guiding centre is the centre of the circle traced out by the particle. The bounce motion is characterised by the motion of the particle's guiding centre traveling along the field line. The drift motion is the path that particle travels around the dipole field. The three of these particles motions trace out shells around the Earth defined as L-shells.

When the electric field is nonzero and constant in equation 1.4 the particles travel on a field line with a guiding center motion defined as the $\mathbf{E} \times \mathbf{B}$ drift [Kivelson and Russell, 1995, Parks, 1991] and written as

$$\mathbf{u}_{E\times B} = \frac{c\mathbf{E} \times \mathbf{B}}{B^2}. \tag{1.7}$$

This drift is not dependent on the charge of the particles thus both ions and electrons move in the same direction perpendicular to both $\mathbf{E}$ and $\mathbf{B}$.

Adding a non-uniform B field into equation 1.4 gives two additional drifts. The gradient B drift is caused by a change in the magnitude of the magnetic field and is expressed as

$$\begin{aligned}\mathbf{u}_{\nabla B} &= \frac{m_s c u_\perp^2}{2qB}\frac{\mathbf{B}\times\nabla B}{B^2} \\ &= \pm\frac{1}{2}u_\perp r_{L,s}\frac{\mathbf{B}\times\nabla B}{B^2}.\end{aligned} \tag{1.8}$$

As the particle gyrates, one side of the orbit sees a stronger magnetic field then the other which leads to the particle experiencing at any instantaneous moment, a change in its gyro radius [e.g. Bittencourt, 2004, Chen, 1984, Stix, 1992]. This indicates that the average drift is perpendicular to both the magnetic field and gradient of the magnetic field.

The curvature of the geomagnetic field also introduces a drift of the form

$$\mathbf{u}_c = \frac{m_s c}{qB^2}\frac{d\mathbf{E}}{dt} = \frac{m_s c v_{||}^2}{qB}\frac{\mathbf{B}\times(\mathbf{B}\cdot\nabla)\mathbf{B}}{B^3}, \tag{1.9}$$

which is due to the centripetal acceleration. As the particle travels along the curved magnetic field the particle's instantaneous gyro radius is larger away from the centre of the curvature and smaller closer in. Both the ∇B and the curvature drifts are dependent on the charge of the particle thereby creating a current where the electrons drift eastward and protons drift westward.

There are three adiabatic invariants which describe the motion of particles due to the dipole shape of the magnetosphere. Here the term adiabatic refers to remaining invariant, or changing on time scales longer then that of the adiabatic invariant. When these conditions are changed slowly, particles can become accelerated or lost from the magnetosphere as they move to different paths and regions of the magnetosphere where they may come in contact with the magnetopause or ionosphere [Baumjohan and Treumann, 1997, Chen, 1984].

1.5.1 The First Adiabatic Invariant

The first invariant describes the circular motion around a field line and is described as the conservation of μ, the magnetic moment, which is defined as

$$\mu \equiv \frac{1}{2}\frac{m u_\perp^2}{\mathbf{B}}. \tag{1.10}$$

This states that a particle will gyrate around a field line of constant $\mathbf{B}$, as illustrated in Figure 1.9 [McIlwain, 1966, Russell, 1999]. Notice that in order to conserve this quantity when $\mathbf{B}$ increases/decreases so must $u_\perp$. Equation 1.10 holds as long as $\mathbf{B}$ changes on time scales longer than the gyro-period of the particle which for an 1 MeV electron with a 60° pitch angle at L = 6 is 10^{-3} seconds [Li, 2002, Roederer, 1970].

The magnetosphere can be thought of as a set of two magnetic mirrors where the magnetic field strength increases at the ends near the Earth as shown in the middle picture of Figure 1.9 showing the bounce motion of particles. As a particle moves along the field lines to larger values of $\mathbf{B}$, μ must be conserved implying that $u_\perp$ increases [e.g. Chen, 1984]. Since the total particle energy is conserved, the parallel velocity must decrease, and when the parallel velocity goes to zero, the particle will no longer be able to travel down the field line and the force on the particle is now dominated by the gradient in the magnetic field and is reflected in the opposite direction towards the region of less dense magnetic field. These particles which are reflected at the mirroring points are defined as trapped.

The trapping of particles in the mirror is not perfect. A particle that has no perpendicular velocity will have a magnetic moment equal to zero and will never feel a gradient in the magnetic field and thus no force to slow the particle down or reflect it. The location of these mirroring points for particles that are trapped along the magnetic mirror can be determined using equation 1.10 [Chen, 1984]. If μ is conserved, it can be shown that the ratio of $u_\perp^2$ to $\mathbf{B}$ must be equal at all points, thus allowing us to determine the perpendicular velocity along the field line, and the pitch angle of the particle. Thus for two locations along a particle's path inside the magnetic mirror ($u_{o\perp}$, $\mathbf{B}_o$) and ($u'_\perp$, $\mathbf{B}'$), μ must be equivalent giving

$$\frac{u_{o\perp}^2}{2\mathbf{B}_o} = \frac{u_\perp'^2}{2\mathbf{B}'}. \tag{1.11}$$

Using the conservation of energy and the knowledge that at the turning point in the mirror (the primed values), the particle will have all of its velocity in the perpendicular direction, then $u_\perp'^2 \equiv u^2$. We can define θ as the pitch angle of a particle, the angle between the

velocity vector and the magnetic field, at the mirror point

$$\frac{\mathbf{B}_o}{\mathbf{B}'} = \frac{u_{o\perp}^2}{u_\perp'^2} = \frac{u_{o\perp}^2}{u^2}, \equiv \sin^2\theta$$

which can also be written as $\tan\theta = u_\perp/u_\parallel$. Thus, particles with small pitch angles or particles on field lines with a relatively weak maximum magnetic field will not mirror and will be lost. The range of pitch angles where this occurs is defined as the loss cone. In the magnetosphere the loss cone includes the range of pitch angles where the mirroring point is inside the ionosphere and atmosphere and the particles may be lost via collisions with particles from the local plasma population as well as through the mirror point. As particles travel along a field line, waves, parallel electric fields and changing magnetospheric conditions may change the ratio of the perpendicular to parallel velocity thus changing the pitch angle and mirroring location of a particle moving it either into or out of the loss cone.

1.5.2 The Second Adiabatic Invariant

The second adiabatic invariant, the longitudinal invariant, describes the bounce motion of a particle along a field line and is given by

$$J = \int_a^b u_\parallel ds, \tag{1.12}$$

where a and b are the start and end points along the particle path s. The equation is multiplied by 2 to get a full bounce. This states that a particle will be confined to constant magnetic lines of force as pictured in Figure 1.9 [McIlwain, 1966, Russell, 1999]. This is conserved for times when $\mathbf{B}$ changes on time scales longer than the time it takes a particle to move up and down a field line. The bounce period for an 1 MeV electron with a pitch angle of 60° at L = 6 R_E is 1 second [Li, 2002, Roederer, 1970].

1.5.3 The Third Adiabatic Invariant

The third adiabatic invariant describes the motion of the particle as it travels around the Earth as shown in Figure 1.9 [Russell, 1999]. This invariant is conserved when $\mathbf{B}$ changes

on time scales longer then the time it takes a particle to drift around the Earth. For a 1 MeV electron with a pitch angle of 60° at L = 6 R_E this is $\approx 10^3$ seconds [Li, 2002, Roederer, 1970]. A particle will travel on paths with a constant magnetic flux through each drift orbit.

$$\Phi = \int \mathbf{B} \cdot d\mathbf{S}. \tag{1.13}$$

The motion described by these three invariants around the inner magnetosphere sweep out shells with constant equatorial magnitudes of $\mathbf{B}$, assuming a dipole field. These surfaces are the L-shells defined in section 1.3. When the magnetosphere becomes distorted from the presence of the solar wind, as long as the invariants are conserved, the particles will follow their trajectories around these L-shells, though the paths will no longer be symmetric about the Earth [McIlwain, 1961]. For L-shells completely inside the magnetosphere, the particles are considered trapped and on closed field lines. If a drift path comes into contact with the magnetopause these particles may be picked up by the solar wind and are no longer considered to be trapped, but may move to open field lines. An approximation for the lifetime of a H^+ particle with a 45° pitch angle for a given density, radius from the Earth (assuming a dipole field), and a given energy can be found in Table B.3.

1.6 Geomagnetic Storms

There are many different types of magnetospheric phenomena which occur, but for this thesis we are interested in geomagnetic storms. These events have distinct magnetic signatures on the surface of the Earth and consequently geomagnetic indices have been established to help categorise these events and their magnitude [Mayaud, 1980, Sugiura, 1964]. The Disturbed storm time (Dst) index (Figure 1.10), or its higher resolution counterpart, the Sym-H index, are the most commonly used in storm studies. These indices, in units of nT, were developed to study the equatorial current systems and their affect on the magnetic field around equatorial latitudes [Kivelson and Russell, 1995, Mayaud, 1980, Sugiura, 1964]. The Kp index is a range index used to determine globally disturbed times as well as global convection which is important in plasmasphere dynamics, and thus inner

magnetospheric phenomena. The auroral electrojet indices, AE, AL, and AU help describe the conditions found in the polar regions, including magnetic perturbations due to substorms [Kamide and Akasofu, 1983]. The relevant indices for this thesis are described in greater detail in section 3.9.

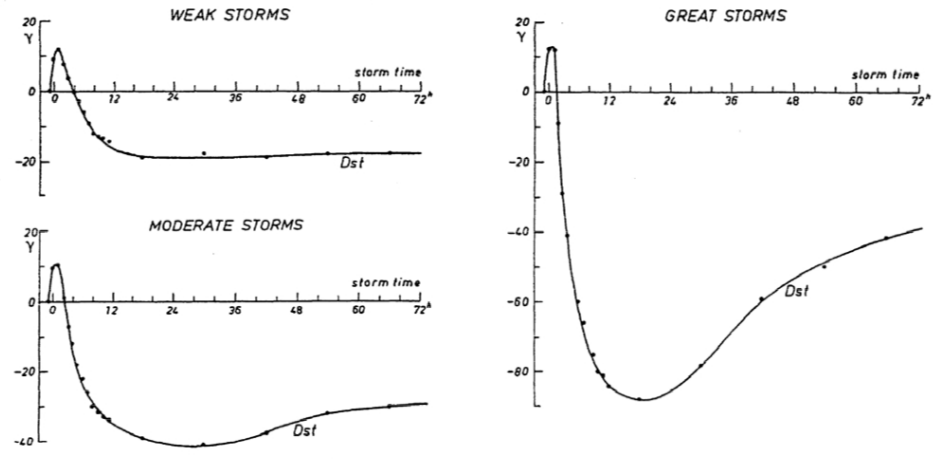

FIGURE 1.10: The average storm signatures in nT for weak, moderate, and great storms [Loewe and Prölss, 1997, and references therein].

Storms are drastic global changes in the structure of the magnetic field as well as energy release due to intense solar wind accompanied by a southward magnetic field [Chapman and Ferraro, 1940, Gonzalez et al., 1994]. For a storm to occur two conditions must be satisfied: the Earth must be in the path of a disturbed SW and the IMF must be southward [Kane, 2005]. Most storms can be divided into three phases, the sudden storm commencement (SSC), the main phase, and the recovery phase. A brief description of each phase is found below, and the definitions used in the thesis are given in Chapter 3

The Sudden Storm Commencement

Many but not all storms have identifiable SSCs. If there is a shock in the SW, a sudden storm commencement will occur. If no shock is associated with the SW driving the storm, then an SSC will not be observed [e.g. Burton et al., 1975, Kane, 2005]. With a shock,

or increase of the solar wind speed and/or density, the magnetopause is compressed towards the Earth. On the ground dayside magnetometers measure a positive increase in the magnetic field, Dst, and Sym -H. This can be seen at the start of all three storms in Figure 1.10 where the Dst is shown to increase to ≈ 10 nT around t = 0. If the IMF is southward, then there is also an increase in the rate of reconnection, thereby initiating a geomagnetic storm. If the IMF is more northward and there is insufficient reconnection to drive a storm, dayside magnetometers will still record an increase in the magnetic field, which is identified as a sudden impulse (SI). For a solar event with a slower increase in the solar wind speed and/or density, then an SSC is unlikely to be observed as the hot particle injection into the ring current will dominate the ground magnetic field signature.

The Main Phase

The storm main phase is dominated by the injection of solar wind particles into the inner magnetosphere and ring current. This phase is characterised by the stretching and thinning of the tail current which decreases the magnetic field signature on the surface of the Earth, as does the increase of particles in the ring current, and can be seen from t = 0 to t = 24 for all three storms in Figure 1.10. Storms are commonly categorised by the amount of change in the magnetic field at the surface of the Earth at the equator due to these increased currents. This relationship is approximated by the Dessler-Parker-Sckopke (DPS) equation [Dessler and Parker, 1959, Sckopke, 1966] and given by

$$\frac{\Delta B}{B_o} = \frac{2E_t}{3E_m}, \tag{1.14}$$

where ΔB is the change in the magnetic field at the surface of the Earth on the Equator, B_o is the average equatorial surface field, E_t is the total energy of the ring current particles, and E_m is the total magnetic energy of the geomagnetic field outside the Earth. This assumes that the entire change in the magnetic field is due to the ring current in a dipole field. In reality many other currents contribute to the observed change in the magnetic field such as the tail current and substorm current wedge [Baker et al., 2001, Turner et al., 2001].

During the main phase the dawn to dusk electric field intensifies leading to inward

convection and erosion of the plasmasphere. This often leads to the formation of plasma plumes in the dusk sector [Kotova, 2007, and references therein]. It is in this region where the ring current particles may overlap with cold plasmaspheric particles. The interaction of these two particle populations can for example lead to the generation of waves such as the EMIC waves [e.g. Chen et al., 2009, Kotova, 2007].

The Recovery Phase

The recovery phase is where loss processes in the magnetosphere start to overtake any new particle injections and we see the geomagnetic field recover to pre - storm levels [Gonzalez et al., 1994, Loewe and Prölss, 1997]. The rate of recovery depends on many parameters including the particle species, the energy of the particles along with their pitch angles and the L-shell location. As these particles are lost, the ring current decreases in intensity and the magnetic field on the surface of the Earth is seen to recover to its pre-storm levels. This is a very ring current biased definition and does not state well the recovering of the geomagnetic field, ionosphere, and plasmasphere.

Throughout the recovery phase, the dawn to dusk electric field tends to recover to pre-storm levels allowing for the plasmasphere to commence re-filling. The dynamics of the dawn to dusk electric field are not well described by Dst or Sym-H as these indices relate to currents in the inner magnetosphere and not magnetospheric convection which is better described by the Kp index. The plasmasphere can take 2 - 3 days to recovery to pre-storm densities at 3 R_E, and upwards of a week of continuous quiet magnetospheric conditions to re-fill to pre- storm levels outwards of 7 R_E [e.g. Darrouzet et al., 2008, Goldstein, 2006].

CME and CIR storms

As noted in Section 1.2 there are two main types of solar wind drivers for geomagnetic activity, CMEs and CIRs [Baker et al., 1996, Gopalswamy, 2008, Turner et al., 2009]. There are clear differences between storms driven by these two events. CMEs are found more often to have a clear SSC associated with them in comparison with CIRs [Borovsky

and Denton, 2006]. During the main phase CME storms are found to have a larger decrease in the Dst index than CIRs [Borovsky and Denton, 2006]. Also, the magnetic field has been found to recover more quickly after CMEs than CIRs [Laughlin et al., 2008]. A list of many of the differences between the two types of storms can be found in Table 1 of Borovsky and Denton [2006].

1.7 Thesis goals

Although there have been many studies looking at EMIC waves, there are still many questions surrounding the generation, propagation, location, and occurrence of these waves. This project is driven by three major questions;

1. What is the relationship between EMIC waves and geomagnetic storms?
2. How are EMIC waves associated with the plasmasphere, and in particular, plasmaspheric plumes?
3. Are EMIC waves a potential loss mechanism for the radiation belts during geomagnetic storms?

These three questions relate to the ultimate goal of understanding the relationship between geomagnetic storms, the plasmasphere and energy loss processes in the magnetosphere.

During 1990 and 1991 the CRRES mission was able to identify EMIC wave events between $3 < L < 8$, and magnetic local times starting at 8 magnetic local time (MLT) passing through midnight to 14 MLT. CRRES was able to collect magnetic and electric field data as well as having a suite of particle instruments. We will use this mission to look at the relationship between EMIC waves, geomagnetic storms, plasmaspheric plumes, and the radiation belts.

2

Electromagnetic Ion Cyclotron Waves

2.1 Introduction

Throughout the magnetosphere many different types of waves with frequencies < 5 Hz exist, commonly referred to as geomagnetic pulsations. The variation in amplitude of these waves can range from less than 10 pT to greater than 100 nT, and frequencies in the 1 mHz to 5 Hz band and sometimes higher, as shown in Table 2.1. Two categories of waves may be defined with respect to propagation in the magnetosphere, hydromagnetic waves and electromagnetic waves. Hydromagnetic waves are pulsations in the 1 - 100 mHz range and with wavelengths on the order of the scale size of the magnetosphere. Because of the scale of these waves, the magnetospheric cavity supports a quasi-monochromatic resonance, and consequently these waves are then not observed to propagate. The electromagnetic waves are characterised with frequencies near the ion cyclotron frequencies

and typically propagate as wave packets in the magnetosphere. The waves studied here are Electromagnetic Ion Cyclotron (EMIC) waves with frequencies below the proton cyclotron frequency, typically 0.5 - 8 Hz in the inner and middle magnetosphere.

TABLE 2.1: The IAGA classification of geomagnetic pulsations [Jacobs et al., 1964].

Notation	Period Range (s)	Frequencies
Continuous		
Pc 1	0.2 - 5	0.2 - 5.0 Hz
Pc 2	5 - 10	0.1-0.2 Hz
Pc 3	10 - 45	22.2-100.0 mHz
Pc 4	45 - 150	6.7-22.2 mHz
Pc 5	150 - 600	1.6-6.7 mHz
Impulsive		
Pi1	1 - 40	25.0-1000.0 mHz
Pi2	40 - 150	6.7-25.0 mHz

2.2 EMIC Waves

EMIC waves are generated in the equatorial region of the inner and middle magnetosphere by the ion cyclotron instability and are observed in the frequency range of $0 < \omega < \Omega_p$ where ω is the wave angular frequency, and Ω_p the proton cyclotron frequency from Equation 1.5 [Fukunishi et al., 1981, Nguyen et al., 2007]. These waves when observed on the ground are classified as Pc 1 and Pc 2 (pulsations continuous). The most common Pc 1 subclass seen as a series of wave packets are called ”pearls” and first seen at the Sodankyla and Tromso observatories by Sucksdroff and Harang in 1936. Since then, many studies have considered the generation, propagation, and other properties of these waves.

The frequency categories for Pc waves are defined in Table 2.1 [Jacobs et al., 1964]. EMIC waves are characterised by frequencies in the range of 0.1 to approximately 5 Hz and defined as the Pc 1-2 band. They are band limited, left-hand polarised waves, and

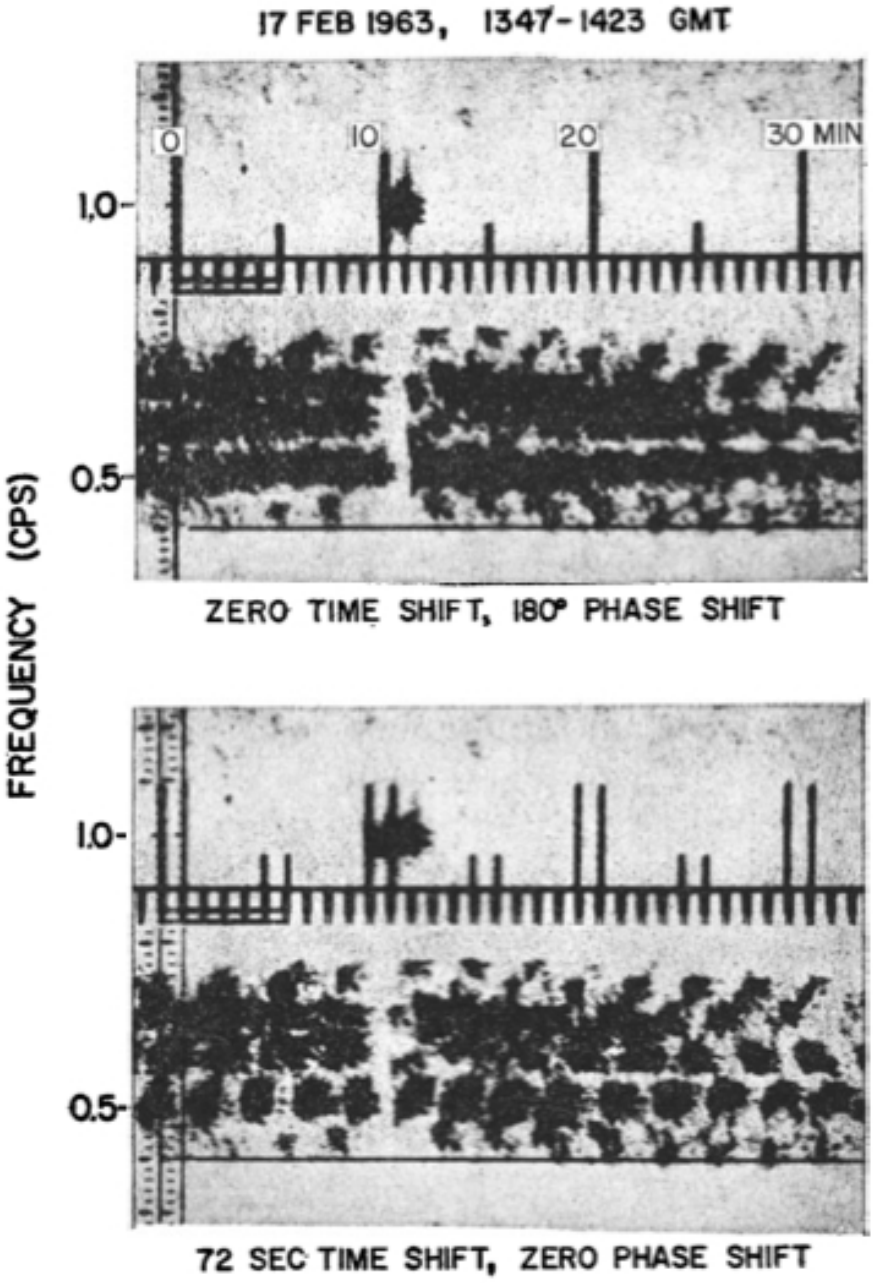

FIGURE 2.1: A pearl or structured Pc 1 pulsation event from conjugate sites showing 180° fine structure phase shift. The top panel is a superposition of the transparencies from Kauai and Tongatapu over a 35 minute interval. The lower panel was obtained by shifting the Kauai transparency to the left by 72 seconds [Tepley, 1964].

propagate along the magnetic field direction. Since EMIC waves propagate parallel to the geomagnetic field they are able to transport energy from the magnetosphere into the ionosphere [Kangas et al., 1998]. Pc 1-2 wave events detected on the ground may last from several minutes to several hours, occurring most frequently under quiet magnetospheric conditions and may show either a structured or unstructured pattern (Figure 2.1) [Kangas et al., 1998, Loto'aniu, 2003].

Kozyra et al. [1984], Anderson et al. [1992a] and references therein show that EMIC waves are generated when the temperature anisotropy is such that the perpendicular temperature of the medium energy ions (10 -100 keV) is greater then the parallel temperature. This convective instability provides the fastest growth rate for a pure proton plasma. Since the ring current generally shows a much higher temperature than the plasmasphere and plasmapause cold particle population and also tends to be anisotropic, it is thought that where and when these two particle populations overlap, wave generation would be expected to occur [Gary et al., 1994]. The wave amplification also occurs in regions with low phase velocity or a minimum in the magnetic field near the magnetic equator [Anderson, 1996, Fraser et al., 1992].

2.3 EMIC Wave Propagation

The basic concepts used to study waves in a plasma originate from Maxwell's equations, the equation of motion from the Lorentz force, and the equation of continuity [e.g. Bittencourt, 2004, Parks, 1991, Smith and Brice, 1964, Stix, 1992]

$$\nabla \cdot \mathbf{E} = 4\pi\rho_c \tag{2.1}$$

$$c\nabla \times \mathbf{B} - \frac{\delta \mathbf{E}}{\delta t} = 4\pi\mathbf{j} \tag{2.2}$$

$$c\nabla \times \mathbf{E} + \frac{\delta \mathbf{B}}{\delta t} = 0 \tag{2.3}$$

$$\nabla \cdot \mathbf{B} = 0 \tag{2.4}$$

$$F = m\frac{d\mathbf{u}}{dt} = q(\mathbf{E} + \frac{1}{c}\mathbf{u} \times \mathbf{B}) \tag{2.5}$$

$$\frac{\delta n}{\delta t} + \nabla \cdot n\mathbf{u} = 0, \tag{2.6}$$

where ρ_c is the charge density, and $\mathbf{j}$ is the current given by $\mathbf{j} = \sum nq_s\mathbf{u}_s$ which sums over the different particle populations s. To solve for the waves observed in plasmas we consider small amplitude oscillations represented by plane waves. All waves can be written as a sum of plane waves thus generality is not lost by solving under this condition. The equation for a monochromatic plane wave is given by

$$\mathbf{s}(\mathbf{r}, t) = \mathbf{s}_o e^{i(\mathbf{k}\cdot\mathbf{r} - wt)}, \tag{2.7}$$

where $\mathbf{s}_o$ is the amplitude of the wave, ω is the wave frequency, and $\mathbf{k}$ is the wave vector. The exponent represents the phase of the disturbance whereby taking the derivative with respect to time and direction provides relations for the frequency, ω, and the wave vector, k, respectively written as [Smith and Brice, 1964]

$$\omega = -\frac{\delta}{\delta t}(\mathbf{k}\cdot\mathbf{r} - wt) \tag{2.8}$$

$$\mathbf{k} = \frac{\delta}{\delta \mathbf{r}}(\mathbf{k}\cdot\mathbf{r} - wt). \tag{2.9}$$

2.3.1 Phase and Group velocity

The wave surface is displaced with a velocity called the phase velocity, v_{ph}, found by setting the derivative of the phase of the disturbance to zero. We can derive v_{ph} in the following manner,

$$\frac{\delta}{\delta t}(\mathbf{k}\cdot\mathbf{r} - wt) = 0 \tag{2.10}$$

$$\begin{aligned} \mathbf{v}_{ph} &= \frac{\omega}{k^2}\mathbf{k} \\ &= \frac{1}{\sqrt{\mu\epsilon}} \end{aligned} \tag{2.11}$$

In a collisionless plasma such as the magnetosphere we can write that $\mu = \mu_o$ and define an effective permittivity of $\epsilon(\omega) = \epsilon_o(1 - \omega_p^2/\omega^2)$ which then gives the phase velocity with respect to the plasma frequency as

$$\begin{aligned} \mathbf{v}_{ph} &= \frac{1}{\sqrt{\mu_o \epsilon_o (1 - \frac{\omega_p^2}{\omega^2})}} \\ \mathbf{v}_{ph} &= \frac{c}{\sqrt{1 - \frac{\omega_p^2}{\omega^2}}}. \end{aligned} \tag{2.12}$$

When the wave frequency is less then the plasma frequency, $\omega < \omega_p$, the phase velocity can be larger than the speed of light. Since the phase velocity depends on the wave frequency, it will spread out as time goes on and thus is dispersive [Parks, 1991].

The group velocity is then defined as the velocity at which the modulation or envelope of the wave's amplitude propagates through space.

$$\mathbf{v}_{gp} = \frac{\delta\omega}{\delta\mathbf{k}}. \tag{2.13}$$

The group velocity cannot exceed the speed of light. The energy in the wave is transported at the group velocity, thus it is this term which is of interest when determining the energy transport via waves in the magnetosphere [Bittencourt, 2004, Parks, 1991].

2.4 Ion Cyclotron Instability

Standard theories of EMIC wave generation show that waves occur when the perpendicular temperature is greater then the parallel temperature. Thus it is generally accepted that EMIC waves are generated and amplified by instabilities in the equatorial region of the magnetosphere resulting from ion cyclotron resonance due to the temperature anisotropy [Cornwall, 1965, Jacobs and Watanabe, 1964]. In this regime the cyclotron instability is not the only instability which can occur, e.g. the fire hose or Harris instabilities [Gary et al., 1976], however it is the fastest growing of the instabilities [Denton et al., 1992, Nguyen et al., 2007, Scharer, 1969, Scharer and Trivelpiece, 1967]. In the magnetosphere this temperature anisotropy can be created, although not exclusively, when KeV protons in the ring current, which provide the free energy for the instability, overlap with cool/cold background plasma in the plasmasphere, which reduces the instability threshold [Loto'aniu, 2003, Mauk and McPherron, 1980]. Winske and Omidi [1992] found that

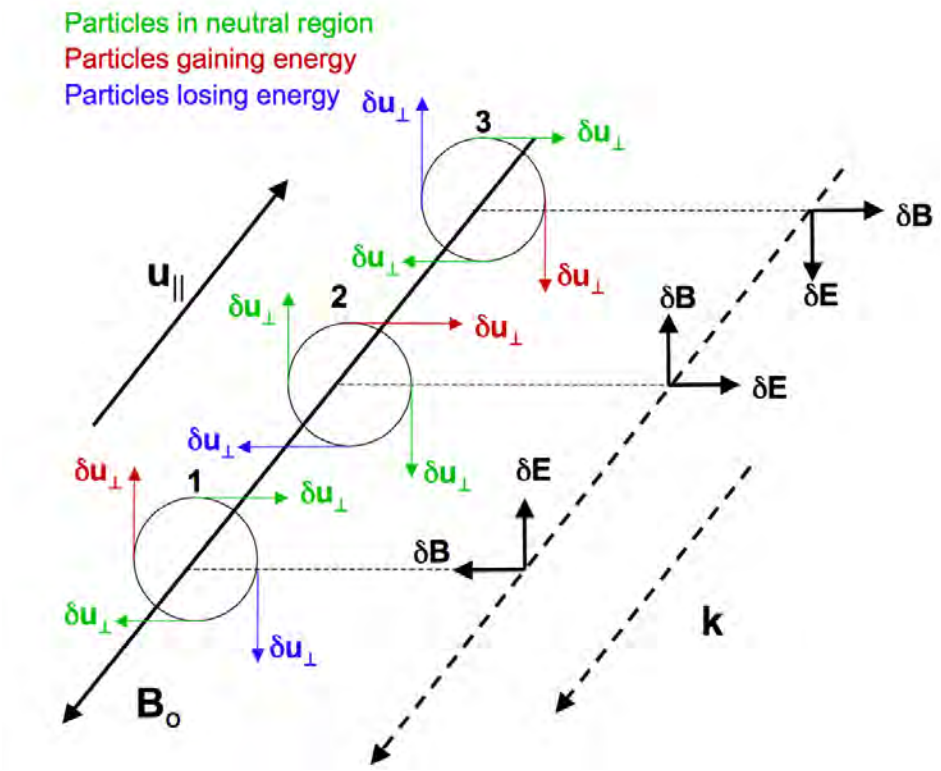

FIGURE 2.2: A schematic of the wave-particle interaction configuration for resonant particles leading to the ion cyclotron instability [modified from Mauk, 1978]. The red arrows represent particles gaining energy, the blue arrows represent particles losing energy, and the green arrows are those particles which are neither gaining or losing energy and are considered to be in a neutral region. Three wave-particle configurations are shown and labeled 1, 2, 3 where the particles are traveling anti-parallel to $\mathbf{B_o}$ and the wave is traveling along $\mathbf{B_o}$.

the instability is driven by the relative field aligned streaming of two ion components and in the electrostatic limit reduces to the non-resonant electrostatic ion cyclotron instability driven by an ion beam. They found that the growth rate of the instability tended to increase with density, velocity (compared to the Alfven velocity), and the parallel to perpendicular temperature ratio.

Strong wave-particle interaction for parallel propagation occurs when the wave perpendicular electric field vector rotates in the same sense as the local ion gyration as shown in Figure 2.2 [Stix, 1992]. Thus an ion moving along the magnetic field will see a constant

wave electric field in its reference frame and the resonant condition can then be written as

$$\mathbf{k}_{||} \cdot \mathbf{u}_{||} = \omega - l\Omega_s, \tag{2.14}$$

where $\mathbf{u}_{||}$ is the parallel velocity, $\mathbf{k}_{||}$ is the parallel wave vector, and $l\Omega_s$ is the lth harmonic of the cyclotron frequency for particle species s [Liemohn, 1967]. Given that the angular frequency $\omega = \omega_r + \omega_i$ is a complex number, then wave growth occurs if the imaginary part is greater then zero. When $\omega < l\Omega_s$, $\mathbf{k}_{||} \cdot \mathbf{u}_{||}$ is a negative number giving that the wave and particles travel in opposite directions along $\mathbf{B_o}$ [e.g. Kennel and Petscheck, 1966, Mauk, 1978]. The resonant particles where $u_\perp$ is parallel to $\delta\mathbf{E}$ (the red arrows in Figure 2.2) will then be able to gain energy and be pushed parallel to $\mathbf{B_o}$ due to the $qu_\perp \times \delta B/c$ force while the particles with $u_\perp$ antiparallel to $\delta\mathbf{E}$ (the blue arrows in Figure 2.2) will lose energy and be pushed in the anti-parallel direction to $\mathbf{B_o}$. Particles with $u_\perp$ perpendicular to $\delta\mathbf{E}$ (the green arrows in Figure 2.2) will neither gain nor lose energy and feel no force and will be referred to as neutral regions. For nearly resonant particles that have a component of $u_\perp$ which is parallel to $\delta\mathbf{E}$ (the red arrows in Figure 2.3), they will be accelerated (although not as much as those in Figure 2.2) and drift clockwise in phase space towards the stable neutral region. Likewise, for particles with a component of $u_\perp$ which is anti-parallel to $\delta\mathbf{E}$ (the blue arrows in Figure 2.3), they will lose energy and drift counterclockwise in phase space towards the stable neutral region.

Assuming an initial random phase distribution, as many particles will lose as gain energy and the wave particle interactions tends to send particles towards the stable neutral region. Depending on the initial distribution of sub or super resonant particles, there will be a net particle-to-wave or wave-to-particle exchange of energy respectively. If there is an energy exchange occurring during the ion cyclotron wave instability, then the pitch angle of the particles may be affected such that a trapped particle may now move into the loss cone or particles previously in the loss cone may become trapped [e.g. Chen, 1984, Cornwall et al., 1970, Kivelson and Russell, 1995, Mauk, 1978]. As particles become lost, the proton distribution becomes more isotropic and the free energy available to generate the instability is reduced, ultimately turning itself off [Tsurutani and Lakhina, 1997].

As previously discussed in Chapter 1, the ring current, plasmasphere, and radiation

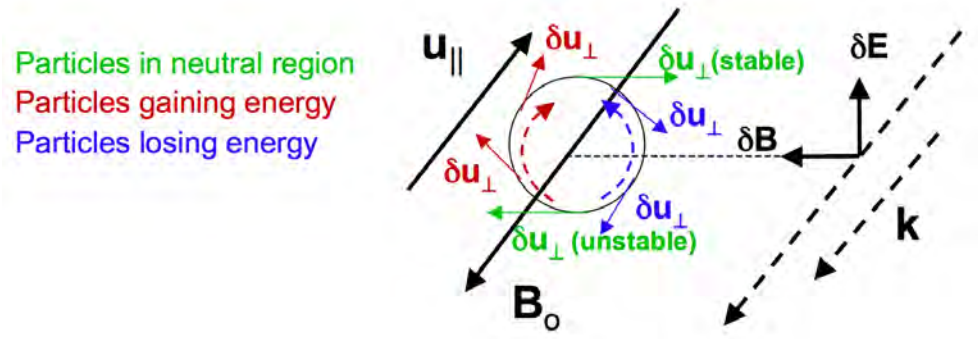

FIGURE 2.3: A schematic of the wave-particle interaction configuration for nearly resonant particles leading to the ion cyclotron instability [modified from Mauk, 1978]. The red arrows represent particles gaining energy, the blue arrows represent particles losing energy, and the green arrows are those particles which are neither gaining or losing energy and are considered to be in a neutral region. The dashed red and blue arrows represent the direction of drift for the particle velocities.

belts can overlap [Cornwall et al., 1970, Criswell, 1969, Hu and Fraser, 1994]. This leads to ideal conditions for the creation of a temperature gradient between $T_{||}$ and $T_{\perp}$ creating a non-isotropic phase distribution which can give rise to the above mentioned ion cyclotron instability. EMIC waves occurring in the region of the ring current are thought to be a loss mechanism during geomagnetic storms for ring current ions by pitch angle scattering them into the loss cone, but to what extent is still debated [Khazanov et al., 2006]. Cornwall et al. [1970] first postulated that EMIC waves and the ion cyclotron instability could be a loss mechanism for the ring current during storms when the ring current is first injected with new particles and has moved in towards the plasmasphere, and then again during the recovery phase when the plasmasphere expands outward. They proposed that the change in the thermal population of the plasma would lower the Alfven speed sufficiently to generate the ion cyclotron resonance [Cornwall, 1965, Cornwall et al., 1970]. There have been many attempts to model the interaction of EMIC waves and ring current particles in a multi - ion magnetosphere [e.g. Jordanova et al., 2001, Khazanov et al., 2006, Thorne and Horne, 1994, 2007], but debate over the mechanism which results in the wave packets being observed on the ground is ongoing.

Figure 2.4 shows the different conditions under which the ion cyclotron instability will occur during geomagnetic storms. First the plasmasphere convects from midnight to dusk creating a plasma plume. This provides the region of enhanced cold plasma needed for the ion cyclotron instability. During a storm, the ring current expands inward producing a free energy source for ion cyclotron instability. Once the instability is established the waves can propagate to the ground where they are observed after propagating through the ionosphere. The instability can also alter the pitch angles of the particles and move them into or out of the loss cone. This will partially fill the loss cone while the instability is active and lead to the decay of the ring current through particle precipitation into the ionosphere and loss of the free energy source needed to maintain the instability.

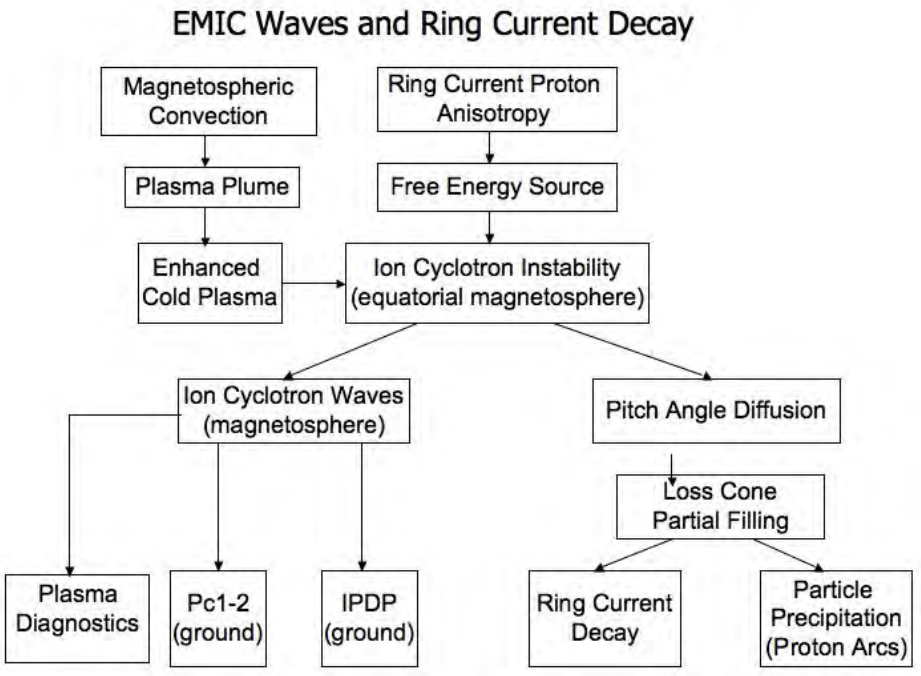

FIGURE 2.4: Flow chart of the paths for generation of the ion cyclotron instability and its affect on waves and particles [Fraser et al., 2004].

2.4.1 Dispersion relations

When studying EMIC waves the phase and group velocities can be used to calculate additional wave parameters. Thus a relation between the frequency of the wave and the wave vector $\mathbf{k}$ defined using physical parameters relating to how the wave moves through the medium, is helpful and called the dispersion relation [Parks, 1991]. These ideas in the early 1960s were first used when ground based studies of the electron whistler dispersion properties were used to probe the magnetosphere and find the electron density in the equatorial region of the plasmasphere [Carpenter and Smith, 1964].

Assuming the small perturbation approximations, Maxwell's equations, the equation of motion, and the continuity equation can now be written as

$$
\begin{aligned}
ic\mathbf{k} \times \mathbf{E}_1 &= i\omega \mathbf{B}_1 && (2.15)\\
ic\mathbf{k} \times \mathbf{B}_1 &= 4\pi \mathbf{j}_1 - i\omega \mathbf{E}_1 && (2.16)\\
i\mathbf{k} \cdot \mathbf{B}_1 &= 0 && (2.17)\\
i\mathbf{k} \cdot \mathbf{E}_1 &= 4\pi \rho_c && (2.18)\\
-i\omega \mathbf{u}_1 &= q\mathbf{E}_1 + \frac{q}{c}\mathbf{u}_1 \times \mathbf{B}_1 && (2.19)\\
-in\omega + in\mathbf{k} \cdot \mathbf{u}_1 &= 0 && (2.20)\\
n &= \frac{ck}{\omega}. && (2.21)
\end{aligned}
$$

Combining these equations and solving under different regimes for the orientation of $\mathbf{E}$ and $\mathbf{B}$ gives us the dispersion relations for waves in plasmas. Combining equations 2.15 and 2.16 gives

$$\mathbf{k} \times \mathbf{k} \times \mathbf{E}_1 = \frac{4\pi i\omega}{c^2}\mathbf{j}_1 - \frac{\omega^2}{c^2}\mathbf{E}_1. \quad (2.22)$$

The current density term can then be substituted for using either $\mathbf{j} = \sum q_s \mathbf{u}_s$ and equation 2.19, or by using Ohm's Law, equation 2.16, which simplifies if there is no magnetic field to $\mathbf{j} = \sigma \mathbf{E}$ [e.g. Chen, 1984]. Equation 2.22 can then be rewritten as

$$k^2 \mathbf{E_1} - (\mathbf{k} \cdot \mathbf{E_1})\mathbf{k} - \frac{\omega^2}{c^2}\epsilon_\mathbf{r} \cdot \mathbf{E_1} = 0, \quad (2.23)$$

where $\epsilon_{\mathbf{r}}$ is the relative dielectric tensor and has the solution

$$\epsilon_{\mathbf{r}} = \begin{bmatrix} S & iD & 0 \\ -iD & S & 0 \\ 0 & 0 & P \end{bmatrix}, \tag{2.24}$$

where

$$\begin{aligned} S &= \frac{1}{2}(R+L) \\ R &= 1 - \sum \frac{\omega_{ps}^2}{\omega(\omega+\Omega_s)} \\ L &= 1 - \sum \frac{\omega_{ps}^2}{\omega(\omega-\Omega_s)} \\ P &= 1 - \sum \frac{\omega_{ps}^2}{\omega^2} \\ D &= \frac{1}{2}(R-L), \end{aligned}$$

and s is the particle species, ω_{ps} is the plasma frequency of particle s, Ω_s is the cyclotron frequency of particle s, and ω is the wave frequency.

The dispersion relation is found when the determinant of $\epsilon_{\mathbf{r}}$ is zero. Assuming that B_o is in the z direction and k is some angle θ to B_o the determinant can be written as

$$\begin{bmatrix} S - n^2 cos^2\theta & iD & n^2 cos\theta sin\theta \\ -iD & S - n^2 & 0 \\ n^2 cos\theta sin\theta & 0 & P - n^2 sin^2\theta \end{bmatrix} \begin{bmatrix} E_x \\ E_y \\ E_z \end{bmatrix} = 0, \tag{2.25}$$

and has a solution of the form

$$(S - n^2)[PS - (Pcos^2\theta + Ssin^2\theta)n^2] - (P - n^2 sin^2\theta)D^2 = 0. \tag{2.26}$$

The general form of the dispersion relation for waves of all frequencies zero to HF propagating in a cold, homogenous, collisionless, infinite multi-component plasma with a uniform background magnetic field can then be given by the quadratic equation [e.g. Gurnett et al., 1965, Stix, 1992]

$$Am^2 - Bm + C = 0, \tag{2.27}$$

where $m = n^2$ and

$$\begin{aligned} A &= Ssin^2\theta + Pcos^2\theta \\ B &= Ssin^2\theta + PS(1 + sin\theta) \\ C &= PRL. \end{aligned}$$

If we then define a term F such that

$$F^2 = (RL - PS)^2 sin^4\theta + 4P^2D^2cos^2\theta,$$

it is easily seen that the solution for the dispersion relation is

$$n^2 = \frac{B \pm F}{2A}, \tag{2.28}$$

or in terms of the tangent of θ given as [Gurnett et al., 1965, Loto'aniu, 2003, Stix, 1992]

$$tan^2\theta = \frac{-P(n^2 - R)(n^2 - L)}{(Sn^2 - RL)(n^2 - P)}. \tag{2.29}$$

The dispersion relation can then be solved under different conditions such as when wave propagation is parallel to the magnetic field ($\theta = 0$) and the solutions reduce to $P = 0$, $n^2 = R$ for right hand propagation, and $n^2 = L$ for left hand propagation [Stix, 1992]. Cutoff frequencies are defined when $n^2 = 0$ and resonances are defined when $n^2 = \infty$. Since EMIC waves propagate parallel to the magnetic field and are in the L-mode we have

$$n^2 = \frac{c^2k^2}{\omega^2} = 1 - \sum \frac{\omega_{ps}^2}{\omega(\omega - \Omega_s)}.$$

By splitting the electrons from the ions in the sum, the dispersion relation can be rewritten as

$$\frac{c^2k^2}{\omega^2} = 1 - \frac{\omega_{pe}^2}{\omega(\omega + \mid \Omega_e \mid)} - \sum \frac{\omega_{ps}^2}{\omega(\omega - \Omega_s)}. \tag{2.30}$$

2.4.2 Propagation in a multi-component plasma

It has been observed that heavy ions in the generation region for EMIC waves can greatly affect their generation, propagation, and absorption properties [Albert, 2003, Summers and Thorne, 2003]. If we assume a cold uniform neutral plasma $N_o = \sum_s N_s$ where N_o is

the number density of cold electrons and N_s is the number density of ion species s, with a uniform background magnetic field in a multi-ion plasma with hydrogen, helium and oxygen ions, the particular solution for the dispersion relation for the left hand polarised EMIC wave from Equation 2.30 is then given as

$$\frac{c^2k^2}{\omega^2} = 1 - \frac{\omega_{pe}^2}{\omega(\omega + \mid \Omega_e \mid)} - \sum_{s=1}^{3} \frac{\omega_{ps}^2}{\omega(\omega - \Omega_s)}, \tag{2.31}$$

where the sum is over the different ion populations (1 = hydrogen (protons), 2 = helium, 3 = oxygen; subsequent numbering of parameters will follow this notation) [Summers and Thorne, 2003]. By expanding and substituting in $\omega_{pe}^2 = (m_s\omega_{ps}^2)/(m_e\eta_s)$ where $\eta_s = N_s/N_o$, M_s is the mass number of ion species s ($M_s = m_s/m_p$) giving $m_1 = m_p$, $m_2 = M_2m_p$, and $m_3 = M_3m_p$ for the relative masses and $\Omega_1 = \Omega_p$, $\Omega_2 = \Omega_1/M_2$, $\Omega_3 = \Omega_1/M_3$, equation 2.30 becomes

$$\frac{c^2k^2}{\omega^2} = 1 - \frac{\omega_{pe}^2}{\omega\Omega_e(\omega/\Omega_e + 1)} - \sum_{s=1}^{3} \frac{\eta_s m_e\omega_{pe}^2}{M_s m_p\omega(\omega - \Omega_1/M_s)}. \tag{2.32}$$

Rearranging the equation and letting $X = \omega/\Omega_1$, $\epsilon = m_e/m_p$, and $\Omega_e = \Omega_1/\epsilon$ gives

$$\frac{c^2k^2}{\omega^2} = 1 - \frac{\omega_{pe}^2}{\omega\Omega_e(1 + \epsilon X)} - \sum_{s=1}^{3} \frac{\eta_s\omega_{pe}^2}{\Omega_e\omega(M_sX - 1)}. \tag{2.33}$$

Factoring out $\omega_{pe}^2/(\Omega_e\omega)$ gives

$$\frac{c^2k^2}{\omega^2} = 1 - \frac{\omega_{pe}^2}{\omega\Omega_e}[\frac{1}{(1 + \epsilon X} + \sum_{s=1}^{3} \frac{\eta_s}{(M_sX - 1)}]. \tag{2.34}$$

Expanding and substituting $\alpha^* = \Omega_e^2/\omega_{pe}^2$, and using $X\epsilon = \omega/\Omega_e$ gives the non-dimensional form [Summers and Thorne, 2003]

$$\frac{c^2k^2}{\omega^2} = \frac{1}{u^2} = 1 - \frac{1}{\alpha^*\epsilon X}(\frac{1}{1 + \epsilon X} + \frac{\eta_1}{X - 1} + \frac{\eta_2}{4X - 1} + \frac{\eta_3}{16X - 1}). \tag{2.35}$$

It can then easily be shown that equation 2.30 simplifies to the cold single ion plasma dispersion relation when the number densities of the heavier ions are set to zero. The values for the parameters in the dispersion relation will change under different magnetospheric conditions. α^* plays an important role in the cold plasma theory and changes

with geomagnetic conditions. Summers and Thorne [2003] used empirical data to look at α^* during periods of $K_p = 1$, 3, and 5 as plotted in figure 2.5 against L, and found that $\alpha^* = 10^{-3}$ is sufficient to ensure minimum electron resonant energies of ≤ 1 MeV.

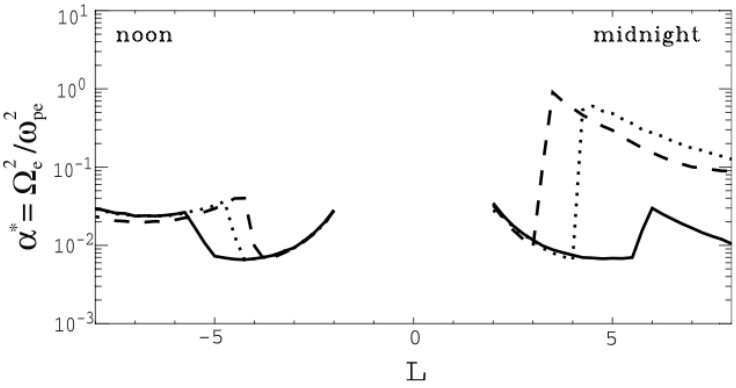

FIGURE 2.5: Profiles of α^* versus geomagnetic radial distance. The Solid, dashed, and dotted line are for increasingly levels of geomagnetic activity, $K_p = 1$, 3, and 5. The minimum value of α^* characterizes the plasmapause [Summers and Thorne, 2003].

2.4.3 Cutoff, Resonance, and Crossover

As stated previously, cutoff frequencies are given by $n^2 = 0$ and resonances by $n^2 = \infty$. Thus cutoff frequencies will occur when $P = 0$, $R = 0$, or $L = 0$ and resonances occur when $tan^2\theta = -P/S$. If we assume that θ is real, then F^2 is positive and n is either completely real or imaginary. Thus when n^2 goes through zero, the wave changes from a region of possible propagation to a region of spatial decay, attenuation, or growth due to instability mechanisms and a reflection occurs (Figure 2.6) [Lund and LaBelle, 1997, Stix, 1992]. As n^2 goes through ∞, absorption and/or reflection is able to occur [Gurnett et al., 1965, Stix, 1992]. In Equation 2.28 there are two branches given for the wave normal surface n^2 which results in 4 of the 8 Clemmow-Mullaly-Allis topological surfaces shown in Figure 2.6 and labeled 1, 2, 3, 4 [Allis, 1959, Papa and Allis, 1961]. When there are multiple ion species there are additional cyclotron resonances, crossovers, and cutoff frequencies for each species [Lund and LaBelle, 1997]. This can be seen during CRRES

orbit 827 (Figure 2.7) where EMIC waves are observed in the helium and hydrogen bands from 01:00 - 01:15 and 01:40 - 02:00.

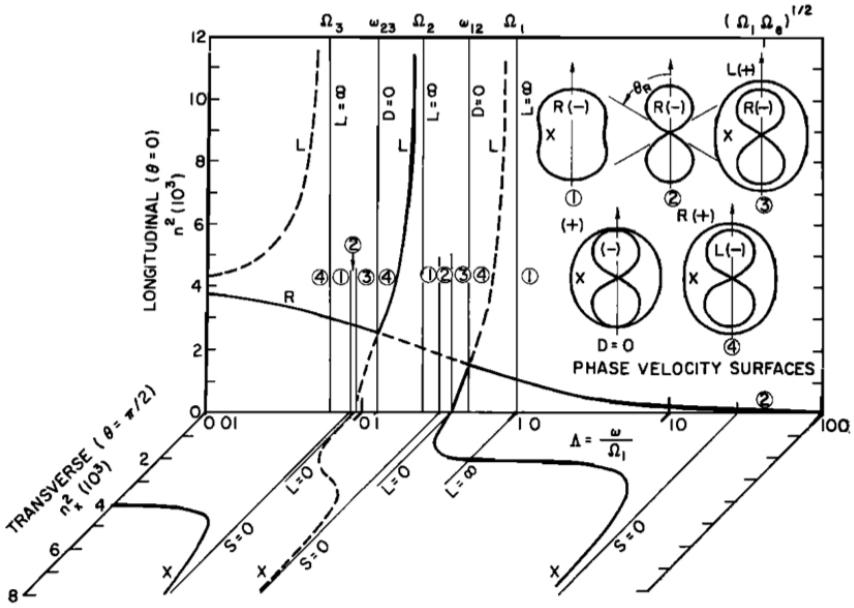

FIGURE 2.6: A plot of the refractive index n^2 for the R, L, and X waves and wave-normal surfaces in each bounded volume [Gurnett et al., 1965]. The crossover bands are labeled $\omega_{1,2}$ between the H^+ and He^+ band and $\omega_{2,3}$ between He^+ and O^+ band. The numbers 1,2,3,4 refer to the topological solutions for the two branches of the wave normal solution.

There are two principal resonances which occur at $\theta = 0$ and $\theta = \pi/2$. For the first case when $\theta = 0$, the resonance occurs when $S = \frac{1}{2}(R + L) \rightarrow \pm\infty$. When $R \rightarrow \infty$ this corresponds to the electron cyclotron resonance for positive ω, and when $L \rightarrow \infty$ this corresponds to the ion cyclotron resonance for positive ω. For $\theta = \pi/2$ resonances occur when $S = 0$ [Lund and LaBelle, 1997, Stix, 1992].

The crossover frequency is defined as the frequency where the right hand and left hand modes are equal (labeled $\omega_{1,2}$ for crossover between the H^+ and He^+ band and $\omega_{2,3}$ for the crossover between He^+ and O^+ band in Figure 2.6). This condition is satisfied when D = 0 [Gurnett et al., 1965, Smith and Brice, 1964], and only occurs when the plasma has positive ions with different charge to mass ratios for frequencies greater then the minimum

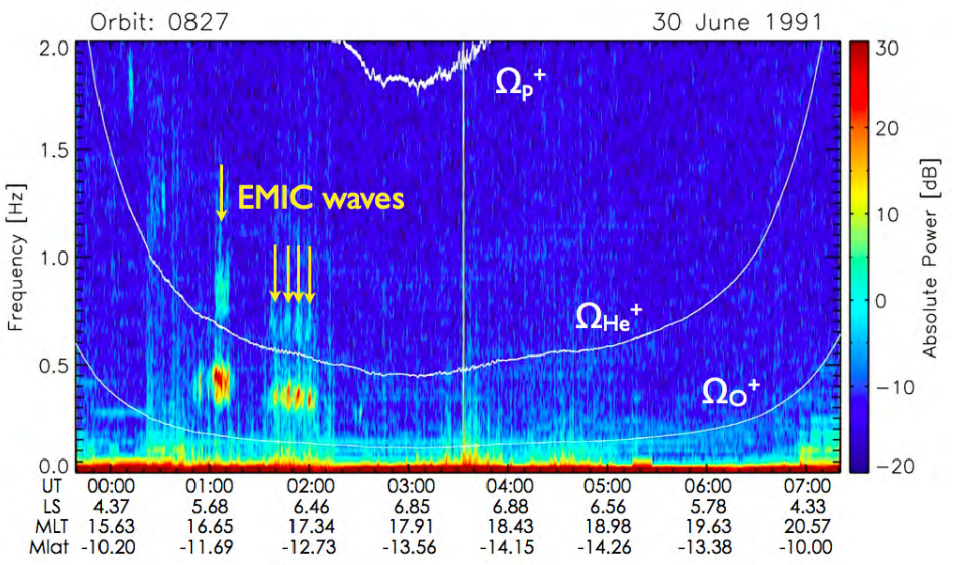

FIGURE 2.7: CRRES data used to identify the EMIC wave events. The three white lines are the oxygen, hydrogen, and helium cyclotron frequencies observed by CRRES. The stop bands for the oxygen and helium are clearly observed at about 01:00 UT and 02:00 UT.

ion gyro frequency and less then the maximum ion gyro frequency [Gurnett et al., 1965, Smith and Brice, 1964]. The crossover frequency can be determined from spectrograms and used to provide estimates of the H^+ density relative to the electron density in the plasma [Gurnett et al., 1965].

When identifying EMIC waves from spectrograms, the existence of the stop bands ($n^2 < 0$) is often used to distinguish between EMIC waves and broad band noise in the same frequency bands. An example of the difference between the two can be seen in Figure 2.8. Band limited EMIC waves can be observed before about 03:30 UT and periods of broadband noise between 04:00 and 05:50 UT, 5:45 and about 07:00 UT, and again at about 07:30 - 07:45 UT as well as after 09:00 UT. Although both the EMIC waves and the broadband noise show an increase in power in the frequency ranges where we expect to see EMIC wave generation, only the events that are band limited or show the stop bands are identified as EMIC waves since the plasma in the magnetosphere is comprised of two or more cold ion species.

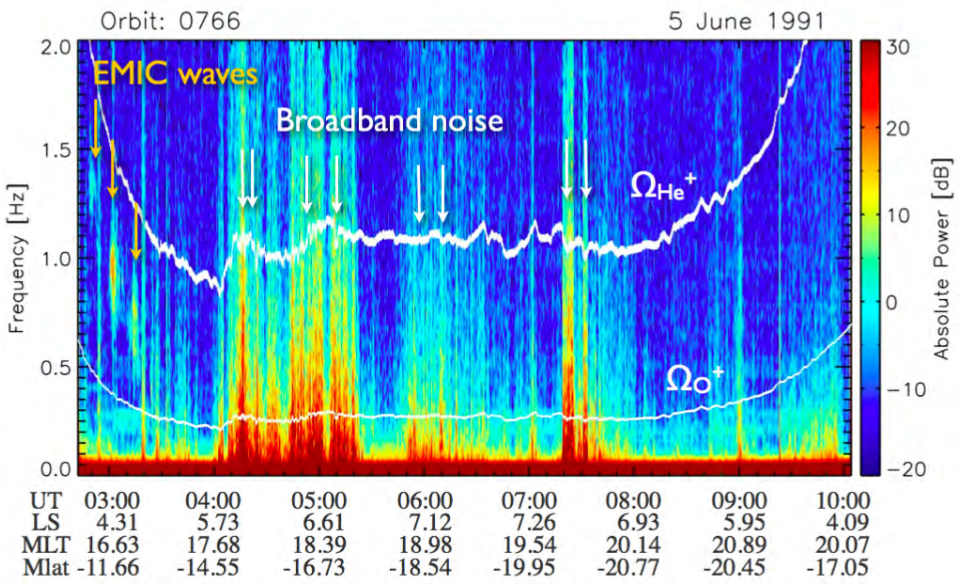

FIGURE 2.8: Orbit 766 EMIC wave event showing EMIC waves and broadband noise. The two white lines are the oxygen (bottom) and hydrogen (top) cyclotron frequencies.

2.5 EMIC Wave Growth in the Magnetosphere

EMIC waves are known to be observed in regions where the plasma can be described as cold, collisionless, and multi-ion specied. Using the theory outlined in Kozyra et al. [1984] we can determine the wave growth for a multi - component 3-ion (H^+, He^+, O^+) plasma. On the ground, most Pc 1 emissions are observed between 0.2 - 5 Hz [Jacobs et al., 1964]. In the CRRES satellite data, (Figure 2.7), EMIC events are observed in the oxygen, helium, and hydrogen bands of growth described by theory. Assuming a bi-Maxwellian distribution for the energetic, anisotropic particle populations, and a Maxwellian distribution for the cold particle populations, the dispersion relation given in Equation 2.30 can be written as [Fraser et al., 1989, Gomberoff and Neira, 1983, Kozyra et al., 1984]

$$\omega^2 = (ck)^2 - \sum_s \omega_{psw}^2 (A_s - \frac{Z(\xi_s)}{\alpha_{||,s}k}[(A_s+1)(\Omega_s - \omega) - \Omega_s]) + \sum_j \omega_{pjc}^2 \frac{\omega}{\omega - \Omega_j}, \quad (2.36)$$

where the summations over s include all ion species but j only sums over ions heavier than H^+ and this notation is used for the rest of the derivation. The plasma frequency is $\omega_{psw(c)}$ for species s and subscript $w(c)$ indicates the warm and cold components. The thermal anisotropy of the bi-Maxwellian distribution is $A_s = (T_\perp/T_{||}) - 1$, $Z(\xi_s)$ the plasma dispersion function, $\xi_s = (\omega - \Omega_s)/\alpha_{||}k$, the parallel thermal velocity for the energetic species s is $\alpha_{||} = (2k_bT_{||}/(m_sm_p))^{.5}$ and the sum over the cold particles includes the cold electrons. The temporal growth rate is then found from the imaginary portion of the dispersion relation and assuming $\omega_r >> \omega_i$, $(ck)^2 >> \omega^2$, $[(\omega_r - \Omega_s)/k\alpha_{||,s}] >> 1$, and the plasma is neutral gives

$$\begin{aligned} \mu &= \frac{\omega_j}{\Omega_p} \\ &= \frac{\sum_s \frac{\Omega_p \eta_{sw}\sqrt{\pi}}{M_s^2\alpha_{||,s}k}[(A_s+1)(1-M_sX)-1]\cdot exp[\frac{-\Omega_p^2(M_sX-1)^2}{M_s^2\alpha_{||,s}^2k^2}]}{\frac{X(\delta+1)(2-X)}{(X-1)^2} + \sum_j(\eta_{jw}+\eta_{jc})\frac{M_jX(2-M_jX)}{(M_jX-1)^2}}. \end{aligned} \tag{2.37}$$

We have defined $\delta = \omega_{ppc}^2/\omega_{ppw}^2$, and $\eta_{jw(c)} = M_j(\omega_{pjw(c)}^2/\omega_{ppw}^2)$. This approximation does not hold near the ion cyclotron frequencies. When the final growth rate is determined, this manifests as asymptotes as ω approaches Ω_s and thus we have forced the cut off regions when plotting the growth rates (Figures 2.9).

The group velocity V_g and wave number k from the real part of the dispersion equation are

$$\begin{aligned} V_g &= \frac{\delta\omega_r}{\delta k} \\ &= \frac{\frac{2\Omega_pc}{\omega_{ppw}}\sqrt{[\frac{1+\delta}{1-X} + \sum_j(\eta_{jw}+\eta_{jc}\frac{M_j}{1-M_jX})]}}{\frac{(1+\delta)(2-X)}{(1-X)^2} + \sum_j \frac{(\eta_{jw}+\eta_{jc})M_j(2-M_jX)}{(1-M_jX)^2}} \end{aligned} \tag{2.38}$$

$$k = \sqrt{\frac{\omega_{ppw}^2}{c^2}[\frac{(1+\delta)X^2}{(1-X)} + \sum_j(\eta_{jw}+\eta_{jc})\frac{M_jX^2}{(1-M_jX)}]}. \tag{2.39}$$

Since the effective wave amplification in the magnetosphere is dependent upon the amount of time spent traveling though the growth region, we are more interested in the convective

growth rate. This quantity is defined as the temporal growth rate divided by the group velocity,

$$\begin{aligned} S &= \frac{\mu}{V_g} \\ &= \frac{\sum_s \frac{\eta_{sw}\sqrt{\pi}}{M_s^2\alpha_{||,s}k}[(A_s+1)(1-M_sX)-1]\cdot exp[-\lambda_s^2]}{\frac{2cX}{\omega_{ppw}}\sqrt{[\frac{1+\delta}{1-X}+\sum_j(\eta_{jw}+\eta_{jc}\frac{M_j}{1-M_jX})]}}, \end{aligned} \tag{2.40}$$

where $\lambda_s = (\Omega_p(1-M_sX))/(M_s\alpha_{||,s}k)$. Substituting in for k gives

$$S = \frac{\sum_s \frac{\eta_{sw}\sqrt{\pi}}{M_s^2\alpha_{||,s}k}[(A_s+1)(1-M_sX)-1]\cdot exp[-\lambda_s^2]}{(\frac{2cX}{\omega_{ppw}}\sqrt{\frac{1+\delta}{1-X}+\sum_j(\eta_{jw}+\eta_{jc}\frac{M_j}{1M_jX})})(\frac{\omega_{ppw}X}{c}\sqrt{[\frac{1+\delta}{1-X}+\sum_j\frac{(\eta_{jw}+\eta_{jc})M_j}{1-M_jX}]})}. \tag{2.41}$$

This simplifies to

$$S = \frac{\sum_s \frac{\eta_{sw}\sqrt{\pi}}{M_s^2\alpha_{||,s}k}[(A_s+1)(1-M_sX)-1]\cdot exp[-\lambda_s^2]}{2X^2[\frac{1+\delta}{1-X}+\sum_j(\eta_{jw}+\eta_{jc}\frac{M_j}{1-M_jX})]}. \tag{2.42}$$

Substituting k into λ_s and using $\omega_{psw}^2 = 4\pi n_{sw}q^2/m_s$, $\Omega_p = qB_o/m_pc$, and $\beta = (8\pi n_{sw}k_bT_{||s})/B_o$ Equation 2.42 simplifies to

$$S = \frac{\mu}{V_g} = \frac{\Sigma_s \frac{\eta_{sw}\sqrt{\pi}}{M_s^2\alpha_{||,s}}[(A_s+1)(1-M_sX)-1]\times exp[\frac{\frac{-\eta_{s,w}}{M_s}\frac{(M_sX-1)^2}{\beta_{sw}X^2}}{\frac{(1+\delta)}{(1-X)}+\Sigma_j\frac{(\eta_{jw}+\eta_{jc})M_j}{1-M_jX}}]}{2X^2[\frac{1+\delta}{1-X}+\Sigma_j(\eta_{jw}+\eta_{jc}\frac{M_j}{1-M_jX})]}, \tag{2.43}$$

where $A = \frac{T_\perp}{T_{||}} - 1$ is a measure of the temperature anisotropy. The wave growth can then be described to occur when

$$A = \frac{T_\perp}{T_{||}} - 1 > \frac{\omega_r}{\Omega_p + \omega_r}. \tag{2.44}$$

To compare the theory with the observations we consider an example event from 1 July, 1991 between 00:55 and 01:15 UT shown in Figure 2.7. The growth rate from equation 2.43 was solved using experimental parameters from CRRES data and assuming a cold density ratio of 95% H^+, 3% He^+ and 2% O^+, for a 3 ion plasma (Table 2.2) and

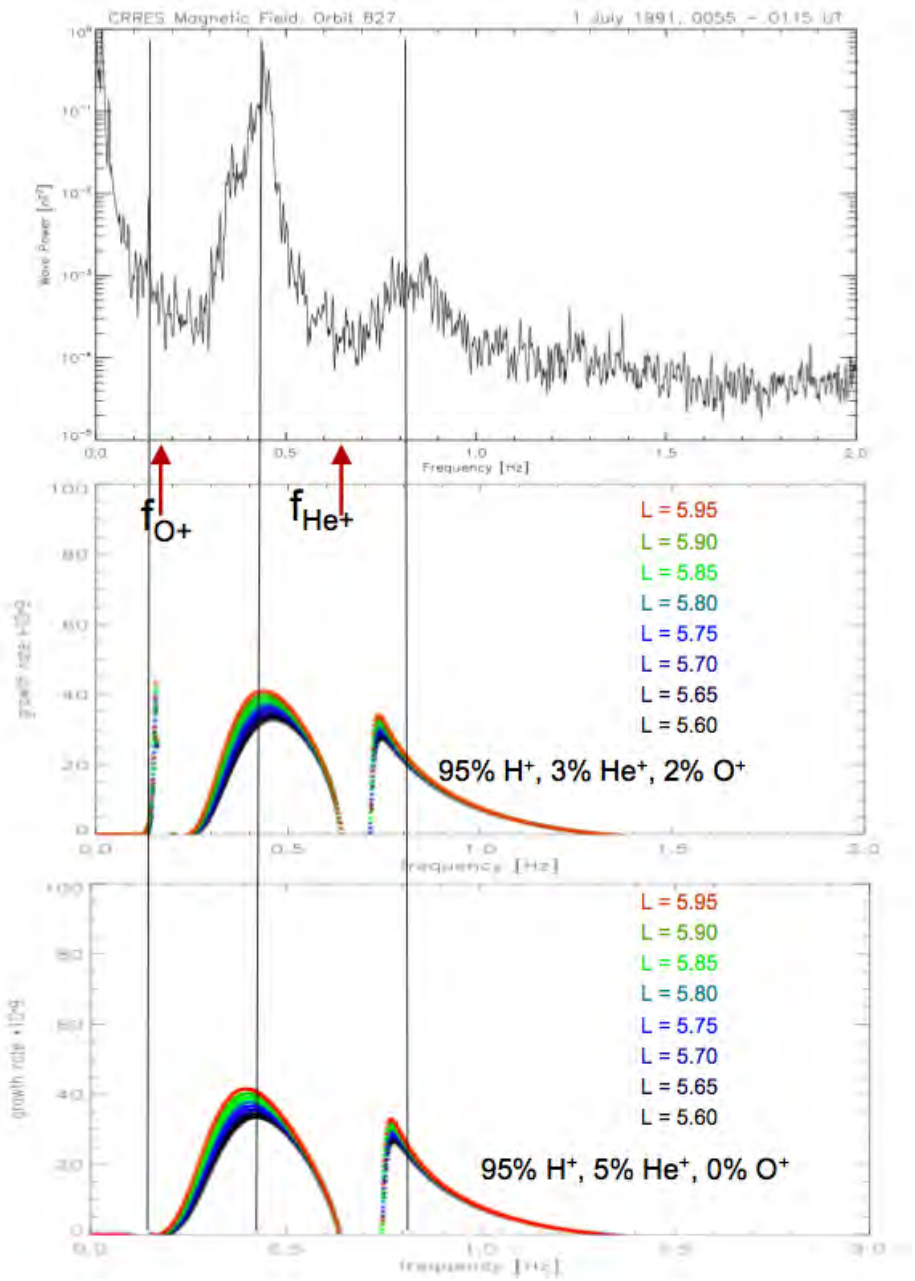

FIGURE 2.9: The wave power spectrum (top panel) and the convective growth rate using the inputs given in Table 2.2 for a 3 ion plasma (middle panel) and a 2 ion plasma (bottom panel). These values come from CRRES data for the event between 00:55 and 01:15 on 1 July, 1991 during orbit 827. The colours in the growth rate plots represent the growth rate found throughout the event as CRRES crossed through different L-shells. The vertical lines represent the peak growth frequencies found in the top panel.

TABLE 2.2: The inputs into the growth rate calculations for Figure 2.9.

Particles	H^+	He^+	O^+
Cold, cm^{-3}	84.55	2.67, 4.45	1.78, 0.0
Warm, cm^{-3}	.88	0.10	0.02
$T_\perp$, keV	30.0	10.0	10.0
A	1.25	1.0	1.0

95% H^+, 5% He^+ for a 2 ion plasma. The plotted convective growth rates against frequency are shown in Figure 2.9. It is assumed that the plasma contains He^+, and possibly O^+, along with the H^+ population since we can observe at least one stop band in the data which would only occur if the plasma has at least two different cold ion populations. In the CRRES satellite data (Figure 2.7) EMIC events are observed in all regions of growth described in the theory outlined in the above sections. The growth region below the oxygen cyclotron frequency in the theory (Figure 2.9) approaches an asymptote thus we don't expect to see waves in this region, and none were observed by CRRES. As seen in Figure 2.7 the wave power peaks where there was predicted wave growth.

Thus far we have focused on EMIC waves generated by the temperature anisotropy due to overlap of the ring current and plasmaspheric particles. Olson and Lee [1983] looked at how SI compressions would be able to generate EMIC waves. As a first order approximation they used a simple Chapman-Ferraro double dipole model for the day side magnetosphere and ignored any effects due to the ring current. They also assumed that the time scale for the SI is slower than the cyclotron or bounce motion of the average particle, and thus the first two adiabatic invariants are conserved giving

$$\frac{W_\perp}{B} = \frac{W_{\perp o}}{B_o} \tag{2.45}$$

$$\frac{W_{||} B^2}{n^2} = \frac{W_{||o} B_o^2}{n_o^2}, \tag{2.46}$$

where $W_\perp$ and $W_{||}$are the perpendicular and parallel particle kinetic energies, B and n are the background magnetic field and the number densities respectively. Olson and Lee

[1983] then assumed the effects of a changing magnetic field, along the field as

$$\frac{W_{||}}{W_{||o}} = (\frac{B}{B_o})^{\gamma}, \tag{2.47}$$

where γ depends on the shape of the field geometry. Using these equations we can define $A = (W_{\perp}/W_{||} - 1)$ as a measure of the anisotropy in the plasma pressure which is easier to consider then the temperature anisotropy when discussing compressions. They found that an SI will compress the dayside magnetosphere efficiently enough to increase A and the growth rate leading to the generation of EMIC waves around noon. They also noted that if an SI were to break the second adiabatic invariant this would likely lead to an even greater enhancement in A not just around noon, but further around the magnetosphere leading to EMIC wave generation in the dawn and dusk sectors. This has since been shown observationally [e.g. Anderson et al., 1992a, Posch et al., 2010, Usanova et al., 2008, 2010] and by modelers [e.g. Jordanova et al., 1996, McCollough et al., 2009].

Anderson et al. [1992a] speculated that since the growth rate is inversely proportional to the Alfven velocity through the term $\alpha^* = \Omega_e^2/\omega_{pe}^2$ (Section 2.4.2), which can be rewritten in terms of the Alfven velocity as $\alpha^* = V_A^2/(\epsilon c^2)$, EMIC waves should be expected to occur in regions where the Alfven velocity peaks. In particular they point out two regions where this is found, at L-values where the magnetic field is relatively weak (i.e. near the magnetopause), and just inside the plasmapause. Where we see EMIC waves, and how this compares to where we expect to see EMIC waves will be discussed in more detail in later chapters.

2.6 Summary

It has been shown that an important factor in generating EMIC waves is the temperature anisotropy and the presence of cold heavy ions (He^+ and O^+) suggesting the occurrence of EMIC waves at times and in regions where these temperature anisotropies are expected to be seen. During geomagnetic storms the ring current moves closer into the inner magnetosphere and can overlap with the cool/cold plasmaspheric plasma. When the storm is recovering, convection is slowed allowing the plasmasphere to expand out, overlap with

the recovering ring current, again creating the necessary anisotropic temperature conditions. The conditions leading to the expansion of the plasmasphere might not take place until the storm has recovered, thus it is prudent to look for these waves not only during a geomagnetic storm, but also for multiple days after. In Chapter 4 we will study where EMIC waves were observed by the CRRES mission and their association with respect to storm and quiet magnetospheric conditions.

3

Data and Data Processing

3.1 The CRRES Mission

The Combined Release and Radiation Effects Satellite (CRRES) mission was operational from 25 July, 1990 until 21 October, 1991. It had an orbital period of 9 hours and 52 minutes with an apogee of 6.3 R_E, perigee of 350 km, and an inclination of 18.3° covering geomagnetic latitudes up to 30° allowing CRRES to pass through the inner radiation belts 4 times a day [Brautigam et al., 2005]. When mapping field lines back to the equator, CRRES was able to view McIlwain L-values up to approximately 8 [McIlwain, 1966, Fraser and Nguyen and references therein]. The initial apogee local time at launch was 08 hrs MLT. The local time of apogee decreased at a rate of 1.3 hr per month, to 14 MLT when the CRRES mission concluded [Brautigam et al., 2005, Fraser and Nguyen, 2001, Fraser et al., 1996, Loto'aniu, 2003]. The details about the instrumentation on board

CRRES were published in a special issue of the Journal of Spacecraft and Rockets, 29, (4), 1992. Instrumentation included the AFGL fluxgate magnetometer which provided three vector component EMIC wave and main field data [Singer et al., 1992]. The University of Iowa/ AFGL Plasma Wave Experiment (PWE) provided the cold electron density data indirectly [Anderson et al., 1992b]. As the mission ended before CRRES completed one full precession around the Earth, we are missing data coverage in much of the dawn to noon sector.

The three component fluxgate magnetic field data were sampled at 16 Hz. The X, Y, and Z sensor signals were sampled by a 12 bit A/D converter at 16 times/1.024 s. The signal from the Y magnetometer component was also able to be amplified six times in either the high gain or low gain mode in order to increase the sensitivity near apogee. The low gain data coverage ranged up to $\pm$45000 nT (with a least significant bit resolution of 22 nT) and the high gain $\pm$850 nT (with a least significant bit resolution of 0.43 nT) [Singer et al., 1992]. When the Y sensor was in the amplified mode, the least significant bit resolution on that sensor was 0.07 nT in high gain and 3.3 nT in low gain. CRRES was in the high sensitivity mode for about 75% of its orbit, out beyond $\approx 3R_E$ [Singer et al., 1992].

The two perpendicular components of electric field in the spin plane were sampled at 32 Hz [Loto'aniu, 2003]. The third unknown electric field component, E_x, can be found assuming a plane wave with $\mathbf{E} \cdot \mathbf{B} = 0$ using the E_y and E_z data along with the B-field components and the relation

$$E_x = -[\frac{dB_y}{dB_x}E_y + \frac{dB_z}{dB_x}E_z]. \tag{3.1}$$

This has been considered by Loto'aniu and Fraser et al. and used to determine the Poynting flux of EMIC waves [Fraser et al., 1992, 1996, Loto'aniu, 2003]. The Poynting flux for plane waves is given by

$$\mathbf{S} = \frac{c}{4\pi}\mathbf{E} \times \mathbf{B} \tag{3.2}$$

and is always in the direction of propagation of the wave group velocity. If the bouncing wave packet model of the EMIC waves is assumed, then one should see wave packet energy bouncing back and forth along the field lines [Fraser and Nguyen, 2001]. Loto'aniu

et al. [2005] were able to measure the Poynting vector for the EMIC waves in the dynamic spectral domain and found that only for events observed between $\pm 11^{\circ}$ magnetic latitude was wave energy observed both towards and away from the equator. For all other events at higher latitudes the wave energy was observed to be moving towards the ionosphere, and not observed to return.

The PWE provide a measure of the intense upper hybrid resonance frequency, f_{uhr}, using

$$f_{uhr}^2 = f_{pe}^2 + f_{ce}^2, \tag{3.3}$$

where f_{ce} and f_{pe} are the electron cyclotron and plasma frequencies [Gurnett and Inan, 1988]. The electron cyclotron frequency can be determined using $f_{ce} = \frac{\Omega_e}{2\pi}$ where Ω_e is from equation 1.5. This and the magnetic field measurements then allow the determination of the electron number density,

$$N_e = 4\pi^2 \epsilon_o \frac{f_{pe} m_e}{q_e^2}. \tag{3.4}$$

Along with B_o the number density provides the local Alfven velocity

$$V_A = \frac{B_o}{\sqrt{4\pi\rho}}, \tag{3.5}$$

where ρ is the plasma density from the number density given in equation 3.4 for a single ion neutral plasma. When solving for a multi component plasma in the absence of heavy ions measurements, a ratio of 75% protons, 20% helium, and 5% oxygen was used unless otherwise stated [e.g. O'Brien et al., 2008, Pierrard et al., 2009].

To calculate the ephemeris parameters, the CRRES software used the Olson and Pfitzer static analytical model of the Earth's magnetic field [Olson and Pfitzer, 1974]. This model is valid from the sub solar region out to beyond the lunar orbit on the night-side magnetotail which includes the CRRES orbit. The internal field model is represented by a fixed dipole and the outer limits of the model take into account quiet time magnetosphere conditions including contributions from the magnetopause, tail, and ring currents [Olson and Pfitzer, 1974].

3.2 Fourier analysis

The study of EMIC wave data usually commences with the construction of dynamic spectra for specific events. For CRRES we usually plot these over 0.1 - 2.0 or 0.1 - 4.0 Hz which covers EMIC waves seen beyond L ≈ 3. All signals can be decomposed into a sum of even and odd signal components, normally in the form of sinusoidal waves, which provides a resultant formula of a frequency spectrum unique to the original signal [Cochran et al., 1967, Cooley and Tukey, 1965, Cooley et al., 1967]. When the original function is a digital signal, this is defined as the Discrete Fourier Transform (DFT) and can be found using the following function.

$$X(m) = \sum_{n=1}^{N} x(n) exp[\frac{-i2\pi(m-1)(n-1)}{N}], \tag{3.6}$$

where x(k) a continuous function. Its inverse is then

$$x(n) = \sum_{m=1}^{N} X(m) exp[\frac{i2\pi(m-1)(n-1)}{N}], \tag{3.7}$$

where n is a sample point and all N samples are evenly spaced and m is related to the frequency by $f(m) = \frac{m}{N\delta t}$. Ideally in order to resolve all the periodic wave frequencies in the original digital signal, the sampling rate of the data must be at least twice the highest frequency. Since the sampling rate is usually set by the data we can determine the highest frequency which will be resolved correctly using the Fourier analysis, the Nyquist frequency, and is given by

$$f_{Nyquist} = \frac{1}{2}\nu, \tag{3.8}$$

where ν is the sampling rate (s^{-1}). If there is a periodic signal in the data at a higher frequency than the Nyquist frequency the signal will fold in at a frequency below the Nyquist frequency. This is called aliasing and corrupts the data [Cochran et al., 1967, Cooley and Tukey, 1965].

Thus the DFT defines a spectrum of a digital time series and can represent the continuous waveform where the sampling rate of the data is at least twice the frequency of the highest frequency in the data. At the practical level filtering must be used in the data logging system to remove all frequencies above the Nyquist frequency.

3.3 Fast Fourier Transform

The Fast Fourier Transform (FFT) is a process which computes the Fourier analysis faster than the DFT. It also reduced the round off errors associated with the computations and the round off errors and computation time are decreased by a factor of $\frac{lnN}{N}$, where N is the number of data points [Cochran et al., 1967, Cooley and Tukey, 1965]. The FFT combines progressively larger weighted sums of data samples to produce the DFT coefficients which is described in detail by Cochran et al. [1967]. These methods are very useful since they are able to show periodicities and their strengths in the input signal.

3.4 Auto-power and Cross-power

Knowing the DFT (or FFT) of the time series the auto power density can be written as

$$P_{xx}(m) = A \mid X(m) \mid^2 = AX(m)X^*(m), \tag{3.9}$$

where m = 1, 2, 3, ..., $\frac{N}{2}$, X^* is the complex conjugate and A is a normalisation factor. With a second time series $Y(m)$ the cross power density between the two time series, or the degree of correlation in the spectral domain between the two series, can be determined as

$$P_{xy}(m) = AX(m)Y^*(m). \tag{3.10}$$

Although P_{xx} is always real, the same is not true for $P_{xy}(m)$ where the real and imaginary components are given as

$$CSP(m) = Re[P_{xy}(m)]$$
$$QSP(m) = Im[P_{xy}(m)].$$

CSP(m) is the cross-spectrum and QSP(m) the quadrature spectrum. Thus the full representation of the cross power spectral density, CPD(m), of the two signals is given as

$$\mid P_{xy}(m) \mid = \sqrt{CSP(m)^2 + QSP(m)^2}. \tag{3.11}$$

Thus equations 3.9 and 3.11 are used to estimate the wave spectral power density.

3.5 Windowing

Since the FFT is computed over a finite time, a box car window is applied which is N sample points long. This window in the time domain is equivalent to a $\frac{sin(f)}{f}$ function in Fourier space which has characteristics of a major spectral peak plus side peaks which diminish in amplitude at nearby frequencies [Cooley and Tukey, 1965, Loto'aniu, 2003]. Energy then will leak into the surrounding frequency bins and smear the spectrum which will affect the reliability of the amplitude estimates. The leakage can be reduced by choosing different window shapes such as a Hanning or Hamming window, which are typically used for sinusoidal signals. Both functions are characterised by a central maximum which falls off with a symmetric taper. The Hanning window was used to process the data for this study. EMIC waves occur in narrow frequency bands, thus the Hanning frequency response was adequate for the time-domaine windowing.

3.6 Wave Polarisation

When determining the wave polarisation we consider the amplitude and phase of the two orthogonal signal components. If we assume a monochromatic wave with transverse wave components in the x-y Cartesian plane, then the angle between the major axis of the polarisation ellipse and the x - axis is defined as the angle of polarisation or azimuthal angle given by

$$tan(2 \cdot \Theta) = \frac{2 \cdot CSP(m)}{[P_{xx}(m) - P_{yy}(m)]}. \tag{3.12}$$

Here Rankin and Kurtz [1970] define ellipticity for this case of a monochromatic wave as

$$\epsilon = tan(\beta), \tag{3.13}$$

where β is the angle of the sin of the ratio of the minor axis to the major axis of the polarisation ellipse given by

$$\beta = sin^{-1}[\frac{2 \cdot QSP(m)}{[P_{xx}(m) + P_{yy}(m)]}]. \tag{3.14}$$

For quasi-monochromatic waves where the amplitudes and phases are functions of time, the frequency band is defined as Δf, and the mean frequency is $f(\bar{m})$, then the polarisation properties are reliable if the complex amplitudes and phases are reasonably constant over time such that the coherence interval, $\Delta\tau$ is between $1/f(\bar{m}) \leq \Delta\tau \leq 1/\Delta f$ [Loto'aniu, 2003].

The wave can then be divided into polarised, $P(m)$, and unpolarised, $U(m)$ signals, the sum of which defines the coherency matrix $C(m) = P(m) + U(m)$. The matrix representation of $C(m)$ is then given as

$$C(m) = \begin{bmatrix} P_{xx} + U_{xx} & P_{xy} \\ P_{yx} & P_{yy} + U_{yy} \end{bmatrix}.$$

[Rankin and Kurtz, 1970]. Thus the sense of polarisation for a quasi-monochromatic wave is written as

$$sin\beta = \frac{2 \cdot Im(P_{xy}(m))}{[(P_{xx}(m) + U_{xx}(m) + P_{yy}(m) + U_{yy}(m))^2 - 4 \cdot Det \mid C(m) \mid]^{1/2}}, \quad (3.15)$$

where $Det \mid C(m) \mid$ is the determinant of the coherency matrix [Loto'aniu, 2003]. Looking at β, the wave, when viewed along the wave vector $\mathbf{k}$, is right-hand polarised (a clockwise rotation) when $\beta \geq 0$ or is left hand polarised (an anti-clockwise rotation) when $\beta \leq 0$.

3.7 Dynamic spectra

Dynamic spectral plots provides information on three quantities, time (normally the x-axis), frequency (normally the y-axis), and power (normally represented by a colour scale) as represented in the example from CRRES (Figure 2.7). These plots are created by taking the data set and computing the FFT for N points. To improve the visualisation of the images smoothing is performed in the frequency or time domain and spectral density parameters such as the auto power (equation 3.9) and cross power (equation 3.11) are computed. The FFT window is then advanced by δ N points and the process is repeated until the end of the data set is reached. Typically one spectrum will overlap the previous by $20 - 50\%$.

3.8 EMIC Waves

For this study EMIC waves were identified visually using CRRES data processed by T.S. Nguyen between 0.1 - 4.0 Hz [Fraser and Nguyen, 2001]. A spectrogram showing EMIC waves is seen in Figure 2.7 where the waves commence around 00:15 UT at frequencies 1.8 - 2.1 Hz, again at 00:30 UT at frequencies 1.0 - 1.3 Hz, again at 00:55 UT at frequencies 0.3 - 0.8 Hz, another at 01:00 - 01:15 UT at frequencies 0.3 - 1.3 Hz, and a series at 01:40 - 02:00 UT at frequencies 0.3 - 0.9 Hz. The helium non-propagation stop band [Young et al., 1981] is clearly observable in the last two intervals over 0.5 - 0.7 Hz and 0.4- 0.6 Hz respectively. The CRRES fluxgate magnetometer bandwidth covered a range of frequencies from 0.1 - 8.0 Hz, but to reduce processing time, the data were limited to 0.1 - 4.0 Hz. The frequency range between 2 - 4 Hz was checked for approximately two thirds of the data set and was found to see less than 5% (corresponding to an approximate total of 46 events) of EMIC waves. There were no EMIC waves found in the data set above 4.0 Hz [Fraser and Nguyen, 2001].

The magnetometer data were processed and studied over 8 hour intervals centred on apogee. During the remainder of the orbit, near perigee, the magnetometer switched into low sensitivity mode. These data intervals corresponded to L-values < 3 where the proton cyclotron frequency was well above 8 Hz. The data gaps and spikes were first removed from the 16 Hz^{-1} data by fitting a second order polynomial curve. A low pass filter was then used and the data were resampled at 0.25 s to remove aliasing. The data were then transformed into the Magnetic Geocentric Solar Ecliptic (MGSE from Appendix A) and the field aligned coordinate system. A Hamming window was applied and the mean removed before the FFT and smoothing was performed [Loto'aniu et al., 2005]. The dynamic spectral analysis used 60 s (240 point) segments with 20 s (80 point) overlap to give a spectral resolution of 0.017 Hz and 1437 FFTs for every 8 hour orbit segment.

3.9 Geomagnetic Indices

In this study we identify EMIC wave properties and associated geomagnetic phenomena in terms of well known magnetic indices. To measure the strength of the ring current (and thus a geomagnetic storm) the Sym-H index, which is a higher resolution and more accurate version of the Dst index, is used. To measure magnetospheric convection and global magnetospheric activity, the Kp index is used [Thomsen, 2004].

3.9.1 Dst index

The Dst index was historically created to measure the strength of the magnetospheric ring current. Dessler and Parker [1959] showed that the change in the magnetic field at the centre of the Earth due to a symmetric ring current is proportional to the magnetospheric particle energy for two particle distributions; an isotropic pitch angle distribution or where all the particles are confined to the equatorial plane. Sckopke [1966] later generalised this result for all pitch angles and particle distributions. In 1957 [Sugiura, 1964] the Dst index was developed in order to measure the ring current intensity based on the ideas of Dessler, Parker, and Sckopke.

When calculating the Dst index it is assumed that the Earth is a non-conducting solid sphere, thus the change in the magnetic field at the centre of the Earth is the same as at the surface on the equator [Dessler and Parker, 1959, Sckopke, 1966, Siscoe and Crooker, 1974]. Due to the equatorial electrojet created from the heating of the ionosphere on the dayside, the 4 stations chosen to compute the Dst are slightly off the equator [Burton et al., 1975, Mayaud, 1980]. The Sq current and an estimate of the Earth's background magnetic field are removed from the magnetometer data. This is done by taking the average of the four quietest days of each month, and subtracting this average from the magnetometer data. The remainder is the change in the magnetic field due to all other currents at the station. The data from the four stations are then averaged together to give the Dst. At the time the Dst index was developed, it was thought that the ring current was completely symmetric and the major contributor to the magnetic disturbance observed at these latitudes on the Earth.

In reality the Dst physically represents the magnetic perturbation due to all currents except for those removed, so many of the other magnetospheric currents have substantial effects on the Dst. Along with including the effects due to all currents, three of the four stations are located in the Northern Hemisphere giving the Dst index a northern hemispheric bias [Turner et al., 2001]. One of the easiest current systems to detect is the magnetopause current [Burton et al., 1975, O'Brien and McPherron, 2000a,b]. Before the injection of particles into the ring current from a storm, there is a positive increase ($\sim$ 10 nT) in the geomagnetic field due to the solar wind compressing the magnetopause inwards towards the Earth. This is called the Sudden Storm Commencement (SSC) (section 1.6). The magnetopause current is sometimes removed from of the Dst and this modified index is called the pressure-corrected Dst or Dst* [e.g. Burton et al., 1975, O'Brien and McPherron, 2000b]. It has been postulated that other magnetospheric currents could contribute substantially to Dst. For example, during a storm the cross tail current could contribute up to 25% of the observed ΔB on the ground [Ohtani et al., 2001, Turner et al., 2001].

3.9.2 Sym-H index

The Sym-H index is calculated in a similar fashion to the Dst index. The Sym-H index uses 6 of 10 stations (those with the best data quality) which are more evenly spaced in longitude and has a time resolution of 1 min instead of the 1 hour used for the Dst index. This allows for more temporal variations to be observed in the index which can be very important when considering space weather phenomena which have time scales of an hour or less, e.g. substorms and EMIC waves [Wanliss and Showalter, 2006].

3.9.3 Kp index

A traditional index used to describe the conditions of the magnetosphere and used as a good measure of magnetospheric convection is the Kp index which is a three hour weighted average of the K indices from a network of 12 geomagnetic observatories [Bartels et al., 1939, NOAA, 2007, Thomsen, 2004]. The K index for a given location takes the geomagnetic variation and converts it into a range scale from 0 to 9. The conversion

tables used are station specific so that the rate of occurrence of certain K levels match with historical records [NOAA, 2007]. Levels of Kp from 0 to 3 are generally considered quiet, a Kp of 4 is moderate geomagnetic activity, and Kp ≥ 5 are defined as storm - level activity [NOAA, 2007].

3.10 Geomagnetic Storm Analysis

Geomagnetic storms in this study were defined using the Kyoto Sym - H index. [Gonzalez et al., 1999, 1994, Kamide et al., 1998, Wanliss and Showalter, 2006]. EMIC waves have time scales on the order of minutes, hence the Sym-H index was used instead of the Dst index in order to more accurately pinpoint the storm phase, and where in that phase the EMIC waves occurred. Although it does not provide the symmetry or the radial position of the ring current and the decrease in the index due to an enhancement of other currents such as the tail current, it is our best indicator as to when there is an increase in the ring current population [e.g. Baker et al., 2001, Friedrich et al., 1999, Turner et al., 2001].

Since every storm has a different strength and phases of different lengths, it is important to be consistent with quantitative definitions based on the temporal evolution of storms for accurate identification of the storms and their phases. This method was preferred over using a set number of days from either the onset of the storm or the Dst/Sym-H minimum of the storm since the lengths of the phases may range from hours to days, and allows comparison of the physical processes occurring during each phase across storms.This allows us to look specifically at the geomagnetic storm processes leading to the generation of EMIC waves.

3.10.1 Pre-onset

A storm is defined as having three phases, pre-onset, main phase, and recovery phase. The pre-onset is defined as the three hours prior to onset of the storm. The onset is defined as where the Sym-H slope turns negative, and stays negative, on its way to the minimum value reached during the storm. This was used in preference to determining the SSC for a storm since we have included both sudden onset and gradual onset storms

[see also Loewe and Prölss, 1997]. These different storm types can be related to upstream solar wind driving; CME driven storms often have a clearly defined SSC, whereas CIR driven storms usually do not [Gonzalez et al., 1999, 1994]. Due to the lack of consistent solar wind monitoring throughout the CRRES mission, CIRs and CMEs could not be confidently distinguished on the statistical scale needed for this study. As another means to quantify the start of the pre-onset phase which was not easily identifiable in the Sym-H index, the three hours before onset was used.

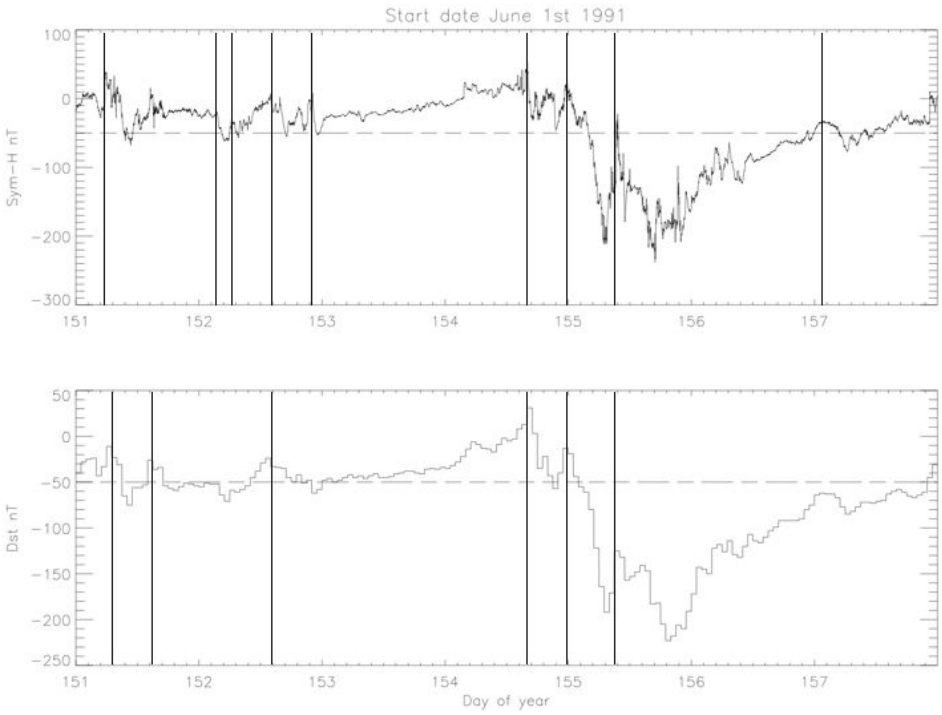

FIGURE 3.1: The Sym-H and Dst indices over the same period of time where the vertical lines show the onsets of storms. Due to the lower temporal and spatial resolution only 6 storms were identified using the Dst index over the same period where 9 were identified using the Sym-H index.

3.10.2 Main Phase

The main phase is defined as the time from the onset of the storm until Sym-H reaches its minimum value, and the slope turns positive. In order to be defined as a storm, the

minimum value must be ≤ -40 nT, which is consistent with many previous storm studies and includes medium to large storms [Gonzalez et al., 2002, 1994, Gosling et al., 1991, Kamide et al., 1998, Khabarova and Yermolaev, 2008, Matsushita, 1962, McPherron and Hsu, 2002, O'Brien and McPherron, 2000a,b, Tsurutani et al., 1997, Wu and Lepping, 2008]. The average length of a main phase identified using the criteria printed here during the CRRES mission was 8 hours. This would have been completely smoothed over in some previous studies which used 9 - 12 hour running averages of the Dst in order to locate events [Bortnik et al., 2008, Engebretson et al., 2008a, Horne et al., 2009]. This also means that the current study has many smaller and shorter storms, as well as some storms which without the running average (such as using the Dst instead of the Sym-H index) appear in our data as multiple storms instead of one large one as can be seen in Figure 3.1.

3.10.3 Recovery Phase

Finally the recovery phase was defined as beginning at the end of the main phase until Sym-H had recovered 80% of the minimum value reached during the storm, or until the onset of the next storm. This means that there may be at most 3 hours of overlap between the recovery phase and the pre-onset phase. How these phases are defined, especially the recovery phase, can greatly affect the results and why these definitions are important will be discussed in section 5.3.2.The recovery phase was the longest of the three phases averaging 17.5 hours, much less than the 4 - 6 days used in many previous studies [Bortnik et al., 2008, Engebretson et al., 2008a, Horne et al., 2009], which lead to an overestimate of the time the magnetosphere was active and the counting of non-storm time EMIC wave events as storm time events.

Discussion

In order to compare the storms in our study, each storm was normalised to a length which was larger then the longest time found for each phase. This was done so that no information about the phase was lost. How this affected a sample storm can be seen in Figures

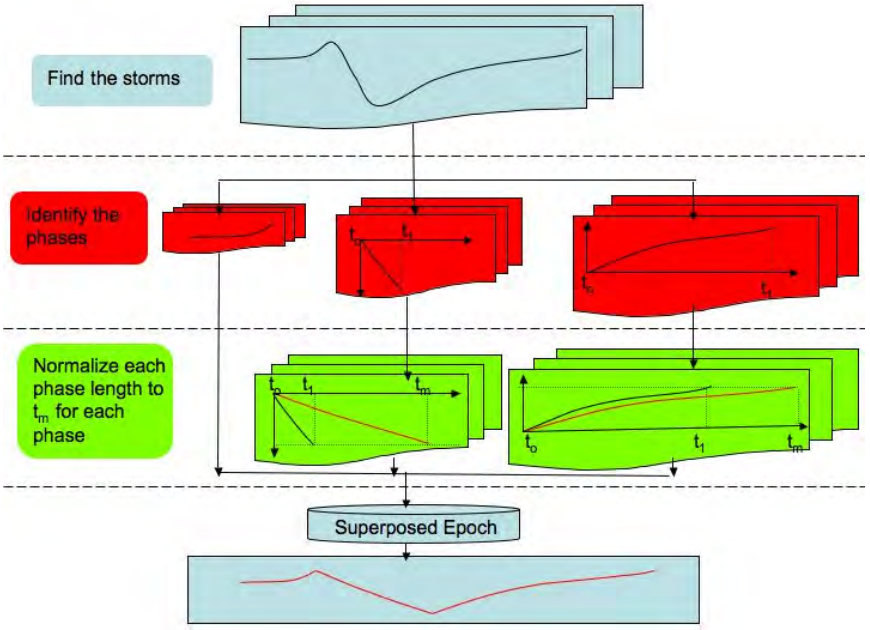

FIGURE 3.2: Flow chart of the normalisation process for the Sym-H index performed prior to the superposed epoch analysis. The first row shows the identification of the geomagnetic storms during the CRRES mission. The red boxes in the second row represent each of the three storm phases, the start of the phase labeled as t_o and the end labeled as t_1. Each phase is then treated separately. The green boxes in the third row illustrate the normalisation of the length of the individual phases to the reference time, t_m, which is longer than the longest duration for each phase. For the pre-onset phase, this is not needed as they are already defined as the same length. A superposed epoch analysis is then performed for each phase and the results are re-combined, represented by the bottom blue box at the bottom.

3.2 and 3.3 and will be discussed in more detail in Chapter 5. In our results each phase is plotted separately so that the details of each phase are preserved and can be easily viewed.

This approach has some caveats. Since Sym-H is a 1-minute averaged quantity there are more clearly defined onsets than are found using Dst. In some cases where Dst might see a double dip storm or large (Dst $<$ -200 nT) storm, Sym-H might see many more particle injections. A buffer between storms was considered, as well as defining overlapping storms as a single storm, but was not used because we did not want to discriminate between geomagnetic storms or ring current particle injections occurring during storms. It was decided that with each new onset, there was the possibility of a new injection of hot

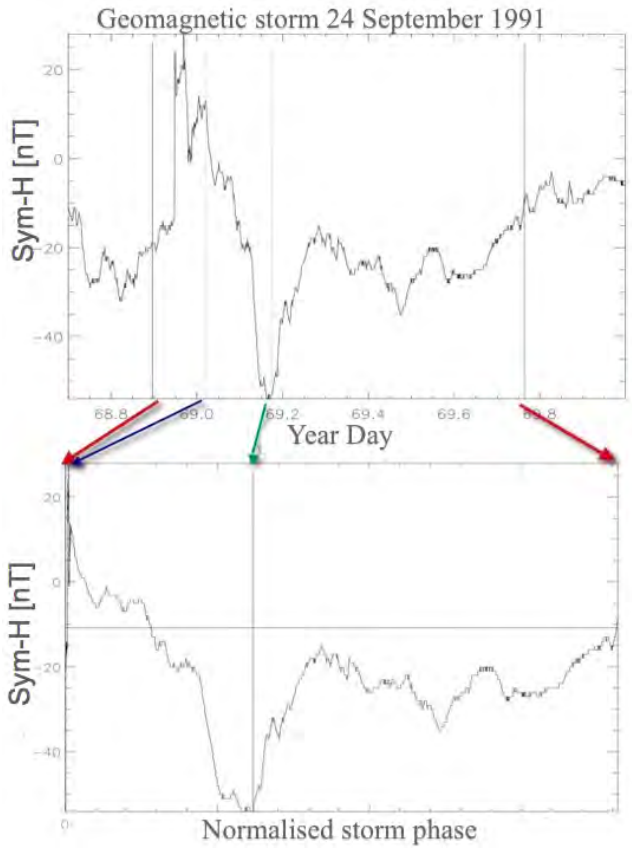

FIGURE 3.3: A typical storm profile in Sym-H occurring during the CRRES mission in the top panel and in the bottom panel how this storm appears after it has been normalised to the longest phase.

ring current ions into the inner magnetosphere, and thus the potential for them to interact with cold plasmaspheric particles leading to the generation of new EMIC waves. In other words, the onset represents the start of the ring current particle injection and the minimum Sym-H value represents the point where the loss of ring current particles exceeds the injection of new particles. The end of the recovery phase would then represent the time when storm processes have receded into the background and the non-storm time magnetospheric processes are once again dominating, which could include such processes as the refilling of the plasmasphere. Each of these phenomena could potentially be important to

EMIC wave generation.

3.11 Superposed Epoch Analysis

A superposed epoch analysis, the last step in the the flow chart shown in Figure 3.2 has been found to be very useful in space physics and geophysics in general when trying to find a common structure or behaviour within a large collection of time series [e.g. Halford et al., 2010, Haurwitz and Brier, 1981, MacDonald et al., 2010, Posch et al., 2010, Samson and Yeung, 1986]. The idea behind a superposed epoch analysis is that it is an informed way to average the data in relation to a specific event in time. Here we will use the onset of storms, the end of the main phase, and the end of the recovery phase as our important event times. Given a set of k time series we can look for a common structure in the time series $y(t)$. If we know that the epoch time (the time used to compare the data sets from such as the onset of a geomagnetic storm) is at t_k we can use the time shifted time series $y_k(t - t_k)$ to estimate the shape of the common behaviour of y as $s(t)$. The estimate of the mean behaviour can then be written as,

$$s(t) = n^{-1} \sum_{k=1}^{n} y_k(t - t_k). \tag{3.16}$$

For example, in looking for the shape of a geomagnetic storm in the Sym-H index, $y_k(t)$ would be set as the Sym-H index during the geomagnetic storm. The epoch time, t_k, could be the onset of the geomagnetic storm, or the end of the main phase (two points commonly taken as epoch points in storm studies), and n would be the number of storms in the study. In Chapter 5 we will use a superposed epoch analysis to look at geomagnetic storms, and when EMIC waves are observed with respect to the storm phases. Each of the phases of the storm will be normalised, in essence giving four key times to use to perform the superposed epoch namely, 3 hours prior to the storm onset, the storm onset, the end of the main phase, and the end of the recovery phase, as shown in Figure 3.3.

Since each storm phase varies in length, the individual phases of each storm were normalised before the superposed epoch was completed. The flowchart in Figure 3.2 describes the normalisation process. After the storm and its phases were identified and

divided as depicted in row 2 of Figure 3.2, each phase was then treated separately. For each phase, the start was defined as t_o and the end of the phase as t_1. The phases were normalized to a span which was larger than the longest duration, defined as t_m, in order that no information was lost as shown in row 3 in Figure 3.2. This step was not needed for the pre-onset phase since they were all the same length by definition. Once all of the phases were normalised, the superposed epoch of each phase is determined. The same process is then used to determine the superposed epoch for the Kp index. The superposed epochs of the phases are then plotted side by side. The final results of this process can be seen in Figures 5.2 and 5.6 where the bottom two panels show the normalised superposed epoch of the Kp index and the Sym-H index. These figures will be discussed in section 5.3.1 and 5.3.2.

In order to study the number of EMIC waves occurring during the storms, we divide each of the phases into bins; using 25% bins for the pre-onset phase (due to the relatively short time period) and 10% bins for the main and recovery phases. In row 2 of Figure 3.2, where the phases have been separated, but not yet normalised, the correct bin length was found and the EMIC waves counted for each bin. Once this had been done for all storms, total counts for each bin, e.g. 0-25% bin in the pre-onset phase, were then added together and this histogram was plotted as the black line in Figure 5.2. A similar process was done to find the mean rate of EMIC occurrence in each bin which we define as the mean rate $< \dot{n} >$ given as

$$< \dot{n} >= N_s^{-1} \sum_{i=0}^{N_s-1} \frac{n_i}{\tau_i}, \tag{3.17}$$

where N_s is the number of storms, n is the number of EMIC waves in the bin, and τ is the bin size for the phase in storm i. For example, if the main phase of a storm lasts 10 hours with 10% bins and there were 5 EMIC waves found in the 30 - 40% bin, then we find that the rate of occurrence would be 5.0 EMIC waves per hour. Once this has been done for all storms and all bins, the rates of occurrence for each bin are then averaged and plotted as the red line in the top panel of Figures 5.2 and 5.6 and the corresponding axis is on the right hand side.

This normalisation combined with the superposed epoch process is assuming that the

important time scales to the system are variable between geomagnetic storms. If we look once again specifically at the geomagnetic process relevant to storms we see an injection of ring current particles into the inner magnetosphere, the point at which loss of ring current particles dominates the development of the ring current, and a point where the ring current has recovered to pre-storm levels. This treatment however does not look at other magnetospheric processes which may also be important during a geomagnetic storm such as the evolution of the plasmasphere. As will be discussed in the later chapters, the formation of a plasmaspheric plume can happen rapidly during the pre-onset and main phase of a geomagnetic storm as well as the eroding and inward motion of the plasmapause. The recovery of the plasmasphere has an even longer time scale than any of the other processes mentioned, and many ground based studies have used this time scale to define the recovery phase of a storm. However since the presence of hot ring current ions is vital for the generation of EMIC waves, we have chosen to define our epochs by characteristics observed in the ring current.

3.12 Summary

In this chapter we have identified the data used in the thesis. The CRRES mission provided data to identify EMIC waves and the local plasma environment conditions. The Kyoto Sym-H index and Kp index were used to identify geomagnetic storms and if the magnetosphere was either disturbed or quiet. We are able to produce spectra to identify individual EMIC wave events, the ambient magnetic field, and the local cold plasma number density. Chapter 4 will look at where CRRES observed EMIC waves and associated magnetospheric conditions. Chapter 5 takes a closer look at the relationship between EMIC waves and geomagnetic storms. The cold plasma number density will be used in Chapter 6 to look at the relationship between EMIC waves and the plasmasphere. In Chapter 7 the ambient magnetic field, the integrated wave power, ephemeris data, and local cold plasma number density are used to calculate the diffusion coefficients for EMIC waves resonating with radiation belt electrons.

4

CRRES EMIC Wave Observations

4.1 Introduction

Electromagnetic ion cyclotron waves have been used to study the magnetosphere and magnetospheric phenomena for over 70 years [e.g. Demekhov, 2007, Engebretson et al., 2008a, Glangeaud et al., 1980, Halford et al., 2010, Jacobs and Watanabe, 1967, Kangas et al., 1998, Tepley and Amundsen, 1965, Tepley, 1961]. Since then EMIC waves have been extensively studied both on the ground and in space, leading to a better understanding of the magnetosphere, its boundary regions, and contributions to space weather such as associations with geomagnetic storms [e.g. Halford et al., 2010], ring current decay [e.g. Jordanova et al., 1996], and decay of radiation belt electrons [e.g. Summers, 2005]. This chapter will briefly review previous research before focusing on the CRRES satellite mission and its observations. We will look at the average location of EMIC waves and

show that they occur preferentially during geomagnetic storm times.

4.2 Ground Based Studies

EMIC wave packets propagate along the geomagnetic field direction from the equatorial generation region towards the ionosphere where some of the wave energy is transmitted through the ionosphere and observed on the ground as shown in Figure 4.1 [Jacobs et al., 1964, Kozyra et al., 1984, Obayashi and Nishida, 1968]. As seen in figure 4.1 this can occur at both ends of the field line at ground conjugate sites [Demekhov, 2007]. The wave itself might appear with a slightly different amplitude and frequency, or not observable at all at various nearby ground stations, due to different attenuation properties of the ionosphere [e.g. Fujita and Tamao, 1988]. Many ground based studies have considered the diurnal occurrence and latitudinal location of Pc 1-2 waves (Figure 4.2) which indicates a general trend for Pc 1-2 wave observations to increase with increasing latitude and maximise near the auroral zones [Fraser, 1968, and references therein]. In the low to middle latitudes, occurrence peaks in the dawn sector, while at higher latitudes the maximum is located around noon or later.

A particular type of Pc 1 wave was originally designated as 'Pearls' because of its regular wave packet structure. These pearls have been observed to occur approximately 180 degrees out of phase on the ground between the hemispheres [Tepley, 1964]. This behaviour can be explained by the Bouncing Wave Packet (BWP) model first introduced by Jacobs and Watanabe [1964] and Obayashi [1965]. The BWP model states that following generation in the equatorial region EMIC wave packets will bounce back and forth between hemispheres along geomagnetic field lines in a fashion similar to VLF whistler waves [Obayashi, 1965]. This occurs when a small amount of energy of the wave packet is reflected from the ionosphere and is re-amplified as it passes through the equatorial source region and back along the field line eventually reaching the conjugate site where the process may be repeated. Significant energy is transmitted into the ionospheric wave guide and eventually to the ground.

In recent years there has been doubt cast on the BWP model and a new idea, the

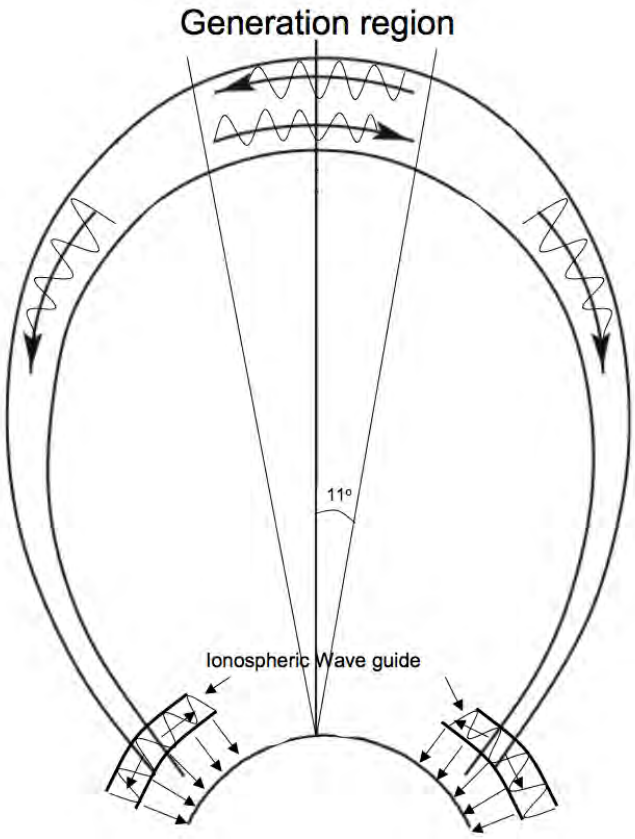

FIGURE 4.1: A cartoon of the results of Loto'aniu et al. [2005] from Trakhtengerts and Demekhov [2007].

Backward Wave Oscillator (BWO) regime has been suggested [Erlandson and Ukhorskiy, 2001, Fraser et al., 1996, Loto'aniu et al., 2005, Trakhtengerts and Demekhov, 2007]. Using CRRES EMIC wave data Loto'aniu et al. [2005] showed that the Poynting flux was directed both towards and away from the equator within 11° of the magnetic equator. while outside this region the Poynting flux was found to only be directed toward the ionosphere (Figure 4.1). Trakhtengerts and Demekhov [2007] performed a quantitative analysis of the BWO and found that it is capable of explaining the CRRES results found by Loto'aniu et al. [2005], but was unable to to replicate the observed wave amplitudes and temporal dynamics. Reconciling the CRRES observations with the BWP model is

still an open question.

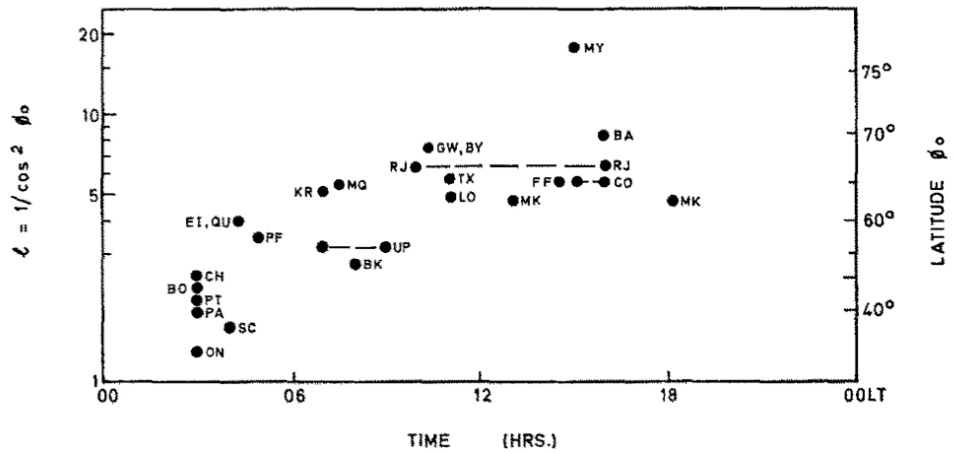

FIGURE 4.2: The variation in the time of Peak Diurnal Occurrence of hydromagnetic emission activity with latitude for twenty three stations around the world from Fraser [1968].

4.3 The Ionospheric Wave Guide

EMIC waves propagating through the magnetosphere are left hand polarised waves guided by the magnetic field direction. In the F2 region of the ionosphere some of the wave energy can become coupled to the right hand isotropic mode, allowing the wave to propagate parallel to the Earth's surface. Some of the left hand mode energy may propagate directly through the ionosphere to the ground [Manchester, 1968, Tepley and Landshoff, 1966]. Therefore EMIC waves are able to travel across field lines parallel to the Earth's surface in the F2 region for thousands of kilometres from the original field line footprint at velocities on the order of 10^2 - 10^3 km s^{-1}. These velocities correspond to the Alfven velocity of right hand polarised magnetosonic waves in the ionosphere [Manchester, 1968, Neudegg, 1997, Tepley and Landshoff, 1966]. This complicates results from ground based measurements for determining the EMIC wave properties, and in particular the location of the source region field line in the magnetosphere cannot be determined from wave amplitudes. It is therefore important to undertake in situ satellite studies which can directly

identify the EMIC wave source field line.

4.4 Satellite Studies

Satellite in situ magnetosphere observations are important in identifying the source region, generation mechanism and propagation characteristics of EMIC waves in the plasmasphere and magnetosphere. An example of an EMIC wave event seen by the CRRES spacecraft is shown in Figure 4.3 which shows the electric field dynamic spectrum in the top panel and the wave dynamic spectrum for the CRRES orbit 512. In the wave spectrum, harmonics of the EMIC waves can be seen at 08:00 UT and in general the EMIC wave frequencies are found to follow the background magnetic field strength. EMIC waves have been observed by many satellites since the 1960's including ATS -1, ATS-6, OGO-5, DE-1, ISEE-1/2, AMPTE/CCE, CRRES, GOES, POLAR, SCATHA and Themis [Anderson, 1996, Loto'aniu, 2003, Nguyen et al., 2007, Usanova et al., 2008, and references therein]. It has been found that EMIC waves occur over a wide range of L-values and local times. Fraser and Nguyen [2001] found that although EMIC waves can be found both inside the plasmapause boundary, and outside in the plasma trough, there was a clear peak around L-values of 5 to 7 and also between 14 to 16 hr MLT sector. These results agree well with other satellite studies including one of the most comprehensive in situ studies using the AMPTE/CCE spacecraft [Anderson et al., 1992a,b]. Anderson et al. found that EMIC waves were most commonly observed at L-values greater than 7 in the pre dawn sector as well as between noon and late dusk as can be seen in the scatter plot in Figure 4.4. CRRES saw a similar occurrence pattern for EMIC waves over the regions covered by the mission as seen in the left hand plot of Figure 4.5. The CRRES mission ended early, consequently not fully precessing around the Earth in MLT and thus did not observe EMIC waves in the high occurrence noon sector (08 - 14 hr MLT).

In research to date, one noticeable sector which is missed by satellite studies is the very inner magnetosphere and plasmasphere. At low L-values, the satellites are moving quickly making it difficult to resolve EMIC waves. In the magnetic field data EMIC

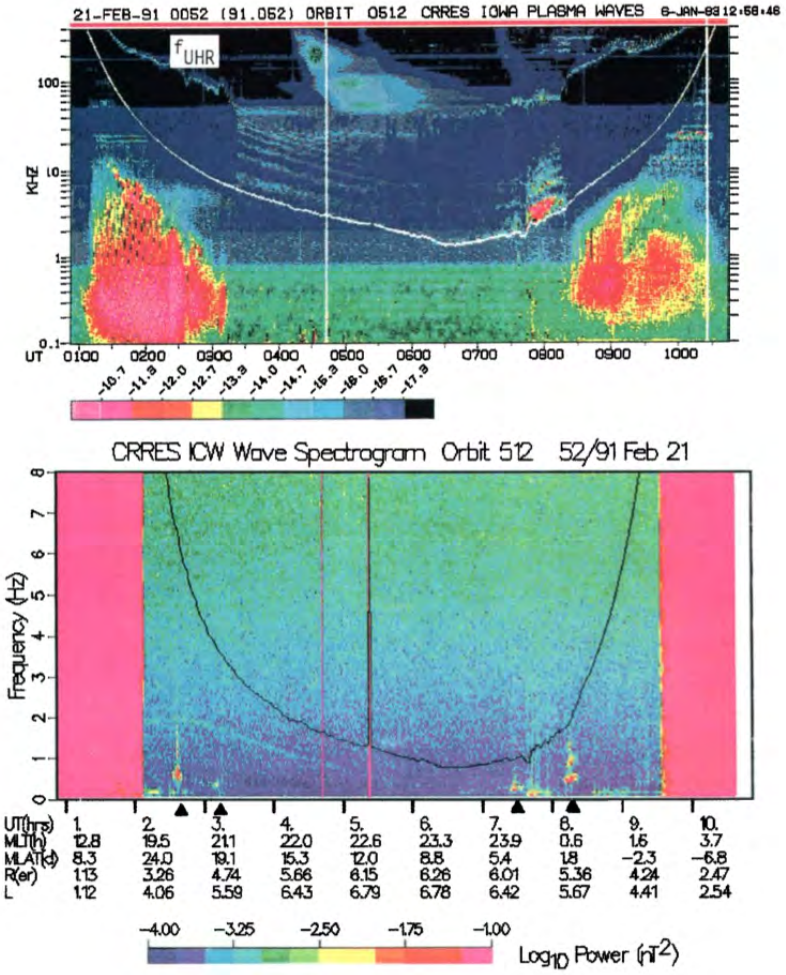

FIGURE 4.3: The upper panel shows the corresponding electric field dynamic spectrum from the PWE where the upper hybrid resonant frequency is identified and the light curve is the electron cyclotron frequency [Fraser et al., 1996]. The lower panel show CRRES EMIC wave dynamic spectra for orbit 512 on 21 Feb., 1991. The dark curve is the proton cyclotron frequency and the triangle markers are the times where EMIC wave events were observed.

wave amplitudes are on the order of 1-10 nT superposed onto a rapidly changing background magnetic field which makes observations even more difficult to resolve. This is compounded with the fact that for many satellites like CRRES, magnetometers operate in a low gain mode making it virtually impossible to detect EMIC waves during these intervals. The convergence of these events for the CRRES mission occur at L = 3, and thus we have not looked for EMIC waves within this region. As it is uncommon for the ring current to extend inward of 3 R_E, it is unlikely that many waves which would occur in this region would be due to interactions between the ring current and plasmasphere during geomagnetic storms [Daglis et al., 1999, Friedel and Korth, 1997]. Since EMIC waves and their relationship to geomagnetic storms will become the focus of this thesis in the following chapters, we are unconcerned about neglecting these events, which are expected to occur at frequencies greater than 4.0 Hz.

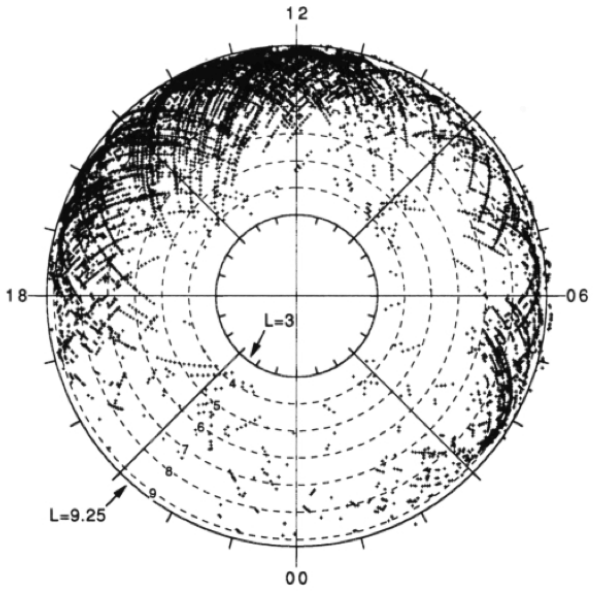

FIGURE 4.4: A scatter plot in MLT/L polar coordinates of EMIC wave occurrences in 5 minute time segments during the AMPTE/CCE satellite mission (day 239 1984 until day 326 1985) [Anderson et al., 1992a].

This chapter considers the occurrence of EMIC waves and their location in the magnetosphere. Here we have considered EMIC waves occurring in the frequency range of

0 .1 - 4.0 Hz whereas Fraser and Nguyen [2001] looked only at waves in the 0.1 - 2.0 Hz band. In the magnetosphere, initially we will be looking at three categories; all the events observed by CRRES; non-storm EMIC waves observed when there was no associated storm; and storm time EMIC waves observed when geomagnetic storm activity was present. Chapter 5 will consider more specifically EMIC waves observed during the geomagnetic storm and categorise them by the phases of the storm. By studying EMIC wave behaviour under various geomagnetic conditions, it is possible to determine the properties associated with the generation and propagation of EMIC waves in the magnetosphere which can lead to a better understanding of ring current and radiation belt particle loss.

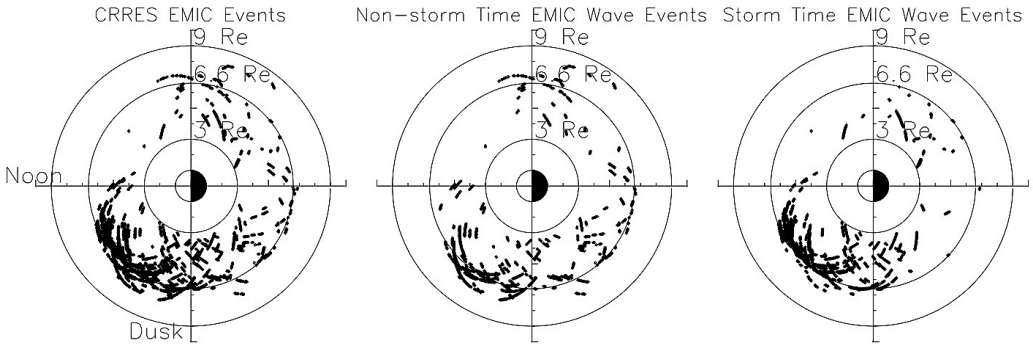

FIGURE 4.5: Left: EMIC wave occurrences during the CRRES mission. Middle: EMIC wave occurrences during non-storm time magnetospheric conditions. Right: EMIC wave occurrences during geomagnetic storms. CRRES did not cover the sector between 08 hr - 14 hr magnetic local times.

4.5 CRRES EMIC wave observations

Throughout its mission time CRRES observed 913 EMIC wave events within the frequency range of 0.1 - 4.0 Hz, as described in Chapter 3.8. The mean duration of the EMIC wave events was ≈ 6.5 minutes. Unfortunately due to the fact that the satellite can only take single point measurements it is unclear if the amount of time that CRRES observes a wave relates to the temporal or spatial scale of the event region. The mean location of the events occurred at 15 hr MLT, L = 6, and a magnetic latitude, MLat, of -6.4°

in the southern hemisphere as shown in Table 4.1 and Figures 4.5 and 4.7. Although the left plot in Figure 4.5 shows the highest occurrence of EMIC waves at around 15 hr MLT there is a second cluster near 05 hr MLT. Similarly in Figure 4.6 there are two regions of enhanced density near dusk and before dawn where we see the majority of EMIC waves.

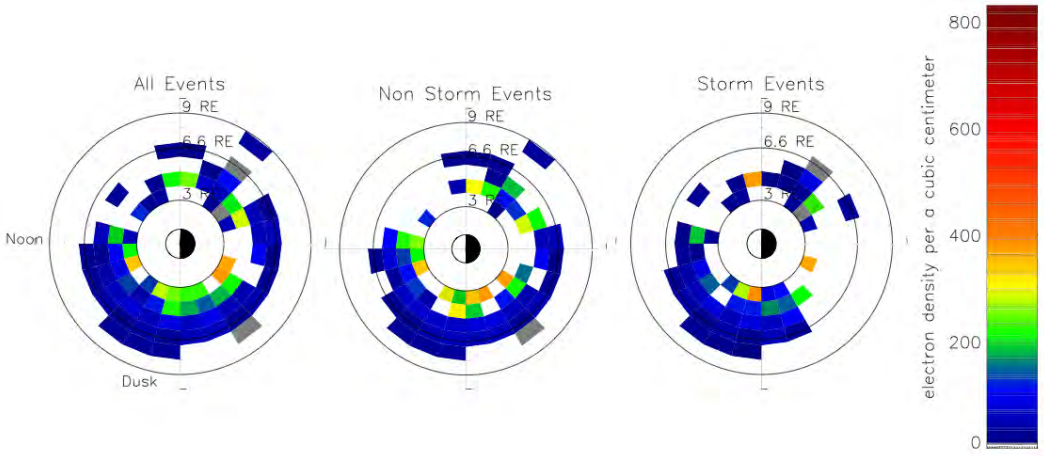

FIGURE 4.6: Left: Mean electron densities associated with EMIC waves during the CRRES mission. Middle: Mean densities for EMIC waves during non-storm time magnetospheric conditions. Right: Mean densities for EMIC waves during geomagnetic storms.

There now exists much evidence that EMIC wave generation is highly dependent on energy sources associated with geomagnetic storm time dynamics in the magnetosphere [Engebretson et al., 2008a, Fraser et al., 1989, 2010, Gomberoff and Neira, 1983, Halford et al., 2010, Heacock and Akasofu, 1973, Jordanova et al., 2001, Khazanov et al., 2006, Kozyra et al., 1984, Wentworth, 1964]. For example, Wentworth [1964] showed EMIC waves appeared in the 2 - 7 days following geomagnetic storm onset/commencement and Fraser et al. [2010] and Halford et al. [2010] showed that EMIC waves are seen in the storm main phase. Consequently the events have been categorised by magnetospheric conditions under non-storm and storm epochs defined in Chapter 3.10 as shown in Table 4.1. Non-storm time events constitute 46.1% of the EMIC waves observed by CRRES. These events had a mean location of 15.2 hr MLT, L = 6.2 and MLat = -8.1° as shown in Figure 4.5. When comparing the left hand plot of Figure 4.5 to the middle plot, it

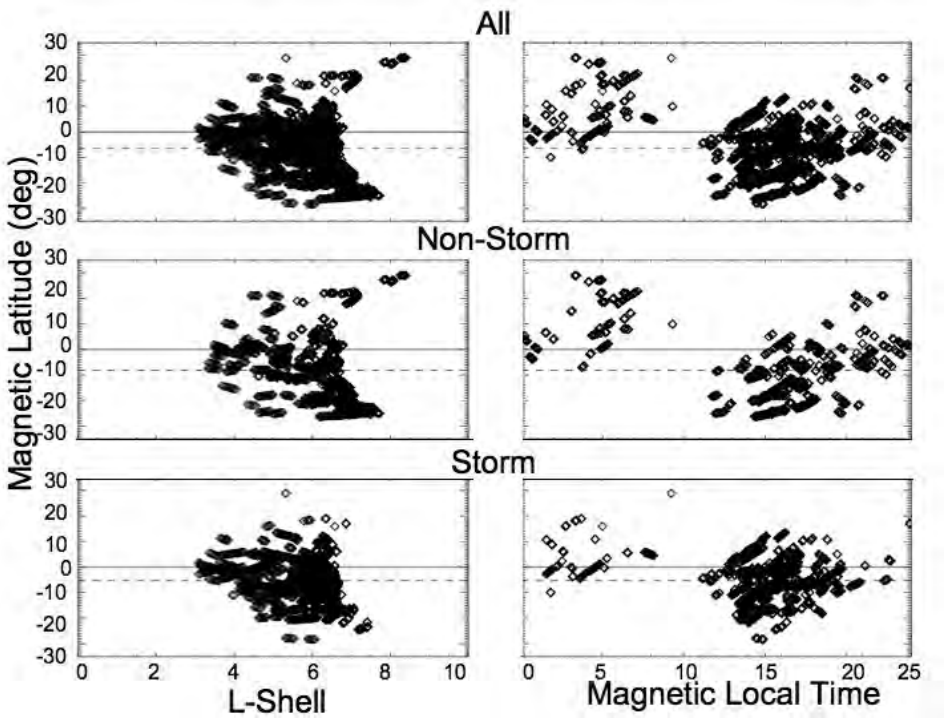

FIGURE 4.7: The left hand column shows magnetic latitudes vs L-shell for all EMIC waves during the CRRES mission (top), during non-storm time conditions (middle), and geomagnetic storm conditions (bottom). The right hand column has the same order but for MLat vs MLT. The diamonds are the observations during EMIC wave events for the given category, the solid line is at 0° and the dashed line is at the mean for the observations.

can be seen that the second cluster, and the majority of EMIC waves observed around midnight, are predominatly non-storm time EMIC waves. The mean event duration was 6.1 minutes. Figure 4.6 and Table 4.1 show the mean electron number density observed during the EMIC wave events was 63.1 cm^{-3}, which agrees well with the quiet time extended plasmasphere conditions expected at these locations [Borovsky and Denton, 2008, Goldstein, 2006]. A second peak in the density is also observed in the same region where the second group of EMIC waves occurred around 5 hr MLT.

In contrast to the non-storm time conditions, 53.9% of the EMIC wave events were observed under magnetospheric storm conditions even though only 34.2% of the CRRES mission was defined as storm time (Table 4.1). Table 4.1 and Figure 4.5 show these storm

TABLE 4.1: The properties of storms and EMIC wave events observed during the CRRES mission including the mean length of the storms and their phases, the percent of CRRES mission which was non-storm time, storm time, and spent in each phase, the number of EMIC wave events observed, the mean Magnetic Local Time (MLT) and L-value of the observed EMIC wave events, and the mean number density observed during the EMIC wave events.

	All	Non-storm time	Storm time
% of CRRES Mission Time	100	65.8	34.2
Number of events	913	421	492
% of events in CRRES Mission	100	46.1	53.9
Mean EMIC MLT	15.0	15.2	15.0
Mean EMIC L	6.0	6.2	5.9
Mean EMIC MLat	-6.4	-8.1	-5.2
Mean Density @EMIC cm^{-3}	60.6	63.1	57.4

time EMIC wave events were found on average at 15.0 hr MLT, L = 5.9, and MLat = -5.2°. There is however a second grouping in the dawn side around 04 to 05 hr MLT. There were very few EMIC waves observed around midnight during geomagnetic storms. They lasted on average for 6.9 minutes, slightly longer than their non-storm time counterparts at 6.1 minutes. Although on average the electron plasma density observed for this set of waves was lower at 57.4 cm^{-3} as shown in Table 4.1 and Figure 4.6, it is still high when compared to the expected values for the average location during storm conditions. This will be further discussed in Chapter 6.4 where we consider enhanced cold plasma densities and plasma plumes.

To test whether the differences in EMIC occurrence between storm and non-storm conditions are significant we use a chi-squared goodness of fit test [Sheskin, 2004]. A null hypothesis is adopted contending that EMIC waves are distributed uniformly throughout storm and non-storm times. The alternative hypothesis states that the occurrence of EMIC waves is not evenly distributed during storm and non-storm times. From Table 4.1 there were 421 non-storm time EMIC wave events and 492 storm time EMIC wave events. By determining when CRRES was under non-storm or storm geomagnetic conditions during

the CRRES mission, we calculate expected values for the number of EMIC waves under the null hypothesis. It was found that 65.8% of the CRRES mission was non-storm time and 34.2% of the time CRRES saw storm conditions, thus our prediction is that 599 EMIC waves should be observed during non-storm times and 311 EMIC waves during storm times. The calculated chi-square of 160.03 is greater than the critical chi-square at 95% confidence level of 3.84 and the the null hypothesis is rejected. Thus the alternative hypothesis is accepted, stating that EMIC waves are not occurring uniformly in time. Inspection of the data shows that EMIC waves are 1.6 times more likely to occur during geomagnetic storms than during non-storm times.

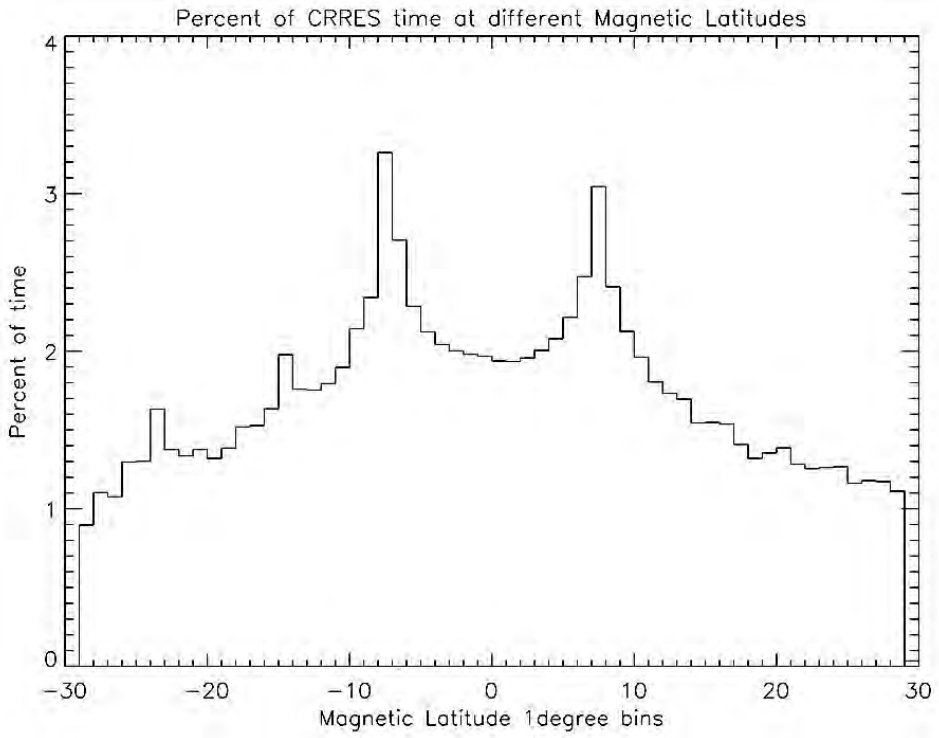

FIGURE 4.8: Histogram of the percentage of time CRRES spent in 1° bins of MLat.

As discussed in Chapter 2.4, EMIC waves are considered to be generated in the equatorial region of the magnetosphere, where $\mathbf{B}_{||}$ is considered a minimum. In Figure 4.7 the magnetic latitude is plotted with respect to L-shell (left hand plots) and magnetic local

time (right hand plots) for all events (top row), non-storm times (middle row), and storm times (bottom row). The mean magnetic latitude for all events is found to be -6.4° off the equator in the southern hemisphere and at -8.1° and -5.2° for non-storm and storm times respectively. Figure 4.8 shows the time spent at various magnetic latitudes over the CRRES mission and indicates a slight bias for CRRES to spend more time off the equator around $\pm$7-8°, although it is fairly evenly split between the hemispheres with the mean magnetic latitude over the entire CRRES mission at -0.2°. To see if EMIC waves show a hemispheric bias we performed a chi-squared test. The null hypothesis is that EMIC waves are distributed uniformly between the northern and southern hemisphere. It was found that CRRES spent about 212 days (305139 minutes or 49.2% of time) in the northern hemisphere and 219 (315144 minutes or 50.8% if time) in the southern hemisphere. If EMIC waves were distributed uniformly through out the magnetosphere then for a total of 5970 minutes of EMIC waves, we should find 2937 minutes occurring in the northern hemisphere and 3033 minutes occurring in the southern hemisphere. In actuality there were about 1 day of EMIC waves (1504 minutes or 25.2%) in the northern hemisphere and 3 days (4466 minutes or 74.8%) of EMIC waves in the southern hemisphere. This gives us a chi-squared value of 735.2, or a P value of less than 0.0001. Thus we find that the null hypothesis is rejected, and there is a statistically significant difference between the time CRRES spent between the hemispheres and where EMIC waves were observed.

One potential explanation of the southern hemisphere bias is that as CRRES precessed around the dusk side, CRRES spent more time in the southern hemisphere while out at radial distances where EMIC waves were expected to be observed as shown in Figures 4.9 and 4.10. While CRRES was in the northern hemisphere and the dusk sector, the majority of the time was spent at lower L-values where fewer EMIC waves were observed. In the right hand plots of Figure 4.7 there is a trend that the EMIC waves occurring in the dawn sector appear to occur in the northern hemisphere (where CRRES was out at farther L-values) while those in the dusk sector are predominantly seen in the southern hemisphere. In Figure 4.10 the mean α^{*} (from Chapter 2.4.2), L-value, background magnetic field, and number density are plotted along with the number of minutes where EMIC waves were observed in bins of magnetic latitude. Although neither the background magnetic

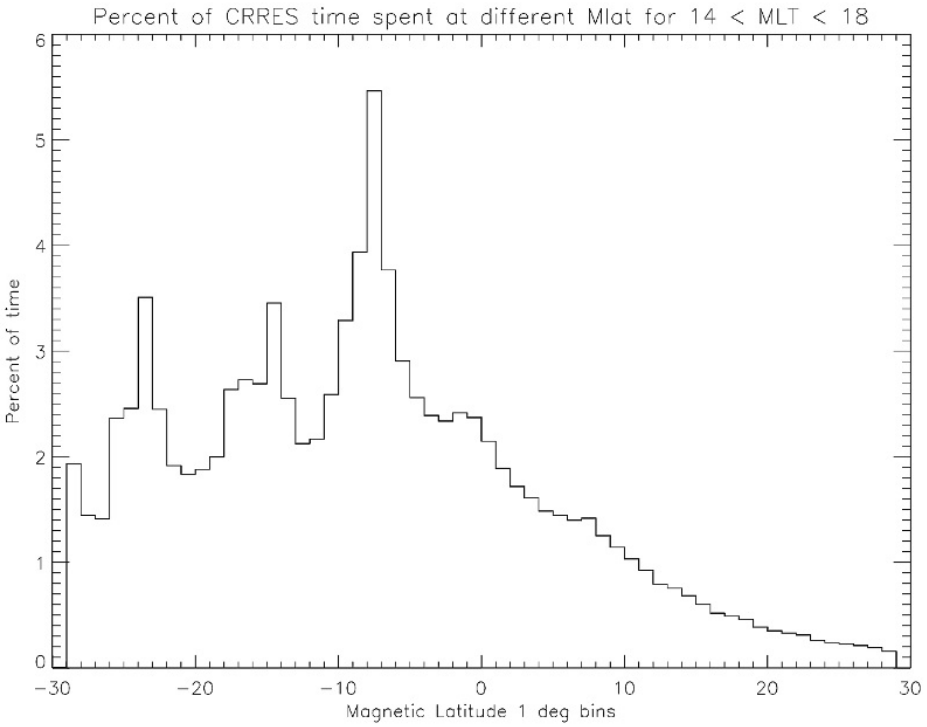

FIGURE 4.9: Histogram of the percentage of time CRRES spent in 1° bins of MLat while in the MLT bin of 14 - 18 hr, where the majority of EMIC waves were observed.

field (panel d), nor the density (panel e) appear to relate to where EMIC waves are seen, the growth parameter α^* (panel a), which is dependent on both the magnetic field and plasma density, agrees well with the EMIC wave occurrences. One surprising aspect of the bottom two panels in Figure 4.10 is the asymmetry between the northern and southern hemispheres, which may be at least partly due to the CRRES orbit. Panel c of Figure 4.10 shows that CRRES was, on average at larger L, in the southern hemisphere. This would explain why there is the asymmetry between the hemispheres for the background magnetic field and density data, and thus the peaks in the growth rate parameter α^*. As stated in Chapter 3.1, EMIC waves were not identified for L < 3. In Panel c of Figure 4.10, the mean L = 3 at MLat 15°, where EMICs are no longer observed in panel b.

As CRRES precesses around the night side towards dusk CRRES started to spend

more time in the southern hemisphere as shown in Figure 4.9 covering 14-18 hr MLT. To try to reduce this effect we can look at the region where the majority of EMIC waves occurred in magnetic local time (14 - 18 hr) and L-value ($L > 3\ R_E$) . CRRES spent about 66.5 days (95841 minutes) in the 14 - 18 hr MLT and $L > 3$ bins, and there were 2.5 days (3619 minutes) of EMIC wave events. In this region CRRES spent 11 days (16978 minutes or 17.7%) in the northern hemisphere and 54.8 days (78863 minutes or 82.3%) in the southern hemisphere. Thus if EMIC waves occur uniformly in the northern and southern hemispheres we would expect to find less than half a day (641 minutes)in the northern hemisphere and about 2 days (2978 minutes) in the southern hemisphere. We found that there was less than half a day (616 minutes or 17%) in the northern hemisphere and over 2 days (3003 minutes or 83%) in the southern hemisphere. This gives a chi-squared value of 0.555 or a P-value of 0.457 and thus the null hypothesis can be accepted.

4.6 Summary

One important consideration with this study is that CRRES did not fully precess in local time around the Earth before the mission ended. Because of this we are missing many EMIC wave observations from 08 hr - 14 hr magnetic local time which were indeed seen by Ampte/CCE [Anderson et al., 1992a,b]. Since it is unlikely that the majority of EMIC waves occurring in the region are due to interactions between the plasmasphere and the ring current we are unconcerned about neglecting them for this study. They are more probably due to compression of the magnetopause, during the pre-onset phase of a storm, or associated with sudden impulses [Anderson and Fuselier, 1994, Guglielmi et al., 2005, McCollough et al., 2009, Usanova et al., 2010]. Here we focus on the bulk of EMIC waves seen by CRRES in the afternoon and evening sectors (Figure 4.5) which are expected to be associated with particle injection from the night side plasmasheet.

The results on the location and occurrence of EMIC waves presented here are more comprehensive than previous CRRES studies but agree well with other satellite studies, particularly Ampte/CCE [Anderson, 1996, Anderson et al., 1992a,b]. It is seen that EMIC

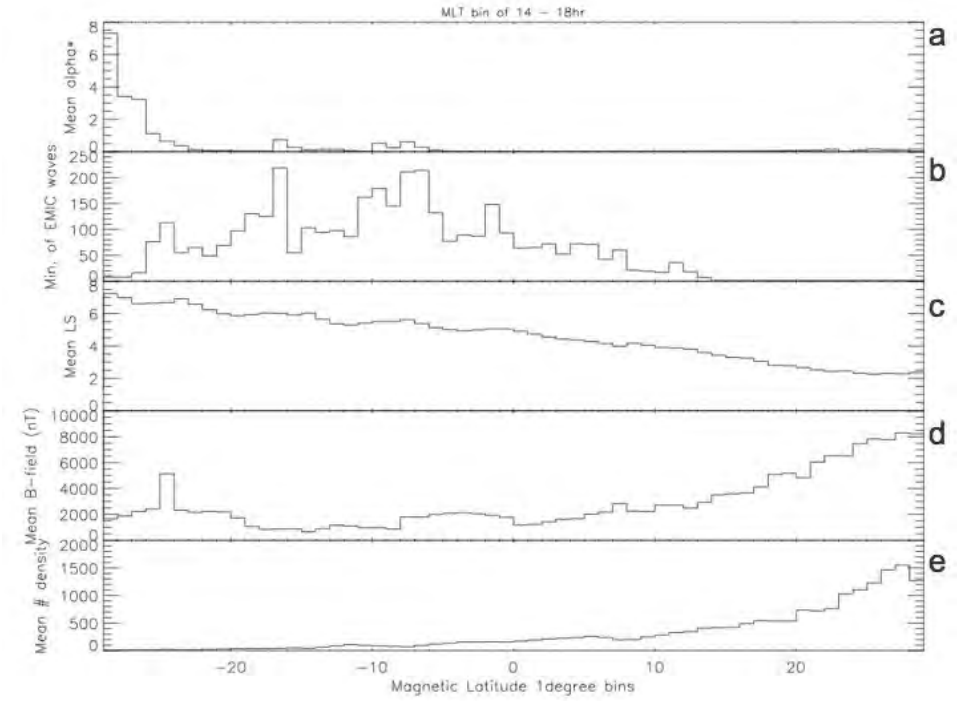

FIGURE 4.10: For the MLT bin of 14 - 18 hr; Panel a shows the average α^* by MLat bin. Panel b shows the number of minutes where EMIC Waves were observed in 1° bins. Panel c is the mean L-value for the MLat bin. Panel d is the mean background magnetic field, and Panel e shows the mean number density.

waves (both non-storm and storm) are more likely to occur in the noon - dusk sector at L = 6, and relatively few are observed in the dawn and midnight hours. Using a chi-squared goodness of fit test we showed that EMIC waves do not occur uniformly during non-storm and storm times. Examination of the data shows that EMIC waves are 1.6 times more likely to occur during geomagnetic storms than during quiet times.

Chapter 2.5 showed that a temperature anisotropy is required for EMIC wave growth and thus it is likely that the overlap between the hot ring current particles and the cold plasmaspheric particles is perhaps not always necessary, but helpful in the creation of EMIC waves in this region of the magnetosphere. The overlap between these two magnetospheric plasmas occurs most notably during geomagnetic storms. In Chapter 5, we will take a closer look at the occurrence patterns for storm EMIC waves by binning the events

by storm phase. Since the Sym-H index is used in determining the phase of the storm, this will consider the correlations between EMIC waves and the ring current, or hot plasma.

A southern hemisphere bias appeared in the data over the entire mission, which was attributed to the orbit of CRRES. Recent work by Engebretson et al (2011, private communication) showed that EMIC waves poleward of the cusp found with Cluster and ground based observations had a northern hemisphere bias in the dawn sector and a southern hemisphere bias in the dusk sector, which looks similar to Figure 4.7.

Although the location of wave occurrence did not appear to agree well with magnetic field strength or plasma density distributions across the hemispheres, they did agree well with the observed increases in α^* which is related to the growth of EMIC waves and proportional to the Alfven velocity.

5

EMIC Wave Occurrence During Geomagnetic Storms

5.1 Introduction

The previous chapters have suggested that EMIC waves are related to geomagnetic storms, and more importantly individual phases of geomagnetic storms. Chapter 1 notes that geomagnetic storms make dramatic changes to the magnetic field of the Earth, and changes in the population of charged particles in the radiation belts modify the ionosphere. For example, EMIC waves propagating along the geomagnetic field from the equatorial region down to the ionosphere are able to mode convert from the left hand mode to the right hand isotropic mode in the ionosphere and propagate parallel to the surface of the Earth through the F2 region wave guide. However this process along with transmission through

the E region will attenuate the wave, resulting in reduced wave power propagating through to the ground. Consequently it is important to observe EMIC waves during geomagnetic storms using the in situ CRRES satellite and compare the results with previous ground based studies. This work has been published in Halford et al. [2010].

5.2 Geomagnetic Storm Effects: past studies

As described in Chapter 2.2, EMIC waves are transverse, left-hand polarised waves that are observed at middle to high latitudes and are generated in the magnetosphere by Doppler shifted cyclotron interaction with energetic and anisotropic ring current protons (10 - 100 keV) [Cornwall, 1965] (Chapter 2.4). During geomagnetic storms the ring current can encroach on the cold enhanced plasma population in the plasmasphere [Criswell, 1969] and plasmaspheric plumes, thereby reducing the instability threshold of the wave generation [Fraser et al., 2005b, Kozyra et al., 1984]. The preferred region of wave growth for EMIC waves is in the equatorial region where the wave vector is parallel to the magnetic field, which is also at a minimum [Fraser et al., 1992, Gary et al., 1994, Gomberoff and Neira, 1983, Kozyra et al., 1984]. An important aspect of understanding the theory and generation mechanism of EMIC waves and their relationship with geomagnetic storms is to know where, when, and under what magnetospheric conditions EMIC waves are observed.

As stated in Chapter 2.4, an important parameter in the generation and growth of EMIC waves is the existence of a hot ion temperature anisotropy. Geomagnetic storms are able to accelerate electrons and are thought to contribute to the 100- 200 keV protons which are higher energy than the particles expected to drive EMIC wave generation, but do contribute to the bulk plasma parameters. Summers et al. [2004] expected from their results that during a period of prolonged storm activity there would be a relativistic electron enhancement in the outer radiation belt which could potentially be due to EMIC wave generation. It has been proposed that the main phase of a geomagnetic storm would provide ideal ring current and plasmaspheric conditions for the overlap of hot and cold particle populations [Engebretson et al., 2008a, Jordanova et al., 2001, Khazanov et al.,

2006, Posch et al., 2010]. Due to convection, the plasmasphere would continue to erode removing the cold particles. Likewise as the storm continues, the ring current particles would continue to be lost, removing the free energy source generating EMIC waves. However during storm recovery convection returns to pre-storm levels and the plasmasphere refills outwards to L-shells where the ring current is located. It is thought that the hot and cold particles may once again overlap and subsequently generate EMIC waves when this occurs.

EMIC waves are frequently observed in association with geomagnetic storms, and when an inflated plasmasphere or plasmaspheric plume is present [Anderson et al., 1992a, Bräysy et al., 1998, Fraser and Nguyen, 2001, Fraser et al., 2005b, 2006, Posch et al., 2010]. Modelling has shown that EMIC waves can play an important role in particle loss of ring current ion and radiation belt electron populations through pitch angle scattering [Jordanova, 2007, Jordanova et al., 1997, Meredith et al., 2003]. Modelling also suggests that EMIC waves occur primarily during the main phase of a geomagnetic storm [Jordanova et al., 2001, Khazanov et al., 2006]. Figure 5.1 shows a scenario with respect to EMIC wave generation the relative locations of the plasmasphere and the ring current during the different phases of a storm. During the pre-onset phase (Figure 5.1 a) EMIC waves are seen, but not due to particle injection. These are thought to be generated by the day side compression of the magnetosphere as described in Chapter 2. During the main phase (Figure 5.1 b) we expect to see plasma plumes in the same region as the ring current, and thus the potential for EMIC waves to be generated. With the first definition of the recovery phase (Figure 5.1 c), it is expected that the ring current and/or the plasmasphere and plasma plumes will be eroding and thus will produce few EMIC waves. Figure 5.1 d shows the late recovery phase with EMIC waves as the plasmasphere expands towards the outer magnetosphere and may once again overlap with the ring current.

There have been many studies on the correlation between EMIC waves and geomagnetic storms [Blum et al., 2009, Bortnik et al., 2008, Engebretson et al., 2008a,b, Fraser et al., 2010, Heacock and Akasofu, 1973, Morley et al., 2009, Spasojevic and Fuselier, 2009, Wentworth, 1964]. When defining storms in individual studies, the parameter most often used for indicating storm activity is the one hour Dst index. The phases of a storm,

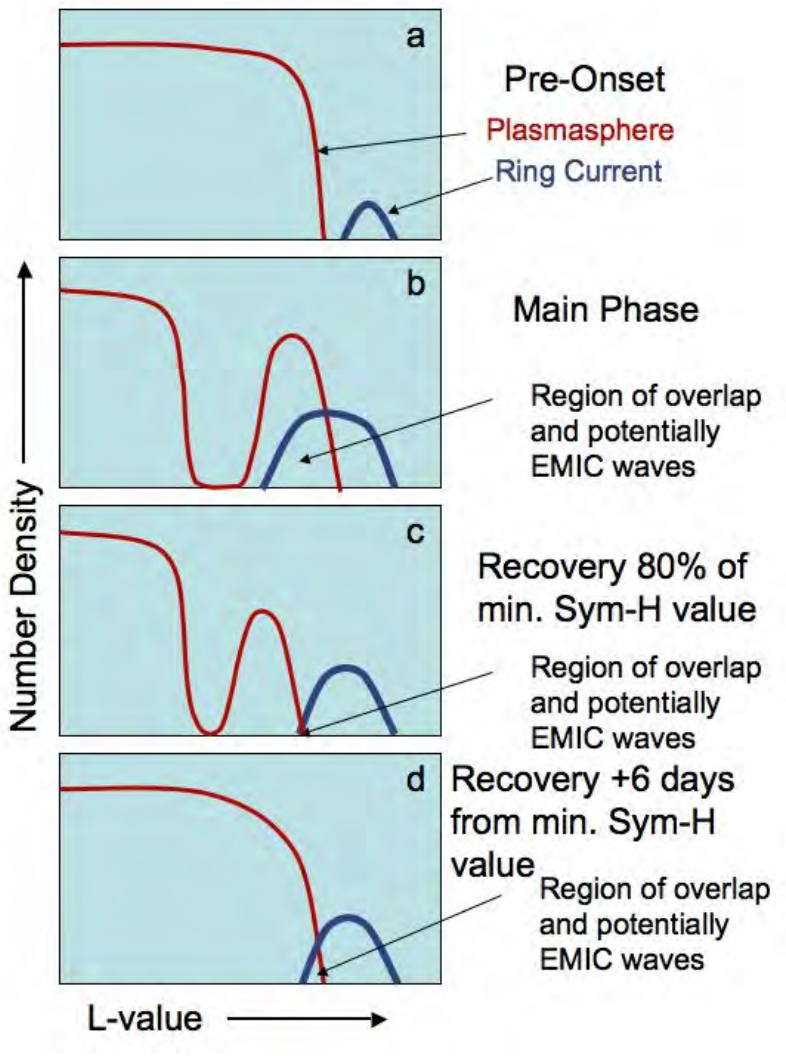

FIGURE 5.1: A cartoon of the relative positions of the plasmasphere (red) and the ring current (blue) as viewed though the path of a CRRES orbit. From the top to the bottom we have the pre-onset, main phase, recovery phase as defined by 80% of the min. Sym-H value, and the recovery phase as defined by 6 days after the min. Sym-H value. The regions where the ring current and plasmaspheric particles overlap are regions where we might expect to find EMIC waves, during the main and early recovery phase the formation of a plasmaspheric plume.

and in particular the recovery phase, were typically defined variously when completing statistics, or looking at individual cases. Many defined their epoch as the minimum value for the Dst index corresponding to the end of the main phase [Blum et al., 2009, Bortnik et al., 2008, Posch et al., 2010, Spasojevic and Fuselier, 2009], some used the onset of the storm [Fraser et al., 2010, Posch et al., 2010] whereas others used the start of the day containing the storm's onset [Engebretson et al., 2008a,b]. The definitions used for the end of the recovery phase have also varied greatly from study to study. Many authors chose the end of their period of study as a number of days from the epoch time which may be the end of the studied interval, but not necessarily the end of the storm, or the effects of the storm on the magnetosphere [Blum et al., 2009, Bortnik et al., 2008, Engebretson et al., 2008a,b, Fraser et al., 2010, Heacock and Akasofu, 1973]. Other studies used properties of the Dst index to define the end of their recovery phases, such as when Dst returns to a predefined quiet time level [Bortnik et al., 2008, Halford et al., 2010, Spasojevic and Fuselier, 2009].

Along with these different definitions of a storm duration and its phases, different conclusions have been drawn with respect to the relationship between EMIC waves and geomagnetic storms. Since many satellites do not carry instrumentation to directly observe fields and thus EMIC waves, particle precipitation, the proton cyclotron instability, or the temperature anisotropy are used as proxies for identifying the presence of EMIC waves [Blum et al., 2009, Spasojevic and Fuselier, 2009, Spasojević et al., 2004]. It was found in these satellite studies that there is a peak in the occurrence of their proxy, and by inference the occurrence of EMIC waves during the main phase of storms, whereas many ground based studies saw maximum occurrences during the recovery phase [Bortnik et al., 2008, Engebretson et al., 2008a, Heacock and Akasofu, 1973, Wentworth, 1964].

5.2.1 Previous Satellite and Ground Based Studies by phase of storm

The SSC/ Pre - Onset

The storm sudden commencement, SSC, as defined in Chapters 1.6 and 3.9 occurs when the magnetosphere, the magnetopause, and the geomagnetic field are compressed on the

day side by an increase in solar wind dynamic pressure or velocity. For Pc waves that are observed to occur during the SSC of a storm, the carrier frequency jumps to a higher level. Kangas et al. [1986, and references therein] show that Pc 1 pulsations are excited after an SSC or a reasonably strong interplanetary shock. For example, there is an enhancement of Pc 1 activity on the ground after a SI in 67% of SI cases [Kangas et al., 1986, 1998]. These waves occurred most frequently around noon MLT and a few minutes after the onset of the SI. As CRRES did not fully precess around the Earth, our study was not able to observe EMIC waves in the noon sector, over 8 hr - 14 hr MLT.

The Main Phase

During the main phase of a storm the occurrence rate of Pc 1 waves observed on the ground is greatly reduced [e.g. Engebretson et al., 2008a, Posch et al., 2010]. Modelling and satellite studies however show an increase in Pc1 occurrence during this phase [e.g. Blum et al., 2009, Bossen et al., 1976, Bräysy et al., 1998, Fraser et al., 2010, Halford et al., 2010, Jordanova et al., 2001]. Spasojevic and Fuselier [2009] looked at proton precipitation, which they considered an indicator of the presence of EMIC waves, during two storm-time case studies. They found during both intervals the components needed to generate EMIC waves, namely enhanced cold plasma number density and a hot proton temperature anisotropy were present, in addition to particle precipitation which would be associated with the EMIC waves. Other ULF waves are found to be produced during this phase of a storm including Pi B waves in the night sector, Pi C pulsations in the dawn sector, and Pc 2 pulsations in the noon sector [Kangas et al., 1998]. These ULF waves are the most prominent wave manifestations of ring current formation, and may potentially perturb the ionosphere by changing the conductivity or fractional particle populations making EMIC wave detection on the ground during the main phase more difficult [Engebretson et al., 2008a, Kangas et al., 1998, Posch et al., 2010]. Intervals of pulsations with diminishing period (IPDP) are also observed in the evening sector frequently during the main phase of a storm [Kangas et al., 1998, Loto'aniu, 2003]. IPDPs are observed on the ground and when mapped to conjugate sites in the magnetosphere, EMIC waves are generally observed.

The Recovery Phase

The largest number of Pc 1 pearl events are observed on the ground during the recovery phase [Engebretson et al., 2008a, Kangas et al., 1998, Loto'aniu, 2003]. Simultaneously Pi B continue on the night side and Pc 2 pulsations are seen decreasing in intensity [Kangas et al., 1998]. This appears to be due to the interactions of the decaying ring current and expanding plasmasphere as illustrated by Kuwashima et al. [1981] who showed that Pc1 events appear at low latitudes early in the recovery phase and move to higher latitudes as the recovery phase progresses.

Many ground based studies [Bortnik et al., 2008, Engebretson et al., 2008a, Heacock and Akasofu, 1973, Wentworth, 1964], have found that EMIC waves are observed more frequently on multiple adjacent days after the minimum Dst of an isolated storm, and not as frequently during the main phase of the storm as predicted by modelling. It has been suggested that this is possibly due to the presence of impulsive noise from broad band waves observed on the ground during geomagnetic storms masking identification of the waves. Also attenuation of EMIC waves in the ionosphere and the ionospheric wave guide during the early part of a storm may inhibit observations on the ground [Bortnik et al., 2008, Engebretson et al., 2008a]. Engebretson et al. [2008b] conducted a limited low Earth orbit study using the three ST5 satellites, with apogee 4500 km, which agreed with the results of their ground based study [Engebretson et al., 2008a]. They interpreted their observations as supporting the idea that EMIC waves are not produced during the main phase and early recovery phase of geomagnetic storms and instead occur during the late recovery phase.

The present study focuses on determining the relationship of EMIC wave occurrences with storm phase during geomagnetic storms (Section 3.10) over the 14 month CRRES mission. Previous ground based studies concluded that EMIC waves are not observed during geomagnetic storm times, while theory and satellite studies suggest that they are primarily generated during such times. As a consequence of CRRES not fully precessing around the day side, our study is limited to focusing on the region where it is thought that the primary generation mechanism for EMIC waves is the interaction between the

storm time ring current and plasmasphere instead of compression. This study takes a more comprehensive look at the occurrence of EMIC waves during the CRRES mission. It should be remembered that satellites provide single location observations and therefore will not see all waves present in the magnetosphere.

5.3 EMIC waves observed by CRRES during geomagnetic storms

5.3.1 Recovery defined by 80% of the minimum Sym-H index

When interpreting our results, it is important to remember that the definitions of our phases and the times we are looking at EMIC waves are storm centric and do not say anything about the shape or location of the plasmasphere [Goldstein, 2006, and references therein]. The shape and phases of the plasmasphere are dominated by convection which is not well described by Sym-H, and instead better follows the Kp index as this is a good measure of convection [Goldstein et al., 2003, Kotova, 2007, Nishida, 1966, Stern, 1977, Thomsen, 2004] . Thus our study is considering EMIC waves and their relationship to the magnetospheric current systems, and we have ignored the possible effects of the cold particle populations by assuming that there will be enough cold plasma available, and that the determining condition is the existence of the hot plasma.

We use a list of 913 EMIC waves occurring during the CRRES mission and 124 storms. Approximately 34% of the CRRES mission time was defined as storm time and 41.5% of those storms observed EMIC waves. The majority of the EMIC waves occurred during the later part of the mission on the early descending phase of the solar cycle. Figure 5.3 shows the distribution of the EMIC waves according to magnetospheric activity. The upper left plot shows the distribution in the equatorial plane of the location of EMIC waves during non-storm times (the black symbols), and during storm times (the green symbols). The distribution in the equatorial plane of the location of EMIC waves for the pre-onset, main, and recovery phases can be seen in the upper right, lower left, and lower right plots respectively. As noted in Table 5.1, of the 913 EMIC waves, 53.9% occurred

TABLE 5.1: The properties of the Storms and EMIC waves observed during the CRRES mission including the mean length of the storms and their phases, the percentage of the CRRES mission which was defined as non-storm time, storm time, and for each phase, the number of EMIC waves observed, the mean Magnetic Local Time (MLT) and L-value of the observed EMIC waves, and the mean number density observed during the EMIC waves.

Total	Non-Storm Time	Storm Time	Pre-Onset	Main	Recovery
Mean length,hrs		29.4	3	9.1	18.3
% of CRRES Mission Time	65.8	34.2	3.5	10.5	21.3
Number of EMIC waves	421	492	34	275	189
% of EMIC waves in CRRES Mission	46.1	53.9	3.8	30.1	20.7
Mean EMIC MLAT, deg	-8.1	-5.2	-5.9	-5.8	-4.6
Mean EMIC MLT, MLT	15.2	15.0	15.1	15.1	14.8
Mean EMIC L-value,	6.2	5.9	5.7	6.0	5.8
Mean number density @EMIC, cm^{-3}	63.1	57.4	68.8	57.6	53.7

during geomagnetic storms. The EMIC waves during the CRRES mission, as defined in Chapter 3, were predominantly observed in the noon - dusk sector with a mean occurrence location at 15.0 hr MLT and L = 5.9 as shown in Figure 5.3 and Table 5.1. Table 5.2 breaks down the occurrence of the storm time EMIC waves by percentage of phase. As shown in Table 5.1, the mean length of the storms was 29.4 hours with the mean main and recovery phase lengths of 9.1 hours and 18.3 hours respectively. Furthermore EMIC waves were found to occur approximately 1.6 times more often during geomagnetic storms than during non-storm time magnetospheric conditions throughout the CRRES mission.

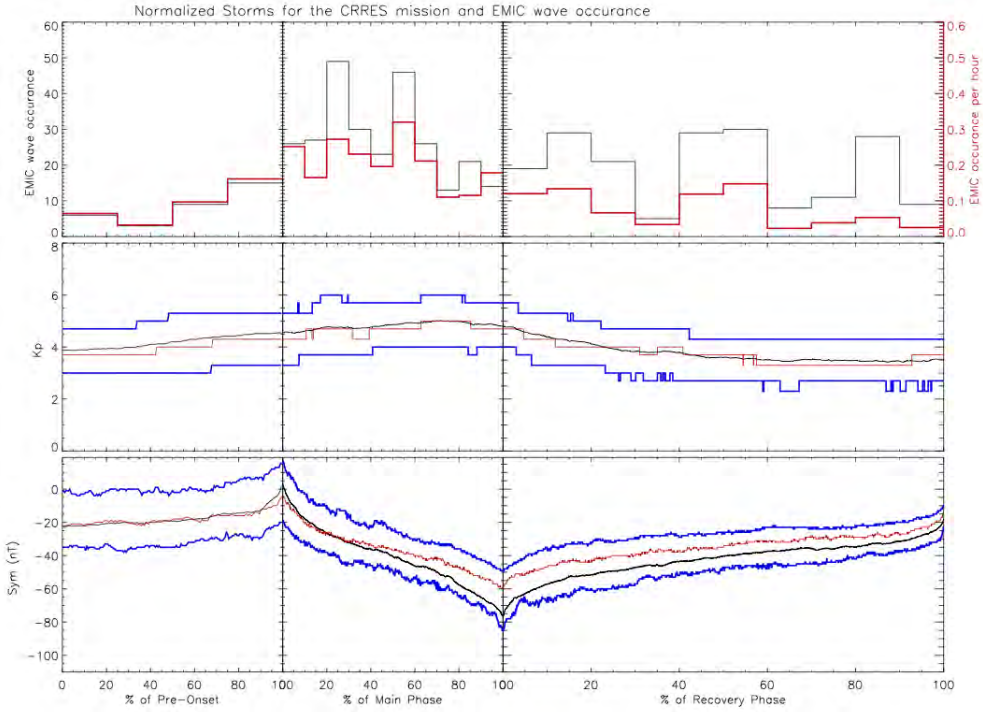

FIGURE 5.2: Top panel: The black histogram is the number of EMIC waves in 25% bins for the pre-onset phase, and 10% bins for the main and recovery phases while the red histogram shows the number of EMIC waves per hour during each bin. Middle panel: the normalised mean Kp index (black), the median (red), and the quartiles (blue). Bottom panel: The mean (black), median (red), and quartiles (blue) of the Sym - H index for the normalised storms occurring during the CRRES missions.

For the EMIC waves in this study, we normalised the storms as discussed in section

TABLE 5.2: The occurrence of EMIC waves as observed by phase of geomagnetic storm and by percentage of phase. The occurrences are presented as the number of EMIC waves observed in each bin of the phase, the percentage of EMIC waves seen during the bin by phase of storm and also by the total EMIC waves observed during storm times.

pre-onset phase	$\leq 25\%$	25-50%	50-75%	$\geq 75\%$
# EMIC waves	7	3	9	15
% of phase	20.52	8.8	26.5	44.2
% of storm	1.42	0.6	1.8	3

main phase	$\leq 10\%$	10-20%	20-30%	30-40%	40-50%
# EMIC waves	26	27	49	30	23
% of phase	9.5	9.8	17.8	10.9	8.4
% of storm	5.3	5.5	10.0	6.1	4.7
	50-60%	60-70%	70-80%	80-90%	$\geq 90\%$
# EMIC waves	46	26	13	21	14
% of phase	16.7	9.5	4.7	7.6	5.1
% of storm	9.3	5.3	2.6	4.3	2.8

recovery phase	$\leq 10\%$	10-20%	20-30%	30 - 40%	40-50%
# EMIC waves	19	29	21	5	29
% of phase	10.0	15.3	11.1	2.6	15.3
% of storm	3.9	5.9	4.3	1.0	5.9
	50-60%	60-70%	70-80%	80-90%	$\geq 90\%$
# EMIC waves	30	8	11	28	9
% of phase	15.9	4.2	5.8	14.8	4.8
% of storm	6.1	1.6	2.2	5.7	1.8

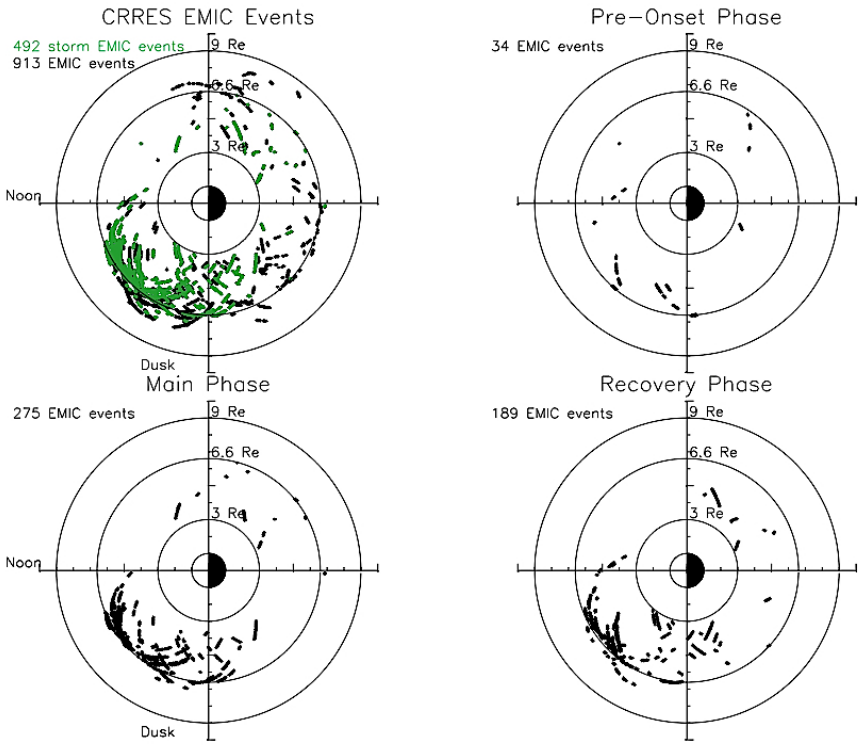

FIGURE 5.3: Equatorial plane cuts of the magnetosphere showing the number of EMIC waves in each phase. Upper Left: The occurrence locations of EMIC waves during (green) geomagnetic storms, (black) non - storm periods. Upper right: Occurrence locations of EMIC waves during the pre-onset phase. Bottom left: Occurrence locations of EMIC waves during the main phase. Bottom right: Occurrence locations of EMIC waves during the recovery phase.

3.10 and counted the number of EMIC waves observed in bins of the current phase. The results of the pre-onset (25% bins), main phase (10% bins), and the recovery phase (10% bins) can be seen in the black line in panel 1 of Figure 5.2 and Table 5.2. The average occurrence rate of EMIC waves in each of the bins is shown as the red line in panel 1 of Figure 5.2. The normalised mean (black line), median (red line), and quartiles (blue lines) for the Kp (middle panel) and Sym-H index (bottom panel) are also shown in this figure. This allowed us to determine if EMIC waves were more likely to occur or be observed during a specific phase, or percent of a phase.

One of the consequences of our definitions is that the pre-onset of the storm may

overlap up to three hours of the recovery phase of the previous storm. This occurred for 41% of the storms. In these situations, 6 EMIC waves were observed. As indicated in Table 5.2 and seen in the top panel of Figure 5.2, the majority of EMIC waves in the pre-onset phase did occur in the last quarter of the phase, close to the occurrence of the onset when one would expect to see a possible magnetospheric compression. Table 5.1, shows that 34 EMIC waves occurred during the pre-onset phase, which is 6.9% of the EMIC waves observed during storms. The CRRES mission was unable to complete one full precession in local time, and thus did not collect much data in the dawn to noon sector, which is easily seen in the top right plot of Figure 5.3. It is very probable that we missed many EMIC waves, especially those generated by magnetopause compression around noon [Anderson and Hamilton, 1993, Anderson et al., 1992a]. Thus we will focus more on the main phase and recovery phase as we are less likely to be missing as many of the waves generated during these phases.

The bottom left plot of Figure 5.3 and Table 5.1 show that the majority of the storm time EMIC waves occurred during the main phase with a mean L = 6.0 and 15.1 hr MLT. In Tables 5.1 and 5.2 it can be seen that on average, the main phase was about half as long as the recovery phase, despite the fact that 55.9% of the storm time EMIC waves occurred during this phase of the storm. The main phase is characterised by the majority of the EMIC waves occurring during the middle bin of the phase with peaks in the 20 - 30% and 50 - 60% bins which is easily seen in the top panel, the black line, of Figure 5.2. The top panel of Figure 5.2 also shows the EMIC occurrence per hour (the red line) and there is a pronounced peak of about 0.32 EMIC waves per hour during the main phase in the 50 - 60% bin with a steady decrease afterwards. The middle panel of the same figure shows that the Kp index also peaks during the main phase. Each of the 10% bins is on average about 54 minutes long.

For the recovery phase Figure 5.3 and Table 5.1 show that the mean position of the EMIC waves is similar to the main phase with L = 5.8 and 14.8 hr MLT. The recovery phase saw three peaks in the EMIC wave occurrence, as shown in the top panel black line, of Figure 5.2, in the 10 - 20%, 40 - 60%, and 80 - 90% bins, and these three peaks are the largest during the storm after the peaks in the main phase. Of the total number

of EMIC waves observed during storms, only 38.4% occurred during the recovery phase. On average each of the 10% bins was about 110 minutes long, over twice as long as the main phase bins, thus they have a higher probability of seeing EMIC waves if the EMIC waves occur uniformly throughout the storm. Although in the histogram of the number of EMIC waves per bin there are three peaks in the recovery phase which rival the peaks in the main phase, when looking at the occurrence rate, the red line in the same panel of the figure, it is clear that the occurrence of EMIC waves declines in the recovery phase where the largest occurrence rate was at around 0.15 EMIC waves per hour. The bottom two panels of Figure 5.2 show that the storm has definitely recovered both in the Kp index and the Sym-H index.

Once again we can perform the chi-squared goodness of fit test for the null hypothesis that EMIC waves occur uniformly throughout the main phase and the recovery phase of the storm with an alternative hypothesis that they do not occur uniformly between the two phases. We will only compare the main phase to the recovery phase since the pre-onset phase sometimes overlaps with the recovery phase, violating the independence assumption of the chi-squared goodness of fit test. As given in Table 5.1 there were 275 EMIC waves observed during the main phase of a storm and 189 during the recovery phase. Of the total time spent in storms, approximately 152 days, about 141 days were classified as either main phase (33.1%) or recovery phase (66.9%). Thus our predicted results are that we should see 154 EMIC waves in the main phase and 310 in the recovery phase. Again for a significance of 0.05, or a 95% confidence, our chi-squared value must be less than 3.84. In contrast, the calculated chi-squared value is 142.3 and thus the null hypothesis is rejected. Examination of the data shows that EMIC waves are more likely to occur during the main phase of a geomagnetic storm than during the recovery phase.

One potential region of generation for EMIC waves during storms is a plasmaspheric plume. Figure 5.4 shows the electron number density observed by CRRES during EMIC wave occurrences which are classified as storm time (top left) EMIC waves, and into the phases of the storm, the pre-onset (top right), the main phase (bottom left), and recovery phase (bottom right). The number densities typically observed when EMIC waves occurred are on the order of magnitude observed in the plasmasphere and in plasmaspheric

plumes (10s cm^{-3}) [Borovsky and Denton, 2008, Goldstein, 2006].

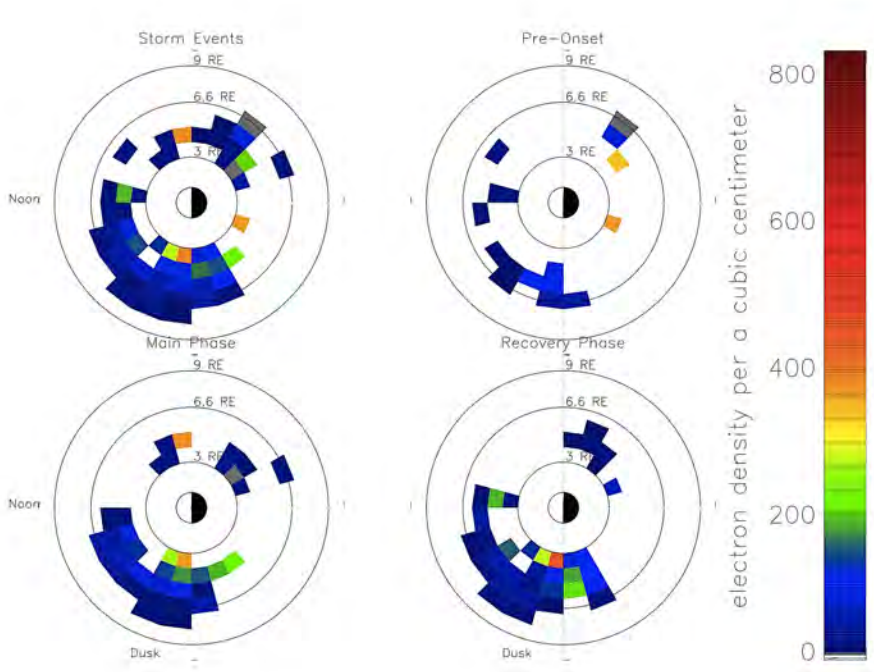

FIGURE 5.4: The mean electron density observed by CRRES during EMIC waves for (top left) storm time EMIC waves, (top right) pre-onset phase, (bottom left) main phase, (bottom right) recovery phase.

Table 5.1 and Figure 5.3 show that the majority of main phase and recovery phase EMIC waves are in the region where plasma plumes are known to occur (around 15 hr MLT and L $\approx$ 5) [Borovsky and Denton, 2008, Goldstein, 2006, and references therein]. This does not show conclusively that (on average) EMIC waves during storms occurred in the plasmasphere or in plasmaspheric plumes, but it is consistent with this scenario [Borovsky and Denton, 2008]. The Kp index (shown in the middle panel of Figure 5.2) which the plasmasphere follows more closely than the Sym-H index, shows a peak in geomagnetic activity during the main phase of the storms. This is also suggestive that plumes may be present, and we will look at this more closely in Chapter 6.

Our results showed that EMIC waves occurred at a mean L-value of 6.2. The lowest

L-value was seen on average during the pre-onset phase where the EMIC waves occurred predominantly at L-values of 5.7. The majority of the EMIC waves observed during storms were found in the main phase, which is consistent with previous CRRES [Fraser and Nguyen, 2001], GOES [Fraser et al., 2010], and other satellite study results [Blum et al., 2009, Horne et al., 2009, Spasojevic and Fuselier, 2009] as well as with modelling [Jordanova, 2007, Jordanova et al., 1997, 2008]. The chi-squared goodness of fit test shows that the observed rates of EMIC occurrence were significantly different to those expected from a model of constant occurrence. In fact we saw almost double the number of predicted EMIC waves during the main phase, 104 predicted EMIC waves compared to the 198 observed EMIC waves.

5.3.2 Recovery defined by the following 6 days from the minimum Sym-H index

Our results do not agree well with previous ground based studies [Bortnik et al., 2008, Engebretson et al., 2008a,b, Posch et al., 2010]. Engebretson et al. [2008a] state that during the early storm recovery phase in their study, which corresponds closer to the end of the recovery phase in our study, the poleward propagation of EMIC waves through the ionosphere is more severely attenuated than during non-storm times. This could account for the different results between the ground based and satellite studies. This disagreement may also be due in part to a difference of definition. Since our definition of a storm and storm time, and more specifically the recovery phase as 20% of the Sym-H min., are not directly comparable to the definitions used by these and other ground-based studies, we have adapted our definitions to align more closely with the previous ground based work and re-examined our results.

Our definition of storms differ in some important aspects from many previous studies examining EMIC waves within storms [Blum et al., 2009, Bortnik et al., 2008, Engebretson et al., 2008a, Horne et al., 2009, Morley et al., 2009, Wentworth, 1964]. Two common methods of defining storms in such studies are: 1) to select either the minimum Dst value or the start of the day which the onset occurred on and define this as the epoch time [e.g.

Blum et al., 2009, Bortnik et al., 2008, Engebretson et al., 2008a] or 2) define the epoch as the minimum Dst or Sym-H value for the storm [e.g. Bortnik et al., 2008, Horne et al., 2009]. For example Engebretson et al. [2008a] and Bortnik et al. [2008] choose the recovery phase to be a period of 4-10 days after the minimum value was reached, regardless of when the storm actually recovered from a current perspective. Bortnik et al. [2008] and Horne et al. [2009] use smoothing functions of 9 - 12 hour running averages of the Dst index to define quiet vs active times which potentially removes some small and moderate storms. Many storms studied include a condition to ensure that they are isolated and/or very large [Bortnik et al., 2008, Engebretson et al., 2008a, Horne et al., 2009]. Relative to these and other such studies we have identified many smaller and shorter storms, which would not have been counted if a running average, or the Dst index, had been used. Since we use Sym-H instead of Dst, we have many storms identified in our data as multiple storms instead of one large one. However, inspection of our superposed epoch of Sym-H gives confidence in our method of storm identification as it shows the expected morphology of storm evolution. By using either the hourly averaged Dst or a smoothed Dst instead of the 1-minute averaged Sym-H to identify storms, a very specific type is selected, which tends to be larger and more drawn out, and the timing of the injection of the ring current particles is not captured on the timescales found for EMIC waves.

Since our method, and thus our results, are not directly comparable to those from previously discussed studies, we have performed the same analysis with changes to two of our phase definitions. The first is the pre-onset phase. Instead of using the 3 hours prior to onset as our definition, we have extended it to 24 hours as an upper limit to taking the start of the day that the onset occurred [Engebretson et al., 2008a,b]. The second change to our phase definitions is with the recovery phase. Instead of defining the end of the recovery phase when the storm has recovered 80% of the minimum Sym-H value, we have defined it as 6 days after the main phase finishes, similar to Engebretson et al. [2008a] and Bortnik et al. [2008]. This, on average, extends our recovery phase by 126.5 hours, or a factor of about 8.23. The results can be seen in Figure 5.6 which is comparable to Figure 5.2 from our original study but uses the new definitions. The difference between the recovery phase definitions can be seen in Figure 5.5 where the Sym-H index is plotted

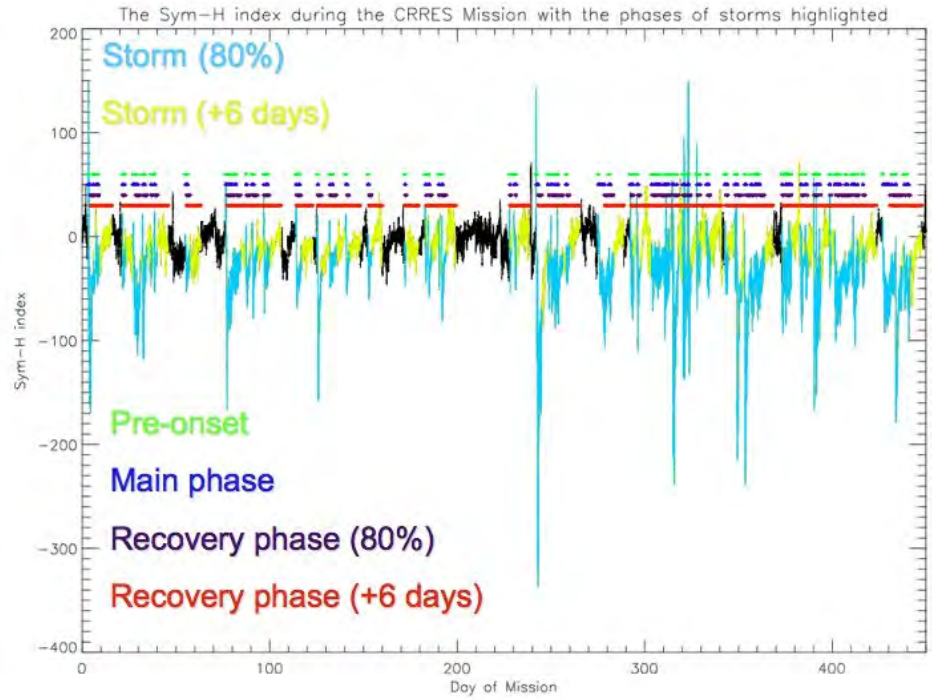

FIGURE 5.5: The Sym-H index over the entire CRRES mission. The light blue sections represent the storms using the 80% of the minimum Sym-H definition for the recovery phase while the yellow sections are the extend 6 days of recovery. Above the Sym-H index the green, blue, purple, and red lines represent the pre-onset, main phase, recovery phase (80%) and the extended recovery phase respectively. This shows the ability of the extended recovery phase to completely overlap other storms.

over the entire mission and the periods of storms for both definitions are highlighted. The recovery using the new definition of plus six days was over plotted in yellow when it extended past the 80% recovery definition, and clearly shows how easily and often it can encompass entire other storms.

With our original study we had some overlap of the recovery phase and the pre-onset phase of the next storm, but were not concerned with this since very few EMIC waves were observed during the periods of overlap. Using the redefined phases over 80% of storms overlap with the phases of others. Sometimes the extended recovery phases can encompass an entire storm, consequently the number of EMIC waves observed during the

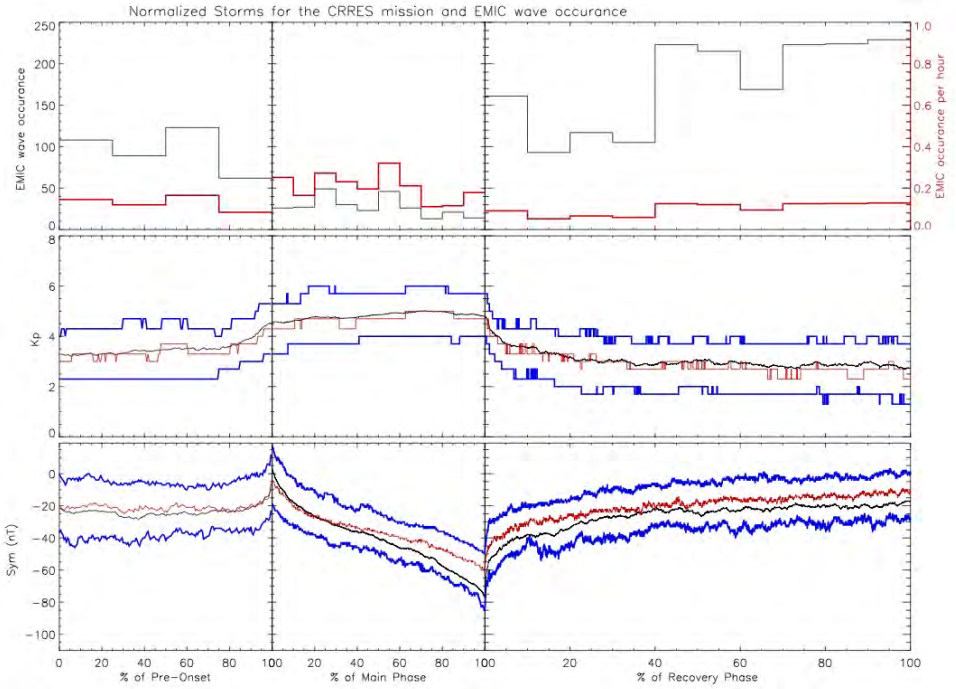

FIGURE 5.6: Same as Figure 5.2 except each phase is divided into 10% bins, the pre-onset phase is defined as 1 day prior to the onset, and the recovery phase is defined as 6 days after the minimum of the storm. Here some of the EMIC waves observed in the pre-onset and main phases are also observed during the new recovery phases from previous storms as well as some of the recovery phases are observed during the new pre-onsets. The main phases and their results have not changed.

main phases of each storm has not changed, but the number of EMIC waves observed during our pre-onset and recovery phases has grown drastically. These phases also contain EMIC waves which are counted in the overlapping phases. Due to the 84% overlap between the main phases and recovery phases as a result of these new definitions, we are unable to perform a chi-squared goodness of fit test as the independence assumption behind the test is violated [Sheskin, 2004]. In the top panel of Figure 5.6 it is shown that although the number of EMIC waves increases considerably during the recovery phase, the average rate of occurrence drastically drops off after a peak in the main phase.

In this extended recovery phase study we do see a large increase in the number of EMIC waves in the later recovery phase when compared with the pre-onset and main

phases. We now also have to remember that the average length of the 10% bin is 2.4 hours for the pre-onset phase, 0.9 hours for the main phase, and 14.4 hours for the recovery phase. Thus most of the EMIC waves observed in the entirety of our recovery phase in the original study now fall on average in the first two bins in this re-defined and extended recovery phase. When comparing the counts in the main and recovery phases, it is easy to see why it appears that there is an increase in the number of EMIC waves observed later in the 'storm'. It then becomes even more important to show the occurrence rate. The peak occurrence rate still remains in the main phase of the storm, but there is a slight increase during the end of the six days of the recovery period which approaches 0.15 EMIC waves per hour. This is likely due to the expansion of the plasmasphere since on average both the Kp and Sym-H indices indicate the storms have recovered. Although we know that there were other storms occurring during this new recovery phase, since they were randomly distributed throughout the phase, their effect on the superposed epoch was averaged out.

Another point to note is that EMIC waves are only about 1.6 times more likely to be observed by CRRES in a geomagnetic storm with our original definition than during non-storm times. Thus by lengthening our recovery phase by more than a factor of two, we are also likely to be including many EMIC waves which may show different wave-particle interaction parameters than those that are associated with the behaviour of geomagnetic storms (i.e. compression vs particle injection). It is interesting to note that there does seem to be a consensus from the ground studies showing an increase of EMIC waves after such a long recovery period [e.g. Bortnik et al., 2008, Engebretson et al., 2008a], perhaps because the ionosphere is less active leading to less attenuation of EMIC waves as they are transmitted to the ground. This may also be due to plasmapause expansion as it can take days to refill out to its quiet time position, and in the process overlap into regions of the ring current [Bortnik et al., 2008, Darrouzet et al., 2008, Engebretson et al., 2008a, Goldstein, 2006]. As stated before, this study is storm-centric and does not consider the effects of plasmaspheric dynamics on EMIC waves or their generation conditions which will be considered in the following chapter. What it can say is that many of these EMIC waves are not occurring during the actual recovery of the storm, and magnetospheric currents, as defined by the Sym-H index.

When considering the geomagnetic activity as described by the Kp index, on average, as shown in the middle panel of Figure 5.6, Kp levels off quickly during the recovery phase and remains steady at about 3. This shows that our storms have recovered, and on average stay recovered during the 6 days after the minimum Dst or Sym-H value, even though we know that there is overlap of storms during this time. We do see an increase not just in the count of EMIC waves, but also in the rate of EMIC wave occurrence at the end of the newly defined recovery phase. Although this increase in rate is still smaller than the peak seen in the main phase, it is probable that this bump could be due to the plasmapause expansion and refilling after a storm as suggested by Heacock and Akasofu [1973]. Darrouzet et al. [2008, and references therein] state that at L = 2.5, after 28 hours of continuously low Kp ($\approx$ Kp < 1), the refilling processes are still insufficient to reach saturated levels. For the plasmasphere to re-fill out to 5 <L< 8 may take upwards of a week, the time frame of when we see increased occurrences in space and on the ground.

5.4 Summary of EMIC wave occurrences during geomagnetic storms.

This chapter considered the occurrence of EMIC waves observed during storms over the CRRES mission. How the storm is defined greatly effects the conclusions of when and where EMIC waves occur during geomagnetic storms. If we were to define a geomagnetic storm by what was happening with the current systems in the magnetosphere, EMIC waves are found to be 1.6 times more likely to occur during storms than non-storm times. During the CRRES mission, the average storm lasted 29.4 hrs with the main and recovery phases lasting 9.1 hrs and 18.3 hrs respectively. CRRES observed EMIC waves during 41.5% of the storms. It is likely that CRRES did not see EMIC waves during all storms due to the intrinsic nature of satellite studies taking point measurements in a large volume. For example during the first part of the CRRES mission, the apogee was in the dawn sector where few EMIC waves are observed leaving little time and relatively few point measurements in the dusk sector. The mean location of the EMIC waves during these

storms is at L = 5.9 and a MLT of 15.0 hr. More than half of the storm time EMIC waves occurred during the main phase, with a peak occurrence rate of 0.32 EMIC waves per hour during the middle of the main phase. There is a fair amount of inter-bin variability over the 10% bins for each phase which is likely due to the relatively low number of events observed in each of these bins. Although we have a large statistical base to work with, it is not large enough to form a smooth trend line.

These results changed slightly when we define the storm by a more plasmaspheric centred definition with the 6 day recovery phase. In this case we see the pre-onset stage of the storm as when the magnetosphere becomes compressed and convection of the magnetic field lines begins. As the main phase starts, convection continues as the plasmasphere becomes eroded and plumes may form. During the early part of the recovery phase the plasmasphere is able to start refilling which, relative to the other storm definition, is a long process taking a matter of days to refill out to L-values of 2 or 3 and upwards of a week to refill to the outer L-values [Darrouzet et al., 2008]. Although the peak occurrence of 0.32 EMIC waves per hour is still located in the main phase, there is a second smaller peak of about 0.15 EMIC waves per hour towards the end of the new recovery phase.

6

EMIC Waves - The Plasmasphere

6.1 The plasmasphere

This chapter will consider the relationship of EMIC waves to the cold plasma density in the plasmasphere. As we showed in Chapter 5, CRRES observed that EMIC wave activity peaks in occurrence during the storm main phase, and again after about 4 to 6 days from the minimum Sym-H value. It is well known that EMIC wave generation is enhanced in the presence of increased cold plasma density, generally thought to be associated with radially extended plasmaspheric drainage plasma plumes and the refilling of the plasmasphere [e.g. Albert, 2003, Gary et al., 1994, Kozyra et al., 1984, Summers and Thorne, 2003]. The density structures and plumes formed during geomagnetic storms in the plasmasphere are also thought to be important in the formation and propagation of EMIC waves [Chen et al., 2009, Fraser et al., 2005a, Horne et al., 2003, Thorne and

Horne, 1994]. This chapter will examine the role of the plasmasphere in influencing the distribution of EMIC waves seen during the storm main and recovery phases, as well as during the 6 days following the minimum Sym-H value of the storm. By comparing like phases between storms and the phases to each other, we are able to improve our understanding of magnetospheric and plasma conditions observed in association with EMIC waves.

When considering the motion of particles in the plasmasphere, unlike in the outer magnetosphere, the primary motion is due to co-rotation with the Earth. Assuming that the ionosphere is rigidly coupled to the atmosphere and is perfectly conducting, the plasma velocity will then be the magnetic field line velocity. Thus the frozen in particles on given field lines will continue to share the same field lines at all times and thus will co-rotate [Goldstein et al., 2003, Kotova, 2007, Nishida, 1966, Stern, 1977]. In order to describe the entire motion, the dawn to dusk magnetospheric convection must also be superposed on the co-rotation.

When combined, the effects of the gradient drift, convection, and corotation, the total velocity, v_D, gives [Kivelson and Russell, 1995]

$$v_D = \frac{B \times \nabla \phi_{eff}}{B^2}. \tag{6.1}$$

The particles drift along constant paths of the potential ϕ_{eff} which can be described as the sum of the potential representing the dawn to dusk electric field (E_o), the potential due to convection, and the potential due to corotation as

$$\phi_{eff} = E_o r sin(\psi) + \frac{\mu B_o R_E^3}{q r^3} - \frac{w_E B_o R_E^3}{r}. \tag{6.2}$$

When considering cold particles, the magnetic moment is approximated as $\mu = 0$ forcing the term $\mu B_o R_E^3 / q r^3$ to zero. Thus at lower L-shells particles will follow paths which circle around the Earth while at higher L-shells, convection becomes more dominant and particles will convect towards the Sun as shown in Figure 6.1. Particles are not able to move between the two regimes unless the magnetospheric conditions change under the original assumptions.

The location of the plasmapause is represented as the boundary between the particles

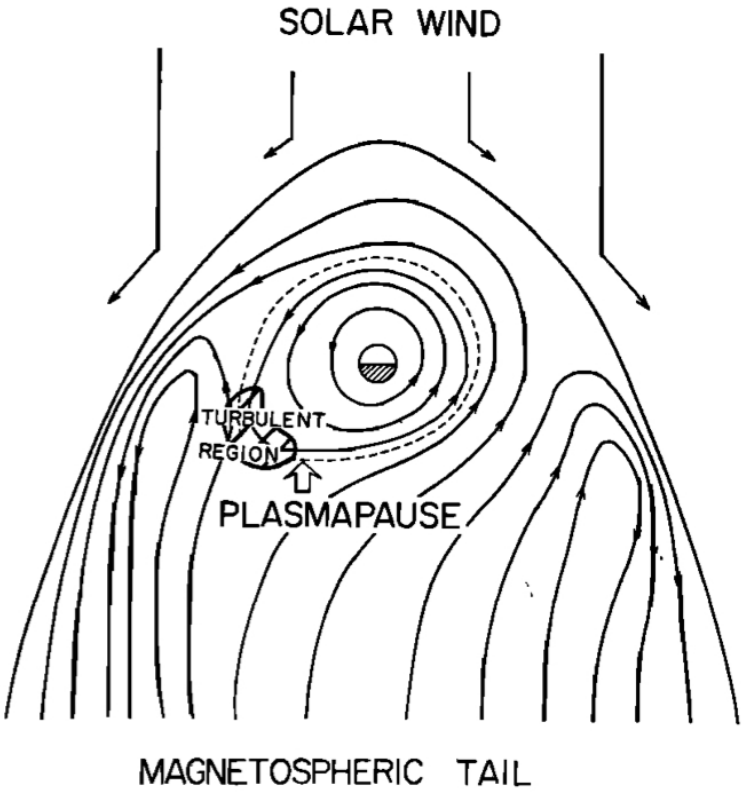

FIGURE 6.1: Drift paths in the equatorial plane for particles in the magnetosphere (from Nishida [1966, and references therein]). The plasmapause boundary is represented by the dashed line.

which are on closed paths around the Earth (those dominated by corotation), and the particles on open paths (those dominated by convection). This boundary is called a separatrix as shown by the dotted line in Figure 6.1, and particles are not able to cross it unless there is a change in the magnetospheric conditions. The boundary is characterised where the flow is zero and can be described by

$$r^2_{zero-flow} = \frac{w_E B_o R_E^3}{E_o}, \tag{6.3}$$

where w_E is the angular velocity of the Earth. During increased magnetic activity the separatrix moves earthward, but it takes time for the plasma and plasmapause to respond. It is this process which leads to the formation of plasmaspheric plumes which will be

discussed later. The position of the plasmapause and the formation of a plasma plume can be seen for different magnetospheric conditions in Figure 6.2 from Kotova [2007].

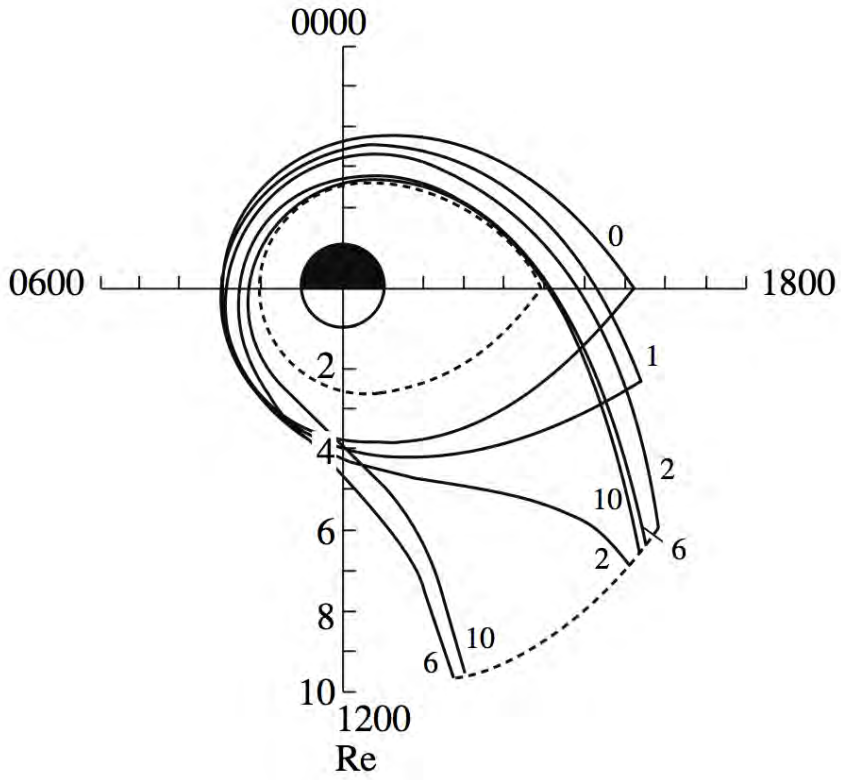

FIGURE 6.2: The plasmapause position at 0, 1, 2, 6, and 10 hours after a sudden increase in the dawn to dusk electric field from 0.28 to 0.58 mV m^{-1} shown in the equatorial plane R-LT taken from Kotova [2007, and references therein].

6.2 The plasmasphere and density structures

Four types of density structures have been observed in the plasmasphere; plasmaspheric tails or plumes, density channels, density notches, and shoulders which are shown (except for the channel) in the pseudo-density image from the EUV instrument from the IMAGE satellite in Figure 6.3 (Burch et al. [2001]). Plasmaspheric plumes, as seen in Figure 6.4, are thought to be the most important of these density structures in regards to

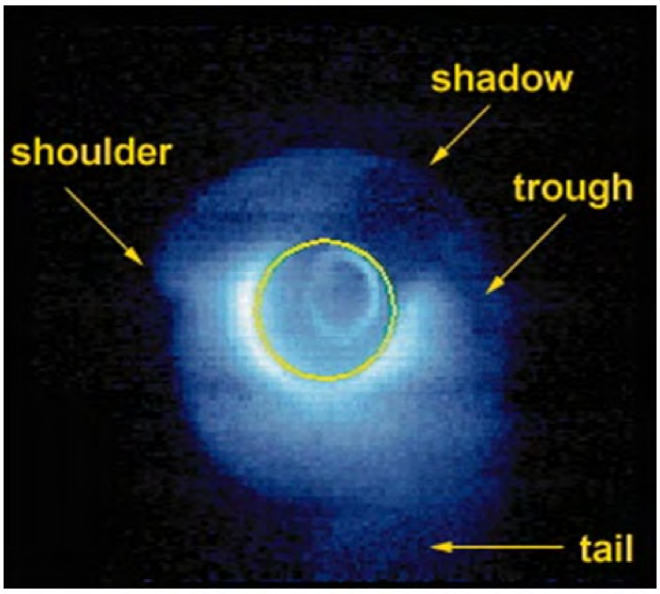

FIGURE 6.3: An image of the plasmasphere with a shoulder (in the dawn sector), a shadow (around midnight), a trough (night sector), and a plasma tail or plume (wrapping around the dusk sector towards noon) at 06:33 UT on 24 May 2000 from the IMAGE spacecraft [Burch et al., 2001]. The Sun is towards the lower left hand corner opposite the shadow region.

the generation and propagation of EMIC waves. As the last closed equipotential formed from the superposition of the co-rotation and convection electric fields moves (is eroded) inward, particles outside are lost from the plasmasphere. This process is observed to start near midnight and move both eastward and westward encompassing the entire night side within a matter of hours as seen in Figure 6.4 panel b [Borovsky and Denton, 2008, Darrouzet et al., 2008, Kotova, 2007]. On the day side, the plasmasphere extends outwards toward the Sun creating a broad plume (Figure 6.4 panels b and c). As the day side plume rotates towards dusk, the plume narrows in MLT (panels e though h of Figure 6.4). Once convection slows down the plume begins to rotate eastward (Figure 6.4 panels i - l).

Most of the observed plasmaspheric structures are related to erosion of the plasmasphere. It may take over a day for the plasmasphere to refill out to L-values around 2.5, and multiple days to weeks to refill out to geosynchronous orbit [Darrouzet et al., 2008]. Even after the plasmasphere has completely refilled to pre-storm levels, it is unlikely

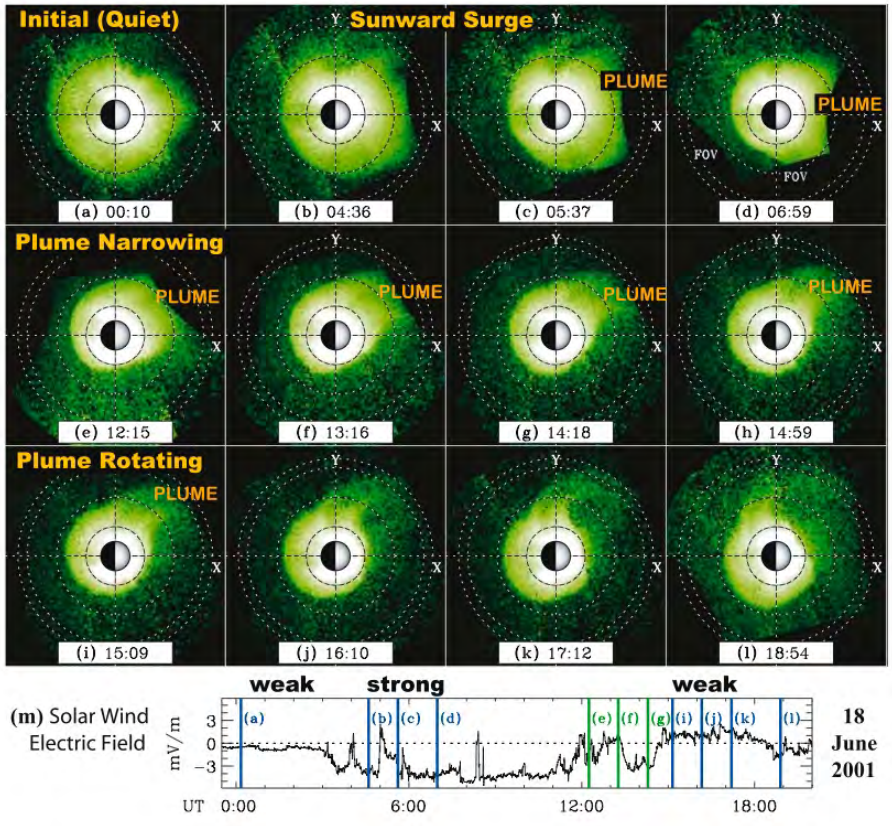

FIGURE 6.4: Images a - l are pseudo-density images from the EUV instrument on board the IMAGE satellite taken on 18 June 2001 projected in the equatorial plane [Darrouzet et al., 2009]. Image m shows the solar wind electric field observed during the time covering a - l [Darrouzet et al., 2009, and references there in].

that the plasmasphere will attain diffusive equilibrium with the ionosphere [Borovsky and Denton, 2008, Darrouzet et al., 2008, Goldstein, 2006, Heacock and Akasofu, 1973, and references therein]. During periods of extended quiet geomagnetic conditions, the plasmasphere can fill to such an extent that no distinct plasmapause boundary may be found. This is illustrated by ISEE results on day 219 and shown in Figure 6.5 [Lemaire, 1999]. During such conditions, there is a smooth radial density transition within the plasmasphere and no plasmaspheric boundary exists, or it is beyond L = 7 [Darrouzet et al., 2008]. In terms of the drift paths for particles in Figure 6.1, the refilling process will be

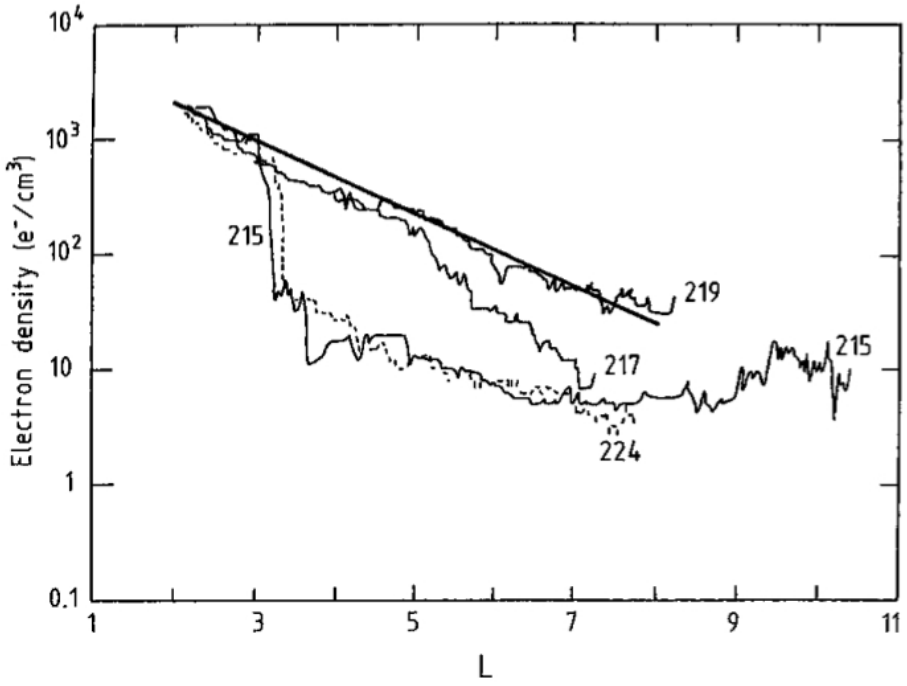

FIGURE 6.5: Four ISEE equatorial electron density profiles over a period of low geomagnetic activity from Lemaire [1999]. The pass on day 219 of 1983 shows an extended quiet time plasmasphere. On day 215 of 1983 a clear plasmapause can be seen near L = 3.

more effective and can approach diffusive equilibrium on paths inside the separatrix as these particles are trapped. Outside the separatrix, particles will drift towards, and can be lost to the magnetopause. Only the field lines within the closed drift paths will be able to approach diffusive equilibrium with the ionosphere as the loss of particles on field lines outside of the separatrix to the magnetopause will dominate.

6.3 CRRES quiet time plasmaspheric densities

For the study of plasma conditions associated with EMIC waves observed by CRRES, the non-storm and quiet time plasmasphere properties are used as a baseline for comparisons. Non-storm, or quiet time, are defined by an absence of a geomagnetic storm, as described

in Chapter 5.2.1. Here we are concerned with dynamics of the plasmasphere rather than the ring current and thus the 6 day extended recovery phase is preferred as it is more closely related to the re-filling time scale of the plasmasphere at large L-values. Therefore, the quiet time employed in this chapter relates to the extended storm time definition. The baseline used for comparison with density observations is the quiet time definition excluding the intervals when EMIC waves were observed. This ensures that our EMIC wave sample is not used in the creation of the baseline and reduces ambiguity. The plasmaspheric density decreases with radial distance from the Earth, and we will consider the mean density that CRRES observed by L-Shell in 0.1 R_E bins. Figure 6.6 shows the mean density over the CRRES mission (the black line) and during the non-EMIC wave quiet times (red line), the baseline.

To determine if the average density baseline is reasonable the standard deviations for the plasmaspheric model developed by Sheeley et al. [2001] are also plotted in Figure 6.6 (the orange and yellow lines). For a saturated plasmasphere, one would expect the density to fall off as L^{-4}, where L is the local L-value, since the flux tube volume will increase as a function of L^4 [Kivelson and Russell, 1995, Sheeley et al., 2001]. As the plasmasphere is rarely fully saturated, and the density in any given flux tube is dependent upon its time history of convection, we do not expect that the enhanced densities we are seeking would be those of a fully saturated plasmasphere, and thus won't necessarily follow the L^{-4} line. Instead, it is the average quiet time number densities that are of interest. Sheeley et al. [2001] used CRRES data to develop an empirical model of the plasmaspheric vs trough densities. They found that the average number density of the plasmasphere at $L = 3$ was 1390 cm^{-3} and fell off at a rate of $L^{-4.83}$ with a standard deviation of ± 440. At $L = 7$ the average plasmaspheric density was 23 ± 21 cm^{-3}. This gave an estimate for the plasmasphere number density, n_e, as a function of L -value as

$$n_e = 1390(\frac{3}{L})^{4.83} \pm 440(\frac{3}{L})^{3.60}. \tag{6.4}$$

The bounded estimate of the plasmaspheric density are plotted in Figure 6.6 for comparison with our baseline estimate. When CRRES was within $L < 3$, there were a significant

number of data readings that were greater than the highest densities measurable by CRRES (1984 cm^{-3}) and thus the Sheeley et al. [2001] model is apparently only valid for $3 \leq L \leq 7$. As many studies use the fixed number of 10 cm^{-3} as a comparison for minimum plasmaspheric densities, it has been included along with the upper limit on CRRES of 1984 cm^{-3} in Figure 6.6 [e.g. Fraser et al., 2010, Kotova, 2007, McCollough et al., 2009, Posch et al., 2010].

In Figure 6.6 the non-EMIC wave quiet time baseline (the red line), hence forth referred to as the quiet time plasmasphere and which we will use for data comparison, appears to agree well with the Sheeley et al. [2001] empirical model (the orange and yellow lines). The lack of a clear plasmapause boundary shows that the quiet time definition provides us with a picture of an extended, and well filled plasmasphere. We do see that the densities become more irregular at $L > 6.5$. This may be due to the plasmasphere taking longer than a week to refill at these distances. Thus there may be a mix of measurements from periods where the plasmasphere has recovered to the position of the satellite, and when it is still depleted.

Due to the superposition of the dawn-dusk electric field and corotation with the Earth, there is a duskward bulge in the plasmasphere, and thus a region of enhanced density. The mean of non-EMIC wave quiet time densities in 2 hour MLT radially outward bins were found and plotted in Figure 6.7. As expected, the densities relating to the bins for MLT's from 16 hr - 20 hr (dark and light blue lines) are on average higher than those from 12 hr - 16 hr (black and purple lines) and 20 hr - 24 hr (green and yellow lines) for L-values greater than 4 where the quiet time bulge is expected to be located, as well as a local peak in quiet time EMIC wave occurrences during the CRRES mission.

To determine if the EMIC waves observed by CRRES occurred in regions of enhanced densities the ratios of the observed density to the quiet time plasmaspheric number density in the same L-bin were calculated and their mean (solid lines) and quartiles (dashed lines) were plotted in Figures 6.8 and 6.9. The ratio for the intervals when EMIC waves were not observed, $n_j(L)$, was found by

$$n_j(L) = \frac{\rho_j(L)}{\rho_q^{ave}(L)}, \tag{6.5}$$

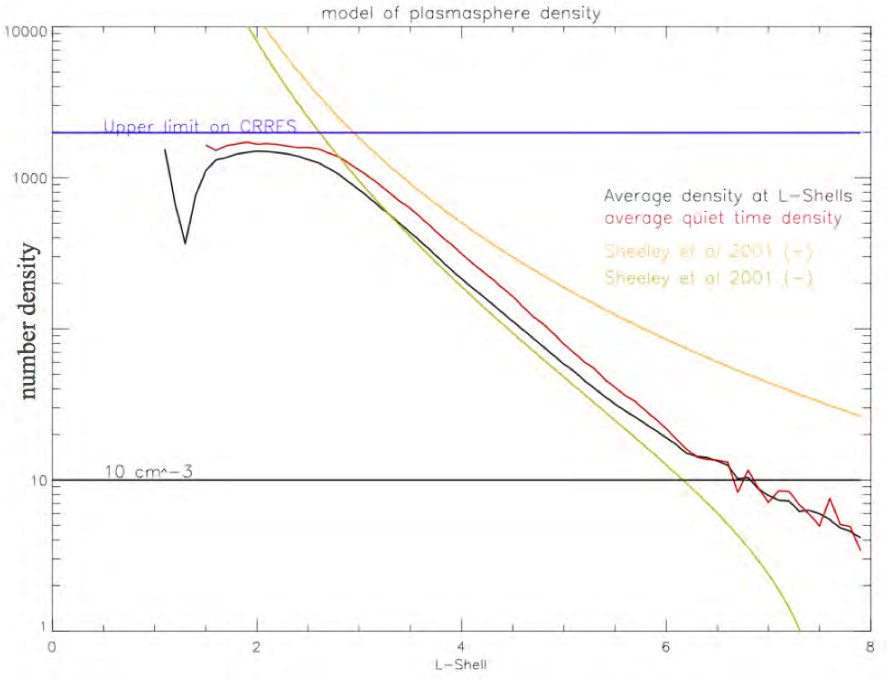

FIGURE 6.6: The mean density that CRRES observed across L-Shells(the black line), the mean density during non-storm intervals as defined by when a storm is not occurring using the recovery phase definition as 80% recovery (red line). The Sheeley et al. [2001] model (light orange and yellow lines), $10cm^{-3}$ (black straight line), and the upper limit of observable densities on CRRES are also plotted (straight blue line).

where the observed number density is $\rho_j(L)$, the quiet time plasmaspheric density baseline is given by $\rho_q^{ave}(L)$, and j is the magnetospheric condition (all, quiet, storm, pre-onset, main, and recovery phases). The ratio was also found for the intervals when EMIC waves were observed ($n_{ej}(L)$) as

$$n_{ej}(L) = \frac{\rho_{ej}(L)}{\rho_q^{ave}(L)}, \tag{6.6}$$

where the observed number density during EMIC waves is $\rho_{ej}(L)$. The blue solid and dotted lines are the mean and quartiles of n_{ej} and the black solid and dotted lines are the mean and quartiles of n_j at a particular L-value and are shown in Figures 6.8 and 6.9.

Having defined the baseline of the quiet time plasmasphere we can now consider if

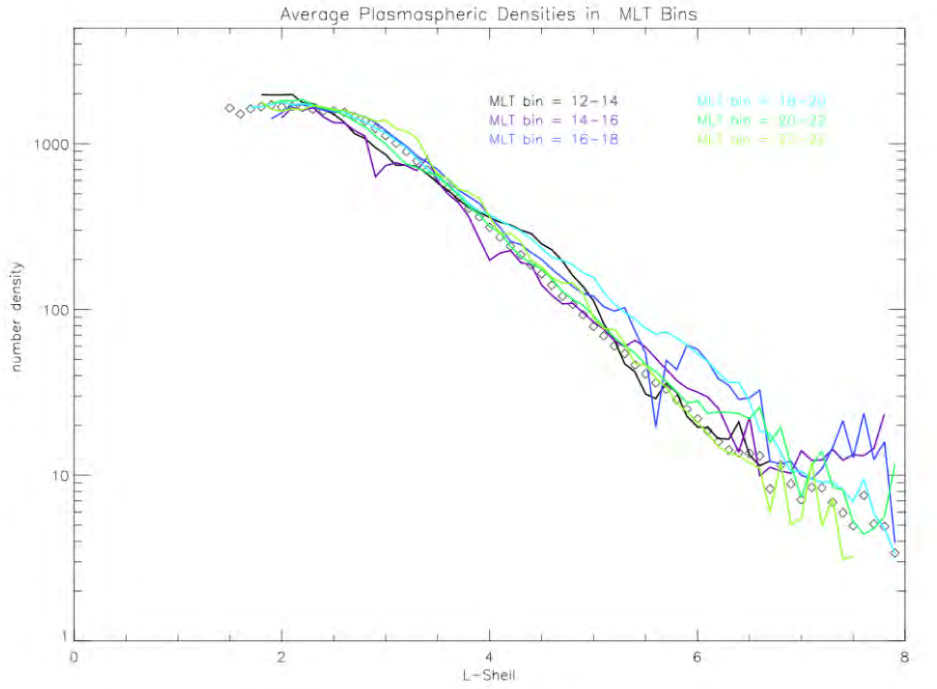

FIGURE 6.7: Using the mean density during non-storm times using the definition of a recovery phase as 6 days after the minimum Sym-H value, plotted are the mean across all MLT's (the open diamonds), and the mean found in the MLT bins of 12 hr -14 hr (black line), 14 hr -16 hr (purple line), 16 hr -18 hr (blue line), 18 hr -20 hr (light blue line), 20 hr -22 hr (green line), and 22 hr -24 hr (yellow line).

the quiet time EMIC waves observed during the CRRES mission are occurring during enhanced densities. Panel c in both Figures 6.8 and 6.9 depict these results for geomagnetic quiet times. Figure 6.8 shows the results across all magnetic local times and Figure 6.9 shows the same results for CRRES observations in the 14 hr - 18 hr MLT bin, where most EMIC waves were observed. In Figure 6.8 panel c, for L $>$ 4.5, the densities observed are higher than the mean plasmaspheric densities. At L $>$ 5.5 more than 75% of the EMIC wave observations showed densities greater than the mean plasmaspheric densities, and those of quiet non-EMIC wave time densities. These results are similar in the 14 hr - 18 hr MLT bin, but are seen for L $>$ 3.5. Panels b - i will be discussed in the next section. These

results suggest that non-storm time EMIC waves are more likely to be seen in association with higher than average plasma densities.

6.4 EMIC waves in the storm time plasmasphere

Many studies have considered the relationship between the plasmasphere, plasmapause, plasma plumes, and EMIC waves [e.g. Chen et al., 2009, Pickett et al., 2010, Posch et al., 2010, Varma et al., 2008, Yuan et al., 2010]. Not only do these regions provide the enhanced cold plasma density to promote wave growth, but the plasmapause, and plasma plumes are also able to provide density enhancements and gradients which may be supportive of wave propagation and amplification [Chen et al., 2009, Horne and Thorne, 1993, Morley et al., 2009].

It has been shown in Chapter 2.5, equations 2.43 and 2.44 that the wave growth is dependent on the background cold plasma number density. As noted in previous sections, as convection increases during the main phase of a geomagnetic storm, the plasmasphere is eroded towards Earth and a plasmaspheric plume with enhanced cold density is created [Darrouzet et al., 2008, Goldstein, 2006, Kotova, 2007, Spasojevic et al., 2003]. It is during this phase that we also have an injection of hot particles into the ring current. Chapter 4.5 showed that EMIC waves were observed more frequently during periods of storms and it is likely that the hot ring current particles would overlap regions of the cold plasma in the outer plasmasphere or plasma plumes. The importance of the hot particle temperature anisotropy has been well defined but the need for enhanced densities of the cold particles has been debated [Gary et al., 1994, Posch et al., 2010, Spasojević et al., 2004, Varma et al., 2008]. Modelling results by Kozyra et al. [1984] and Jordanova [2007] and satellite results from Young et al. [1981] and Anderson et al. [1992a] suggest that enhanced cold densities are needed for the generation of EMIC waves. Recently, Posch et al. [2010] have found that Pc1 waves observed on the ground were only loosely related to the occurrence of plasma plumes and enhanced densities in the magnetosphere. However with ground based studies it is difficult to determine the L-values on which the waves were generated and propagated in the magnetosphere, due to the ionospheric wave

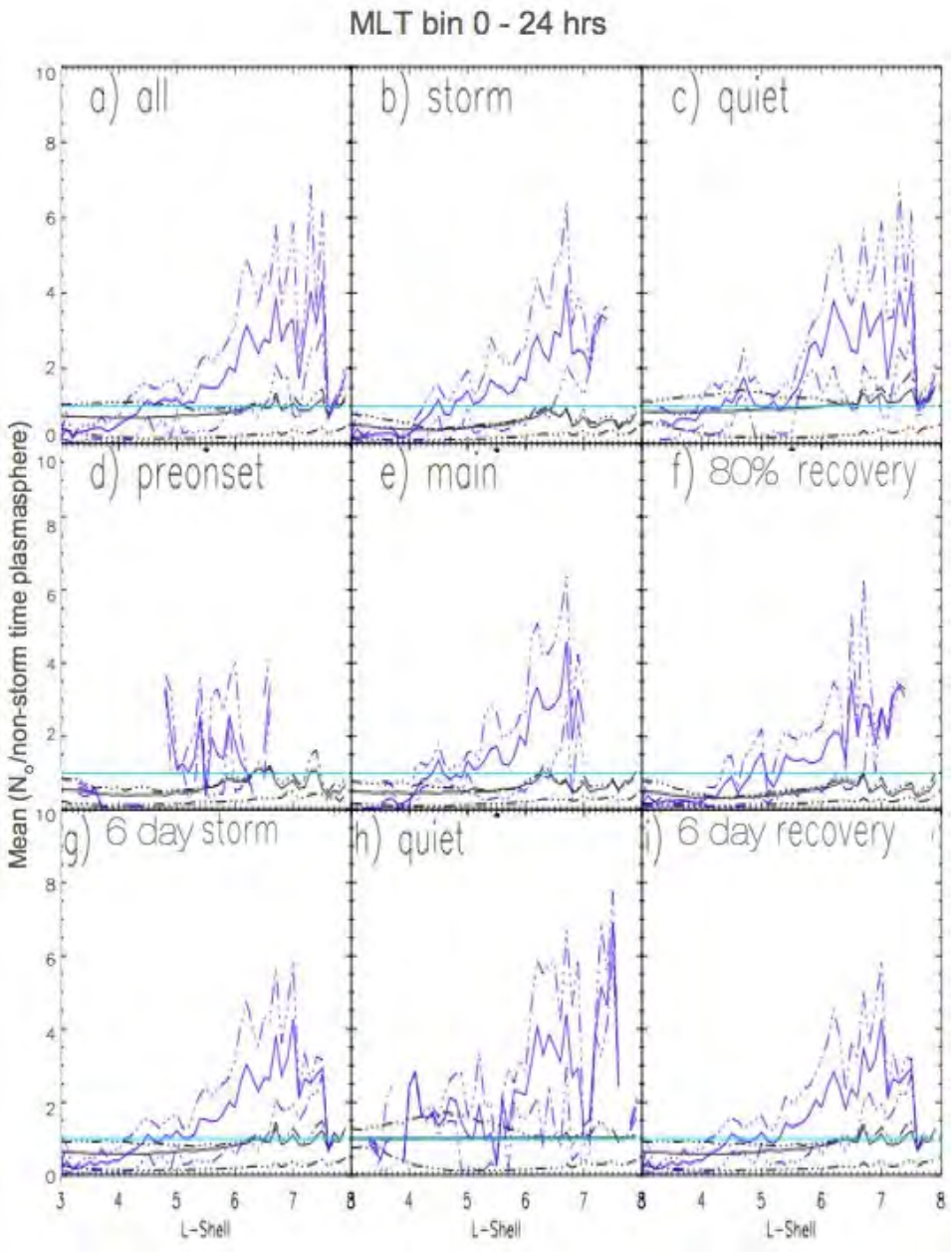

FIGURE 6.8: The means of the ratio of density observed during EMIC waves over the mean density observed by CRRES during (a) non-storm times, as defined by the + 6 day recovery excluding the EMIC wave events, (b) storm as defined by the 80% recovery, (c) quiet as defined by the 80% recovery, (d) the pre-onset, (e) the main phase, (f) the 80% recovery phase, (g) storm time using the + 6 day recovery, (h) the quiet time as defined using the + 6 day recovery, (i) and the + 6 day recovery are plotted as blue lines, and the quartiles are the blue dashed lines. The black lines in the plots represent the mean ratios for the times when EMIC waves were not observed during the specified magnetospheric conditions, and the quartiles are the black dashed lines.

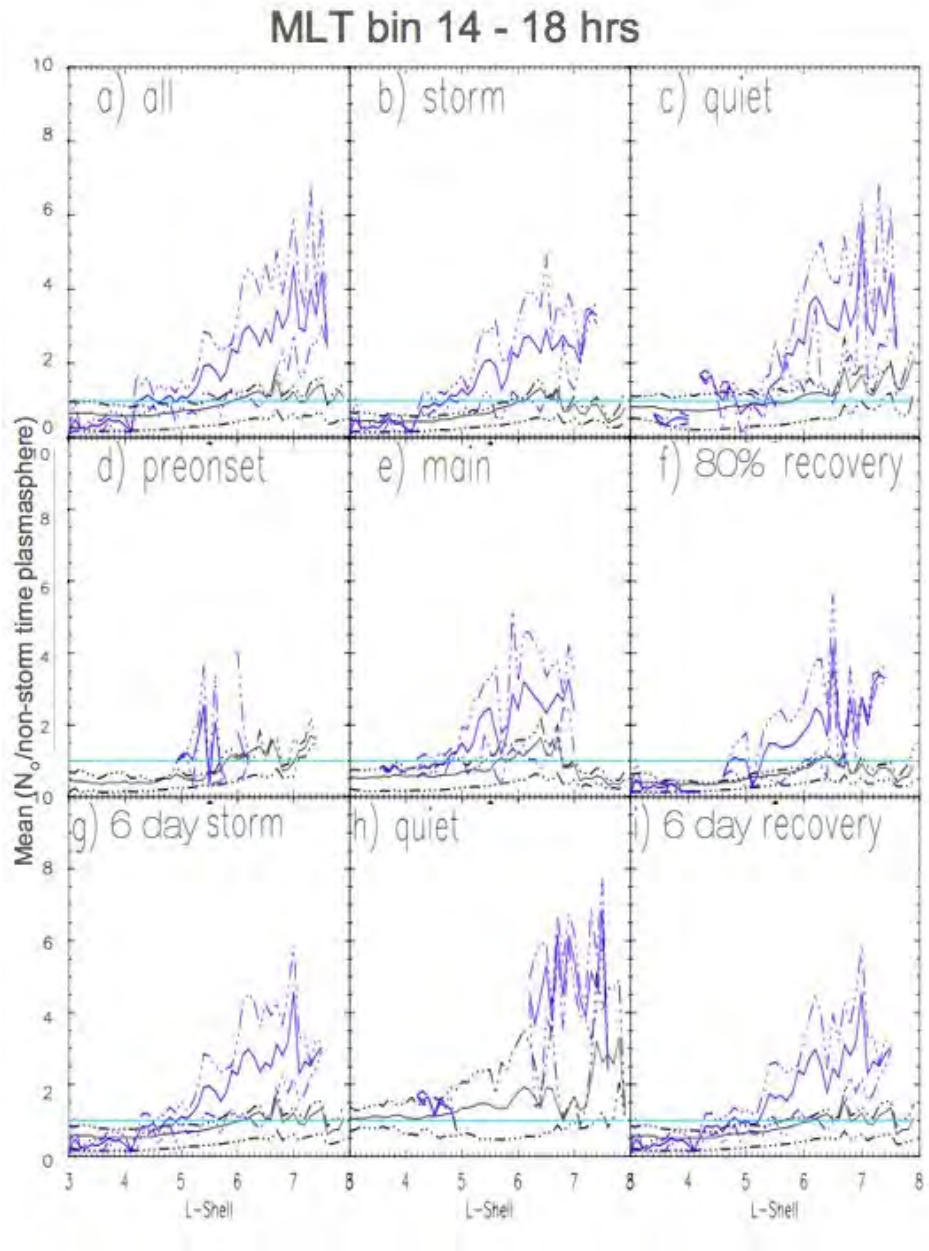

FIGURE 6.9: The means of the ratio of density observed during EMIC waves occurring in the 14-18 MLT bin over the mean density observed by CRRES during (a) non-storm times, as defined by the + 6 day recovery excluding the EMIC wave events, (b) storm as defined by the 80% recovery, (c) quiet as defined by the 80% recovery, (d) the pre-onset, (e) the main phase, (f) the 80% recovery phase, (g) storm time using the + 6 day recovery, (h) the quiet time as defined using the + 6 day recovery, (i) and the + 6 day recovery are plotted as blue lines, and the quartiles are the blue dashed lines. The black lines in the plots represent the mean ratios for the times when EMIC waves were not observed during the specified magnetospheric conditions, and the quartiles are the black dashed lines.

guide allowing for propagation parallel to the Earth's surface and that the ionosphere may also absorb significant wave energy during transition to the ground. With in situ measurements we can directly measure the plasma density during EMIC wave events and compare those measurements to observations during quiet and storm times in order to determine if EMIC waves are associated with regions of enhanced or depleted plasma densities. Unfortunately the CRRES orbit did not slice radially through the plasmasphere thereby making it difficult to identify the plasmaspheric features such as an extended plasmasphere, and/or plasma plumes in their early stages.

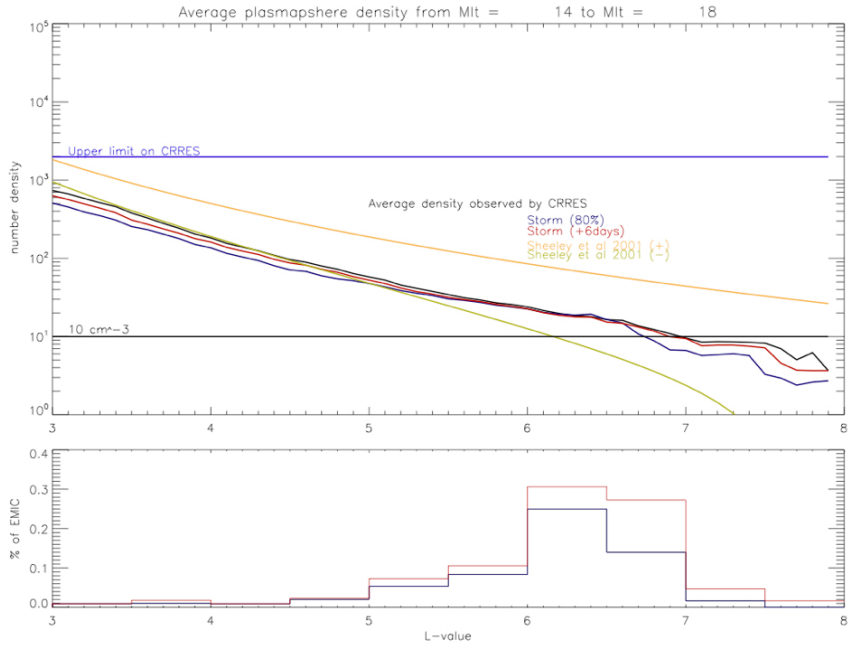

FIGURE 6.10: The mean storm time densities by L-shell observed by CRRES between magnetic local times of 14 hr - 18 hr. The blue line is the storms as defined by the 80% recovery phase definition and the red is the storms as defined by the plus 6 day recovery definition. The yellow and orange lines are the Sheeley et al. [2001] model which outside of an L-shell of 3 include the mean densities observed by CRRES during quiet magnetospheric conditions. The overall mean of observed densities by CRRES is also plotted in black for comparison. The upper observable limit and 10 cm^{-3} are also plotted. Bottom panel: The associated percent of EMIC wave occurrence during geomagnetic storms by L-value in the 14 hr - 18 hr. magnetic local time bin.

Figure 6.8 shows that under all magnetospheric conditions EMIC waves occurring at

TABLE 6.1: The magnetospheric conditions, the K-S test results (M), the 95% confidence levels, and if the hypothesis was accepted or rejected. If M is greater than the 95% confidence level, the null hypothesis is rejected. The MLT bin used here is 14 hr - 18 hr which includes the majority of EMIC wave events.

Magnetospheric Condition	M	95% confidence level	Hypothesis?
All	0.439	0.023	rejected
Quiet	0.477	0.037	rejected
Storm	0.435	0.029	rejected
Pre-onset	0.129	0.137	accepted
Main	0.425	0.040	rejected
Recovery	0.395	0.044	rejected

$L > 5$ were in regions of enhanced densities. Figure 6.9 is confined to the 14 hr - 18 hr. MLT where the majority of EMIC waves were observed and where plasmaspheric plumes are expected to be observed. Once again EMIC waves appear to occur in regions of enhanced densities. Figures 6.8 and 6.9 show that on average and at most L-values the quiet time densities are higher than those of the main phase, which are higher than those found in the recovery phase as is expected. This however does not hold for $L > 7$ where the main phase densities drastically decrease. This suggests the possibility of the presence of plasmaspheric plumes since the densities become elevated at $L > 5$, outside of where the plasmapause is typically expected to reside. The quiet time densities for the extended recovery phase also appear larger than those when using the 80% recovery phase definition. This is an expected result since the plasmasphere has had on average more time to recover and thus would be expected to show higher plasmaspheric densities.

In order to determine the statistical significance of this result we can perform the Kolmogorov - Smimov (K-S) test [Sheskin, 2004]. This statistical test evaluates the hypothesis that the two independent samples could come from the same parent population. Population 1 will be defined as the number densities when CRRES does not observe EMIC waves (the black lines in Figures 6.8 and 6.9). Population 2 will be defined as the

number densities recorded by CRRES when EMIC waves were observed (the blue lines in Figures 6.8 and 6.9). The null hypothesis for this test is that the densities for both populations come from a similar distribution or parent population, and the alternative hypothesis is that the density found during EMIC waves is larger. The results can be seen in Table 6.1. For all magnetospheric conditions, except for the pre-onset phase, it was found that the null hypothesis was rejected, and thus through inspection of the data we see that EMIC waves occur during periods of enhanced densities. Due to the low number of observed EMIC waves during the onset phase, it is likely that there is insufficient data to reject the null hypothesis though the data are suggestive that higher densities are also associated with EMIC events during this time. Although we conclude that the EMIC waves in all other magnetospheric conditions are associated with regions of enhanced densities, this test does not determine whether they were found in plasmaspheric plumes, an extended plasmasphere, or another plasmaspheric structure. During the main phase of a storm in the bin of $5.5 \leq$ L ≤ 6.5 and $14 \leq$ MLT ≤ 18, we see that EMIC waves are found on average in densities that are 300% larger than when an EMIC wave is not present under the same conditions. Although this seems large, it is not unreasonable, for example if the non-EMIC waves density is found to be 10 cm^{-3}, then the density expected on average during an EMIC wave event is 30 cm^{-3}, not unreasonable. This is of course specific to magnetospheric conditions and magnetospheric locations as can be seen in Figures 6.8 and 6.9.

6.5 Plasmaspheric plumes and EMIC waves

As stated previously, the CRRES orbit is not ideal for identifying plasmaspheric plumes. When processing the density data for CRRES, plasmaspheric boundaries as well as plasma plume boundaries are frequently found by eye as seen in Figure 6.11, or by using a change in the density by a set factor, for example 5 for the plasmapause and exceeding the Sheeley et al. [2001] model for plasma plumes as described and used by Moldwin et al. [2004]. Figure 6.11 shows the density over the outbound pass of orbit 547 where the plasmapause boundary and a plume are easily identified. However due to the timescales at which

plumes form and change as well as the orbit of CRRES, it is not known that all plumes which CRRES passes through will show this type of signature in the data. To illustrate, the CRRES orbit 931 has been overlaid on figure 5 from Spasojevic et al. [2003] modelling the plume formation during a storm on 26 -27 June 2001 and shown in Figure 6.12. If a similar plume had formed during this orbit, CRRES would have only detected the two boundaries highlighted in panels e and h, but would have been in regions of enhanced densities for panels a - e and h. Thus during plume formation and throughout the existence of a plume, CRRES may only observe two large and clear boundaries as would have been the case in Figure 6.12. Using only the density point measurements of the satellite it would be difficult to know if these boundaries are either due to the plasmapause or a plume. In situations like Figure 6.12, CRRES would not see four boundary crossings as in Figure 6.11, three shown in Figure 6.11 and presumably another plasmapause crossing on the inbound half of the orbit. This complicates the identification of plumes and the occurrence of EMIC waves in plumes during the CRRES mission.

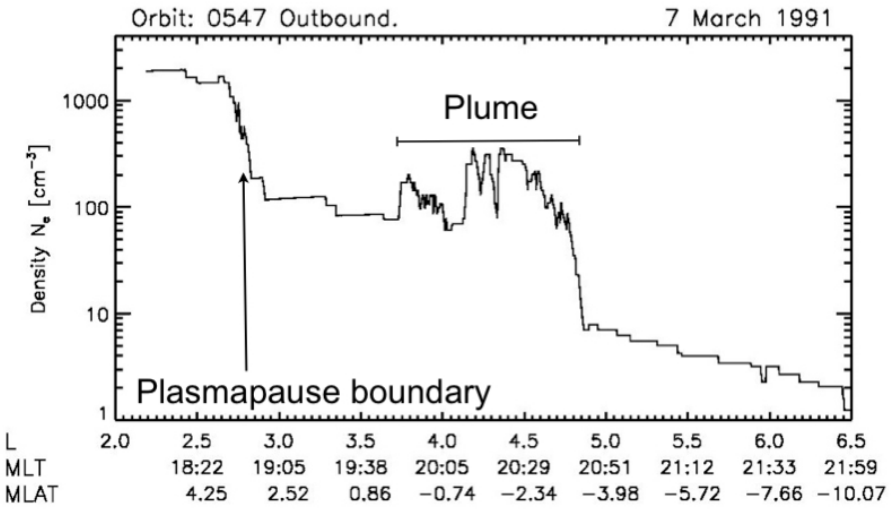

FIGURE 6.11: The density for the outbound portion of orbit 547 where the plasmapause boundary and a plume are highlighted.

Although it is difficult to identify plasmaspheric structures from a single, or a few consecutive orbits of CRRES, a statistical consideration can provide an average pattern

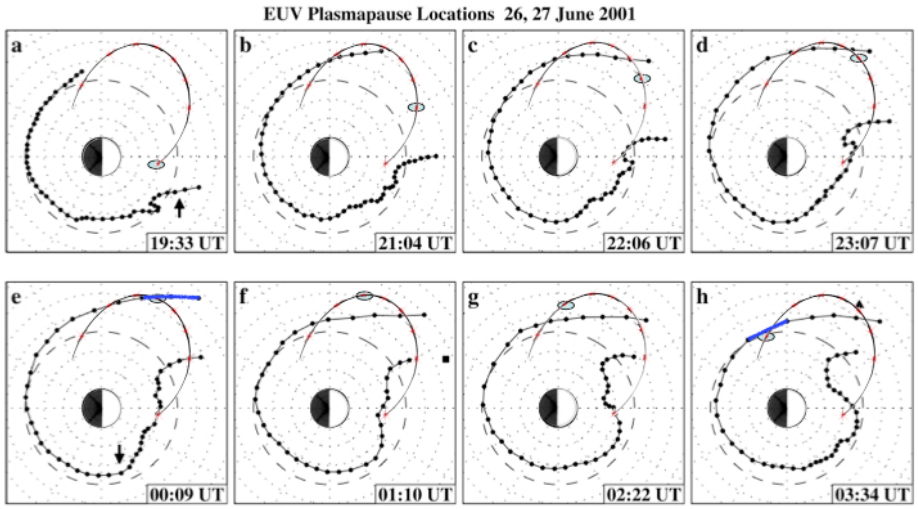

FIGURE 6.12: Modified from Spasojevic et al. [2003] the formation of a plasma plume on 26, 27 June 2001 with orbit 931 of CRRES over plotted. Although CRRES would have been traveling through the plume for approximately panels b - e and re-enter at panel h, no plasmapause nor plume boundary would have been observed and CRRES would have seen a continuous region of enhanced density throughout this time.

of how the plasmasphere reconfigures during different phases of a geomagnetic storm. We will focus on the magnetic local time bin of 14 hr - 18 hr where during geomagnetic storms the majority of the EMIC waves were observed and is the region where plumes are found to exist. Figure 6.10 shows the average storm time density using observations both with and without waves by L-shell. Although there are no signatures of plasmaspheric structures present, it is easy to see that the densities are reduced earthward of L = 5 when compared to the quiet time densities from Figure 6.6 and the Sheeley et al. [2001] model, while similar levels are seen at higher L-shells.

The mean densities observed during the pre-onset phase of a storm are shown in Figure 6.13. As with the storm time densities in Figure 6.10 the densities with L $<$ 5 are reduced

when compared with the quiet time values from Figure 6.6 and the Sheeley et al. [2001] model. It appears that convection has not only started on average during this phase, but that the plasmasphere may have already eroded substantially. Although the densities at L $>$ 5 are similar to those observed during quiet geomagnetic conditions and convection has likely started in the inner magnetosphere, it is not known if this is a signature of a plasma plume forming. The higher densities seen in the top panel of Figure 6.13 agree well with where the higher occurrences of EMIC waves (bottom panel) are found.

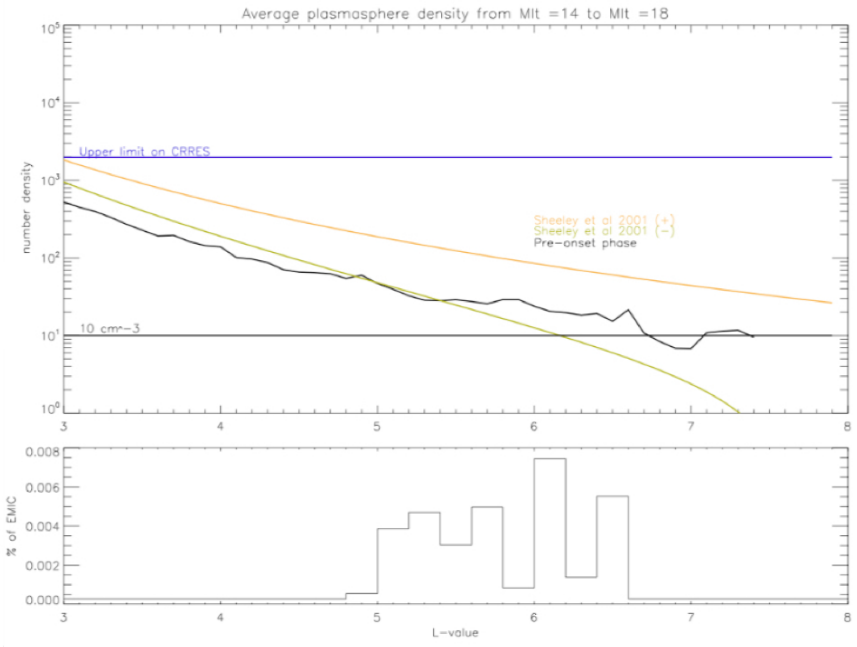

FIGURE 6.13: Top panel: The mean pre-onset phase densities by L-value observed by CRRES between magnetic local times of 14 hr - 18 hr. The black line represents the mean densities observed during the 3 hours period to the onset of a storm. The yellow and orange lines are the Sheeley et al. [2001] model which outside of an L-shell of 3 encompass the mean densities observed by CRRES during quiet magnetospheric conditions. The upper observable limit and 10 cm^{-3} are also plotted. Bottom panel: The associated percent of EMIC wave occurrence during the pre-onset phase by L-value in the 14 hr - 18 hr. magnetic local time bin.

During the main phase of a geomagnetic storm when the majority of EMIC waves are seen by CRRES, it is also expected that plumes would be fully formed in the plasmasphere

[Spasojevic et al., 2003]. The main phase average densities are shown in Figure 6.14, and as with the storm and pre-onset averages, are reduced within L = 5, but there may be a possible plume signature between L = 5 and 7. The bottom panel of Figure 6.14 shows the peak occurrence of EMIC waves in the middle of the possible plume signature (top panel), and then a drop off at L-values larger than 7 where the densities appear on average to be depleted. This suggests that EMIC waves occur inside plumes during the main phase, agreeing with plume location and time of occurrence.

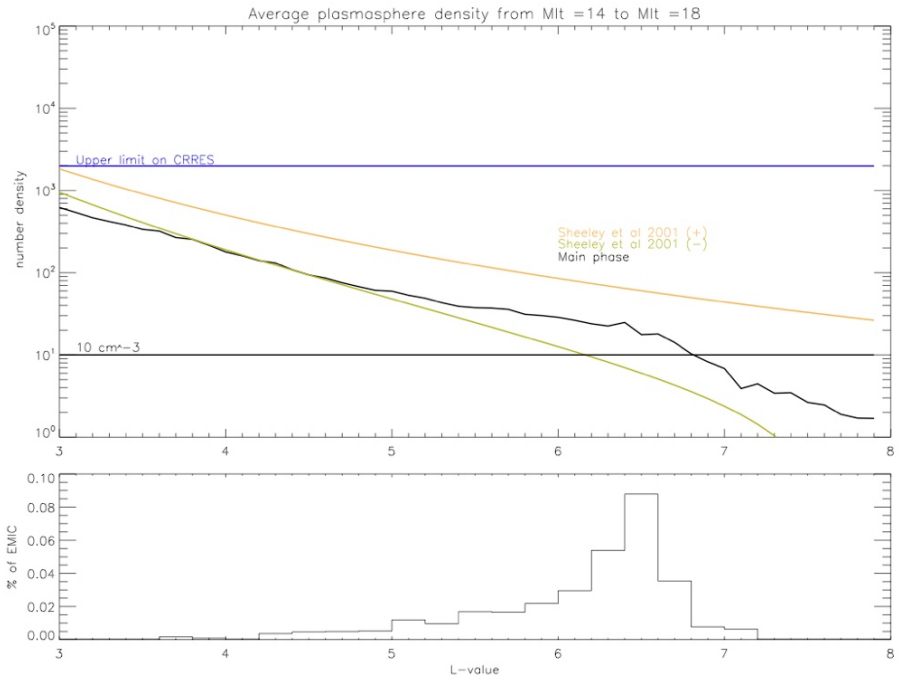

FIGURE 6.14: Top panel: The mean main phase densities by L-value observed by CRRES between magnetic local times of 14 hr - 18 hr. The black line represents the mean densities observed during the main phase of a storm. The yellow and orange lines are the Sheeley et al. [2001] model which outside of an L-shell of 3 encompass the mean densities observed by CRRES during quiet magnetospheric conditions. The upper observable limit and 10 cm^{-3} are also plotted. Bottom panel: The associated percent of EMIC wave occurrence during the main phase by L-value in the 14 hr - 18 hr. magnetic local time bin.

Figure 6.15 shows plots using both definitions of the recovery phase, the black line represents the 80% recovery of the minimum Sym-H index observed during the storm, and

the plus 6 day definition is represented by the red line. Although a plume may still persist during the early stages of the recovery phase as the plasmasphere commences refilling, the plume signature in Figure 6.14 is no longer found on average. It is clear from Figure 6.15 that between the end of the 80% recovery and the extended 6 day definitions of the recovery phases the plasmasphere is refilling extensively, nearly back to the average quiet time levels of Figure 6.6. As the plasmasphere expands towards the ring current, the occurrence of EMIC waves increases at L-shells where the ring current is expected to be located, and able to supply the free energy needed for EMIC wave growth.

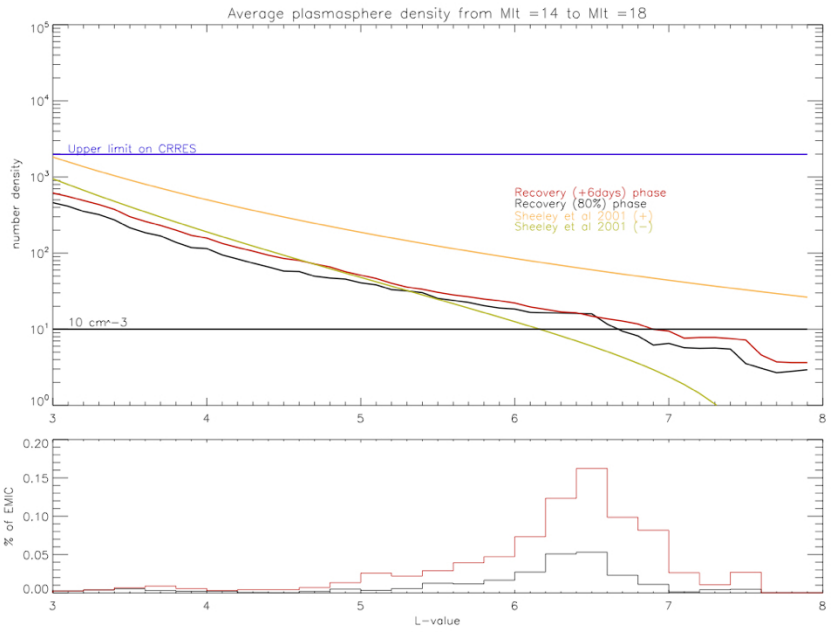

FIGURE 6.15: Top panel: The mean recovery phase densities by L-value observed by CRRES between magnetic local times of 14 hr - 18 hr. The black line represents the mean densities observed during the the recovery phase of a storm as defined by the 80% recovery of the minimum Sym-H value, and the red line represents the mean densities observed during the recovery phase as defined by the plus 6 days since the minimum Sym-H value. The yellow and orange lines are the Sheeley et al. [2001] model which outside of an L-shell of 3 encompass the mean densities observed by CRRES during quiet magnetospheric conditions. The upper observable limit and 10 cm^{-3} are also plotted. Bottom panel: The associated percent of EMIC wave occurrence during the recovery phase by L-value in the 14 hr - 18 hr. magnetic local time bin.

6.6 EMIC waves and density gradients

It has been suggested in the literature that the magnetospheric path for field aligned propagation of EMIC waves with the most wave gain is on steep negative density gradients, and thus we may expect to observe the majority of EMIC waves either on the inside edge of the plasmapause, along the outside edge of plasma plumes, or along density structures in plumes [Chen et al., 2009, Horne and Thorne, 1993, Morley et al., 2009, Rauch and Roux, 1982, Roux et al., 1982]. The locations where the largest wave amplifications are observed according to theory is along these negative density gradients. Chen et al. [2009] have recently used the HOTRAY ray tracing code developed by Horne [1989], and later applied to EMIC waves by Horne and Thorne [1993]. Chen et al. [2009] studied the wave gain of EMIC waves traveling through the magnetosphere with a storm time plasma plume which included density gradients throughout the structure. They found that the largest wave gain was located at these density gradients. Morley et al. [2009] found that in order to explain the timing between an EMIC wave observed in space and on the ground to agree, the wave had to travel along the density gradient at the outside edge of a plasmaspheric plume. To pursue the concept that EMIC waves may be associated with negative density gradients associated with plumes, a statistical study of the gradients around the EMIC wave events was undertaken. Also, three CRRES orbits with EMIC wave events were selected in order to examine individual events. Orbit 961 shows EMIC wave events in the pre-onset and main phase of a geomagnetic storm, orbit 931 included events in the main phase of a geomagnetic storm, and orbit 927 shows events during the early recovery phase of a geomagnetic storm.

6.6.1 Statistical study: linear fit

In order to determine the probability of EMIC waves occurring on a negative density gradient we considered the density observed within $\pm$ 2 minutes of the occurrence of an EMIC wave event. To take into consideration the decrease in plasmaspheric density with increasing radial distance, the density data were normalised to the Sheeley et al. [2001] plasmaspheric model. This process removes the expected plasmaspheric density profile

while preserving the sign of any additional density gradients as observed in Figure 6.16. Following the identification and normalisation of the EMIC wave events, a straight line was fitted to the density data using a f(x) = A + Bx model and minimising the chi-squared error. Here f(x) is the electron number density observed by CRRES and x the satellite position data. In order to determine the quality of fit, the coefficient of determination, r^2, was calculated where r^2 indicates the percentage of the variance described by the fitted line [Sheskin, 2004]. For example an $r^2 = 0.8$ indicates 80% of the variance in the data can be described by the fitted line. The r^2 value is calculated by finding

$$r^2 = 1 - \frac{SS_{err}}{SS_{tot}}, \tag{6.7}$$

where SS_{tot} is the total sum of the squares defined by $SS_{tot} = \sum_i (y_i - \bar{y})^2$ where $\bar{y}$ is the average of the data points and SS_{err} is the sum of squares of the residuals defined as $SS_{err} = \sum_i (y_i - f_i)^2$ where f is the fitted line [Sheskin, 2004].

The fitted lines determined from the density data were selected for positive and negative slopes. A chi-squared test was performed to determine the bias in the sign of the gradient. The null hypothesis used in the chi-squared test was the presence of an equivalent number of positive and negative gradients. The 95% confidence level would be $\chi^2 \leq 3.84$, and a chi-squared value within this range would indicate that the null hypothesis would be expected. The results from both the r^2 test and the chi-squared tests can be found in Table 6.2. Less than half of the events had 50% of the variance observed in the density described by a straight line and for all fits the slope was found to be random. This procedure was also performed for events in the 14 hr -18 hr MLT bin where plasma plumes are expected to occur. Similar results to Table 6.2 are shown in Table 6.3 and again less than half of the events had 50% of the variance observed described by a straight line fit and that a linear fit is inadequate for the other half. With less than half of the observed densities during EMIC wave events able to be fitted to a straight line we can then say that less than half of the observed EMIC waves occurred along either positive or negative density gradients. The chi-squared test for the the fitted lines which had a $r^2 \geq 0.5$ show that CRRES did not observe a correlation between negative density gradients and EMIC wave occurrence. For those events which had a $r^2 < 0.5$, the hypothesis that we are confidently

able to determine the sign of the density gradient is no longer valid and the chi-squared results are no longer meaningful. However, the lack of a straight line fit to the density data for these events is supportive of the conjecture that the EMIC waves observed by CRRES are not correlated with negative density gradients.

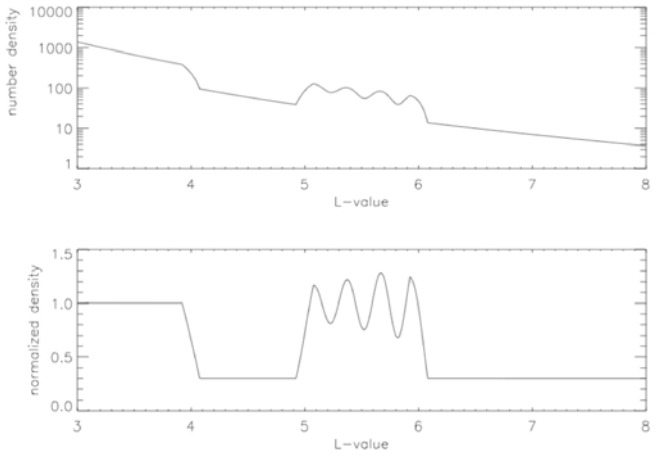

FIGURE 6.16: The number density and normalised number density for CRRES orbit 810. Normalising the number density using the Sheeley et al. [2001] model of the plasmaspheric density removes the expected decrease in density as one moves away from the Earth while preserving the sign of additional density gradients within the data.

6.6.2 Statistical study: Superposed epoch analysis

A superposed epoch analysis can help visualise the results from the previous section and is also not dependent on whether the data is linear or non-linear. One concern with performing a superposed epoch with respect to time is that the satellite may be on the inbound portion of the orbit when observing EMIC waves, but the negative density gradient is defined by looking from the Earth outward. Another concern is that the EMIC wave can be continuously observed as the satellite moves from the outbound to inbound portion of its orbit. In order to take these concerns into account, we have added a step into the superposed epoch process as shown in Figure 6.17. Similar to normalising the phases of the storms in Chapter 5.3.1, we first identified the EMIC wave events $\pm$ 5 minutes. The

TABLE 6.2: The r^2 and corresponding chi-squared statistics for the linear fit of the density $\pm$ 2 minutes around the start/end for all EMIC wave events.

$r^2 \geq$	number	positive	negative	chi-squared
0.9	58	23	35	0.874
0.8	139	55	84	2.46
0.7	209	100	109	0.086
0.6	283	137	146	0.064
0.5	350	169	181	0.143
0.4	419	200	219	0.306
0.3	480	234	246	0.104
0.2	552	271	281	0.058
0.1	625	309	316	0.013
0.0	910	458	452	0.009

TABLE 6.3: The r^2 and corresponding chi-squared statistics for the linear fit of the density $\pm$ 2 minutes around the start/end for EMIC wave events between 14 hr $<$ MLT$<$ 18 hr.

$r^2 \geq$	number	positive	negative	chi-squared
0.9	31	14	17	0.065
0.8	85	37	48	0.378
0.7	123	66	57	0.260
0.6	181	98	83	0.399
0.5	224	116	108	0.080
0.4	271	141	130	0.185
0.3	311	164	147	0.412
0.2	358	187	171	0.274
0.1	398	207	191	0.246
0.0	517	271	246	0.468

EMIC position and density array is then normalised. This step is not needed for the 5 minutes surrounding the event as they are all already the same lengths, similar to when normalising the storm lengths, the pre-onset phase was not normalised. Once the density and position data for the EMIC wave event duration were normalised, the three sections are reassembled. The new density array is then sorted by radial distance. Ordering the density data observed by relative distance from the Earth assures that all gradients are oriented with respect to the Earth and not along the satellite path.

As we are most interested in the region where plasma plumes are expected we will focus on the bin 14 hr $<$MLT$<$18 hr. Figure 6.18 shows the superposed epoch for all EMIC wave events which occurred between 14 hr $<$ MLT $<$18 hr. The black line represents the mean and the green lines represent the quartiles. All three lines are smooth and straight showing that CRRES observed no correlation between EMIC waves and negative density gradients. These results are consistent with results from section 6.6.1 where the split between positive and negative density gradients is fairly even. Averaging data from random slopes will give a flat superposed output. If there is significant variability and many of the curves are not linear as presumed from the results of section 6.6.1 then one would get wide quartiles such as seen in Figures 6.18 and 6.19. Chen et al. [2009] looked specifically at the generation of EMIC waves due to the density gradients from a plume. As stated before, we are unable to know for certain from our single point measurements if we are inside a plume, but are reasonably sure that on average during the main phase of a storm a plume should be present in the 14 hr - 18 hr MLT bin. Figure 6.19 shows EMIC waves occurring during the main phase of a storm and although there is more variation in the mean and quartiles due to the averaging of fewer events, the mean and quartiles are still reasonably flat throughout the superposed epoch.

To highlight these results we will consider three orbits each containing multiple EMIC wave events. These events were chosen from the second half of the CRRES mission where CRRES spent more time in the dusk sector, and provided good data for the majority of the orbit. The chosen orbits included at least one of the three phases of a storm. The first event, orbit 961, highlights EMIC waves occurring throughout the pre-onset and the main phase of a moderate storm. There were no storms occurring for more than 6 days prior

to the start of this event, thus the pre-onset phase does not fall into the 6 day recovery of a prior storm. The second orbit, 931, falls completely during the main phase of a large storm and a was included in the 6 day recovery of a previous storm. The final orbit, 927, occurs during the early part of the 80% recovery phase of a large storm.

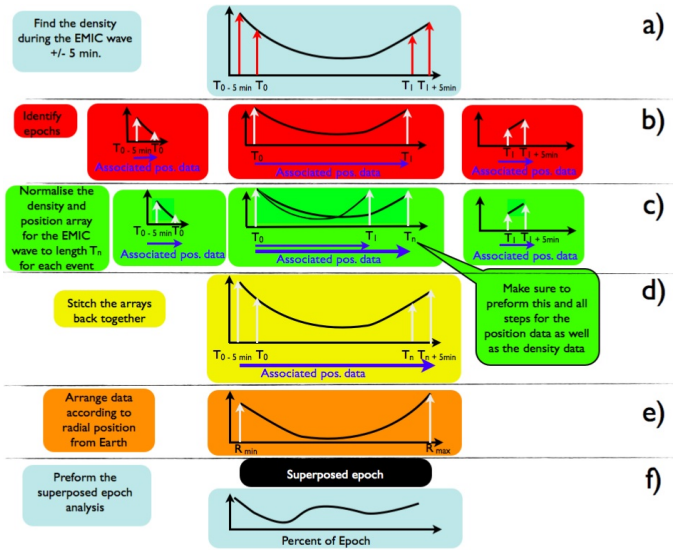

FIGURE 6.17: Flow chart of the normalisation process for the Sym-H index performed prior to the superposed epoch analysis. The first row shows the identification of the EMIC wave events. The red boxes in the second row represent each of the arrays associated with the epochs of interest, 5 minutes before till the start of the EMIC Wave event, the duration of the EMIC Wave event, and the 5 minutes following the EMIC Wave event. The start of the arrays are labeled as t_o and the end labeled as t_1. Each array is then treated separately in the next step. The green boxes in the third row illustrate the normalisation of the length of the individual EMIC wave duration to, t_m, which is longer than the longest duration for the observed EMIC waves during the CRRES mission. For the preceding and following 5 minutes surrounding the event, this is not needed as they are already defined as the same length. The previous three steps are performed for both the density data and the position data. The yellow box show where the arrays are then stitched together and in the orange box rearranged according to their relative distance from the Earth. A superposed epoch analysis is then performed and represented by the blue box at the bottom.

6.6.3 Case 1: Pre-onset/Main phase EMIC

Figure 6.20 shows a set of EMIC waves occurring during the pre-onset and part of a main phase of this storm. There is a clear SSC associated with this storm whose onset starts

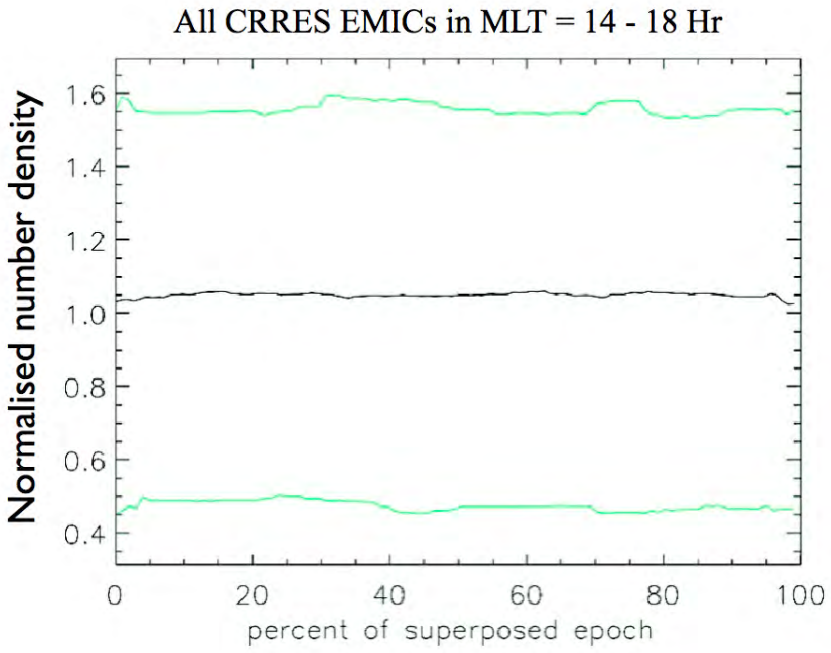

FIGURE 6.18: The superposed epoch of the density $\pm$ 5 minutes surrounding an EMIC wave events in the bin MLT = 14 hr - 18 hr. The black line represents the mean of the superposed epoch while the green line are the quartiles.

at 15:32 UT on the 27 August 1991 while CRRES is around 15 hr MLT. The minimum Sym-H was seen at 18:33 UT on the 27 August 1991 with an 80% recovery occurring at 7:38 UT on the following day. The number densities observed on this orbit shows an eroding plasmasphere and potentially the formation of a plume on the inbound pass. Prior to 12:00 UT it appears that the plasmasphere is reasonably full, and the density then quickly decreases at L $>$ 4. This density profile suggests that the plasmasphere has started eroding. However without solar wind or other consistent space based magnetometer data monitoring convection, it is difficult to know if convection has started. Over 17:40 - 18:45 UT CRRES encounters an enhanced density structure which has elevated densities similar to those found in plumes or an extended plasmasphere at L-values $>$ 4. CRRES then encounters the plasmapause at 19:00 UT. The background magnetic field shows a

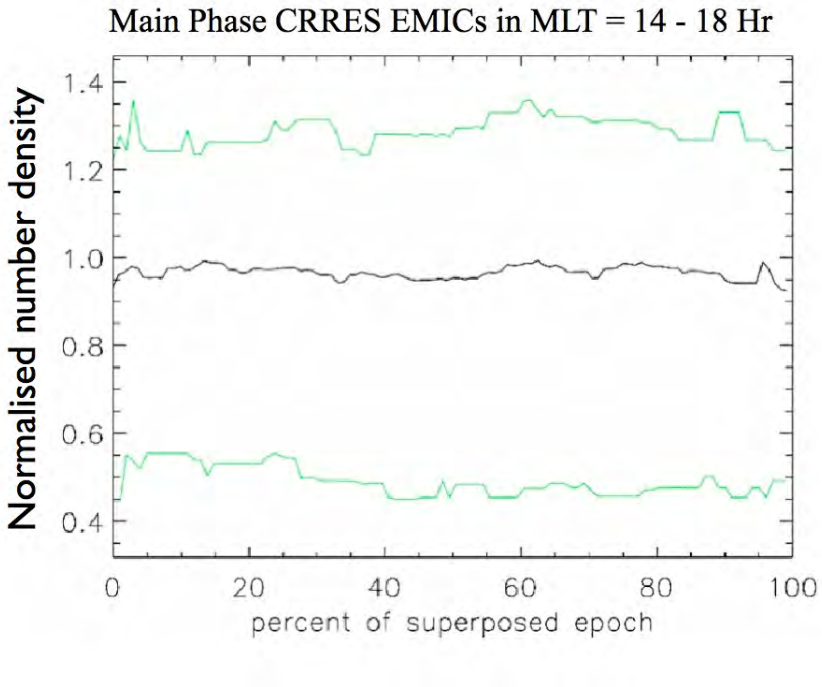

FIGURE 6.19: The superposed epoch of the density $\pm$ 5 minutes surrounding an EMIC wave events in the bin MLT = 14 hr - 18 hr during geomagnetic storms. The black line represents the mean of the superposed epoch while the green line are the quartiles.

relative increase from 15:15 UT just before the start of the SSC through to 17:35 UT, an hour before the minimum Sym-H was observed. The EMIC waves are also found to start at about 15:15 UT and continue until 18:00 UT. Although the EMIC waves do not align with the number density, they do agree relatively well with the start of the SSC and the change in the background magnetic field, which can also be seen in the cyclotron frequencies plotted in the spectrogram. As stated previously, during the pre-onset phase of a geomagnetic storm it is likely that these waves would be due to compression. These waves however also continue throughout most of the main phase of the storm. With the lack of solar wind data is is difficult to confirm the increase in the magnetic field is due to the presence of a magnetospheric compression or perhaps the overlap of the ring current with the plasmasphere or a plume. During the time when the EMIC waves are occurring,

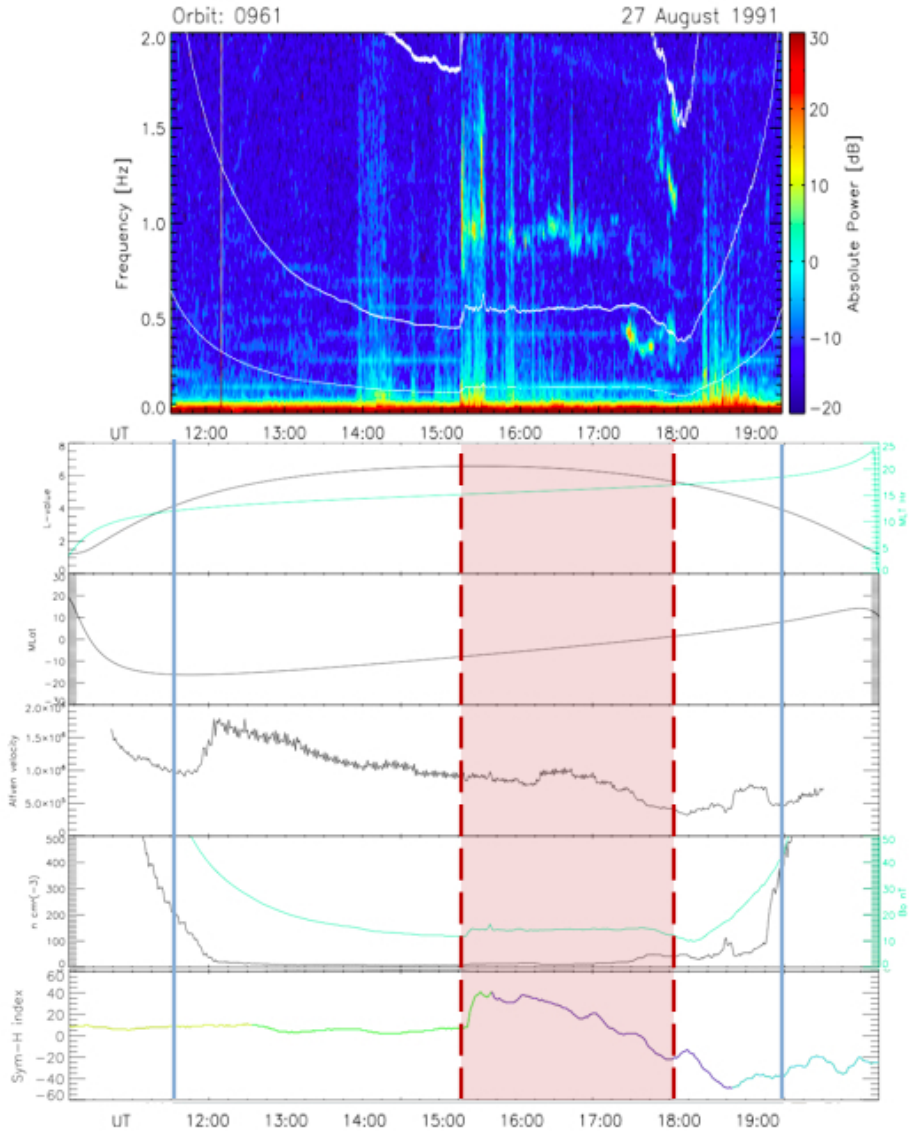

FIGURE 6.20: The spectrogram during orbit 961 (top panel), the L-values (black line) and MLT (green line) during the orbit (second panel), the magnetic latitude (third panel), the Alfven velocity (fourth panel), the density (black line) and background magnetic field (green line) during the orbit (fifth panel), and the Sym-H index (bottom panel). The red dotted lines highlight the region where EMIC waves are observed and the light blue lines highlight the time period over which there was good data from CRRES (used to create the spectrogram). Pre-onset and main phase EMIC waves can be observed from 15:15 - 18:00 on 27 August 1991.

CRRES was in the 15 hr MLT to 17 hr MLT sector where effects from magnetospheric compression are likely still able to be observed. When CRRES encounters the plume density enhancement at 17:40 UT, EMIC waves appear in both the helium and hydrogen bands. However the waves discontinue as the magnetic field decreases even though the density remains elevated. Thus for this orbit EMIC waves were observed both outside and inside the plume, and although a few EMIC waves were observed along the density gradient, many more were not.

6.6.4 Case 2: Main Phase EMIC

During the geomagnetic main phase the free energy source of EMIC waves is thought to be associated with ring current particle injection and the presence of enhanced cold plasma density either through an eroded plasmapause or a plasma plume. Figure 6.21 shows CRRES orbit 931 associated with the main phase of a storm and 5 EMIC wave events. The EMIC waves are observed over 17:50 - 19:00 UT 14 August 1991. This storm does not show a well defined SSC, and the onset was taken at 12:22 UT on 14 August 1991 where the slope in Sym-H turned negative and stayed relatively negative until it reached the minimum value at 5:35 UT on the 15 August 1991. The storm recovered 80% at 16:17 UT on the same day. Throughout the main phase of the storm five compression events can be seen after 18:30 UT. However no EMIC waves were observed at these times. As CRRES travelled into the outer magnetosphere a clear plasmapause boundary is observed, but a plasma plume or other density structure is encountered at L = 4 and MLT = 13 hr at 14:15 UT, for 15 minutes. During this time broad band noise was observed without clearly observable EMIC waves. After this event the plasmasphere electron densities remained slightly elevated until 22:00 UT where CRRES on the inbound portion of its orbit crosses the plasmapause. Between 17:50 UT and 20:00 UT Pc5 waves can be seen in both the magnetic field data and the cyclotron frequencies plotted in the spectrogram. Hence the EMIC waves are possibly modulated by the longer period Pc5 waves which also relate to changes in the observed density [Fraser et al., 2010, Loto'aniu et al., 2009]. However, after 19:20 UT Pc5 waves and their associated density modulations continue

but the EMIC waves have ceased. As with the previous case study, these EMIC waves appear to follow the magnetic field more closely than the density gradients. For this orbit, the EMIC waves were observed in slightly elevated densities and during a Pc5 event, but not with significant density gradients.

6.6.5 Case 3: 80% Sym Recovery phase EMIC

As with the main phase, during the early recovery we may expect to see plasma plumes or density structures to help with EMIC wave generation and propagation [Borovsky and Denton, 2008, Chen et al., 2009, Horne and Thorne, 1993, Morley et al., 2009]. Figure 6.22 shows CRRES orbit 927 which has EMIC waves during the 80% recovery phase of a geomagnetic storm. The EMIC waves were seen over 21:50 - 23:50 UT on the 12 August 1991. Like Case 1, this storm has a clear SSC with the onset at 03:49 UT on 12 August 1991. The minimum Sym-H value occurred at 18:59 UT on the same day and recovered to 80% almost a day and a half later at 00:13 UT on 14 August 1991. While CRRES was outbound from the inner magnetosphere, the plasmasphere appears eroded and encounters a plume over 21:10 -23:10 UT on 12 August 1991. EMIC waves appear when CRRES moved to $L > 4.5$. EMIC waves commence at the time of a decrease in the Alfven velocity which continues throughout the duration of the EMIC waves and has a slight increase before they cease. In the cyclotron frequencies plotted in the spectrogram, Pc5 waves commence at 22:20 UT when strong EMIC waves are observed. This is also seen in the magnetic field data. As with Case 2 the Pc5 waves appear to modulate the EMIC waves [Loto'aniu et al., 2009]. In the hydrogen cyclotron frequency modulation, two Pc5 wave packets are clearly observed. The stronger EMIC waves relate to the first Pc5 wave packet. Later on the inbound orbit, at 01:50 UT on 13 August 1991, a second plume structure is observed in the plasma density data with an associated decrease in the Alfven velocity. Here the plasmapause is encountered and the plasmasphere appears to have refilled out to $L = 2.7$. During this second plume no EMIC or Pc5 waves are observed. Once again the EMIC waves appear to correlate better with the magnetic field than any of the observed density structures. This CRRES orbit showed EMIC waves occurring during a plume with

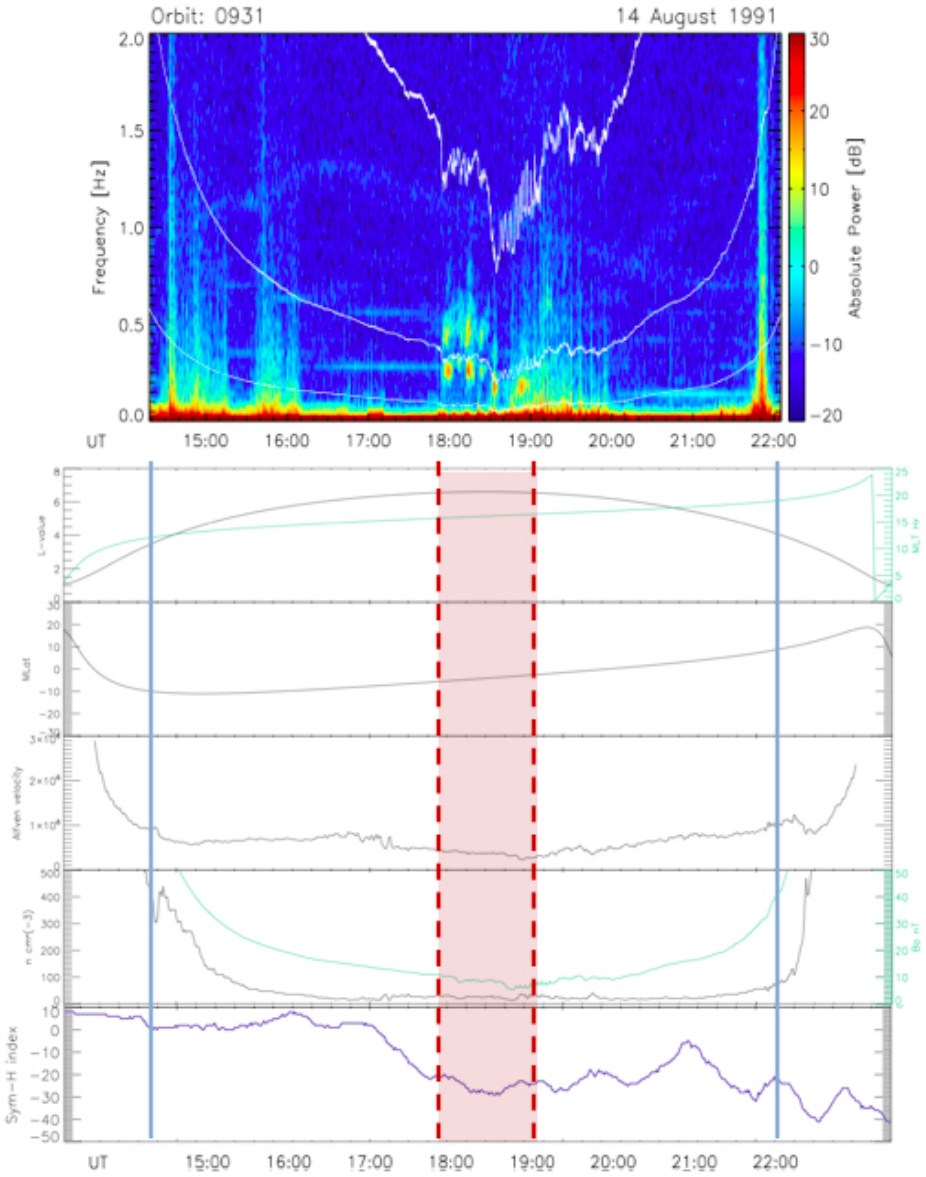

FIGURE 6.21: The spectrogram during orbit 931 (top panel),the L-values (black line) and MLT (green line) during the orbit (second panel), the magnetic latitude (third panel), the Alfven velocity (fourth panel), the density (black line) and background magnetic field (green line fifth panel) over the orbit (fifth panel) , and the Sym-H index (bottom panel). The red dotted lines highlight the region where EMIC waves are observed and the light blue lines highlight the time period over which there was good data from CRRES (what is used to create the spectrogram). Main phase EMIC waves can be observed from about 17:50 - 19:00 on 14 August 1991.

density structures and a Pc5 wave. The EMIC waves however correlate better with the Pc5 wave modulations than the observed density structure.

6.6.6 Case study discussion

Throughout the three examples presented EMIC waves are observed sometimes within plumes but without clearly associated density gradients and showed better correlation with magnetic field variations. In case 1 (Figure 6.20) the waves are only observed in the helium band after the density increases. This suggests that the local plasma properties and relative populations have changed. Although the EMIC waves are first seen in the hydrogen band associated with the increased density, they cease with the decrease in the magnetic field. The growth equations for EMIC waves in Chapter 2.5, shows that both the magnetic field and density play significant roles along with the temperature anisotropy in the generation of waves. Case 2 (Figure 6.21) and case 3 (Figure 6.22) shows EMIC waves in both the helium and hydrogen bands suggesting the presence of helium as well as hydrogen. Although the plasma density is elevated in case 2 for the majority of the orbit ($n > 10$ cm^{-3}) and there are observable compressions in the Sym-H index, the EMIC waves do not commence until the Pc5 waves are observed. The EMIC waves observed in case 3 also appear to correlate with the Pc5 events observed in the geomagnetic field.

6.7 Summary

In this chapter we studied the relationship between the plasmasphere and EMIC waves. The primary result of the statistical study shows that EMIC waves occur in regions where the cold plasma density is significantly enhanced under all magnetospheric conditions except the pre-onset phase of a geomagnetic storm. We suspect that the pre-onset results may differ from the other conditions due to insufficient statistics, and a more comprehensive study is needed. It is not obvious that even if the pre-onset EMIC waves are associated with magnetospheric compressions instead of an enhancement in the ring current that the cold plasma density levels would be expected to differ. On average, the quiet time densities were larger than the main phase densities which were larger than the

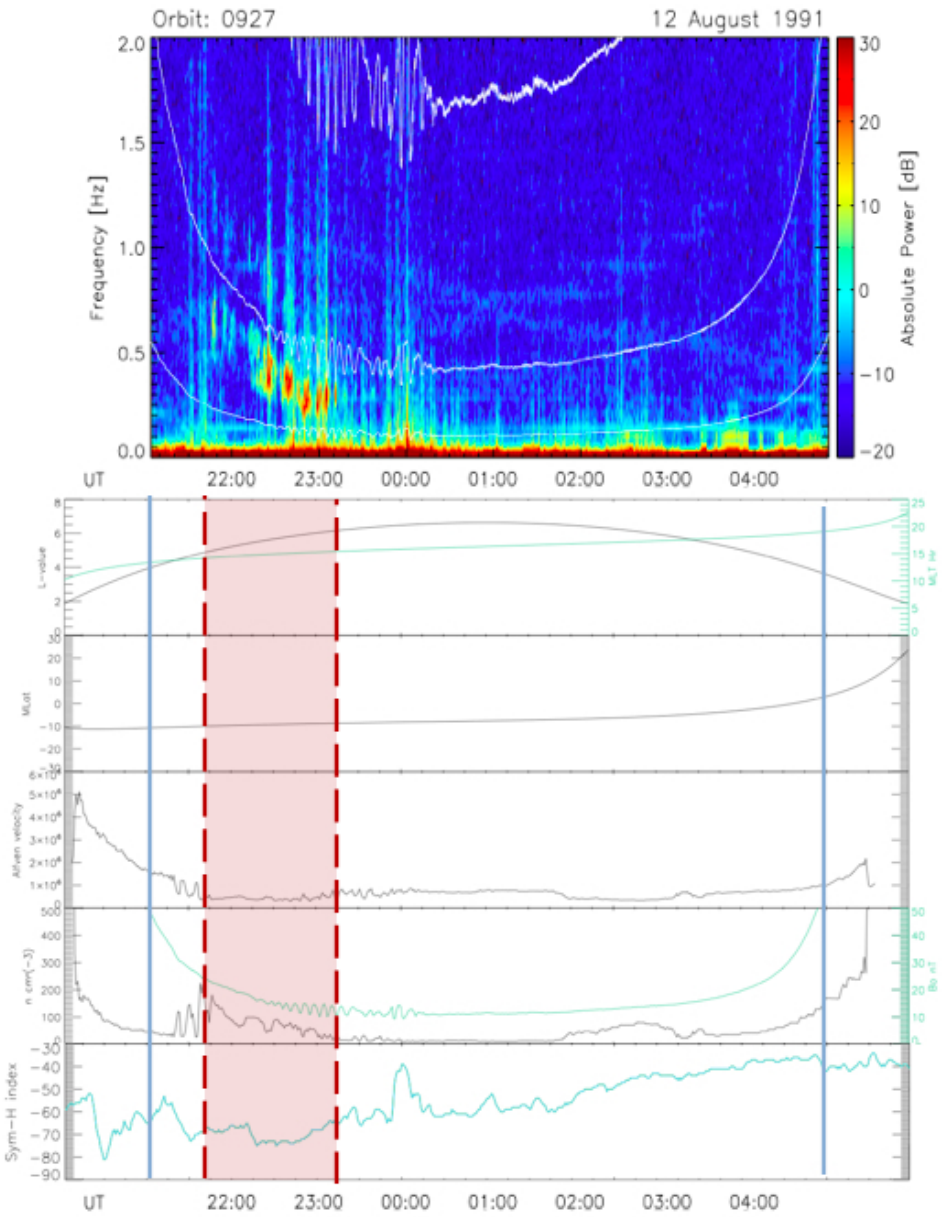

FIGURE 6.22: The spectrogram during orbit 927 (top panel), the L-values (black line) and MLT (green line) during the orbit (second panel), the magnetic latitude (third panel), the Alfven velocity (fourth panel), the density (black line) and background magnetic field (green line) over the orbit (fifth panel), and the Sym-H index (bottom panel). The red dotted lines highlight the region where EMIC waves are observed and the light blue lines highlight the time period over which there was good data from CRRES (what is used to create the spectrogram). Recovery phase as defined by 80% of the minimum Sym-H value EMIC waves can be observed from about 21:50 - 23:20 on 12 August 1991.

densities observed during the 80% recovery phase. At L $>$ 7, the densities observed in the main phase drastically decease while the quiet and recovery phase densities remain elevated suggesting the possible presence of a plume around $5 < L < 7$ during the main phase.

Whether these enhanced densities are due to plumes is debatable as CRRES, with an elliptical orbit, was not able to detect the presence of a plume in its early stages. On a statistical basis a plume like structure associated with EMIC waves was seen during the main phase of the geomagnetic storms. It was also shown that EMIC wave occurrence peaked in the middle of the average plume signature. Although there were no clear regions on average of enhanced densities or plume signatures during the 80% recovery of a storm, there was a distinct difference between the 80% recovery and the extended recovery phase which had higher densities on average. During this time it is clear that the plasmasphere has started refilling out to $L > 7$.

Since CRRES did not precess completely around the dayside of the magnetosphere and the mission ceased round 14 hr MLT, our studies were restricted to EMIC waves in the dusk sector, the region where it is expected that the ring current and plasmasphere or plumes may overlap. When comparing our results to those of some ground based studies in particular Posch et al. [2010] we are able to see a more distinct correlation between EMIC wave occurrences and possible plasma plume locations. Ground based studies may not observe many main phase EMIC waves due to interference or shielding from the ionosphere as well as seeing the EMIC waves on other field lines than the one they were generated and propagated on in the magnetosphere.

The need for density gradients leading to strong EMIC wave growth was not supported by the CRRES data. Using CRRES observations we were unable to detect a statistical correlation between negative density gradients and EMIC waves. With the three case studies, there was no clear indicator that EMIC waves were associated with local density gradients. In fact many of the waves appeared to correlate better with other magnetospheric parameters including Sym-H compressions, the magnetic field or Alfven velocity, and Pc5 wave modulation. The case study observations also agree well with the statistical results. Statistically the majority of EMIC waves occurred within the average plume,

away from an observable and large plasmapause/ density gradient. Although the waves occurred during intervals of enhanced densities (i.e. $n > 10$ cm^{-3} for $L > 5$), negative density gradients were not found more frequently than positive density gradients, and a straight line fit to the data was only appropriate for less than half of the observed EMIC wave events. One motivation for looking at EMIC waves relative to density gradients is that this has been a suggested mechanism which can increase the wave power allowing the waves to more easily resonate with radiation belt particles [Chen et al., 2009, Summers and Thorne, 2003] which is considered in the following chapter.

7

Pitch Angle Diffusion of Radiation Belt Electrons by EMIC Waves

7.1 Introduction

Relativistic electrons, and their precipitation, have been found to play a critical role in the effects of space weather on technology [Baker, 1996, Friedel et al., 2002]. In general geomagnetic storms have been associated with enhancements of the radiation belts, and many studies have looked into the cause of these enhancements [Friedel et al., 2002, and references therein]. Although wave-particle interactions play an important role, relatively little research has considered the capability of EMIC waves to contribute to the loss of relativistic electrons in the radiation belts [Thorne, 2010]. In this chapter we will look into the potential for EMIC waves to contribute to the loss of relativistic electrons in the

radiation belts. Section 7.2 will describe some of the loss processes found in the radiation belts. Section 7.3 briefly summarises studies that have found correlations between EMIC waves and electron particle precipitation. Then in Section 7.4 we will describe the formulation developed by Summers [2005] which considers local pitch-angle diffusion coefficients for EMIC waves acting on both radiation belt electrons and protons. Finally Section 7.6 studies how the calculated local diffusion coefficients differ from Summers [2005] when the magnetic field and cold particle data measured by CRRES are used as inputs to the model.

7.2 Losses in the Radiation Belts.

Although much radiation belt research is focused on flux enhancements, there have also been flux decreases, or losses observed in the radiation belts [e.g. Green et al., 2004, Horne et al., 2003, 2009, Reeves et al., 2003]. The precipitation of MeV electrons into the ionosphere and upper atmosphere may also have space weather effects; changing the conductivity of the ionosphere, as well as depleting ozone and increasing NO_x levels which may affect terrestrial climate [Rodger et al., 2010a, Rozanov et al., 2005, Thorne and Horne, 1997]. Reeves et al. [2003] noted in their study of 276 storms during the years 1989 - 2000, that 53% of storms saw increased fluxes of radiation belt electrons, 28% remained the same, and 19% saw a net decrease. Although around half of storms are found to have a net increase in flux, most storms show a decrease during the pre - onset and main phase [Blake et al., 1997, Horne et al., 2009, Meredith et al., 2003, Reeves et al., 2003, Summers and Thorne, 2003, Summers et al., 2004, Yahnina et al., 2003]. The recovery phase of the storm is where the radiation belts are found to relatively consistently see an increase in the electron flux, although not necessarily to pre-storm levels [Borovsky and Denton, 2009, Friedel et al., 2002, Horne et al., 2003, Li et al., 1997, Meredith et al., 2001, Miyoshi et al., 2008, Morley et al., 2010, Reeves, 1998, Summers et al., 2004]. In order to successfully model the radiation belts, both the increase in radiation belt particles and the loss processes must be understood.

7.2.1 The Dst Effect

During the main phase of a geomagnetic storm, particles enter the ring current and cause a net decrease in the magnetic field at the surface of the Earth, and subsequently this decrease is used to identify storms in the Dst index as discussed in Chapter 3.9. This change is also observed in the ambient magnetic field in the magnetosphere, which can affect the flux levels of particles at any given location as depicted in Figure 7.1 [Green and Kivelson, 2001, Green et al., 2004, Onsager et al., 2002]. As the particles rearrange themselves in order to preserve the third adiabatic invariant (discussed in Chapter 1.5.3) as the background magnetic field changes slowly when compared to the drift timescales, a satellite may see a relative increase or decrease in the local particle population as shown in Figure 7.1. Although these particles are not truly lost or gained, as they will return to their previous paths as the ring current decays, a satellite such as CRRES will observe a local change during this period. This process does not remove these particles from the magnetosphere unless they move on to open drift paths or are moved into the loss cone. Most studies will attempt to account for this effect in order to study the mechanisms which provide a realistic net loss to the radiation belts [Friedel et al., 2002, Reeves et al., 2003].

7.2.2 Radial Diffusion

Radial diffusion driven by enhanced ULF wave activity was initially thought to be the dominante loss process of the outer radiation belts, and violates the third adiabatic invariant [Li and Temerin, 2001]. Unlike the Dst effect, instead of a general shift Earthwards for the particles followed by a move back as a storm recovers, the particles move Earthward or are lost through contact with the magnetopause on their new drift paths after either drifting outward through radial diffusion or the the drift path that they are on becomes open. Although this mechanism is effective outside geosynchronous orbit, it alone is unable to describe the radiation belt dynamics observed inside geosynchronous orbit, especially the peak loss observed at L= 4.

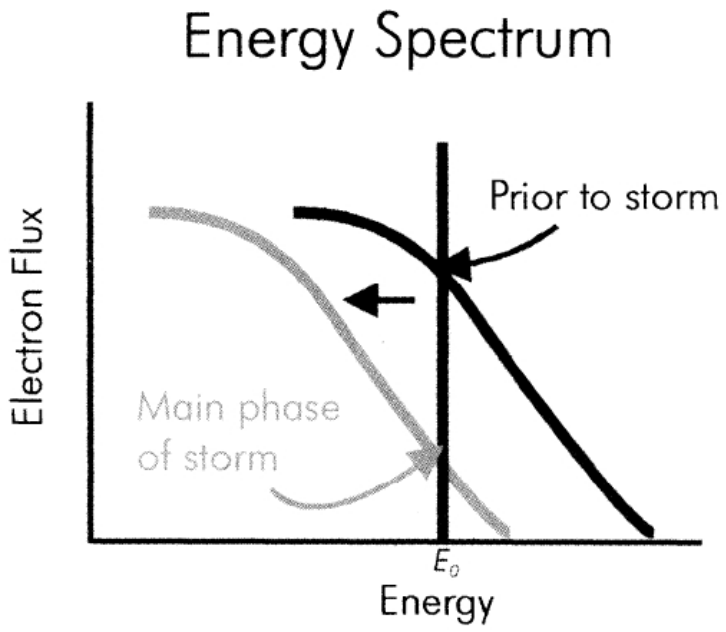

FIGURE 7.1: A cartoon showing the Dst effect on the radiation belt electron flux at a fixed location, prior to a geomagnetic storm and during the main phase of a storm from Green and Kivelson [2001].

7.2.3 VLF Waves

VLF Chorus Emissions

Chorus waves at $0.01 - 0.8 f_{ce}$ Hz have been thought to contribute to both the acceleration and the loss of radiation belts and are excited by a cyclotron resonance with injections of anisotropic 10 - 100 keV electrons into the inner magnetosphere [Meredith et al., 2001, Summers, 2005]. They are found generally from midnight around through dawn and around to noon and are confined within 15° of the magnetic equator (Figure 7.2) [Li et al., 2007, Thorne, 2010]. They are able to pitch angle scatter radiation belt electrons which can lead to diffuse auroral precipitation [Thorne, 2010]. This would move the mirror point of the particle into the atmosphere where it can collide with other particles, and become lost [Thorne, 2010]. It has been observed that Chorus waves intensify with an increase in geomagnetic activity. Chorus waves also potentially play a role in the next suggested

mechanism for radiation belt loss, the VLF Hiss.

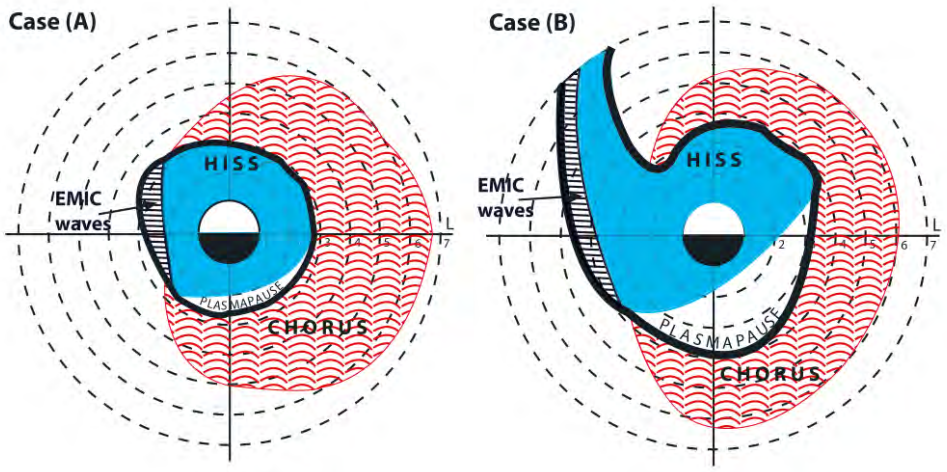

FIGURE 7.2: A cartoon showing the expected regions for EMIC wave, Chorus, and Hiss interaction with MeV radiation belt particles from Summers et al. [2007]. Case A represents a compressed magnetosphere and Case B represents a highly geomagnetic active magnetosphere.

VLF Hiss Emissions

The plasmaspheric hiss is a broadband whistler wave, which is observed under all magnetospheric conditions inside the plasmasphere, although the intensity does increase with geomagnetic activity [Summers et al., 2007, Thorne, 2010]. Hiss emissions are found in the frequency range of 0.1 and 3 kHz. This emission is thought to be responsible for the electron loss which creates the slot region between the inner and outer radiation belts [Lyons and Thorne, 1972, Meredith et al., 2001]. Modelling and ray tracing suggests that the hiss is due to the propagation of coherent chorus waves from outside the plasmasphere into the magnetosphere [Bortnik et al., 2011]. As the Chorus waves move to lower L-shells they enter into the plasmasphere and become trapped. Within the plasmasphere these discrete chorus waves merge together and can produce the hiss emissions observed (shown in Figure 7.2) [Meredith et al., 2001, Summers et al., 2007, Thorne, 2010]. Hiss emissions are also thought to scatter radiation belt electrons into the loss cone [Thorne, 2010].

7.2.4 EMIC Waves

EMIC waves are able to pitch-angle scatter radiation belt electrons into the loss cone region, and have been found to be associated with observed electron precipitations. Thus these waves are potentially able to produce a rapid and localised loss region in the radiation belts during geomagnetic storms as depicted in Figure 7.2 [Li et al., 2007, Loto'aniu et al., 2006, Summers, 2005, Summers and Thorne, 2003]. The big question with EMIC waves is, are they able to scatter "geophysically interesting energies" [Thorne, 2010]. Recently there has been extensive work done on the ability of EMIC waves to pitch angle scatter radiation belt electrons, and at what energies [Horne et al., 2009, Li et al., 2007, Loto'aniu et al., 2006, Meredith et al., 2003, Shprits et al., 2008, Summers, 2005, Summers and Thorne, 2003, Thorne et al., 2006, Ukhorskiy et al., 2010, Yahnin and Yahnina, 2007].

7.3 EMIC Waves and Particle Precipitation

EMIC waves are thought to contribute to precipitation loss of MeV electrons, but as with all potential loss mechanisms to what extent and under what magnetospheric conditions is still debated. Only recently has observational evidence been reported to directly link EMIC wave activity with electron precipitation. The ground based study by Rodger et al. [2008] using the AARDDVARK network and chains of riometers and magnetometers described in Rodger et al. [2008, and references therein] looked at four EMIC wave events which also show precipitation in the same localised regions. The satellite study of Sandanger et al. [2007] found that EMIC waves were not just found to be related to the loss of radiation belt electrons, but that these interactions were not restricted to a region inside or outside the plasmapause, nor were they restricted to the evening/noon MLT sector. They do point out that localised areas such as the plasmapause and plasma plumes may be more conductive to supporting EMIC wave-particle interactions, and that these regions do show strong pitch angle diffusion and EMIC wave occurrence. To what extent and what energies EMIC waves are able to resonate with radiation belt particles is debated [e.g. Horne et al., 2005, Meredith et al., 2003, Thorne, 2010] and this chapter works towards

answering this question.

7.4 Modelling EMIC Wave Resonance with Radiation Belt Electrons

There have been many studies which have considered EMIC waves and their interactions with radiation belt particles [e.g. Chen et al., 2009, 2010, Jordanova, 2007, Summers, 2005, Summers and Thorne, 2003]. Here we focus on the equatorial pitch angle diffusion coefficients outlined in Summers [2005]. Gendrin [1981] showed that, when using the principle that wave particle energy remains constant in the wave frame, the way in which particles diffuse in both energy and pitch angle can be deduced once their distribution functions are known. Summers et al. [1998] developed theory for calculating diffusion curves for electron cyclotron resonance with field aligned R-mode and L-mode electromagnetic waves in a relativistic plasma. In this study they found that EMIC waves are ineffective for accelerating radiation belt electrons, but that they can induce rapid pitch angle scattering along the plasmapause. In order to quantify the ability of EMIC waves to pitch angle scatter radiation belt particles the appropriate resonant diffusion coefficients, most commonly found using quasi-linear diffusion theory, must be determined. Summers [2005] derived an exact closed form analytical expression using quasi-linear theory for the local pitch angle diffusion coefficients in a pure H^+ plasma where no integration is involved resulting in a very fast computation time.

Summers [2005] gives the pitch angle diffusion rate, $D_{\alpha\alpha}$, as

$$D_{\alpha\alpha} = \frac{\pi\Omega_\sigma^2}{2W_o}\frac{(1)}{\gamma^2}\sum_{s=\pm1}\sum_{j=1}^{N}(1-\frac{\omega_j\mu}{k_j\upsilon})^2\frac{W_s(k_j)}{\mid \upsilon\mu - d\omega_j/dk_j \mid}, \tag{7.1}$$

where $W_o = B_o^2/8\pi$ is the magnetic energy density of the background magnetic field, Ω_σ is the gyro-frequency of the resonating particle species that we are resonating with, $\mu = cos(\alpha)$ where α is the pitch angle of the particle, υ is the electron speed, j is the ion species, γ is the Lorentz factor, and W_s is the wave spectral energy density. ω_j, k_j, and

$d\omega_j/dk_j$ correspond to each wave mode which satisfies the resonance condition

$$\omega_j - v\mu k_j = -s\frac{q \mid \Omega_\sigma \mid}{\mid q \mid \gamma} \tag{7.2}$$

and the appropriate dispersion relation $k_j = k(\omega_j)$, where s = 1 (R-mode waves) or s = -1 (L-mode waves). We will be using s = -1 for application to EMIC waves. The linear theory dispersion relation for a multi-ion plasma is derived in Chapter 2 Equation 2.30 and written as

$$\frac{c^2k^2}{\omega^2} = 1 - \frac{\omega_{pe}^2}{\omega(\omega - \mid \Omega_e \mid)} - \sum_{j=1}^{n}\frac{\omega_{pj}^2}{\omega(\omega - \Omega_j)}. \tag{7.3}$$

Assuming that we are dealing with a three ion plasma (H^+, He^+, and O^+) and charge neutrality, then we can write the non-dimensional form of equation 7.3 derived in Chapter 2 and given in Equation 2.35 as

$$\frac{1}{u^2} = 1 - \frac{1}{\alpha^*\epsilon x}\left(\frac{1}{1+\epsilon x} + \frac{\eta_1}{x-1} + \frac{\eta_2}{4x-1} + \frac{\eta_3}{16x-1}\right), \tag{7.4}$$

where $u = \omega/(kc)$ is the dimensionless wave phase speed and $x = \omega/\Omega_{H^+}$ is the dimensionless wave frequency and $\epsilon = m_e/m_p$ and $\eta_j = N_j/N_o$ is the fractional composition of the the ion species such that $\sum_{j=1}^{3}\eta_j = 1$. Here we have also used the non-dimensional parameter α^* introduced in Chapter 2.4.2 and given as

$$\alpha^* = \frac{\Omega_e^2}{\omega_{pe}^2} = \frac{V_A^2}{\epsilon c^2} = \frac{B_o^2}{4\pi N_o}\frac{1}{m_e c^2}. \tag{7.5}$$

Thus α^* can be thought of either as proportional to the Alfven velocity, V_A^2, or the magnetic energy $\frac{B_o^2}{4\pi N_o}$ [Summers and Thorne, 2003], and in Chapter 4.5 was shown to correlate with peaks in EMIC wave activity.

In a pure hydrogen plasma equations 7.3 and 7.4 reduce to

$$\left(\frac{ck}{\omega}\right)^2 = 1 - \frac{(1+\epsilon)/\alpha^*}{(\omega/\mid \Omega_e \mid -s)(\omega/\mid \Omega_e \mid +s\epsilon)} \tag{7.6}$$

$$\frac{1}{u^2} = 1 - \frac{1}{\alpha^*\epsilon x}\left(\frac{1}{1+\epsilon x} + \frac{\eta_1}{x-1}\right) \tag{7.7}$$

$$u^2 = \frac{\alpha^*\epsilon(1+\epsilon x)(1-x)}{\alpha^*\epsilon(1+\epsilon x)(1-x) + 1 + \epsilon}. \tag{7.8}$$

For the remainder of this study we will assume a pure hydrogen plasma, and for a more detailed overview of these equations and this estimate see Summers [2005] and references therein.

TABLE 7.1: The median inputs used to calculate the diffusion coefficient $D_{\alpha\alpha}$ for all CRRES EMIC waves, non - storm time EMIC waves, and storm time EMIC waves including L-Shell, the magnetic latitude (MLat), the equatorial magnetic field B_{eq}, the wave parameter α^*, and the wave amplitude db, as well as the inputs for the Summers [2005] model.

	model	All	non-storm time	Storm Time
% of events in CRRES Mission		100	45.9	54.1
Median L-Shell	4	6.31	6.49	6.05
Median MLat deg	0	$-6.98°$	$-9.23°$	$-6.57°$
Median B_{eq} nT	488.4	111.65	144.57	139.62
Median α^*	2.3×10^{-3}	6.0×10^{-3}	6.0×10^{-3}	6.0×10^{-3}
Median db nT	1	0.35	0.31	0.38

The code used to run the test data, and inputs from CRRES data is a modified version of J. Koller's code [personal communication 2010], which is an implementation of the Summers [2005] equations, from a collaboration at Los Alamos with J. Koller, S. Morley, and R. Friedel. In order to test the code, we first reproduced the results from Summers and Thorne [2003] shown in Figure 7.3 (which is the same as Figure 4 in Summers [2005]). The assumptions for the test case are that the EMIC waves occurred at L = 4 with plasma parameters $\alpha^* = 2.3 \times 10^{-3}$, $N_o = 1000$ cm^{-3}, and wave amplitude of $db = 1$ nT as described in Table 7.1. The wave spectrum is considered to be a Gaussian with centre frequency $\omega_m = \epsilon \mid \Omega_e \mid /3$. The bandwidth was set to $\sigma = 1$ and $\delta\omega/\Omega_p = 1/6$ which corresponds to the waveband $1/6 < \omega/\Omega_p < 1/2$. Our results agree with Summers [2005] as can be seen in our Figure 7.3. As stated by Summers [2005] for electrons in the energy range of 1.25 - 5 MeV, pitch angle diffusion can extend into the loss cone and the local maximum scattering rates can be quiet high. Thus EMIC waves may be an important mechanism contributing to radiation belt electron loss.

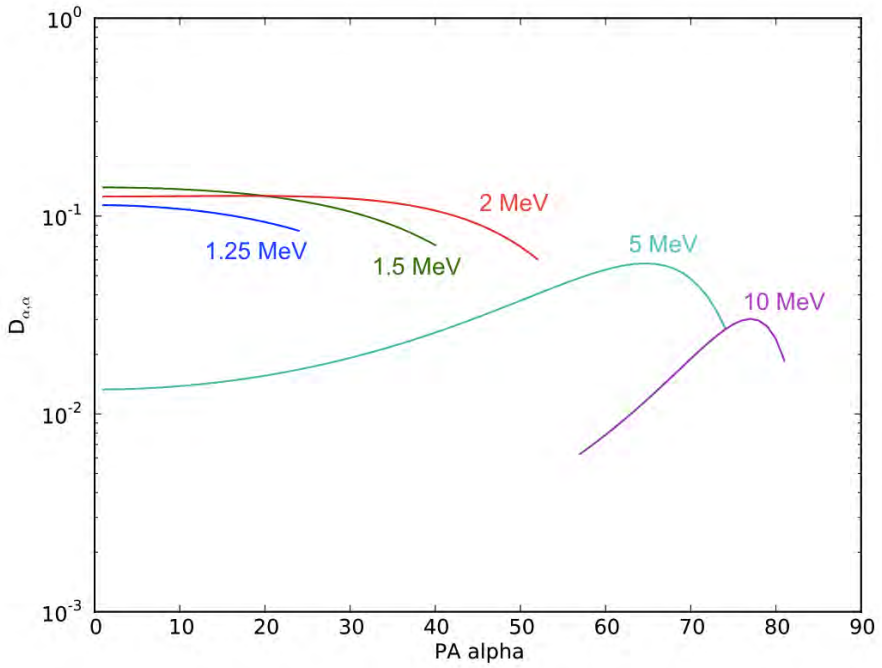

FIGURE 7.3: The equatorial pitch angle diffusion coefficients found fromSummers [2005]. Compare with their Figure 4, for EMIC waves at L=4 assuming $\alpha^* = 0.0023$ and a wave amplitude of 1nT resonating with radiation belt electrons of energies 1.25 (dark blue), 1.5 (green), 2 (red), 5 (light blue), and 10 (purple) MeV.

7.5 The Loss Cone and Strong Diffusion Limit

When discussing the diffusion coefficients there are two important concepts to consider; the strong diffusion limit and the loss cone. The loss cone, discussed briefly in Chapter 1.5.1, describes the set of pitch angles where particles are lost from the magnetosphere. In the magnetosphere, the loss cone is partially controlled by the height at which collisions dominante, removing particles from the field lines. This height is nominally taken as between 100 - 200 km above the Earth and the associated last mirroring point has been plotted in Figure 7.4 [Abel and Thorne, 1998]. The exobase of the atmosphere and where parallel electric fields which can increase the size of the loss cone by increasing

the parallel velocity of the particles starts to occur around 2000 km [Pierrard et al., 2009, Reynolds et al., 2001, Rodger et al., 2010b]. For $3 < L < 8$, the size of the loss cone varies between a few degrees at L = 8 to 13° at L = 3 for a mirroring height of 2000 km. Between $5 < L < 7$, where the majority of the EMIC waves were observed by CRRES, the mirroring pitch angle differs by a few degrees when assuming loss starting at either 100 or 2000 km.

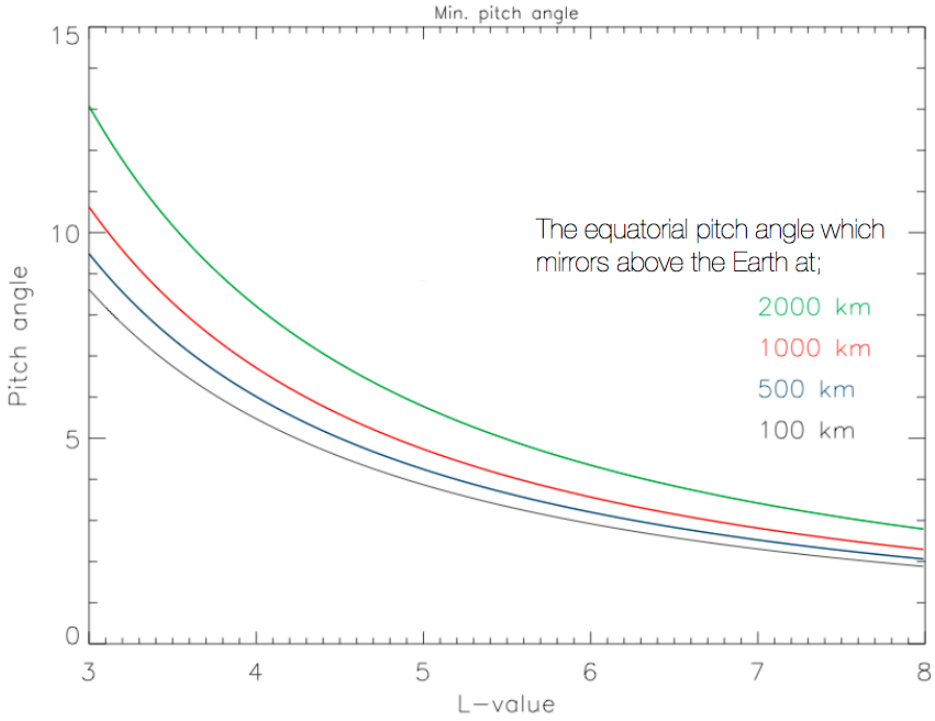

FIGURE 7.4: The last mirroring equatorial pitch angle is plotted over $3 < L < 8$ for mirroring heights of 2000 km (green), 1000 Km (red), 500 km (blue), and 100 km (black).

Whether a strong diffusion or the weak diffusion regime exists is determined by the strong diffusion limit. In the strong diffusion regime, the diffusion time scales are shorter than the bounce time scales such that the particles diffuse across the loss cone within a quarter bounce period [Kennel and Petscheck, 1966, Shprits et al., 2009, Summers et al.,

2005]. Assuming a dipole magnetic field, the strong diffusion limit can be written as

$$D_{SD} = \frac{0.205c}{L^4(E+1)R_E}\left(\frac{4LE(E+2)}{4L-3}\right)^{1/2}, \tag{7.9}$$

where E is the particle energy and c is the speed of light (Figure 7.5) [Summers et al., 2005]. If the bounce averaged diffusion is greater than D_{SD} than the pitch angle distribution (PAD) inside of the loss cone becomes isotropic, and the loss of particles is limited by the size of the loss cone and the bounce frequency. If the diffusion rate is less than the strong diffusion regime, the resultant rate of particle precipitation is determined by pitch angle diffusion.

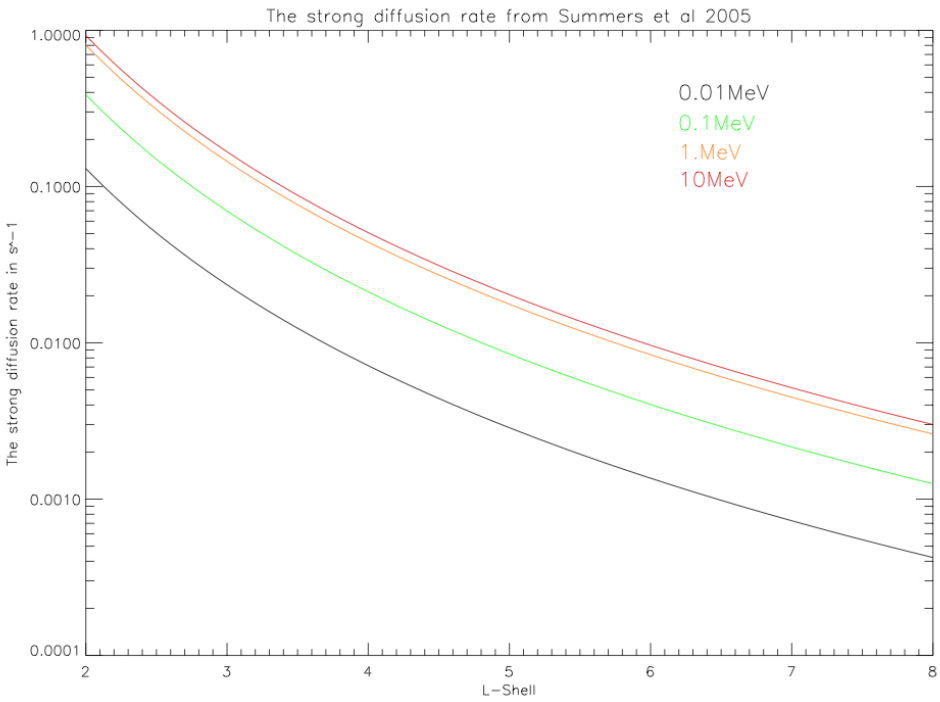

FIGURE 7.5: The strong diffusion limit, assuming a dipole field, is plotted for $2 < L < 8$ and for energies of 0.01 MeV (black line), 0.1 MeV (green line), 1.0 MeV (orange line), and 10 MeV (red line).

In this current study we will not calculate the bounce average diffusion coefficients, which could then be compared to the strong diffusion limit and state which regime we

are in, but instead are only calculating the local pitch angle diffusion coefficients. Lyons and Thorne [1972] showed that the bounce average diffusion rates are about an order of magnitude less than the local diffusion rates. We will use this estimate to then compare our median calculated local $D_{\alpha\alpha}$ to the strong diffusion limit.

7.6 Pitch Angle Diffusion Coefficients

To prepare the CRRES data, we have used the wave power spectral density, P, [nT^2 Hz^{-1}] prepared by R. Grew at each time step in the CRRES mission where good data existed. A constant frequency resolution with a 1600 point FFT, a sample rate of 8 Hz, a 400 point step, and 10 mHz frequency resolution was used to help automate the data preparation process. When the EMIC wave event occurred off the equator, the local magnetic field and L-value were used to determine the equatorial magnetic field assuming a dipole. This equatorial magnetic field value was then used in calculating the α^* of the EMIC.

The wave power was then averaged to a one minute resolution. We then determined which band, the H band defined as $0.4f_{cp}$ to f_{cp} or the He band defined as $0.4f_{cHe}$ to f_{cHe}, had the highest integrated power in the band. The band was recorded as well as its integrated wave power,

$$\int_{0.4f_{ci}}^{f_{ci}} Pdf, \tag{7.10}$$

where f_{ci} is either the proton or helium cyclotron frequency of the dominant band and P is the wave power for a given frequency. The equatorial pitch angle diffusion coefficients were then found at each minute where an EMIC wave was observed in the CRRES data for electrons with energies of 1.25, 1.5, 2, 5, and 10 MeV. In Figures 7.6- 7.11, the median $D_{\alpha\alpha}$ was determined for each pitch angle and plotted for electrons with energies of 1.25 MeV (blue lines), 1.5 MeV (green lines), 2 MeV (red lines), 5 MeV (light blue lines), and 10 MeV (purple lines).

As with wave studies in the previous chapters, the events were divided into six categories; All EMIC waves, non-storm, storm, pre-onset, main phase, and recovery, where the definition of the 80% from the minimum Sym-H value is used for the recovery. The diffusion coefficient $D_{\alpha\alpha}$ was then found for each minute of the EMIC wave occurrence.

By finding the diffusion coefficient at each minute of the EMIC wave instead of using the averaged characteristics during the entire EMIC wave event, we have the ability to investigate the variability of $D_{\alpha\alpha}$ during a single EMIC wave event. This also allows for future division of the phases of a storm into smaller bins, and account for EMIC waves which may fall into multiple bins.

7.6.1 $D_{\alpha\alpha}$ for all CRRES EMIC Waves

Figure 7.6 shows the median diffusion coefficient $D_{\alpha\alpha}$, as a function of pitch angle, for all EMIC waves observed during the CRRES mission. From Table 7.1, the median of the inputs used as CRRES data to calculate the pitch angle diffusion coefficients were L = 6.3, magnetic latitude of $-6.9°$, an equatorial magnetic field of 111.7 nT, an $\alpha^* = 6.0 \times 10^{-3}$, and a wave amplitude of $db = 0.35$ nT. These values differ slightly from those found in Table 4.1 because here we report the median instead of the mean values over the mission. The median is preferred in this section since at the edges of an event the diffusion coefficients may be negligible or even zero, and not all events produced non-zero $D_{\alpha\alpha}$s and were then ignored. The median is also less affected by large outliers, of which we had a few, and thus gives a better representation of what is expected during an average CRRES EMIC wave.

Unlike the smoothly varying results from Summers [2005] shown in Figure 7.3, Figure 7.6 shows relatively smooth variation for pitch angles less than $55°$ at which point there is a large increase in $D_{\alpha\alpha}$ for electrons with an energy of 1.25 MeV. However, the curve for the 5 MeV and 10 MeV electrons seem to follow those shown in Figure 7.3, but with the peak at slightly higher pitch angles than found by Summers [2005]. In general, the median $D_{\alpha\alpha}$ for all CRRES EMIC waves are relatively similar to those found by Summers [2005]. Hence a similar conclusion can be drawn that for electrons with energies below 5 MeV, the scattering rates can be very high ($\geq 10^{-1}$ s^{-1}), and extends into the loss cone. In Figure 7.6 $D_{\alpha\alpha}$ for electrons with energies of 10 MeV also extends into the loss cone, but with lower values.

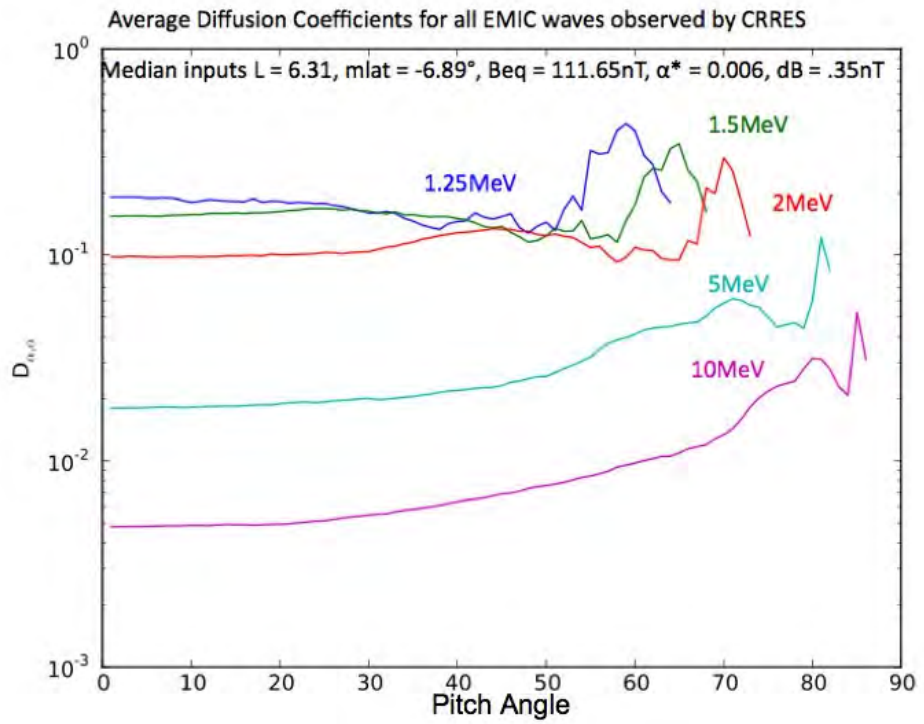

FIGURE 7.6: The median diffusion coefficients found from Summers [2005] for the EMIC waves observed by CRRES resonating with radiation belt electrons of energies 1.25 MeV (blue), 1.5 MeV (green), 2 MeV (red), 5 MeV (light blue), and 10 MeV (purple).

7.6.2 Storm vs Non-Storm EMIC waves

Figures 7.7 and 7.8 show the median diffusion coefficients observed during non storm and storm times respectively. The medians of the CRRES data used to calculate the equatorial pitch angle diffusion coefficients from the non storm time EMIC waves, in Table 7.1, were L-shell = 6.49, magnetic latitude = $-9.23°$, an equatorial magnetic field strength of 144.7 nT, $\alpha^* = 6.0 \times 10^{-3}$, and wave amplitude $db = 0.31$ nT. Compared with Figure 7.6, Figure 7.7 shows lower diffusion coefficients, but there are still observable diffusion coefficients at relatively high levels in the region of the loss cone.

The median of the inputs used for the storm time EMIC waves, in Table 7.1, were an L = 6.05, magnetic latitude = $-6.57°$, an equatorial magnetic field of 139.6 nT, $\alpha^* =$

TABLE 7.2: The median inputs used to calculate the diffusion coefficient $D_{\alpha\alpha}$ for EMIC waves during the pre-onset phase, main phase, and recovery phase of a geomagnetic storm, including L-Shell, the magnetic latitude (MLat), the equatorial magnetic field B_{eq}, the wave parameter α^*, and the wave amplitude db.

	pre-onset	main phase	recovery phase
% of events in CRRES Mission	3.7	30.1	20.7
Median L-Shell	5.9	6.21	6.21
Median MLat deg	$-7.16°$	$-6.43°$	$-4.11°$
Median B_{eq} nT	141.17	116.72	126.79
Median α^*	6.7×10^{-3}	5.0×10^{-3}	9.0×10^{-3}
Median db nT	0.3	0.42	0.31

6.0×10^{-3}, and a wave amplitude of $db = 0.38$ nT. As shown in Figure 7.8 $D_{\alpha\alpha}$ remains approximately constant across most pitch angles until about $55°$ where we see a rise and then fall for electron energies of 1.25 MeV, 1.5 MeV, and 2 MeV. The diffusion coefficients found from EMIC waves during storm intervals are slightly higher than those found during the non-storm times, especially at pitch angles greater than 55 degrees.

For both non storm and storm time EMIC waves, the diffusion coefficients are above the strong diffusion rate as approximated using Equation 7.9. For electrons with energies considered here, the strong diffusion rate at L > 4 is of the order of 10^{-2} s^{-1}. Thus the $D_{\alpha\alpha}$ shown in Figures 7.6, 7.7, and 7.8, are all currently above the strong diffusion rate at the outer L-shells, and although we do not look at the bounce averaged diffusion rates here, it is expected that they would also possibly exceed the strong diffusion rate for the lower energies shown in Figure 7.5. Lyons and Thorne [1972] showed that averaging $D_{\alpha\alpha}$ over the bounce orbit of the electrons, produced an order of magnitude reduction from the original value although this is also dependent upon the field model used in the integration of the bounce path. Consequently for both the storm and non-storm $D_{\alpha\alpha}$, it is possible that the bounce averaged diffusion coefficients for the 1 MeV, 1.5 MeV, and 2 MeV electrons will continue to be above the strong diffusion coefficient at pitch angles

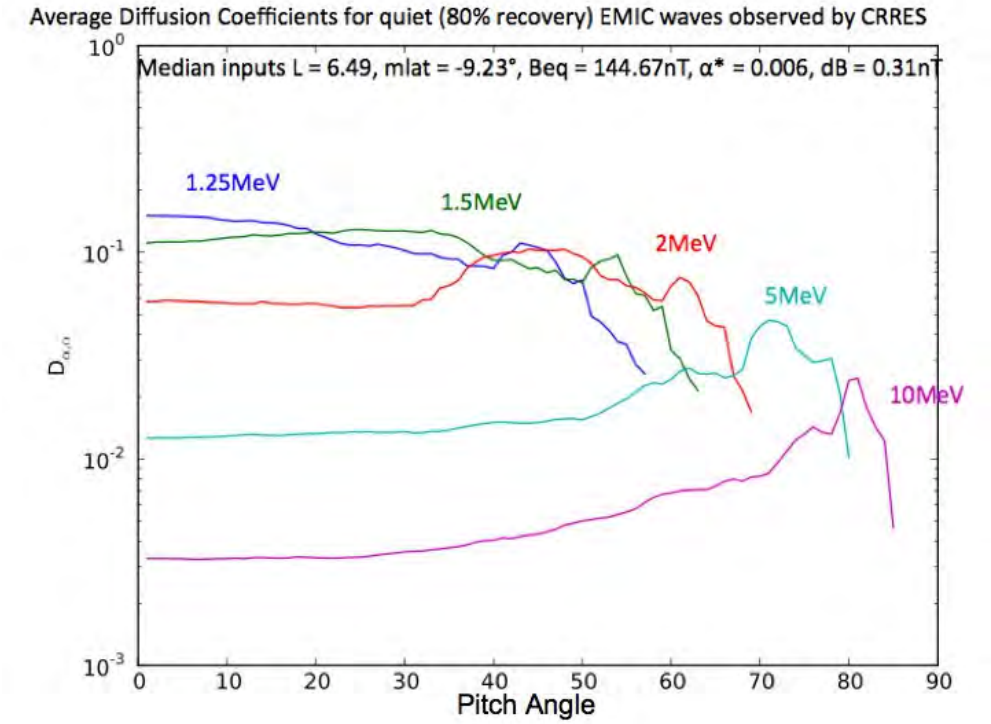

FIGURE 7.7: The median diffusion coefficients found from Summers [2005] for EMIC waves observed by CRRES during non-storm intervals resonating with radiation belt electrons of energies 1.25 MeV (blue), 1.5 MeV (green), 2 MeV (red), 5 MeV (light blue), and 10 MeV (purple).

near and in the loss cone.

One caveat of our results that should not be forgotten about is that we plotted the median $D_{\alpha\alpha}$ as a function of pitch angle for the various groups of EMIC waves. Not all EMIC waves will show the same characteristic curves. One future study with this data set is to determine the average range of pitch angles affected by any given EMIC wave. We have shown that EMIC waves measured using CRRES data and following the Summers [2005] approximation for pitch angle diffusion coefficients, can resonate with MeV electrons in the radiation belts depending on the pitch angle distributions.

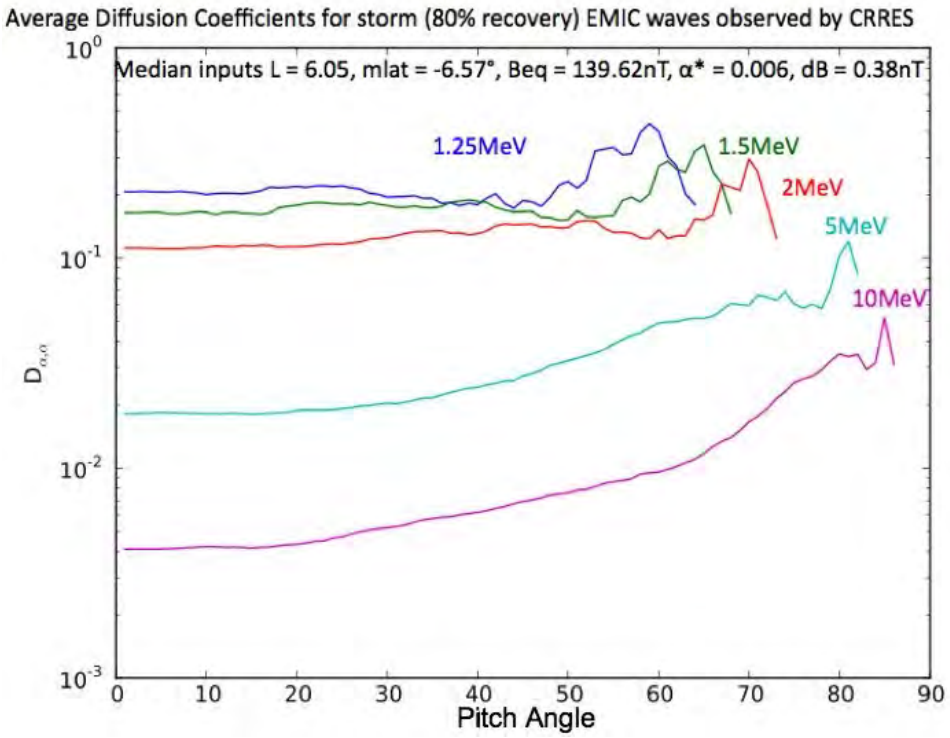

FIGURE 7.8: The median diffusion coefficients found from Summers [2005] for EMIC waves observed by CRRES during geomagnetic storms resonating with radiation belt electrons of energies 1.25 MeV (blue), 1.5 MeV (green), 2 MeV (red), 5 MeV (light blue), and 10 MeV (purple).

7.6.3 Pitch Angle Diffusion Coefficients by Phase of Storm

In the previous subsection, it has been shown that EMIC waves observed by CRRES can resonate with radiation belt electrons, and that storm time diffusion coefficients are on the average higher than those during the non-storm times. Here we consider how the diffusion coefficients change throughout the phases of a geomagnetic storm.

Figure 7.9 shows the median $D_{\alpha\alpha}$ for EMIC waves which occurred during the pre-onset phase of a geomagnetic storms across all pitch angles. The median parameter used to calculate the pitch angle diffusion coefficients are summarised in Table 7.2 were L = 5.9, magnetic latitudes = $-7.2°$, an equatorial magnetic field strength = 141.2 nT, $\alpha^* = 6.7 \times 10^{-3}$ and wave amplitude 0.3 nT. The peak $D_{\alpha\alpha}$ are found at pitch angles greater

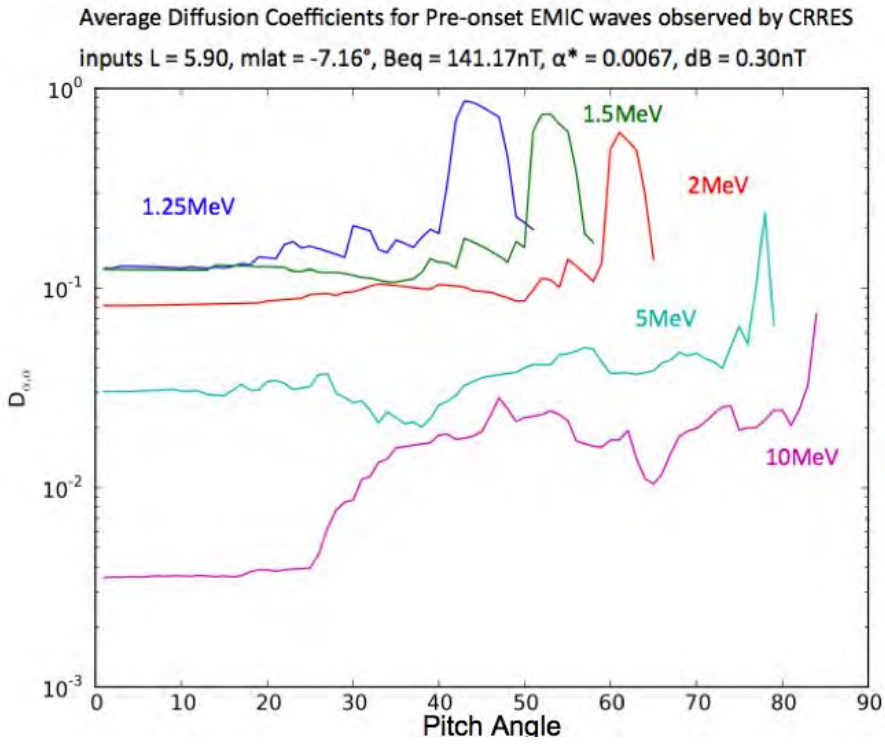

FIGURE 7.9: The median diffusion coefficients found from Summers [2005] for EMIC waves observed by CRRES during the pre-onset phase of a storm resonating with radiation belt electrons of energies 1.25 MeV (blue), 1.5 MeV (green), 2 MeV (red), 5 MeV (light blue), and 10 MeV (purple).

than 50° for electrons with energies of 1.5 MeV, and 2 MeV while the peak for 1.25 MeV is in the low to mid 40°. The diffusion coefficients for these energy ranges are close to 10^{-1} s^{-1} which is over an order of magnitude above the strong diffusion coefficient shown in Figure 7.5 , and thus the bounce average diffusion coefficients are also expected to stay above this level. The peaks in $D_{\alpha,\alpha}$ starting around 40° for the 1.25 MeV electrons are likely due to a few events. Looking at the individual power spectral densities for the events which produced non - zero $D_{\alpha,\alpha}$s at these pitch angles and for these energies as well as including a multi - ion estimate for the $D_{\alpha,\alpha}$ should help explain the shape of the median curve, but is beyond the scope of this thesis.

The highest occurrence rates for EMIC waves observed by CRRES occur during the

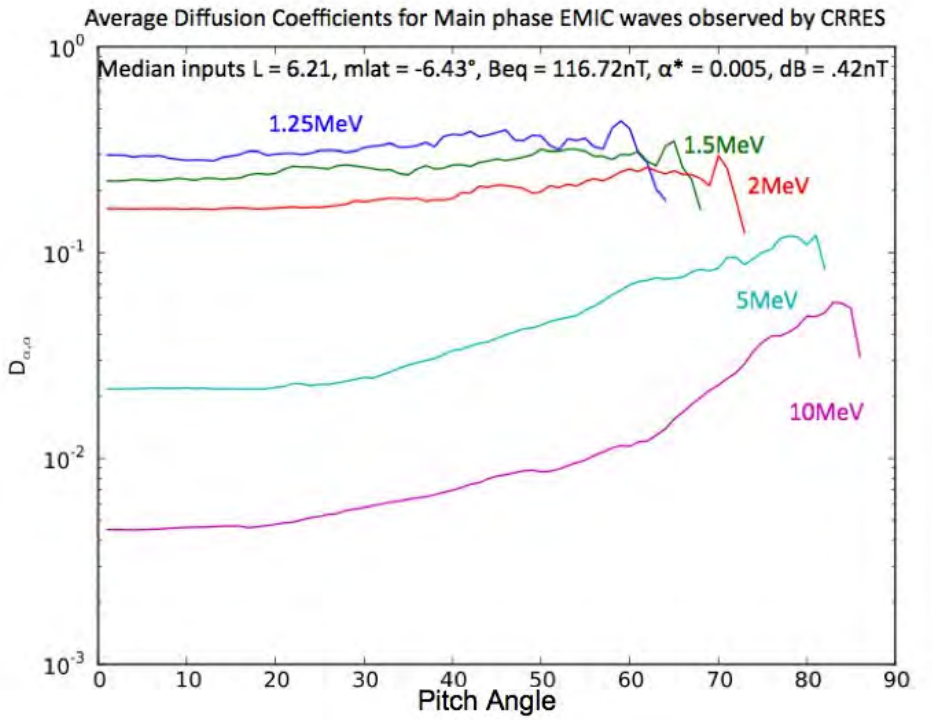

FIGURE 7.10: The median diffusion coefficients found from Summers [2005] for EMIC waves observed by CRRES during the main phase of a storm resonating with radiation belt electrons of energies 1.25 MeV (blue), 1.5 MeV (green), 2 MeV (red), 5 MeV (light blue), and 10 MeV (purple).

main phase of a storm [Halford et al., 2010], and where the conditions, the encroaching ring current on the plasmasphere and plasmaspheric plumes, are thought to be optimal for EMIC waves to resonate with radiation belt electrons [Friedel et al., 2002, Jordanova et al., 2008, Millan and Thorne, 2007]. Figure 7.10 shows the median diffusion coefficient for EMIC waves which occurred during the main phase of geomagnetic storms. The median inputs for the main phase calculations in the Summers [2005] estimate, shown in Table 7.2 were L = 6.2, magnetic latitudes = $-6.43°$, an equatorial magnetic field strength of 116.7 nT, $\alpha^* = 5.0 \times 10^{-3}$ and wave amplitude of 0.42 nT. The electrons with energies of 1.25 MeV, 1.5 MeV, and 2 MeV all have diffusion coefficients greater than 10^{-1} s^{-1}, which is well above the strong diffusion limit, and the bounce averaged diffusion coefficients are

also expected to stay above this level. However it is important to remember that bounce averaging is dependent on the field model, as is the estimate of the strong diffusion limit, used for the path integration and thus this is just an estimate and bounce averaging is still needed to be included to confirm this hypothesis. The diffusion coefficients observed during the main phase of a storm are on average higher than those observed during the pre-onset phase, and thus are more efficient at resonating with the radiation belt electrons.

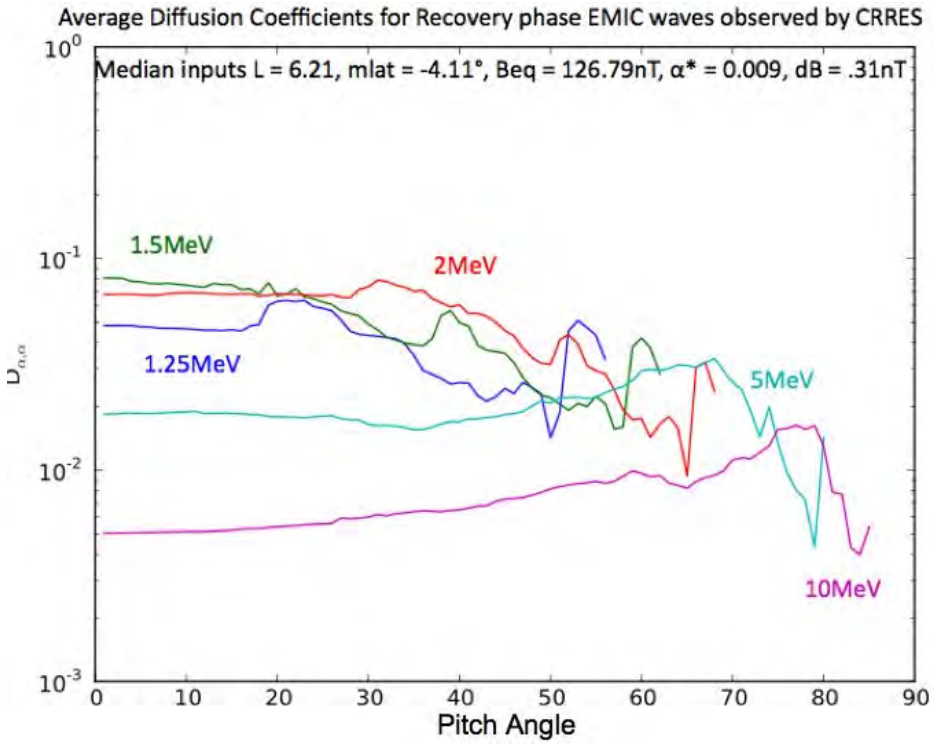

FIGURE 7.11: The median diffusion coefficients found from Summers [2005] for EMIC waves observed by CRRES during the recovery phase of a storm resonating with radiation belt electrons of energies 1.25 MeV (blue), 1.5 MeV (green), 2 MeV (red), 5 MeV (light blue), and 10 MeV (purple).

Figure 7.11 shows the median diffusion coefficient for EMIC waves which occurred during the recovery phase of a geomagnetic storms. The median inputs into the Summers [2005] model, and shown in Table 7.2 were L = 6.2, magnetic latitudes = $-4.11°$, an equatorial magnetic field strength of 126.8 nT, $\alpha^* = 9.0 \times 10^{-3}$ and wave amplitude of

0.31 nT. The electrons with energies of 1.25 MeV, 1.5 MeV, and 2 MeV all have diffusion coefficients less than 10^{-1} s^{-1} which is starting to approach the strong diffusion limit as shown in Figure 7.5. It is not known whether the bounce averaged diffusion coefficients would stay above this limit but assuming bounce averaging will lower $D_{\alpha\alpha}$ by an order of magnitude, is unlikely that during the recovery phase a strong diffusion regime would exist. The diffusion coefficients observed during the recovery phase of a storm are on average lower than those observed during the pre-onset or main phase and are thus thought to be less efficient at resonating with radiation belt electrons than EMIC waves occurring during the other phases of the storm.

7.7 Discussion

The dynamic behaviour of the radiation belts is of great interest for their potential space weather contributions. Although the majority of storms show a net increase in the radiation belts (53% with an increase and 28% no change) [Reeves et al., 2003], 19% of storms show a net decrease and most storms show a decrease in MeV electron flux during the pre-onset and main phase of geomagnetic storms [e.g. Blake et al., 1997, Horne et al., 2009, Reeves et al., 2003, Thorne, 2010, Yahnina et al., 2003]. EMIC waves have been identified as a potential loss mechanism for the radiation belts through theory and observation [e.g. Erlandson and Ukhorskiy, 2001, Jordanova et al., 2008, Meredith et al., 2003, Spasojevic and Fuselier, 2009, Spasojević et al., 2004, Summers and Thorne, 2003]. This chapter has shown that for electrons with energies between 1.25 and 10 MeV, there were EMIC wave events where the pitch angle diffusion extends into the loss cone (around $5-10^{\circ}$ depending on L-value and geomagnetic conditions). It is expected that at least for energies between 1.25 - 2 MeV, the bounce averaged diffusion coefficients will exceed the strong diffusion limit under most magnetospheric conditions. While in the strong diffusion regime, the amount of particle precipitation observed is then controlled by the size of the loss cone and the pitch-angle gradient of the particle distribution function. If instead we are in the weak regime, then the rate of particle precipitation is controlled by pitch angle diffusion and the pitch angle distribution. The diffusion coefficients for electrons at

energies 1.25, 1.5, and 2 MeV, were found on average for the pre-onset and main phase of the storm to be likely to stay in the strong diffusion regime when bounce averaged. This suggests that the majority of particle precipitation due to EMIC waves would occur during the main phase of a storm. However, diffusion was still observed during the recovery phase and non-storm periods and thus there would still be particle precipitation, but within the weak diffusion regime. In order to better determine whether the diffusion coefficients are in the strong or weak diffusion regime, the bounce averaged diffusion coefficients will need to be determined along with the strong diffusion limit for a non-dipole field.

One interesting observation of this chapter is that although Summer's assumed location and plasma parameters of EMIC waves differs greatly from the mean and median locations and plasma parameters of EMIC waves observed by CRRES, we have similar results for the estimated $D_{\alpha,\alpha}$s. This is due in large part to the α^* term which although is not explicitly written, is embedded in the Equation 7.4 and is proportional in part to the ratio of the local magnetic field squared to the local cold plasma density. As one moves from the inner magnetosphere outward there is a decrease in the local magnetic field and density keeping this ratio similar, especially in regions where the density is enhanced.

On average the highest diffusion coefficients are found during the main phase of a storm, and the lowest during the recovery phase. In Chapter 5 we showed that the highest rates of occurrence for EMIC waves observed by CRRES occurred during the main phase and dropped off quickly during the recovery phase of a storm. In Chapter 6 we showed that on average plumes were observed during the main phase of a storm, and EMIC waves occurred in regions of enhanced densities. Many studies have stated that the radiation belts often see a decrease in MeV flux during the pre-onset and/or main phase of geomagnetic storms [e.g. Horne et al., 2009, Reeves et al., 2003]. The results from the last three chapters support this observation. If EMIC waves are an important mechanism in radiation belt loss, we see that the observed EMIC wave occurrence, the enhanced densities where EMIC waves are observed, and associated diffusion rates all suggest the main phase of a storm as being the interval when one would expect to observe the highest rates of radiation belt MeV electron losses due to EMIC waves.

8

Conclusions and Future Research

8.1 Conclusions

Throughout this thesis we have looked at EMIC waves and their relationship to the inner magnetosphere, particularly in the dusk sector due to the fact that CRRES did not fully precess around the Earth. Subsequently we have focused this study on the afternoon and dusk sector where it is thought that during geomagnetic storms, the primary generation mechanism of EMIC waves, is in part due to the overlap between the plasmaspheric and ring current particles. Thus we have been able to emphasise the relationship between EMIC waves during geomagnetic storms and the plasmasphere, plasmaspheric plumes, and the radiation belts.

As the thesis was completed a picture of a typical EMIC wave as observed by CRRES and how it might interact with the inner magnetosphere started to emerge. The typical

EMIC wave occurred in the middle magnetosphere at L = 6.0, MLT = 15.0, MLat = -6.4, and in a background plasma density of 60.6 cm^{-3}. The average location of EMIC waves in the dusk sector occurring in the southern hemisphere is due to the orbital tilt of CRRES. It was also observed that the peaks in EMIC wave occurrence agreed best with the peaks in α^* which is related to the growth of EMIC waves and proportional to the Alfven velocity. However, this does not differentiate between EMIC waves occurring under different geomagnetic conditions.

When the waves were divided into two groups, those occurring during non-storm and storm conditions, differences started to emerge although there were still many similarities. With 53% of EMIC waves occurring during geomagnetic storms compared to 46.1% during non-storm conditions, EMIC waves were 1.6 times more likely to occur during a geomagnetic storm. On average, non-storm EMIC waves were found to occur at L = 6.2, MLT = 15.2 hr, and in densities of 63.1 cm^{-3}. Outside of storm-times, the EMIC wave amplitudes were lower while occurring at higher L-values (Table B.5). Storm time EMIC waves were observed at similar MLT (MLT = 15.0 hr), but at slightly lower L-values (L = 5.9) and densities (51.4 cm^{-3}). The observed wave amplitudes were higher at 0.38 nT, although the median $\mathbf{B}_{eq}$ was less at 139.62 nT and the α^* did not change (Table B.5).

During a storm, the assumed conditions under which the EMIC wave is generated are different and the waves have slightly different properties, which eventually result in important differences with how they are able to interact with the radiation belt electrons. Thus for determining EMIC occurrence statistics, waves were subdivided into groups according to geomagnetic storm phase. Throughout the CRRES mission, 124 geomagnetic storms were identified with an average duration of 29.4 hours. Defining the end of the recovery phase as 80% recovery from the minimum Sym-H value, the average length of the main and recovery phases were 9.1 and 18.3 hours respectively. The main phase saw 275 EMIC waves compared to 189 EMIC waves during the recovery phase. EMIC waves were found to be statistically more likely to occur during the main phase of a geomagnetic storm. As the main phase was, on average, half as long as the recovery phase, and each storm was of a varying length, an occurrence rate of EMIC waves was considered instead of simple counts. The peak occurrence rate of 0.32 EMIC waves per hour occurred in the

50-60% bin of the main phase. During the 80% recovery phase, a peak occurrence rate of 0.15 EMIC waves per hour was found, about half of the peak occurrence rate observed during the main phase. As plasma plumes are known to occur during the main phase of geomagnetic storms, these results lend support to the idea that EMIC waves may potentially occur in plasma plumes and may be a loss mechanism for the relativistic electrons in the radiation belts.

Many ground based studies use a different definition for the recovery phase which is generally taken as between 4-10 days after the minimum Sym-H value [Bortnik et al., 2008, Engebretson et al., 2008a,b, Posch et al., 2010]. Using the definition of the recovery phase as + 6 days from the minimum Sym-H, an increase in the count of EMIC waves was observed in the recovery phase, and the total counts when compared to those in the main phase, were very large agreeing well with the results from ground based studies. The occurrence rates, however, were much lower than those found in the main phase. There was an increase in the occurrence rate observed towards the end of the 6 day recovery. This is consistent with expected plasmaspheric recovery in the outer magnetosphere which has an average occurrence rate of 0.15 EMIC waves per hour, again about half of the peak occurrence rate observed during the main phase. The result of an increase of EMIC waves in the recovery phase when compared with the main phase agrees well with the ground studies, however the maximum occurrence rate still occurred in the main phase.

The field of space physics uses many models to better understand the physics of the inner magnetosphere and it is very important that we are able to set reasonable boundary conditions and have a feel for the range of input parameters and outcomes. Knowing what the typical characteristics of space phenomena, specifically in this case EMIC waves, will help guide models and our understanding of the role of EMIC waves in the inner magnetosphere. When looking at the values for a 'typical EMIC wave' during the phases of a geomagnetic storm (as defined by the 80% recovery), it was found that EMIC waves occurring during the pre-onset phase were on average found at slightly lower L-values and had background densities which were the highest observed under any geomagnetic condition (Table B.5). This is indicative that on average the plasmasphere was potentially

well filled before the onset of the storms where EMIC waves were observed in the pre-onset phase. The EMIC wave amplitudes were the lowest of the three phases. The main phase EMIC waves were found on average at the highest L-values for the three phases. The EMIC wave amplitudes observed during the main phase were the largest of any observed and the median α^* was the weakest (Table B.5). This is a very interesting result as Summers and Thorne [2003] report that as α^* decreases, the minimum resonant energy of radiation belt electrons also decreases, possibly into the region of geophysically interesting energies. The recovery phase waves were found on average to have the highest α^*, but otherwise average characteristics (Table B.5). As shown here, the typical values depend greatly on the magnetospheric conditions and can have large effects on how and if the waves will interact with their environment.

This picture of the 'typical EMIC wave' occurring in a region of MLT = 15 hr, L = 6, at higher densities ($>$ 10 cm^{-3}) and during the main phase of geomagnetic storms suggests the idea that they may also be occurring in plasmaspheric plumes. When comparing the average density observed during EMIC waves to the average density observed when EMIC waves were not present by L-value and geomagnetic condition, it was found that EMIC waves were found in regions of enhanced densities. For most geomagnetic conditions at L $>$ 5 more than 75% of the EMIC waves occurred in regions with densities larger than those found during quiet geomagnetic conditions. This implies that the majority of EMIC waves are occurring in either an extended plasmasphere, in a detached plasma region, or in a plasmaspheric plume. As it is difficult to identify individual plume events using only the CRRES data, a statistical method was used to identify where and when plumes were likely to be occurring. Enhanced densities and possible plume like features were observed at L $>$ 5 during the pre-onset and main phases of geomagnetic storms. The occurrence location of EMIC waves correlates with these areas of enhanced density and plume-like signatures. The plasmasphere also appeared to have fully recovered during the extended recovery phase. Although these results do not conclusively state that EMIC waves occur inside plasmaspheric plumes, it is very suggestive of this result showing that statistically EMIC waves are found in regions of enhanced density.

It has been suggested that EMIC waves would preferentially occur along negative

plasma density gradients, for example along the plasmapause or the outside edge of a plasmaspheric plume [Horne and Thorne, 1993, Morley et al., 2009, Rauch and Roux, 1982, Roux et al., 1982, Thorne and Horne, 1994]. More recently this has been extended to include the possibility of EMIC waves occurring along local negative density gradients inside plasmaspheric plumes [Chen et al., 2009]. About half of the EMIC wave events were found to be fit to a straight line with 50% of their variance described, and no matter the quality of the fit, the sign of the slope was found to be randomly distributed. Thus we can conclude that for the 50% of events where a straight line fit can be used to describe the data, no correlation between a negative density gradient and EMIC waves was found. For the other 50% of EMIC waves, the density data is likely to be non-linear and not associated with a strong negative density gradient across the entire EMIC wave event. A superposed epoch which is not dependent on the linearity of the data was also performed for the EMIC waves occurring in the dusk sector as well as for those in the dusk sector during the main phase of a geomagnetic storm. For both subsets no correlation was found for the occurrence of EMIC waves and a negative density gradient. Consequently we concluded that the EMIC waves observed by CRRES did not occur preferentially along negative density gradients.

Case studies were then examined to take a closer look at the dynamics observed in individual events. Three orbits, 927, 931, and 961, containing EMIC waves during storms were chosen. Orbit 961 showed a set of EMIC waves which correlated with an increase in the local magnetic field. Towards the end of the interval there was an increase in the cold plasma density. When the density increased the waves in the hydrogen band increased in frequency and the EMIC wave was also observed in the helium band. Although the density remained high, the EMIC waves cut out when the local magnetic field decreased. The EMIC's in orbit 931 occurred during a period of elevated density but did not line up with any observed density gradients. However the EMIC waves did appear to start with and be modulated by Pc 5 waves, which are able to perturb the local density although this was not obvious within our data. Orbit 927 showed EMIC waves occurring during a region of enhanced densities which also exhibited periods of relatively large density gradients. The EMIC waves again did not line up with the density gradients, but did appear to be

modulated by the Pc 5 waves and ceased as the first large Pc 5 wave packet ended. Later in the same orbit there was another plasma plume like signature, but no EMIC waves were observed. Between the first and second plumes, the Sym-H index recovered 20 nT, thus potentially the population of hot ions needed for EMIC wave generation may have been removed from the region. These results along with the statistical studies performed on the occurrence of EMIC waves and density gradients indicate that EMIC waves do not preferentially occur along negative density gradients.

With the description of what the 'typical inner magnetospheric EMIC wave' looks like under different geomagnetic conditions, and local cold plasma conditions, we can consider how these waves interact with the radiation belts. CRRES data were used as input to estimate the pitch angle diffusion coefficient outlined in Summers [2005]. EMIC waves were found to be able to create pitch angle diffusion sufficient to effectively scatter radiation belt electrons between energies of 1.25 - 5.0 MeV into the loss cone. The largest diffusion coefficients, well above the strong diffusion limit for these energies, are found during the main phase of the storm when the highest rates of EMIC wave occurrence and the formation of plasmaspheric plumes are also found. These results when considered together, suggests EMIC wave generation occurs during the main phase of a storm where there is an overlap of enhanced cold plasma from the formation of plasma plumes and injection of hot ring current ions. Once the EMIC waves are generated, they are able to resonate with electrons in the radiation belt, potentially precipitating them into the ionosphere thereby contributing to the loss of both ring current ions and radiation belt electrons during the main phase of geomagnetic storms.

8.2 Future Research

Although we have created a more complete picture of what a typical CRRES era inner magnetospheric EMIC wave looks like, there is still much to learn.

1) Throughout this thesis we looked closely at the approximately 54 % of EMIC waves observed by CRRES during geomagnetic storms. However, 46% of the EMIC waves were observed during non- storm times. Unfortunately during the CRRES mission there were

no consistent solar wind data with high resolution (1 minute or less) to look more closely at what might be driving these events. Qin et al. [2007] have developed a list of hourly solar wind values with a quality control measure which includes the time period of the CRRES mission. As a first look, we can use this data to try to correlate SW dynamic pressure (when the data is at least better than average) to our EMIC wave events.

2) High speed streams are one such SW event type which may be related to EMIC waves. High speed streams have been found to be correlated with recurrent substorm events in the inner magnetosphere [e.g. Lyons et al., 2009] and can produce weaker geomagnetic storms than studied in this thesis. Other studies have found EMIC or Pc 1 waves to be correlated with these high speed streams and recurrent substorm events. Ishida et al. [1987] showed that plasma characteristics of Pc 1 waves at geosynchronous orbit may potentially be affected by the particle injections of substorms. Bossen et al. [1976] found that for most of the Pc 1 events identified using the ATS satellite occurred within 1.75 hr of a substorm expansion onset. More recently Posch et al. [2010] found many Pc 1 waves on the ground occurring within the first 2 days of high speed stream events. Mavromichalaki and Vassilaki [1998] have compiled a list of fast plasma streams which include the years 1990 - 1991. With this list we should be able to compare EMIC wave occurrences with fast plasma streams and compare our results to those with ground based studies.

3) As Cluster and GOES have both been operating and observing EMIC waves since the early 2000s, they are also prime missions to look at the relationship between EMIC waves and substorms. Frey and Mende [2006] have complied a list of substorms from 2000 - 2005. This would allow for a statistical look at the relationship between EMIC waves and substorm particle injections. Including this with an event or statistical study of the high speed streams could help identify any link between substorms and their particle injections or compressions from the high speed streams which may also drive these reoccurring substorm events.

4) Within this thesis we have not focused our results on EMIC waves occurring during non-storm or quiet conditions. This is in part due to CRRES observing the end of the solar maximum when there were many geomagnetic storms. Conversely, Cluster has been active throughout the most recent and very quiet solar minimum and has observed

many EMIC wave events which are not associated with geomagnetic storms or strong compression events [Zhang 2011 private communication]. However statistics have not yet been performed to determine whether a storm bias is still present. The Cluster results throughout this very quiet minimum when compared to our CRRES results should provide a unique opportunity to determine whether a bias in EMIC occurrence to storm time is observed throughout a solar cycle and what occurrence rates for EMIC waves are expected under extended quiet magnetospheric conditions.

5) Currently Cluster is able to look at EMIC waves out towards L = 14. Zhang and others [private communication 2011] have found many EMIC waves at these outer L-values during very quiet conditions when compressions in the SW have not been observed. They have concluded that many of these waves are also due to a potential temperature anisotropy from the overlaps of an extended plume and ring current interaction. Creating occurrence statistics using the Cluster data and including them with our results would create a larger map of where and when EMIC waves are found within the magnetosphere. As many ground based studies look at higher L-value regions, this may potentially help solve the disagreement between satellite and ground based studies.

6) Throughout this thesis we have compared CRRES and other satellite results to those found on the ground. It is very clear that especially during the main phase of geomagnetic storms the two groups see very different results. This includes satellite studies which find the majority of EMIC waves occurring during the main phase [e.g. Halford et al., 2010] to ground studies which reported not observing a single EMIC wave event during the main phase of many geomagnetic storms [e.g. Engebretson et al., 2008a]. Ground based studies have found that the EMIC waves observed when traced back into the magnetosphere do not appear to be generated within plasmaspheric plumes or even in regions of enhanced densities [Posch et al., 2010]. Our results on the other hand find that EMIC waves observed by CRRES consistently are found in these regions of enhanced densities and are very probably in regions of plasmaspheric plumes. The missing piece for this picture is the ionosphere. Once an EMIC waves enters the ionosphere, it is able to propagate parallel to the surface of the Earth making it difficult to determine the generation region. One method to better understand the extent of the ionospheres effect on the propagation

of EMIC waves would be to have clear statistical maps of where and when EMIC waves are observed both in space and on the ground. It is vital that these statistics be performed with the same method and definitions as can be seen by our study on the occurrence of EMIC wave during the recovery phase using two different definitions (80% vs + 6 day) and methods (counts vs rates). Determining how these maps differ is one technique which can provide a better understanding of the role the ionosphere can play in the propagation of EMIC waves from the equatorial region of the magnetosphere where they are generated to where they are observed on the ground.

7) Within our results of EMIC waves occurring during storms we have not yet identified a relationship between EMIC waves and the strength of the geomagnetic storm. By comparing the results from moderate (-40 nT $>$ Sym - H $>$ -80 nT), strong (-80 nT $>$ Sym-H $>$ -150nT) and great storms (-150 nT $>$ Sym-H), a picture can be formed on how important the strength of the ring current and thus potentially the hot ion component is to EMIC waves.

8) The CDA web can provide 1 minute resolution hot ion density data for the majority of the CRRES mission. Using the hot electron density data we should be able to better compare the contributions of the cold plasma with the hot ion data. For example during orbit 927 two regions of enhanced plasma density were observed but EMIC waves were only seen in the first region. When looking at the hot ion data quick look plots on the CDA website, it is clear that there is a decrease in the hot plasma density in the second region of cold enhanced density when compared to the first.

9) As previously stated the highest rates of EMIC wave occurrences and pitch angle diffusion coefficients are found during the main phase of geomagnetic storms as well as when the plasmasphere appear to show plasmaspheric plume signatures. When all of these relations are considered together it appears that EMIC waves may potentially be an important contributor to radiation belt dynamics during geomagnetic storms. However, more complete statistics are needed to describe how many of the observed EMIC waves were able to resonate with radiation belt electrons. Meredith et al. [2003] showed that only a small fraction of EMIC waves were resonant with 2 MeV or less electrons, but that the majority of these events occurred in the dusk sector. Expanding on these results

with respect to location and magnetospheric conditions will help identify when and where EMIC waves will be able to interact with geophysically interesting energies of electrons within the radiation belts and better define their role as a loss mechanism. These results will also be useful in modelling the processes in the inner magnetosphere and radiation belts during geomagnetic storms.

10) As one last future research point, it would be remiss to not mention the new mission set to launch in August 2012, the two Radiation Belt Storms Probe (RBSP) satellites. RBSP will be able to test the results from this thesis and add to our understanding of how EMIC waves are generated, propagate, and interact with radiation belt electrons. As with CRRES, RBSP will launch during the peak of the solar cycle when many geomagnetic storms should be occurring, allowing for advantageous comparisons with the CRRES results. One major difference between CRRES and RBSP is that the RBSP mission consists of two satellites allowing for multipoint measurements from the same instruments. This will provide a better definition of the temporal and spatial scale of features observed by the satellites. Another important difference is that the ACE satellite will hopefully still be operational providing SW data throughout the mission. As with CRRES the two satellites will have near equatorial elliptical orbits with apogees inside of geosynchronous [Reeves, 2007]. During the first year RBSP will be traveling around the night side of the magnetosphere leading to direct comparisons with the CRRES mission, and the ability to fill in the gaps especially as it moves into the noon sector.

8.3 The Final Word

CRRES has greatly increased the understanding of EMIC waves and their role within the near-Earth Space environment. This thesis has shown where and when EMIC waves in the inner magnetosphere are expected to occur, how plumes, but more importantly enhanced cold plasma densities play a large role in EMIC wave occurrences, and how EMIC waves are able to resonate with radiation belt electrons helping to contribute to the main phase loss in the radiation belts.

A

Coordinate systems

A.1 Earth Centered Inertial Coordinates (ECI)

From the center of mass of the Earth, The z axis is in the direction of the rotational axis of the Earth (North is positive), the z axis is in the direction of the vernal equinox (the point in space where the Earth's equatorial plane and the ecliptic plane intersect), and the y axis completes the right hand orthogonal system.

A.2 Geographic Coordinates (GEO)

From the center of the Earth, the x axis is in the equatorial plane toward the Greenwich meridian, the z axis is in the direction of rotation and the y axis completes the coordinate

system.

A.3 Geomagnetic Coordinates (MAG)

The z axis is parallel to the dipole axis, the x axis is in the dipole equatorial plane pointing towards the Sun, and the y axis is in the dipole equatorial plane perpendicular to x.

A.4 Geocentric Solar Ecliptic (GSE)

From the Earth the x axis is towards the sun, the z axis is perpendicular to the ecliptic plane, and the y axis is in the dipole equatorial plane and perpendicular to the the x axis. This is a right hand cartesian coordinate system.

A.5 Geocentric Solar Magnetic (GSM)

The x axis is toward the Sun, the x- z plan contains the dipole axis of the Earth and the z-axis is along it. The y axis is in the magnetic equator perpendicular to z. This is a right hand cartesian coordinate system.

A.6 Magnetic Geocentric Solar Ecliptic (MGSE)

From the Earth the x axis is in the positive spin axis direction (9° from the sun), the y-axis interests the ecliptic and pin planes and points toward dusk, and the z-axis completes a right hand rectangular coordinate system. This is a right hand cartesian coordinate system [Brautigam et al., 2005, Loto'aniu et al., 2005].

B

Look up Tables

TABLE B.1: The gyro radii for electrons assuming a dipole field in kilometres.

Electrons				
L	10 eV	1 keV	100 keV	10 MeV
1.5	0.001	0.0012	0.12	3.9
2	0.003	0.028	0.29	9.2
3	0.009	0.095	0.99	31
4	0.022	0.22	2.4	74
5	0.044	0.44	4.6	140
6	0.076	0.76	7.9	250
7	0.12	1.2	13	400
8	0.18	1.8	19	590

TABLE B.2: The gyro radii for protons assuming a dipole field in kilometres.

Protons				
L	10 eV	1 keV	100 keV	10 MeV
1.5	0.51	0.51	5.1	51
2	0.12	1.2	12	120
3	0.40	4.0	40	410
4	0.96	9.6	96	960
5	1.9	19	190	1900
6	3.2	32	320	3200
7	5.1	51	510	5200
8	7.7	77	770	7700

TABLE B.3: Life times for H^+ with 45° pitch angles in hours assuming a dipole field.

R_E	3	3.5	4	4.5	5
n_H in cm^{-3}	800	470	300	210	150
3keV	2.2	3.7	5.7	8.2	11.5
10 keV	1.7	2.9	4.6	6.5	9.1
30 keV	3.2	5.4	8.5	12	16.8
50 keV	7.6	12.9	20	29	40
100 keV	40	69	110	153	215

TABLE B.4: The dipole magnetic field in nT for L-Shells 1 through 9 and magnetic latitudes from 0° to 30°, the magnetic latitudes and L-shells observed over the CRRES orbit.

L-Shell	B_{eq}	B_5	B_{10}	B_{15}	B_{20}	B_{25}	B_{30}
1	35000	36215.6	40064.9	47224.8	59084.0	78267.9	109750
2	4375	4526.95	5008.11	5903.10	7385.51	9783.49	13718.7
3	1296.3	1341.32	1483.89	1749.07	2188.3	2898.81	4064.8
4	546.875	565.869	626.0411	737.887	923.188	1222.94	1714.84
5	280	289.725	320.519	377.798	472.672	626.143	877.997
6	162.037	167.665	185.486	218.633	273.537	362.352	508.1
7	102.041	105.585	116.807	137.682	172.257	228.186	319.97
8	68.359	70.734	78.2518	92.2359	115.399	152.867	214.355
9	48.011	49.679	54.959	64.7802	81.0481	107.363	150.548

TABLE B.5: The complete look up table for the CRRES results from Chapters 4, 5, and 7.

	All	Non-Storm Time	Storm Time	Pre-Onset	Main	Recovery
Mean length,hrs			29.4	3	9.1	18.3
% of CRRES Mission Time	100	65.8	34.2	3.5	10.5	21.3
Number of EMIC waves	913	421	492	34	275	189
% of EMIC waves in CRRES Mission	100	46.1	53.9	3.8	30.1	20.7
Mean EMIC MLAT, deg	-6.4	-8.1	-5.2	-5.9	-5.8	-4.6
Mean EMIC MLT, MLT	15.0	15.2	15.0	15.1	15.1	14.8
Mean EMIC L-value,	6.0	6.2	5.9	5.7	6.0	5.8
Mean number density @EMIC, cm^{-3}	60.6	63.1	57.4	68.8	57.6	53.7
Median L-Shell	6.31	6.49	6.05	5.9	6.21	6.21
Median MLat deg	$-6.98°$	$-9.23°$	$-6.57°$	$-7.16°$	$-6.43°$	$-4.11°$
Median B_{eq} nT	111.65	144.57	139.62	141.17	116.72	126.79
Median α^*	6.0×10^{-3}	6.0×10^{-3}	6.0×10^{-3}	6.7×10^{-3}	5.0×10^{-3}	9.0×10^{-3}
Median db nT	0.35	0.31	0.38	0.30	0.42	0.31

C

Acknowledgement of Collaboration

The program used for calculating the individual equatorial pitch angle diffusion coefficients is a modified version of an original code written by Joseph Koller at LANL. The modifications included fixes for bugs in the original code, to run through and store the results for the individual EMIC wave events, plot the median outputs, and print out the median inputs. The work for Chapter 7 was driven in large part by discussions and collaborations with Dr. Morley, Dr. Koller, and Dr. Friedel prior to and during my visit to LANL Dec 2010 - Jan 2011.

D

Acknowledgement of Authorship

A portion of Chapter 4 and most of Chapter 5 are based on co-authored work published in the Journal of Geophysical Research December 2010 with my advisors Dr. Brian Fraser and Dr. Steven Morley. The majority of this work was performed and written by me, Alexa J. Halford.

References

Abel, B., and R. M. Thorne (1998), Electron scattering loss in Earth's inner magnetosphere 1. dominant physical processes, *Journal of Geophysical Research*, *103*, 2385, doi:10.1029/97JA02919.

Akasofu, S.-I. (1980), The solar wind -magnetosphere energy coupling and magnetospheric disturbances, *Planetary and Space Science*, *28*, 495–509.

Akasofu, S.-I. (1983), Solar-wind disturbances and the solar wind -magnetosphere energy coupling function, *Progress in Solar-Terrestrial Physics*, *34*, 173–183.

Akasofu, S.-I., and L. J. Lanzerotti (1975), The Earth's magnetosphere, *Physics Today*, *28*, 28.

Albert, J. M. (2003), Evaluation of quasi-linear diffusion coefficients for EMIC waves in a multispecies plasma, *Journal of Geophysical Research*, *108*(A6), 9, doi: 10.1029/2002JA009792.

Allen, J. A. V., C. E. McIlwain, and G. H. Ludwig (1959), Satellite observations of electrons artificially injected into the geomagnetic field, *Proceedings of the National Academy of Sciences*, pp. 1152–1171.

Allis, W. P. (1959), Waves in plasma, *Sherwood Conference Contr. Fusion*, p. 32.

Anderson, B. J. (1996), Recent observations of electromagnetic ion cyclotron waves in space, *Advances in Space Research*, *17 No 10*, 41–50.

Anderson, B. J., and S. Fuselier (1994), Response of thermal ions to electromagnetic ion cyclotron waves, *Journal of Geophysical Research*, *99 No A10*, 19,413–19,425.

Anderson, B. J., and D. C. Hamilton (1993), Electromagnetic ion cyclotron waves stimulated by modest magnetospheric compressions, *Journal of Geophysical Research*, *98*, 11,369, doi:10.1029/93JA00605.

Anderson, B. J., R. E. Erlandson, and L. J. Zanetti (1992a), A statistical study of Pc 1-2 magnetic pulsations in the equatorial magnetosphere 1. equatorial occurrence distributions, *Journal of Geophysical Research*, *97*, 3075–3088.

Anderson, R. R., D. A. Gurnett, and D. L. Odem (1992b), CRRES plasma wave experiement, *Journal of Spacecraft and Rockets*, *29*, 570–573.

Baker, D. N. (1996), Solar wind-magnetosphere drivers of space weather, *Journal of Atmospheric and Terrestrial Physics*, *58*, 1509–1526.

Baker, D. N. (1998), What is space weather?, *Advances in Space Research*, *22*, 7–16.

Baker, D. N., T. I. Pulkkinen, V. Angelopoulos, W. Baumjohann, and R. L. McPherron (1996), Neutral line model of substorms: Past results and present view, *Journal of Geophysics Research*, *101 No A6*, 12,975 –13,010.

Baker, D. N., T. I. Pulkkinen, J. Buchner, and A. J. Klimas (1999), Substorms: A global instability of the magnetosphere - ionosphere system, *Journal of Geophysics Research*, *104 No A7*, 14,601 –14,611.

Baker, D. N., N. E. Turner, and T. Pulkkinen (2001), Energy transport and dissipation in the magnetosphere during geomagnetic storms, *Journal of Atmospheric and Terrestrial Physics*, *63*, 421–429.

Baker, D. N., S. G. Kanekal, X. Li, S. P. Monk, J. Goldstein, and L. Burch (2004), An extreme distortion of the Van Allen belt arising from the Halloween solar storm in 2003, *Nature*, *432*, 878–881.

Balogh, A., V. Bothmer, N. U. Crooker, and R. Forsyth (1999), The solar origin of corotating interaction regions and their formation in the inner heliosphere, *Space Science Reviews*, *89*, 141–178.

Barkhausen, H. (1913), Telephonie ohne draht, *Die Naturwissenschaften*, *1*, 359.

Barr, R., D. Jones, and C. Rodger (2000), ELF and VLF radio waves, *Journal of Atmospheric and Terrestrial Physics*, *62*, 1689–1718.

Bartels, J., N. H. Heck, and H. F. Johnston (1939), The three-hour index measuring geomagnetic activity, *Journal of Geophysical Research*, *44*, 411, doi: 10.1029/TE044i004p00411.

Baumjohan, W., and R. A. Treumann (1997), *Basic Space Plasma Physics*, Imperial College Press, London.

Bittencourt, J. A. (2004), *Plasma Physics*, Springer Science + Business Media LLC, New York, New York.

Blake, J. B., D. N. Baker, N. Turner, K. W. Ogilvie, and R. P. Lepping (1997), Correlation of changes in the outer-zone relativistic-electron population with upstream solar wind and magnetic field measurements, *Geophysical Research Letters*, *24*, 927, doi: 10.1029/97GL00859.

Blum, L. W., E. A. Macdonald, S. P. Gary, M. F. Thomsen, and H. E. Spence (2009), Ion observations from geosynchronous orbit as a proxy for ion cyclotron wave growth during storm times, *Journal of Geophysical Research*, *114*(A10), A10,214.

Borovsky, J. E., and M. H. Denton (2006), Differences between CME-driven storms and CIR-driven storms, *Journal of Geophysical Research*, *111*, doi: 10.1029/2005JA011447.

Borovsky, J. E., and M. H. Denton (2008), A statistical look at plasmaspheric drainage plumes, *Journal of Geophysical Research*, *113*, 09,221, doi:10.1029/2007JA012994.

Borovsky, J. E., and M. H. Denton (2009), Relativistic-electron dropouts and recovery: A superposed epoch study of the magnetosphere and the solar wind, *Journal of Geophysical Research*, *114*, 02,201, doi:10.1029/2008JA013128.

Bortnik, J., J. W. Cutler, C. Dunson, T. E. Bleier, and R. L. McPherron (2008), Characteristics of low-latitude Pc1 pulsations during geomagnetic storms, *Journal of Geophysical Research*, *113*, 04,201, doi:10.1029/2007JA012867.

Bortnik, J., L. Chen, W. Li, R. M. Thorne, and R. B. Horne (2011), Modeling the evolution of chorus waves into plasmaspheric hiss, *Journal of Geophysical Research*, *116*, 08,221, doi:10.1029/2011JA016499.

Bossen, M., R. L. McPherron, and C. T. Russell (1976), A statistical study of Pc 1 magnetic pulsations at synchronous orbit, *Journal of Geophysical Research*, *81*, 6083–6091.

Brautigam, D. H., G. P. Ginet, J. M. Albert, J. R. Wygant, D. E. Rowland, A. Ling, and J. Bass (2005), CRRES electric field power spectra and radial diffusion coefficients, *Journal of Geophysical Research*, *110*, 02,214, doi:10.1029/2004JA010612.

Bräysy, T., K. Mursula, and G. Marklund (1998), Ion cyclotron waves during a great magnetic storm observed by Freja double-probe electric field instrument, *Journal of Geophysical Research*, *103*, 4145, doi:10.1029/97JA02820.

Burch, J. L., D. G. Mitchell, B. R. Sandel, P. C. Brandt, and M. Wüest (2001), Global dynamics of the plasmasphere and ring current during magnetic storms, *Geophysical Research Letters*, *28*, 1159, doi:10.1029/2000GL012413.

Burton, R., R. L. McPherron, and C. Russell (1975), An empirical relationship between interplanetary conditions and Dst, *Journal of Geophysical Research*, *80 No 31*, 4204–4214.

Carpenter, D. L. (1988), Remote sensing of the magnetospheric plasma by means of whistler mode signals, *Rev. Geophys*, *26*, 535, doi:10.1029/RG026i003p00535.

Carpenter, D. L., and R. L. Smith (1964), Whistler measurements of electron density in the magnetosphere, *Review of Geophysics and Space Physics*, *2*, 415.

Chapman, S., and V. Ferraro (1940), The theory of the first phase of a geomagnetic storm, *Journal of Geophysical Research*, *45*, 245–268.

Chen, F. F. (1984), *Introduction to Plasma Physics and Controlled Fusion*, Plenum Press, New York, New York.

Chen, L., R. M. Thorne, and R. B. Horne (2009), Simulation of EMIC wave excitation in a model magnetosphere including structured high-density plumes, *Journal of Geophysical Research*, *114*(A7), 1–11, doi:10.1029/2009JA014204.

Chen, L., R. M. Thorne, V. K. Jordanova, C.-P. Wang, M. Gkioulidou, L. Lyons, and R. B. Horne (2010), Global simulation of EMIC wave excitation during the 21 April 2001 storm from coupled RCM-RAM-HOTRAY modeling, *Journal of Geophysical Research*, *115*, 07,209, doi:10.1029/2009JA015075.

Cliver, E., and H. Hudson (2002), CMEs: How do the puzzle pieces fit together?, *Journal of Atmospheric and Terrestrial Physics*, *64*, 231–252.

Cochran, W., J. Cooley, D. Favin, H. Helms, R. Kaenel, W. Lang, G. Maling, D. Nelson, C. Rader, and P. Welch (1967), What is the fast fourier transform?, *Audio and Electroacoustics, IEEE Transactions on*, *15*(2), 45 – 55.

COMET Program (2004), www.meted.ucar.edu/hao/aurora/.

Cooley, J., and J. Tukey (1965), An algorithm for the machine calculation of complex fourier series, *Mathematics of Computation*, *19*(90), 297–301.

Cooley, J., P. Lewis, and P. Welch (1967), Historical notes on the fast fourier transform, *Audio and Electroacoustics, IEEE Transactions on*, *15*(2), 76 – 79.

Cornwall, J. M. (1965), Cyclotron instabilities and electromagnetic emission in the ultra low frequency and very low frequency ranges, *Journal of Geophysical Research*, *70*, 61.

Cornwall, J. M., F. V. Coroniti, and R. M. Thorne (1970), Turbulent loss of ring current protons., *Journal of Geophysical Research*, *75*, 4699, doi:10.1029/JA075i025p04699.

Cowley, S. W. H. (2003), Solar-wind-magnetosphere-ionosphere interactions in the Earth's plasma environment, *Philosophical Transactions: Mathematical*, *361*, 113–126.

Criswell, D. R. (1969), Pc 1 micropulsation activity and magnetospheric amplification of 0.2- to 5.0-Hz hydromagnetic waves, *Journal of Geophysical Research*, *74*, 205, doi:10.1029/JA074i001p00205.

Daglis, I., R. Thorne, W. Baumjohann, and S. Orsini (1999), The terrestrial ring current: Origin, formation, and decay, *Reviews of Geophysics*, *37*, 407–438.

Daglis, I. A. (2006), Ring current dynamics, *Space Science Reviews*, *124*, 183, doi: 10.1007/s11214-006-9104-z.

Darrouzet, F., D. L. Gallagher, N. André, D. L. Carpenter, I. Dandouras, P. M. E. Décréau, J. Keyser, R. E. Denton, J. C. Foster, J. Goldstein, M. B. Moldwin, B. W. Reinisch, B. R. Sandel, and J. Tu (2008), Plasmaspheric density structures and dynamics: Properties observed by the cluster and IMAGE missions, *Space Science Reviews*, p. 52, doi:10.1007/s11214-008-9438-9.

Darrouzet, F., D. L. Gallagher, N. André, D. L. Carpenter, I. Dandouras, P. M. E. Décréau, J. de Keyser, R. E. Denton, J. C. Foster, J. Goldstein, M. B. Moldwin, B. W. Reinisch, B. R. Sandel, and J. Tu (2009), Plasmaspheric density structures and dynamics: Properties observed by the Cluster and IMAGE missions, *Space Science Reviews*, *145*, 55, doi:10.1007/s11214-008-9438-9.

Demekhov, A. G. (2007), Recent progress in understanding Pc 1 pearl formation, *Journal of Atmospheric and Solar-Terrestrial Physics*, *69*, 1609–1622.

Denton, R. E., M. K. Hudson, and I. Roth (1992), Loss-cone-driven ion cyclotron waves in the magnetosphere, *Journal of Geophysical Research*, *97*, 12,093–12,103, doi: 10.1029/92JA00954.

Dessler, A. J., and E. N. Parker (1959), Hydromagnetic theory of geomagnetic storms, *Journal of Geophysical Research*, *64*, 2239–2251.

Dungey, J. W. (1965), The length of the magnetospheric tail, *Journal of Geophysical Research*, *70*, 1753.

Engebretson, M. J., M. R. Lessard, J. Bortnik, J. C. Green, R. B. Horne, D. L. Detrick, A. T. Weatherwax, J. Manninen, N. J. Petit, J. L. Posch, and M. C. Rose (2008a), Pc1-Pc2 waves and energetic particle precipitation during and after magnetic storms: Superposed epoch analysis and case studies, *Journal of Geophysical Research*, *113*(A1), 22, doi:10.1029/2007JA012362.

Engebretson, M. J., J. L. Posch, A. M. Westerman, N. J. Otto, J. A. Slavin, G. Le, R. J. Strangeway, and M. R. Lessard (2008b), Temporal and spatial characteristics of Pc1 waves observed by ST5, *Journal of Geophysical Research*, *113*, 07,206, doi: 10.1029/2008JA013145.

Erlandson, R. E., and A. J. Ukhorskiy (2001), Observations of electromagnetic ion cyclotron waves during geomagnetic storms: Wave occurrence and pitch angle scattering, *Journal of Geophysical Research*, *106*, 3883, doi:10.1029/2000JA000083.

Fejer, J. A. (1965), Geometry of the magnetospheric tail and auroral current systems, *Journal of Geophysical Research*, *70*, 4972, doi:10.1029/JZ070i019p04972.

Fraser, B. J. (1968), Temporal variations in Pcl geomagnetic micropulsations, *Planetary and Space Science*, *16*, 111, doi:10.1016/0032-0633(68)90048-2.

Fraser, B. J., and T. S. Nguyen (2001), Is the plasmapause a preferred source region of electromagnetic cyclotron waves in the magnetosphere, *Journal of Atmospheric and Solar-Terrestrial Physics*, *63*, 1225–1247.

Fraser, B. J., W. J. Kemp, and D. J. Webster (1989), Ground-satellite study of a Pc 1 ion cyclotron wave event, *Journal of Geophysical Research*, *94*, 11,855, doi: 10.1029/JA094iA09p11855.

Fraser, B. J., J. C. Samson, Y. D. Hu, R. L. McPherron, and C. T. Russell (1992), Electromagnetic ion cyclotron waves observed near the oxygen cyclotron frequency by ISEE 1 and 2, *Journal of Geophysical Research*, *97*, 3063, doi:10.1029/91JA02447.

Fraser, B. J., H. J. Singer, W. J. Hughes, J. R. Wygant, R. R. Anderson, and Y. D. Hu (1996), CRRES poynting vector observations of electromagnetic ion cyclotron waves near the plasmapause, *Journal of Geophysical Research*, *101*, 15,331–15,343, doi: 10.1029/95JA03480.

Fraser, B. J., H. J. Singer, M. Adrian, and D. Gallagher (2004), Relationship between plasma density structure and EMIC and ULF waves at synchronous orbit, *Inner Magnetosphere Interactions conference, Yosemite National Park*.

Fraser, B. J., J. L. Horwitz, J. A. Slavin, Z. C. Dent, and I. R. Mann (2005a), Heavy ion mass loading of the geomagnetic field near the plasmapause and ULF wave implications, *Geophysical Research Letters*, *32*, 04,102, doi:10.1029/2004GL021315.

Fraser, B. J., H. J. Singer, M. Adrian, and D. L. Gallagher (2005b), The relationship between plasma density structure and EMIC waves at geosynchronous orbit, in *Geophysical Monograph*, edited by J. L. Burch, M. Schulz, and H. Spence, 159, p. 55.

Fraser, B. J., T. M. Loto'aniu, and H. J. Singer (2006), Electromagnetic ion cyclotron waves in the magnetosphere, in *Magnetospheric ULF Waves: Synthesis and New Directions. Geophysical Monograph.*, vol. 169, edited by K. Takahashi, P. J. Chi, R. E. Denton, and R. L. Lysak, p. 195.

Fraser, B. J., R. S. Grew, S. K. Morley, J. C. Green, H. J. Singer, T. M. Loto'aniu, and M. F. Thomsen (2010), Storm time observations of electromagnetic ion cyclotron waves at geosynchronous orbit: GOES results, *Journal of Geophysical Research*, *115*, 05,208, doi:10.1029/2009JA014516.

Frey, H., and S. Mende (2006), Substorm onsets as observed by IMAGE-FUV, *Proc. 8th Int. Conf. Substorms*.

Friedel, R., and A. Korth (1997), Review of CRRES ring current observations, *Advances in Space Research*, *20*, 311–320.

Friedel, R. H. W., G. D. Reeves, and T. Obara (2002), Relativistic electron dynamics in the inner magnetosphere - a review, *Journal of Atmospheric and Solar-Terrestrial Physics*, *64*, 265–282.

Friedrich, E., G. Rostoker, M. Connors, and R. L. McPherron (1999), Influence of the substorm current wedge on the Dst index, *Journal of Geophysical Research*, *104*, 4567–4576.

Fujita, S., and T. Tamao (1988), Duct propagation of hydromagnetic waves in the upper ionosphere. i - electromagnetic field disturbances in high latitudes associated with localized incidence of a shear Alfven wave, *Journal of Geophysical Research*, *93*, 14,665, doi:10.1029/JA093iA12p14665.

Fukunishi, H., T. Toya, K. Koike, and M. Kuwashima (1981), Classification of hydromagnetic emissions based on frequency-time spectra, *Journal of Geophysical Research*, *86 No A11*, 9029–9039.

Gary, S. P., M. D. Montgomery, W. C. Feldman, and D. W. Forslund (1976), Proton temperature anisotropy instabilities in the solar wind, *Journal of Geophysical Research*, *81*, 1241, doi:10.1029/JA081i007p01241.

Gary, S. P., M. B. Moldwin, M. F. Thomsen, D. Winske, and D. J. Mccomas (1994), Hot proton anisotropies and cool proton temperatures in the outer magnetosphere, *Journal of Geophysical Research*, *99*, 23,603, doi:10.1029/94JA02069.

Gendrin, R. (1981), General relationships between wave amplification and particle diffusion in a magnetoplasma, *Reviews of Geophysics and Space Physics*, *19*, 171.

Gintzburg, M. (1966), Origin of radiation belts, *Physical Review Letters*, *16*, 327–329, http://link.aps.org/doi/10.1103/PhysRevLett.16.327.

Glangeaud, F., J.-L. Lacoume, H. Fargetton, R. Gendrin, S. Perraut, and V. A. Troitskaia (1980), Cross-spectral analysis of Pc 1 emissions recorded at different stations, *Journal of Geophysical Research*, *85*, 4115, doi:10.1029/JA085iA08p04115.

Goldstein, J. (2006), Plasmasphere response: Tutorial and review of recent imaging results, *Space Science Reviews*, *124*, 203–216.

Goldstein, J., B. R. Sandel, M. R. Hairston, and P. H. Reiff (2003), Control of plasmaspheric dynamics by both convection and sub-auroral polarization stream, *Geophysical Research Letters*, *30*, doi:10.1029/2003GL018390.

Gomberoff, L., and R. Neira (1983), Convective growth rate of ion cyclotron waves in a $H^+ - He^+$ and $H^+ - He^+ - O^+$ plasma, *Journal of Geophysical Research*, *88*, 2170, doi:10.1029/JA088iA03p02170.

Gonzalez, W., B. Tsurutani, and A. Gonzalez (1999), Interplanetary origin of geomagnetic storms, *Space Science Reviews*, http://www.springerlink.com/index/JU5875756487P774.pdf.

Gonzalez, W., B. Tsurutani, and A. C. de Gonzalez (2002), Geomagnetic storms contrasted during solar maximum and near solar minimum, *Advances in Space Research*, http://linkinghub.elsevier.com/retrieve/pii/S0273117702802526.

Gonzalez, W. D. (1990), A unified view of solar wind-magnetosphere coupling functions, *Planetary Space Science*, *38*, 627–632.

Gonzalez, W. D., J. Joselyn, Y. Kamide, H. Kroehl, G. Rostoker, B. Tsurutani, and V. Vasyliunas (1994), What is a geomagnetic storm?, *Journal of Geophysical Research*, *99*, 5771–5792.

Gopalswamy, N. (2008), Solar connections of geoeffective magnetic structures, *Journal of Atmospheric and Terrestrial Physics*, *70*, 2078–2100.

Gosling, J. T. (1996), Corotating and transient solar wind flows in three dimensions, *Annual Reviews in Astronomy and Astrophysics*, *34*, 35–73.

Gosling, J. T., J. R. Asbridge, S. J. Bame, W. C. Feldman, and R. D. ZWICKL (1980), Observations of large fluxes of he^+ in the solar wind following an interplanetary shock, *Journal of Geophysical Research*, *85*, 3431, doi:10.1029/JA085iA07p03431, a&AA ID. AAA028.074.028.

Gosling, J. T., D. J. McComas, J. L. Phillips, and S. J. Bame (1991), Geomagnetic activity associated with Earth passage of interplanetary shock disturbances and coronal mass ejections, *Journal of Geophysical Research*, *96*, 7831, doi:10.1029/91JA00316.

Green, J. C., and M. G. Kivelson (2001), A tale of two theories: How the adiabatic response and ULF waves affect relativistic electrons, *Journal of Geophysical Research*, *106*, 25,777, doi:10.1029/2001JA000054.

Green, J. C., T. G. Onsager, T. P. O'Brien, and D. N. Baker (2004), Testing loss mechanisms capable of rapidly depleting relativistic electron flux in the Earth's outer radiation belt, *Journal of Geophysical Research*, *109*, 12,211, doi:10.1029/2004JA010579.

Gruntman, M. (1994), Neutral solar wind properties: Advance warning of major geomagnetic storms, *Journal of Geophysical Research*, *99, A10*.

Guglielmi, A., J. Kangas, J. Kultima, and A. Potapov (2005), Solar wind dependence of the Pc1 wave activity, *Advances in Space Research*, *36*, 2413, doi: 10.1016/j.asr.2003.11.024, cOSPAR.

Gurnett, D. A., and U. S. Inan (1988), Plasma wave observations with the dynamics Explorer 1 spacecraft., *Reviews of Geophysics*, *26*, 285, doi:10.1029/RG026i002p00285.

Gurnett, D. A., S. D. Shawhan, N. M. Brice, and R. L. Smith (1965), Ion cyclotron whistlers, *Journal of Geophysical Research*, *70*, 1665–1688, doi: 10.1029/JZ070i007p01665.

Halford, A. J., D. N. Baker, S. K. Morley, and B. J. Fraser (2008), Energy transport, and dissipation in the magnetosphere during non-storm time substorms., *2008 Western Pacific Geophysics Meeting*.

Halford, A. J., B. J. Fraser, and S. K. Morley (2010), EMIC wave activity during geomagnetic storm and nonstorm periods: CRRES results, *Journal of Geophysical Research*, *115*, 12,248, doi:10.1029/2010JA015716.

Haurwitz, M. W., and G. W. Brier (1981), A critique of the superposed epoch analysis method: Its application to solar weather relations, *Monthly Weather Review*, *109*, 2074.

Heacock, R., and S. Akasofu (1973), Periodically structured Pc 1 micropulsations during the recovery phase of intense magnetic storms, *Journal of Geophysical Research*, *78*, 5524–5536.

Horne, R. B. (1989), Path-integrated growth of electrostatic waves - the generation of terrestrial myriametric radiation, *Journal of Geophysical Research (ISSN 0148-0227)*, *94*, 8895, doi:10.1029/JA094iA07p08895.

Horne, R. B., and R. M. Thorne (1993), On the preferred source location for the convective amplification of ion cyclotron waves, *Journal of Geophysical Research*, *98*, 9233.

Horne, R. B., N. P. Meredith, R. M. Thorne, D. Heynderickx, R. H. A. Iles, and R. R. Anderson (2003), Evolution of energetic electron pitch angle distributions during storm time electron acceleration to megaelectronvolt energies, *Journal of Geophysical Research (Space Physics)*, *108*, 1016, doi:10.1029/2001JA009165.

Horne, R. B., R. M. Thorne, Y. Y. Shprits, N. P. Meredith, S. A. Glauert, A. J. Smith, S. G. Kanekal, D. N. Baker, M. J. Engebretson, J. L. Posch, M. Spasojevic, U. S. Inan, J. S. Pickett, and P. M. E. Decreau (2005), Wave acceleration of electrons in the Van Allen radiation belts, *Nature*, *437*, 227, doi:10.1038/nature03939.

Horne, R. B., M. M. Lam, and J. C. Green (2009), Energetic electron precipitation from the outer radiation belt during geomagnetic storms, *Geophysical Research Letters*, *36*, 19,104, doi:10.1029/2009GL040236.

Horwitz, J. L., R. H. Comfort, and C. R. Chappell (1984), Thermal ion composition

measurements of the formation of the new outer plasmasphere and double plasmapause during storm recovery phase, *Geophysical Research Letters*, *11*, 701, doi: 10.1029/GL011i008p00701.

Hu, Y., and B. Fraser (1994), Electromagnetic ion cyclotron wave amplification and source regions in the magnetosphere, *Journal of Geophysical Research*, *99*, 263–272.

Hundhausen, A., S. Bame, J. Asbridge, and S. Sydoriak (1970), Solar wind proton properties: Vela 3 observations from July 1965 to June 1967, *Journal of Geophysical Research*, *75 No 25*, 4643–4657.

Ieda, A., S. Machida, T. Mukai, Y. Saito, T. Yamamoto, A. Nishida, T. Terasawa, and S. Kokubun (1998), Statistical analysis of the plasmoid evolution with Geotail observations, *Journal of Geophysical research*, *103*, 4453–4465.

Ishida, J., S. Kokubun, and R. L. McPherron (1987), Substorm effects on spectral structures of Pc 1 waves at synchronous orbit, *Journal of Geophysical research*, *92*, 143–158.

Jacobs, J. A., and T. Watanabe (1964), Micropulsation whistlers, *Journal of Atmospheric and Terrestrial Physics*, *26*, 825, doi:10.1016/0021-9169(64)90180-1.

Jacobs, J. A., and T. Watanabe (1967), Theoretical notes on whistlers and periodic emissions in the hydromagnetic regime, *Planetary Space Science*, *15*, 799–809.

Jacobs, J. A., Y. Kato, S. Matsushita, and V. A. Troitskaya (1964), Classification of geomagnetic micropulsations, *Journal of Geophysical Research*, *69*, 180, doi: 10.1029/JZ069i001p00180.

Johnson, F. (1960), The gross character of the geomagnetic field in the solar wind, *Journal of Geophysical Research*, *65 No 10*, 3049–3057.

Jordanova, V. K. (2007), Modeling geomagnetic storm dynamics: New results and challenges, *Journal of Atmospheric and Terrestrial Physics*, *69*, 56, doi: 10.1016/j.jastp.2006.06.016.

Jordanova, V. K., J. U. Kozyra, and A. F. Nagy (1996), Effects of heavy ions on the quasi-linear diffusion coefficients from resonant interactions with electromagnetic ion cyclotron waves, *Journal of Geophysical Research*, *101*, 19,771, doi:10.1029/96JA01641.

Jordanova, V. K., J. U. Kozyra, A. F. Nagy, and G. V. Khazanov (1997), Kinetic model of the ring current-atmosphere interactions, *Journal of Geophysical Research*, *102*, 14,279, doi:10.1029/96JA03699.

Jordanova, V. K., C. J. Farrugia, R. M. Thorne, G. V. Khazanov, G. D. Reeves, and M. F. Thomsen (2001), Modeling ring current proton precipitation by electromagnetic ion cyclotron waves during the May 14-16, 1997, storm, *Journal of Geophysical Research*, *106*, 7, doi:10.1029/2000JA002008.

Jordanova, V. K., J. Albert, and Y. Miyoshi (2008), Relativistic electron precipitation by EMIC waves from self-consistent global simulations, *Journal of Geophysical Research*, *113*, doi:10.1029/2008JA013239.

Kamide, Y., and S.-I. Akasofu (1983), Notes on the auroral electrojet indices., *Reviews of Geophysics and Space Physics*, *21*, 1647.

Kamide, Y., N. Yokoyama, W. Gonzalez, B. T. Tsurutani, I. A. Daglis, A. Brekke, and S. Masuda (1998), Two-step development of geomagnetic storms, *Journal of Geophysical Research*, *103*, 6917, doi:10.1029/97JA03337.

Kane, R. P. (2005), Sun Earth relation: Historical development and present status a brief review, *Advances in Space Research*, *35*, 866, doi:10.1016/j.asr.2005.03.142.

Kangas, J., A. Aikio, and J. V. Olson (1986), Multistation correlation of ULF pulsation spectra associated with sudden impulses, *Planetary and Space Science*, *34*, 543, doi:10.1016/0032-0633(86)90092-9.

Kangas, J., A. Guglielmi, and O. Pokhotelov (1998), Morphology and physics of short-period magnetic pulsations, *Space Science Reviews*, *83*, 435–512.

Kennel, C. F., and H. E. Petscheck (1966), Limit on stably trapped particle fluxes, *Journal of Geophysical Research*, *71*, 1.

Khabarova, O., and Y. Yermolaev (2008), Solar wind parameters' behavior before and after magnetic storms, *Journal of Atmospheric and Terrestrial Physics*, http://linkinghub.elsevier.com/retrieve/pii/S1364682607002945.

Khazanov, G. V., K. V. Gamayunov, D. L. Gallagher, and J. U. Kozyra (2006), Self-consistent model of magnetospheric ring current and propagating electromagnetic ion cyclotron waves: Waves in multi-ion magnetosphere, *Journal of Geophysical Research*, *111*(A10), doi:10.1029/2006JA011833.

Kivelson, M. G., and C. T. Russell (1995), *Introduction to Space Physics*, Cambridge University Press, Cambridge, United Kingdom.

Kotova, G. A. (2007), The Earth's plasmasphere: State of studies (a review), *Geomagnetism and Aeronomy*, *47*, 409, doi:10.1134/S0016793207040019.

Kozyra, J. U., T. E. Cravens, A. F. Nagy, E. G. Fontheim, and R. S. B. Ong (1984), Effects of energetic heavy ions on electromagnetic ion cyclotron wave generation in the plasmapause region, *Journal of Geophysical Research*, *89*, 2217–2233.

Kuwashima, M., T. Toya, M. Kawamura, T. Hirasawa, H. Fukunishi, and M. Ayukawa (1981), Comparative study of magnetic Pc1 pulsations between low latitudes and high latitudes, in *Memoirs of National Institute of Polar Research*, 88.

Lathuillere, C., M. Menvielle, J. Lilensten, and T. Amari (2002), From the Sun's atmosphere to the Earth's atmosphere: an overview of scientific models available for space weather developments, *Annales Geophysicae*, *1081–1104*, 20, http://www.ann-geophys.net/20/1081/2002/angeo-20-1081-2002.pdf.

Laughlin, L. K., N. E. Turner, and E. J. Mitchell (2008), Geoeffectiveness of CIR and CME events: Factors contributing to their differences, *Journal of the Southeastern Association for Research in Astronomy*, *2*, 19.

Lemaire, J. F. (1999), Hydrostatic equilibrium and convective stability in the plasmasphere, *Journal of Atmospheric and Terrestrial Physics*, *61*, 867, doi:10.1016/S1364-6826(99)00044-9.

Lemaire, J. F., and K. I. Gringauz (1998), *The Earth's Plasmasphere*, Cambridge University Press, Cambridge, United Kingdom.

Lewis, W. S. (2011), http://mms.space.swri.edu/index.html.

Li, W., Y. Y. Shprits, and R. M. Thorne (2007), Dynamic evolution of energetic outer zone electrons due to wave-particle interactions during storms, *Journal of Geophysical Research*, *112*, 10,220, doi:10.1029/2007JA012368.

Li, X. (2002), Radiation belts and substorm particle injections, in *Procceedings of the Sixth International Conference on Substorms*, edited by R. M. Winglee, p. 305, University of Washington, Seattle.

Li, X., and M. A. Temerin (2001), The electron radiation belt, *Space Science Reviews*, *95*, 569.

Li, X., D. N. Baker, M. Temerin, D. Larson, R. P. Lin, G. D. Reeves, M. Looper, S. G. Kanekal, and R. A. Mewaldt (1997), Are energetic electrons in the solar wind the source of the outer radiation belt?, *Geophysical Research Letters*, *24*, 923, doi:10.1029/97GL00543.

Liemohn, H. B. (1967), Cyclotron-resonance amplification of VLF and ULF whistlers, *Journal of Geophysical Research*, *72*, 39–55, doi:10.1029/JZ072i001p00039.

Lockwood, M. (2005), Solar outputs, their variations and their effects on Earth, *The Sun, Solar Analogs, and the Climate*, p. 109.

Loewe, C. A., and G. W. Prölss (1997), Classification and mean behavior of magnetic storms, *Journal of Geophysical Research*, *102*, 14,209, doi:10.1029/96JA04020.

Loto'aniu, T. M. (2003), The propagation of electromagnetic ion cyclotron wave energy in the magnetosphere, Ph.D. thesis, University of Newcastle, Australia.

Loto'aniu, T. M., B. J. Fraser, and C. L. Waters (2005), Propagation of electromagnetic ion cyclotron wave energy in the magnetosphere, *Journal of Geophysical Research*, *110*, 07,214, doi:10.1029/2004JA010816.

Loto'aniu, T. M., R. M. Thorne, B. J. Fraser, and D. Summers (2006), Estimating relativistic electron pitch angle scattering rates using properties of the electromagnetic ion cyclotron wave spectrum, *Journal of Geophysical Research*, *111*, 04,220, doi: 10.1029/2005JA011452.

Loto'aniu, T. M., B. J. Fraser, and C. L. Waters (2009), The modulation of electromagnetic ion cyclotron waves by Pc 5 ULF waves, *Annales Geophysicae*, *27*, 121, doi: 10.5194/angeo-27-121-2009.

Lui, A. T. Y. (2000), Tutorial on geomagnetic storms and substorms, *IEEE Transactions on Plasma Science*, *28 No. 6*, 1854–1866.

Lund, E., and J. LaBelle (1997), On the generation and propagation of auroral electromagnetic ion cyclotron waves, *Journal of Geophysical Research*, *102*, 17,241–17,253, http://www.agu.org/pubs/abs/nja/97JA01455/97JA01455.bak.

Lundstedt, H. (2006), The Sun, space weather and GIC effects in Sweden, *Advances in Space Research*, *37*, 1182, doi:10.1016/j.asr.2005.10.023.

Lyons, L., and R. M. Thorne (1972), Parasitic pitch angle diffusion of radiation belt particles by ion cyclotron waves, *Journal of Geophysical Research*, *77*, 5608.

Lyons, L. R., D.-Y. Lee, H.-J. Kim, J. A. Hwang, R. M. Thorne, R. B. Horne, and A. J. Smith (2009), Solar-wind-magnetosphere coupling, including relativistic electron energization, during high-speed streams, *Journal of Atmospheric and Solar-Terrestrial Physics*, *71*, 1059.

MacDonald, E. A., L. W. Blum, S. P. Gary, M. F. Thomsen, and M. H. Denton (2010), High-speed stream driven inferences of global wave distributions at geosynchronous orbit: relevance to radiation-belt dynamics, *Proceedings of the Royal Society A: Mathematical, Physical and Engineering Sciences*, pp. 1–12, doi:10.1098/rspa.2010.0076.

Manchester, R. N. (1968), Correlation of Pc 1 micropulsations at spaced stations, *Journal of Geophysical Research*, *73*, 3549, doi:10.1029/JA073i011p03549.

Matsushita, S. (1962), On geomagnetic sudden commencements, sudden impulses, and storm durations, *Journal of Geophysical Research*, *67*, 3753, doi: 10.1029/JZ067i010p03753.

Mauk, B., and R. L. McPherron (1980), An experimental test of the electromagnetic ion cyclotron instability within the Earth's magnetosphere, *Physics of Fluids*, *23*, 2111–2127.

Mauk, B. H. (1978), Alfven/ion cyclotron waves and the ion cyclotron instability with the Earth's magnetosphere, Ph.D. thesis, University of California, La Jolla, California.

Mavromichalaki, H., and A. Vassilaki (1998), Fast plasma streams recorded near the Earth during 1985-1996, *Solar Physics*, *183*, 181.

Mayaud, P. N. (1980), Derivation, meaning and use of geomagnetic indices, in *Geophysical Monograms*, 22, America Geophysical Union.

McCollough, J. P., S. R. Elkington, and D. N. Baker (2009), Modeling EMIC wave growth during the compression event of 29 June 2007, *Geophysical Research Letters.*, *36*(18), L18,108, doi:10.1029/2009GL039985.

McIlwain, C. (1961), Coordinates for mapping the distribution of magnetically trapped particles, *Journal of Geophysical research*, *66*, 3681.

McIlwain, C. (1966), Magnetic coordinates, *Space Science Reviews*, *5*, 585–598, http://www.springerlink.com/index/J22522X561K78374.pdf.

McPherron, R. L., and T.-S. Hsu (2002), A comparison of substorms occurring during magnetic storms with those occurring during quiet times, *Journal of Geophysical Research*, *107*, http://www.agu.org/pubs/crossref/2002/2001JA002008.shtml.

Meredith, N., R. Thorne, R. Horne, D. Summers, B. Fraser, and R. Anderson (2003), Statistical analysis of relativistic electron energies for cyclotron resonance

with EMIC waves observed on CRRES, *Journal of Geophysical Research*, *108*, http://earth.agu.org/pubs/crossref/2003/2002JA009700.shtml.

Meredith, N. P., R. B. Horne, and R. R. Anderson (2001), Substorm dependence of chorus amplitudes: Implications for the acceleration of electrons to relativistic energies, *Journal of Geophysical Research*, *106*, 13,165, doi:10.1029/2000JA900156.

Meredith, N. P., R. B. Horne, S. A. Glauert, D. N. Baker, S. G. Kanekal, and J. M. Albert (2009), Relativistic electron loss timescales in the slot region, *Journal of Geophysical Research*, *114*, 03,222, doi:10.1029/2008JA013889.

Millan, R., and R. M. Thorne (2007), Review of radiation belt relativistic electron losses, *Journal of Atmospheric and Terrestrial Physics*, *69*, 362–377.

Miyoshi, Y., K. Sakaguchi, K. Shiokawa, D. Evans, J. Albert, M. Connors, and V. Jordanova (2008), Precipitation of radiation belt electrons by EMIC waves, observed from ground and space, *Geophysical Research Letters*, *35*, 23,101, doi: 10.1029/2008GL035727.

Moldwin, M. B., J. Howard, J. Sanny, J. D. Bocchicchio, H. K. Rassoul, and R. R. Anderson (2004), Plasmaspheric plumes: CRRES observations of enhanced density beyond the plasmapause, *Journal of Geophysical Research*, *109*, 05,202, doi: 10.1029/2003JA010320.

Morley, S. K., S. T. Ables, M. D. Sciffer, and B. J. Fraser (2009), Multipoint observations of Pc1-2 waves in the afternoon sector, *Journal of Geophysical Research*, *114*(A9), A09,205, doi:10.1029/2009JA014162, http://www.agu.org/pubs/crossref/2009/2009JA014162.shtml.

Morley, S. K., R. H. W. Friedel, E. L. Spanswick, G. D. Reeves, J. T. Steinberg, J. Koller, T. Cayton, and E. Noveroske (2010), Dropouts of the outer electron radiation belt in response to solar wind stream interfaces: global positioning system observations, *Proceedings of the Royal Society A: Mathematical, Physical and Engineering Sciences*, pp. 1–23, doi:10.1098/rspa.2010.0078.

Moussas, X., J. Polygiannakis, and P. Preka-Papadema (2005), Solar cycles: A tutorial, *Advances in Space Research*, *35*, 725–738.

Neudegg, D. (1997), Polar magnetosphere - ionosphere coupling:ULF wave and particle signatures, Ph.D. thesis, University of Newcastle, Australia.

Neugebauer, M., and C. Snyder (1966), Mariner 2 observations of the solar wind, 1, average properties, *Journal of Geophysical Research*, *71 No.19*, 4469.

Neugebauer, M., and C. Snyder (1967), Mariner 2 observations of the solar wind, 2, relation of plasma properties to the magnetic field, *Journal of Geophysical Research*, *71 No 19*, 4464–4484.

Nguyen, S. T., J. Perez, and J. F. Fennell (2007), A study of the electromagnetic proton cyclotron instability as a generation mechanism for EMIC waves in the Earth's magnetosphere using SCATHA data, *Journal of Geophysical research*, *112*, A12,203–A12,203.

Nishida, A. (1966), Formation of plasmapause, or magnetospheric plasma knee, by the combined action of magnetospheric convection and plasma escape from the tail, *Journal of Geophysical Research*, *71*, 5669.

NOAA (2007), http://www.swpc.noaa.gov/info/Kindex.html.

Obayashi, T. (1965), Hydromagnetic whistlers, *Journal of Geophysical Research*, *70*, 1069–1078.

Obayashi, T., and A. Nishida (1968), Large-scale electric field in the magnetosphere, *Space Science Reviews*, *8*, 3, doi:10.1007/BF00362569.

O'Brien, T., and R. L. McPherron (2000a), An empirical phase space analysis of ring current dynamics- solar wind control of injection and decay, *Journal of Geophysical Research*, *105 No A4*, 7707–7719.

O'Brien, T., and R. L. McPherron (2000b), Forecasting the ring current index Dst in real time, *Journal of Atmospheric and Terrestrial Physics*, *62*, 1295–1299, http://linkinghub.elsevier.com/retrieve/pii/S1364682600000729.

O'Brien, T. P., Y. Y. Shprits, and M. B. Moldwin (2008), Eigenmode analysis of pitch-angle diffusion of energetic electrons in the outer zone, *Journal of Atmospheric and Solar Terrestrial Physics*, *70*, 1738, doi:10.1016/j.jastp.2008.05.011, elsevier Ltd.

Ohtani, S., M. Nose, A. Lui, G. Rostoker, and H. J. Singer (2001), Storm-substorm relationship- contribution of the tail current to Dst, *Journal of Geophysical Research*, *106*, 21,199–21,209, http://www.agu.org/pubs/crossref/2001/2000JA000400.shtml.

Olson, J. V., and L. C. Lee (1983), Pc1 wave generation by sudden impulses, *Planetary and Space Science*, *31*, 295, doi:10.1016/0032-0633(83)90079-X.

Olson, W. P., and K. A. Pfitzer (1974), A quantitative model of the magnetospheric magnetic field., *Journal of Geophysical Research*, *79*, 3739, doi:10.1029/JA079i025p03739, a&AA ID. AAA012.084.261.

Onsager, T. G., G. Rostoker, H.-J. Kim, G. D. Reeves, T. Obara, H. J. Singer, and C. Smithtro (2002), Radiation belt electron flux dropouts: Local time, radial, and particle-energy dependence, *Journal of Geophysical Research (Space Physics)*, *107*, 1382, doi:10.1029/2001JA000187.

Papa, R. J., and W. P. Allis (1961), Waves in a plasma in a magnetic field, *Planetary and Space Science*, *6*, 100, doi:10.1016/0032-0633(61)90009-5.

Parker, E. N. (1957), Sweet's mechanism for merging magnetic fields in conducting fluids, *Journal of Geophysical Research*, *62*, 509, doi:10.1029/JZ062i004p00509.

Parker, E. N. (1965), Dynamical theory of the solar wind, *Space Science Reviews*, *4*, 66–708, http://www.springerlink.com/index/V13U053030077N74.pdf.

Parks, G. K. (1991), *Physics of Space Plasmas*, Addison-Wesley Publishing Company, Redwood City, CA 94065.

Petschek, H. E. (1964), Magnetic field annihilation, *The Physics of Solar Flares*, *50*, 425.

Pickett, J. S., B. Grison, Y. Omura, M. J. Engebretson, I. Dandouras, A. Masson, M. L. Adrian, O. Santolík, P. M. E. Décréau, N. Cornilleau-Wehrlin, and D. Constantinescu (2010), Cluster observations of EMIC triggered emissions in association with Pc1 waves near Earth's plasmapause, *Geophysical Research Letters*, *37*, 09,104, doi: 10.1029/2010GL042648.

Pierrard, V., J. Goldstein, N. André, V. Jordanova, G. A. Kotova, J. F. Lemaire, M. W. Liemohn, and H. Matsui (2009), Recent progress in physics-based models of the plasmasphere, *Space science Reviews*, *145*, 193 – 229, doi:10.1007/s11214-0089480-7.

Posch, J. L., M. J. Engebretson, M. T. Murphy, M. H. Denton, M. R. Lessard, and R. B. Horne (2010), Probing the relationship between electromagnetic ion cyclotron waves and plasmaspheric plumes near geosynchronous orbit, *Journal of Geophysical Research*, *115*, 11,205, doi:10.1029/2010JA015446.

Pulkkinen, T. (2007), Space weather: Terrestrial perspective, *Living Reviews in Solar Physics*, *4*, 1.

Qin, Z., R. E. Denton, N. A. Tsyganenko, and S. Wolf (2007), Solar wind parameters for magnetospheric magnetic field modeling, *Space Weather*, *5*, 11,003, doi: 10.1029/2006SW000296.

Rankin, D., and R. Kurtz (1970), Statistical study of micropulsation polarizations, *Journal of Geophysical Research*, *75*, 5444, doi:10.1029/JA075i028p05444.

Rauch, J. L., and A. Roux (1982), Ray tracing of ULF waves in a multicomponent magnetospheric plasma - consequences for the generation mechanism of ion cyclotron waves, *Journal of Geophysical Research*, *87*, 8191.

Reeves, G. D. (1998), Relativistic electrons and magnetic storms: 1992-1995, *Geophysical Research Letters*, *25*, 1817, doi:10.1029/98GL01398.

Reeves, G. D. (2007), Radiation belt storm probes: A new mission for space weather forecasting, *Space Weather*, *5*, 11,002, doi:10.1029/2007SW000341.

Reeves, G. D., K. L. McAdams, R. H. W. Friedel, and T. P. O'Brien (2003), Acceleration and loss of relativistic electrons during geomagnetic storms, *Geophysical Research Letters*, *30*, 36, doi:10.1029/2002GL016513.

Reynolds, M. A., D. J. Meléndez-Alvira, and G. Ganguli (2001), Equatorial coupling between the plasmasphere and the topside ionosphere, *Journal of Atmospheric and Terrestrial Physics*, *63*, 1267, doi:10.1016/S1364-6826(00)00229-7.

Rodger, C. J., T. Raita, M. A. Clilverd, A. Seppälä, S. Dietrich, N. R. Thomson, and T. Ulich (2008), Observations of relativistic electron precipitation from the radiation belts driven by EMIC waves, *Geophysical Research Letters*, *35*, 16,106, doi: 10.1029/2008GL034804.

Rodger, C. J., M. A. Clilverd, A. Seppälä, N. R. Thomson, R. J. Gamble, M. Parrot, J.-A. Sauvaud, and T. Ulich (2010a), Radiation belt electron precipitation due to geomagnetic storms: Significance to middle atmosphere ozone chemistry, *Journal of Geophysical Research*, *115*, 11,320, doi:10.1029/2010JA015599.

Rodger, C. J., B. R. Carson, S. A. Cummer, R. J. Gamble, M. A. Clilverd, J. C. Green, J.-A. Sauvaud, M. Parrot, and J.-J. Berthelier (2010b), Contrasting the efficiency of radiation belt losses caused by ducted and nonducted whistler-mode waves from ground-based transmitters, *Journal of Geophysical Research*, *115*, 12,208, doi: 10.1029/2010JA015880.

Roederer, J. G. (1970), Dynamics of geomagnetically trapped radiation, *Physics and Chemistry in Space*, *2*, 166.

Roux, A., S. Perraut, J. L. Rauch, C. de Villedary, G. Kremser, A. Korth, and D. T. Young (1982), Wave-particle interactions near omega he^+ observed on board geos 1 and 2. ii - generation of ion cyclotron waves and heating of he^+ ions, *Journal of Geophysical Research*, *87*, 8174.

Rozanov, E., L. Callis, M. Schlesinger, F. Yang, N. Andronova, and V. Zubov (2005), Atmospheric response to noy source due to energetic electron precipitation, *Geophysical Research Letters*, *32*, 14,811, doi:10.1029/2005GL023041.

Russell, C. T. (1999), http://www-ssc.igpp.ucla.edu/ssc/tutorial/magnetosphere.html.

Samson, J. C., and K. L. Yeung (1986), Some generalizations on the method of superimposed epoch analysis, *Planetary and Space Science*, *34*, 1133, doi:10.1016/0032-0633(86)90025-5.

Sandanger, M., F. Søraas, K. Aarsnes, K. Oksavik, and D. S. Evans (2007), Loss of relativistic electrons: Evidence for pitch angle scattering by electromagnetic ion cyclotron waves excited by unstable ring current protons, *Journal of Geophysical Research*, *112*, 12,213, doi:10.1029/2006JA012138.

Scharer, J. (1969), Ion-cyclotron instabilities resulting from a thermally anisotropic plasma, *Plasma Physics*, *11*, 1–10, http://www.iop.org/EJ/article/0032-1028/11/1/001/ppv11i1p1.pdf.

Scharer, J., and A. Trivelpiece (1967), Cyclotron wave instabilities in a plasma, *Physics of Fluids*, *10*, 591.

Sckopke, N. (1966), A general relation between the energy of trapped particles and the disturbance field near the Earth, *Journal of Geophysical Research*, *71*, 3125–3130.

Sheeley, B. W., M. B. Moldwin, H. K. Rassoul, and R. R. Anderson (2001), An empirical plasmasphere and trough density model: CRRES observations, *Journal of Geophysical Research*, *106*, 25,631, doi:10.1029/2000JA000286.

Sheskin, D. J. (2004), *Handbook of Parametric and Nonparametric Statistical Procedures* 3^{rd} *ed.*, Chapman and Hall/CRC, United states of America.

Shprits, Y. Y., D. A. Subbotin, N. P. Meredith, and S. R. Elkington (2008), Review of modeling of losses and sources of relativistic electrons in the outer radiation belt ii:

Local accelertion and loss, *Journal of Atmospheric and Solar-Terrestrial Physics*, *70*, 1694–1713.

Shprits, Y. Y., L. Chen, and R. M. Thorne (2009), Simulations of pitch angle scattering of relativistic electrons with MLT-dependent diffusion coefficients, *Journal of Geophysical Research*, *114*, 03,219, doi:10.1029/2008JA013695.

Singer, H. J., W. P. Sullivan, P. Anderson, F. Mozer, P. Harvey, J. Wygant, and W. William (1992), Fluxgate magnetometer instrument on the CRRES, *Journal of Spacecraft and Rockets*, *29*, 599–601.

Singh, A. K., D. Siingh, and R. P. Singh (2010), Space weather: Physics, effects and predictability, *Surveys in Geophysics*, *31*, 581, doi:10.1007/s10712-010-9103-1.

Siscoe, G. L., and N. U. Crooker (1974), On the partial ring current contribution to Dst, *Journal of Geophysical Research*, *79*, 1110–1112.

Smith, R., and N. Brice (1964), Propagation in multicomponent plasmas, *Journal of Geophysical Research*, *169*, 5029.

Spasojevic, M., and S. A. Fuselier (2009), Temporal evolution of proton precipitation associated with the plasmaspheric plume, *Journal of Geophysical Research*, *114*, 12,201, doi:10.1029/2009JA014530.

Spasojevic, M., J. Goldstein, D. L. Carpenter, U. S. Inan, B. R. Sandel, M. B. Moldwin, and B. W. Reinisch (2003), Global response of the plasmasphere to a geomagnetic disturbance, *Journal of Geophysical Research*, *108*, 1340, doi:10.1029/2003JA009987.

Spasojević, M., H. U. Frey, M. F. Thomsen, S. A. Fuselier, S. P. Gary, B. R. Sandel, and U. S. Inan (2004), The link between a detached subauroral proton arc and a plasmaspheric plume, *Geophysical Research Letters*, *31*, 04,803, doi:10.1029/2003GL018389.

Stern, D. P. (1977), Large-scale electric fields in the Earth's magnetosphere, *Reviews of Geophysics and Space Physics*, *15*, 156.

Stix, T. (1990), Waves in plasmas: Highlights from the past and present, *Physics of Fluids B Plasma Physics*, *2 No 8*, 1729–1743.

Stix, T. H. (1992), *Waves in Plasmas*, American Institute of Physics, New York.

Sugiura, M. (1964), Hourly values of equatorial Dst for the IGY, *Ann. of the Int. Geophys. Year*, *9*, 9–45.

Summers, D. (2005), Quasi-linear diffusion coefficients for field-aligned electromagnetic waves with applications to the magnetosphere, *Journal of Geophysical Research*, *110*, 08,213, doi:10.1029/2005JA011159.

Summers, D., and R. Thorne (2003), Relativistic electron pitch-angle scattering by electromagnetic ion cyclotron waves during geomagnetic storms, *Journal of Geophysical Research*, *108*, 1143.

Summers, D., R. M. Thorne, and F. Xiao (1998), Relativistic theory of wave-particle resonant diffusion with application to electron acceleration in the magnetosphere, *Journal of Geophysical Research*, *103*, 20,487–20,500.

Summers, D., C. Ma, N. Meredith, R. Horne, and R. Thorne (2004), Modeling outer-zone relativistic electron response to whistler-mode chorus activity during substorms, *Journal of Atmospheric and Solar-Terrestrial Physics*, *66*, 133–146, http://linkinghub.elsevier.com/retrieve/pii/S136468260300213X.

Summers, D., R. L. Mace, and M. A. Hellberg (2005), Pitch-angle scattering rates in planetary magnetospheres, *Journal of Plasma Physics*, *71*(3), 237–250, doi: 10.1017/S0022377804003186.

Summers, D., B. Ni, and N. Meredith (2007), Timescales for radiation belt electron acceleration and loss due to resonate wave-particle interactions: 2. evaluation for VLF chorus, ELF hiss, and electromagnetic ion cyclotron waves, *Journal of Geophysical Research*, *112, A04207*.

Tascione, T. F. (1994), *Introduction to the space environment, 2nd ed.*, Krieger Publishing Company, Malabar, FL.

Tepley, L. (1964), Low-latitude observations of fine-structured hydromagnetic emissions, *Journal of Geophysical Research*, *69*, 2273, doi:10.1029/JZ069i011p02273.

Tepley, L., and K. D. Amundsen (1965), Observations of continuous sub-ELF emissions in the frequency range 0.2 to 1.0 cycle per second, *Journal of Geophysical Research*, *70*, 234, doi:10.1029/JZ070i001p00234.

Tepley, L., and R. K. Landshoff (1966), Waveguide theory for ionospheric propagation of hydromagnetic emissions, *Journal of Geophysical Research*, *71*, 1499.

Tepley, L. R. (1961), Observations of hydromagnetic emissions, *Journal of Geophysical Research*, *66*, 1651, doi:10.1029/JZ066i006p01651.

Thomsen, M. F. (2004), Why Kp is such a good measure of magnetospheric convection, *Space Weather*, *2*, 11,004, doi:10.1029/2004SW000089.

Thorne, R., and R. Horne (1994), Energy transfer between energetic ring current h^+ and o^+ by electromagnetic ion cyclotron waves, *Journal of Geophysical Research*, *99*, 17,275–17,282.

Thorne, R. M. (2010), Radiation belt dynamics: The importance of wave-particle interactions, *Geophysical Research Letters*, *37*, 22,107, doi:10.1029/2010GL044990.

Thorne, R. M., and R. B. Horne (1997), Modulation of electromagnetic ion cyclotron instability due to interaction with ring current o^+ during magnetic storms, *Journal of Geophysical Research*, *102*, 14,155, doi:10.1029/96JA04019.

Thorne, R. M., and R. B. Horne (2007), Comment on Khazanov et al.[2002] and Khazanov et al.[2006], *Journal of Geophysical Research*, *112*(A12), 4, doi: 10.1029/2007JA012268.

Thorne, R. M., R. Horne, V. K. Jordanova, and J. Bortnik (2006), Interaction of EMIC waves with thermal plasma and radiation belt particles, in *Magnetospheric ULF Waves: Synthesis and New Directions. Geophysical monograph*, 169.

Trakhtengerts, V., and A. Demekhov (2007), Generation of Pc 1 pulsations in the regime of backward wave oscillator, *Journal of Atmospheric and Terrestrial Physics*, *69*, 1657–1656, http://linkinghub.elsevier.com/retrieve/pii/S1364682607001848.

Tsurutani, B., W. Gonzalez, and Y. Kamide (1997), Magnetic storms, *Surveys in Geophysics*, http://www.springerlink.com/index/X1682724W2460202.pdf.

Tsurutani, B. T., and G. S. Lakhina (1997), Some basic concepts of wave-particle interactions in collisionless plasmas., *Reviews of Geophysics*, *35*, 491, doi: 10.1029/97RG02200.

Tsurutani, B. T., W. D. Gonzalez, A. L. C. Gonzalez, F. L. Guarnieri, N. Gopalswamy, M. Grande, Y. Kamide, Y. Kasahara, G. Lu, I. Mann, R. McPherron, F. Soraas, and V. Vasyliunas (2006), Corotating solar wind streams and recurrent geomagnetic activity: A review, *Journal of Geophysical Research*, *111*, A07,801.

Turner, N. E., D. N. Baker, T. I. Pulkkinen, J. L. Roeder, J. F. Fennell, and V. K. Jordanova (2001), Energy content in the storm time ring current, *Journal of Geophysical Research*, *106 A9*, 19,149–19,156.

Turner, N. E., W. Cramer, S. Earles, and B. Emery (2009), Geoefficiency and energy partitioning in CIR-driven and CME-driven storms, *Journal of Atmospheric and Terrestrial Physics*, *71*, 1023–1031.

Ukhorskiy, A. Y., Y. Y. Shprits, B. J. Anderson, K. Takahashi, and R. M. Thorne (2010), Rapid scattering of radiation belt electrons by storm-time EMIC waves, *Geophysical Research Letters*, *37*, 09,101, doi:10.1029/2010GL042906.

Usanova, M. E., I. R. Mann, I. J. Rae, Z. C. Kale, V. Angelopoulos, J. W. Bonnell, K.-H.

Glassmeier, H. U. Auster, and H. J. Singer (2008), Multipoint observations of magnetospheric compression-related EMIC Pc1 waves by THEMIS and CARISMA, *Geophys. Res. Lett*, *35*, doi:10.1029/2008GL034458.

Usanova, M. E., I. R. Mann, Z. C. Kale, I. J. Rae, R. D. Sydora, M. Sandanger, F. Søraas, K.-H. Glassmeier, K.-H. Fornacon, H. Matsui, P. A. Puhl-Quinn, A. Masson, and X. Vallières (2010), Conjugate ground and multisatellite observations of compression-related EMIC Pc1 waves and associated proton precipitation, *Journal of Geophysical Research*, *115*, 07,208, doi:10.1029/2009JA014935.

Varma, P., G. Ahirwar, and M. S. Tiwari (2008), EMIC waves around the plasma-pause region, *Planetary and Space Science*, *56*, 1023, doi:10.1016/j.pss.2008.01.007.

Vasyliunas, V. M. (1975), Theoretical models of magnetic field line merging, 1, *Reviews of Geophysics*, *13*, 303, doi:10.1029/RG013i001p00303.

Wagner, W. (1984), Coronal mass ejections, *Annual Reviews in Astronomy and Astrophysics*, *22*, 267–289.

Wanliss, J. A., and K. M. Showalter (2006), High-resolution global storm index: Dst versus Sym-H, *Journal of Geophysical Research*, *111*, 02,202, doi:10.1029/2005JA011034.

Wentworth, R. C. (1964), Enhancement of hydromagnetic emissions after geomagnetic storms, *Journal of Geophysical Research*, *69*, 2291, doi:10.1029/JZ069i011p02291.

White, R. (1966), The Earth's radiation belts (Earth radiation belt, particle motion and magnetic cavity), *Physics Today*, *19 No 10*, 25.

Wilcox, J. (1966), Solar and interplanetary magnetic fields, *Science*, *152*, 161–166, http://www.sciencemag.org/cgi/content/citation/152/3719/161.

Williams, D. J. (1983), The Earth's ring current: Causes, generation, and decay, *Space Science Reviews*.

Willis, D. M. (1970), The electrostatic field at the magnetopause, *Planetary and Space Science*, *18*, 749, doi:10.1016/0032-0633(70)90056-5.

Winske, D., and N. Omidi (1992), Electromagnetic ion/ion cyclotron instability: Theory and simulations, *Journal of Geophysical Research*, *97*, 14,779–14,799.

Wu, C., and R. P. Lepping (2008), Geomagnetic activity associated with magnetic clouds, magnetic cloud-like structures and interplanetary shocks for the period 1995-2003, *Advances in Space Research*, *41*, 335–338, http://linkinghub.elsevier.com/retrieve/pii/S0273117707001044.

Yahnin, A. G., and T. A. Yahnina (2007), Energetic proton precipitation related to ion-cyclotron waves, *Journal of Atmospheric and Solar-Terrestrial Physics*, *69*, 1690–1706.

Yahnina, T., A. Yahnin, J. Kangas, and J. Manninen (2003), Energetic particle counterparts for geomagnetic pulsations of Pc1 and IPDP types, *Annales Geophysicae*, *4*, 2281–2292, http://www.ann-geophys.net/21/2281/2003/angeo-21-2281-2003.pdf.

Young, D. T., S. Perraut, A. Roux, and C. de Villedary (1981), Wave-particle interactions near Ω_{He^+} observed in GEOS 1 and 2 1. propagation of ion cyclotron waves in He^+ - rich plasma, *Journal of Geophysical Research*, *86, A8*, 6755–6772.

Yuan, Z., X. Deng, X. Lin, Y. Pang, M. Zhou, P. M. E. Décréau, J. G. Trotignon, E. Lucek, H. U. Frey, and J. Wang (2010), Link between EMIC waves in a plasmaspheric plume and a detached sub-auroral proton arc with observations of Cluster and IMAGE satellites, *Geophysical Research Letters*, *37*, 07,108, doi:10.1029/2010GL042711.

List of Publications

D.1 Publications

D.1.1 Refereed Papers

Halford, A.J., B.J. Fraser, S.K. Morley, EMIC Wave Activity During Geomagnetic Storm and Non Storm Periods: CRRES results, *Journal of Geophysical Research*, December 2010, doi:10.1029/2010JA015716

Halford, A.J., S.K. Morley, and B.J. Fraser, A parametric analysis of magnetospheric energy budgets of non-stormtime substorms, *Australian Institute of Physics, 18th National Congress*, 2008

Engebretson, M.J., J.L. Posch, A.J. Halford, G.A. Shelburne, A.J. Smith, M. Spasojevic, U. S. Inan, and R.L. Arnoldy, Latitudinal and seasonal variations of quasi periodic and periodic VLF emissions in the outer magnetosphere, *Journal of Geophysical Research*, 109, A05216, 2004

D.1.2 Masters Thesis

Halford, A.J., Energy transfer in the magnetosphere during isolated substorm Events, Masters Thesis University of Colorado Boulder, 2007

D.1.3 Publications of Meteorites

ACK astrom.10jul02 COD 673 OBS M. Hicks, A. Halford, S. Stierwalt, F. Galvez

AA91587 C2002 7 10.24620 20 8 20.53 - 5 0 43.2637

AA91587 C2002 7 10.24806 20 8 19.92 - 5 0 43.4637

AA91587 C2002 7 10.24974 20 8 19.37 - 5 0 43.5637

AA91587 C2002 7 10.25155 20 8 18.78 - 5 0 43.7637

AA91587 C2002 7 10.25274 20 8 18.40 - 5 0 43.8637

AA91587 C2002 7 10.25395 20 8 18.00 - 5 0 44.2637

RZO1LDB C2002 7 10.29503 21 32 32.02 + 7 31 26.0637

RZO1LDB C2002 7 10.30256 21 32 31.82 + 7 31 33.0637

RZO1LDB C2002 7 10.31012 21 32 31.61 + 7 31 39.8637

D.2 Presentations

D.2.1 Presenting Author

2010 -

Halford, A.J., B.J. Fraser, S.K. Morley, EMIC wave occurrence and plasmaspheric density during geomagnetic storms, Fall American Geophysical Union poster, 2010

Halford, A.J., Stormy with a chance of Precipitation, 3 min. Thesis competition faculty finalist June 2010, competitor at university level August 4th 2010, invited to present at Research Expo August 31

Invited interview on 1233 ABC Newcastle radio with Carol Duncan for science week on August 16th, 2010.

2009 -

Halford, A.J., B.J. Fraser, S.K. Morley, EMIC wave occurrence during geomagnetic storm events:CRRES results, Fall American Geophysical Union poster, 2009

Halford, A.J., B.J. Fraser, S.K. Morley, A preliminary look at EMIC wave occurrences during geomagnetic storm events, Australian Space Science Conference conference talk, 2009

2008 -

Halford, A.J., S.K. Morley, B.J. Fraser, Understanding the sources of variability in determining quiet time substorm energy budgets, Australian Institute of Physics conference talk, 2008

Halford, A.J., S.K. Morely, B.J. Fraser, Understanding the sources of variability in determining energy budgets, Australian Space Science Conference conference talk, 2008

Halford, A.J., D.N. Baker, S.K. Morley, B.J. Fraser, Energy transport and dissipation in the magnetosphere during non-storm time substorms, American Geophysical Union Western Pacific Geophysics Meeting conference talk, 2008

** Halford, A.J., Space Weather: Substorms, RHD Poster Session, August 2008

2007 -

Halford, A.J., D. Baker, J. Weygand, Energy Transport, Storage, and Dissipation in the Magnetosphere During Substorms, Spring American Geophysical Union, Acapulco Mexico poster, 2007

Halford, A.J., D. Baker, J. Weygand, Energy Transport, Storage, and Dissipation in the Magnetosphere During Isolated Substorm events, Joint Assembly conference poster, 2007

2005 -

Halford, A.J., D.N. Baker, R. Weigle, J. Weygand, A statistical study of geomagnectic activity during times when cluster is in the plasma sheet. Cedar - Geospace Environment Modeling joint meeting conference poster, Santa Fe New Mexico, 2005

2004 -

Halford, A.J., X. Li, Temerin, A new look at the Temerin-Li model Inner Magnetosphere Interactions Yosemite National Park CA Febuary, 2004

Halford, A. J., D.N. Baker, et al., A closer look at the Dst, GEM Snowmass Colorado June, 2004

Halford, A.J., R. Weigel, D. Baker, Sensitivity tests of the Temerin-Li model, American Geophysical Union Fall Conference poster, 2004

2002 -

*Halford, A.J., M.J., Engebretson, J.L., Posch, A.J., Smith, U.S. Inan, Latitudinal and seasonal variations of quasiperiodic and periodic ELF-VLF Emissions, American Geophysical Union Spring Meeting poster paper, 2002

* Received Outstanding student paper award for poster at Spring 2002 American Geophysical Union conference

** Voted Best Poster by participating students

D.2.2 Presentations and Posters I am an Author on but did not Present Myself

Stierwalt, S.R., B.J. Buratti, M.D. Hicks, A.J. Halford, First Ground-Based Look at Compositional Differences in the Uranian Satellites, American Geophysical Fall Meeting 2002

Engebretson, M.J., J.L. Posch, G.A. Shelburne, A.J. Halford, A.J. Smith, M. Spasojevich, U.S. Inan, R.L. Arnoldy, Diurnal Variations of Quasi-Periodic and Periodic VLF emissions in the Outer Magnetosphere, American geophysical Union Fall meeting 2003